

# Gravity-Wave Breakdown in a Rotating Boussinesq Fluid: Linear and Nonlinear Dynamics

Habilitationsschrift

zur

Erlangung des akademischen Grades

doctor rerum naturalium habilitatus (Dr. rer. nat. habil. )

der Mathematisch-Naturwissenschaftlichen Fakultät

der Universität Rostock

vorgelegt von

Ulrich Achatz, geb. am 31. Oktober 1963 in München

aus Kühlungsborn

Kühlungsborn, 20. März 2006



# Contents

<b>I</b>	<b>Introduction</b>	<b>4</b>
1	Statement of the problem	5
2	Gravity waves in a rotating Boussinesq fluid	13
<b>II</b>	<b>Linear stability theory</b>	<b>18</b>
3	Basic instability concepts	19
3.1	Normal modes . . . . .	20
3.2	Singular vectors . . . . .	20
4	Linear stability of inertia-gravity wave packets	22
4.1	Wave packet and model hierarchy . . . . .	22
4.1.1	The linear model for the general IGW packet . . . . .	23
4.1.2	Approximation of the IGW by a one-dimensional profile . . . . .	24
4.1.3	Approximation by a stratified constant-shear layer . . . . .	26
4.2	Analysis in the shear-layer approximation . . . . .	27
4.2.1	Normal modes and singular vectors . . . . .	27
4.2.2	Energetics and temporal development . . . . .	34
4.3	Analysis of the 1D profile . . . . .	39
4.3.1	Normal modes and short-term singular vectors . . . . .	40
4.3.2	Singular vectors for long optimization times . . . . .	45
4.3.3	Energetics and temporal development . . . . .	47
4.4	General inertia-gravity wave packets . . . . .	64

4.5	Summary . . . . .	69
<b>5</b>	<b>General monochromatic gravity waves</b>	<b>73</b>
5.1	The linear model . . . . .	73
5.2	Growth factors . . . . .	75
5.2.1	Short optimization times . . . . .	77
5.2.2	Longer optimization times . . . . .	80
5.3	Energetics and time development . . . . .	84
5.3.1	Inertia-gravity waves . . . . .	88
5.3.2	High-frequency gravity waves . . . . .	96
5.4	Impact of the controlling parameters . . . . .	105
5.4.1	Reynolds number . . . . .	105
5.4.2	Rotation . . . . .	107
5.5	Mean growth from random initial conditions . . . . .	108
5.6	Summary . . . . .	112
<b>III</b>	<b>Nonlinear dynamics</b>	<b>114</b>
<b>6</b>	<b>Monochromatic inertia-gravity waves</b>	<b>115</b>
6.1	Model setup . . . . .	116
6.2	Energetics . . . . .	119
6.3	NMs and SVs of a statically unstable IGW . . . . .	121
6.3.1	Parallel modes ( $\alpha = 0^\circ$ ) . . . . .	125
6.3.2	Transverse modes ( $\alpha = 90^\circ$ ) . . . . .	127
6.4	SVs of a statically stable IGW . . . . .	130
6.4.1	Short optimization time $\tau = 5\text{min}$ . . . . .	133
6.4.2	Long optimization time $\tau = 30\text{min}$ . . . . .	137
6.5	Comparison to observations . . . . .	138
6.6	Summary . . . . .	142



<b>7 Monochromatic high-frequency gravity waves</b>	<b>145</b>
7.1 Perturbation of the wave by normal modes . . . . .	147
7.1.1 Statically unstable HGWs . . . . .	151
7.1.2 Statically stable HGWs . . . . .	154
7.2 Singular vectors . . . . .	158
7.3 Summary . . . . .	162
<b>8 Summary and conclusions</b>	<b>165</b>
<b>A Technical aspects</b>	<b>170</b>
<b>B The shear-layer approximation</b>	<b>172</b>
<b>C WKB theory</b>	<b>174</b>
C.1 General theory . . . . .	174
C.2 Optimal perturbations of IGWs . . . . .	175
C.3 Parallel SVs of HGWs . . . . .	177
<b>D Projection onto free normal modes</b>	<b>179</b>
<b>Bibliography</b>	<b>181</b>

# Part I

## Introduction

# Chapter 1

## Statement of the problem

By now it is widely acknowledged that internal gravity waves (GWs) play an important role in both oceanic and atmospheric dynamics (Müller et al., 1986; Fritts and Alexander, 2003, e.g.). Nonetheless, for a long time they have been more or less a mere nuisance for modern weather prediction. Each time an atmospheric state departs from the geostrophic equilibrium between the pressure gradient force and the Coriolis force a corresponding balance is reestablished by the radiation of GWs (Rossby, 1938; Cahn, 1945). Since the equilibrated forces are each separately quite large this can have dramatic consequences. Slight errors in the estimate of the initial atmospheric state, determined in some way from observations, can lead to corresponding imbalances, and thus cause spurious GW oscillations at amplitudes large enough for spoiling the whole forecast. In conjunction with modern data assimilation techniques this is nowadays managed by normal mode initialization (Machenhauer, 1977; Tribbia, 1984; Temperton, 1988). The leading GWs are filtered from the initial state in such a way that the associated oscillations are reduced to a minimum.

Simply filtering GWs from the fluid-dynamical fields, however, is not sufficient since besides the artificially initialized waves many others are indeed radiated from spontaneous flow imbalances (near frontal of convective systems), but also from flow over topography and strong wind shear near upper-tropospheric jets<sup>1</sup>. These can transport momentum

---

<sup>1</sup>The troposphere extends from the ground to the tropopause, marked by a local minimum of the large-scale temperature, at about 15km altitude. The adjacent atmospheric layer is the stratosphere which ranges up to the stratopause near 50km altitude. That altitude exhibits a temperature maximum

and energy over long distances. In case of an upwards propagation they can, due to energy conservation in a vertically decreasing ambient density field, grow substantially in amplitude. Unless they are absorbed at some critical layer (Bretherton, 1966; Booker and Bretherton, 1967) or get deflected at wind or stratification gradients (Chimonas and Hines, 1986; Fritts and Yuan, 1989a; Bühler and McIntyre, 1999) they eventually become subject to instabilities and wave breaking. The associated effects are all but unimportant.

An experience many air plane travellers share is that of clear-air turbulence (CAT) disturbing the flight. In fact, CAT remains a serious concern for the aviation industry, and it also critically affects the mixing and stratosphere-troposphere exchange of chemical constituents. Therefore its generation by breaking GWs is presently an intense field of research (Shapiro, 1980; Pavelin et al., 2002; Whiteway et al., 2003; Lane et al., 2004; Koch et al., 2005, e.g.). Another aspect is the impact of small-scale GWs of orographic origin on the predicted larger-scale flow. It has been recognized that small-scale topography, even if not resolved in weather-forecast or climate models, leads to the radiation of nonnegligible GWs which typically break in the lower stratosphere, thus exerting, via the corresponding momentum deposition, a drag on the flow which must be taken into account for reasonable predictions or simulations. This is presently done via suitably formulated parameterization schemes (Palmer et al., 1986; McFarlane, 1987; Scinocca and McFarlane, 2000).

A region of the atmosphere not only influenced but really controlled by GWs is the mesosphere. This altitude range (about 50–90km) is marked by a strong departure of the temperature field from its radiative equilibrium. The coldest region of the atmosphere as a whole is the summer (!) polar mesopause (near 90km altitude) with temperatures approaching 100K, while the winter mesosphere is remarkably warm (Lübken and von Zahn, 1991; Lübken, 1999, e.g.). This is probably the most prominent effect of GW breaking and the associated momentum and energy deposition in the atmosphere (Hines, 1960; Houghton, 1978; Lindzen, 1981; Holton, 1982, 1983; Garcia and Solomon, 1985). As an example, the left panel in Fig. 1.1 shows the zonal mean (i.e. averaged over the geographic longitude) of the mean January temperature according to a simulation of

---

which is due the absorption of solar radiation by the ozone layer there

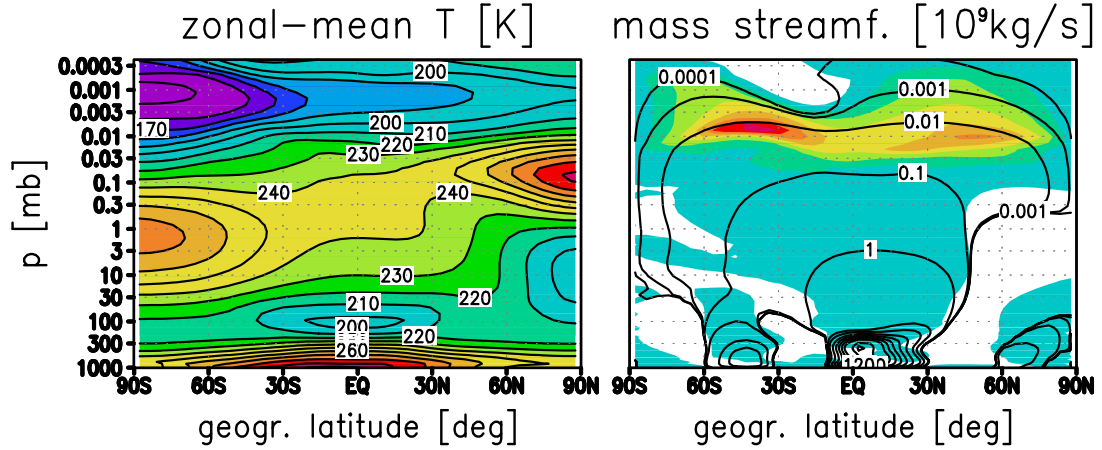


Figure 1.1: For January, the zonal-mean temperature (left panel, in units of K) and the mass streamfunction of the zonal-mean flow (right, contours in units of  $10^9 \text{ kg/s}$ ), according to a simulation by Becker and Schmitz (2003). The direction of the movement along the streamlines in the right panel can be inferred from the meridional (i.e. south-northwards) velocity, which is indicated by shading, with a shading interval of  $2 \text{ m/s}$ . Only regions with positive meridional velocity are shown. In both panels the altitude is indicated by pressure levels.

the atmosphere in a simplified general circulation model by Becker and Schmitz (2003). In conjunction with the Coriolis force the momentum deposition causes a zonal-mean flow from the mesospheric summer pole to the winter pole (right panel). The resulting upwelling at the summer pole is accompanied by an expansion of the air masses, due to the vertical decrease of the ambient pressure, and thus leads to strong adiabatic cooling. This explains the extremely low temperatures in the mesosphere over the summer pole. The downwelling and adiabatic heating over the winter pole leads at the same time to the increased temperatures there. A conspicuous secondary effect of this is that the positive gradient of the temperature from summer to winter causes, via the thermal-wind relation, a strong vertical gradient in the zonal-mean zonal (i.e. west-eastwards) wind so that it changes sign near the mesopause. This is shown in Fig. 1.2, where for a comparison also the zonal-mean zonal wind is shown which results from an integration of the model without a parameterization of the impact of the GWs. A further consequence of GW breaking in the middle atmosphere is that turbulence can be excited (Lindzen, 1981)

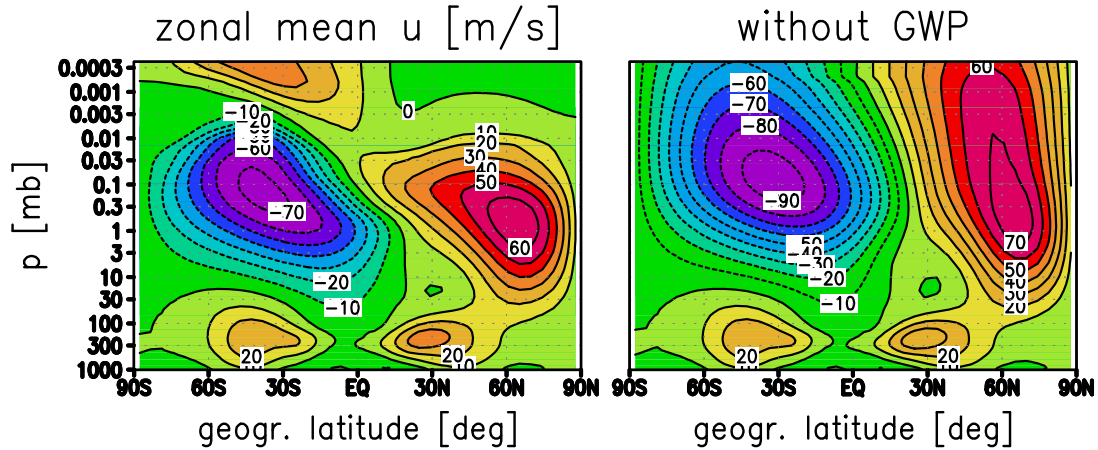


Figure 1.2: From the same simulation as shown in Fig. 1.1, the zonal-mean zonal wind (left panel, in units of m/s). The right panel shows the corresponding result obtained in an integration without GW parameterization.

which might be of relevance for the heat budget in the upper mesosphere (Lübken, 1997; Becker and Schmitz, 2002; Müllemann et al., 2003).

Unfortunately, while this overall picture is commonly agreed upon, many details in GW excitation, propagation, and finally breaking are not sufficiently understood yet, so that one is confronted with an uncomfortably large number of widely accepted, but quite different, schemes for the parameterization of the impact of GWs on the large-scale flow in the middle atmosphere (Lindzen, 1981; Medvedev and Klaassen, 1995; Hines, 1997a,b; Alexander and Dunkerton, 1999; Warner and McIntyre, 2001). A central problem is our lack of sufficient knowledge about the final nonlinear GW breakdown, a process which is also fundamental for the other GW effects described above. We do not sufficiently know how the turbulence produced there behaves, which already poses problems to studies of GWs in simulations with parameterized turbulent scales. Moreover, the GW breaking itself has so far resisted all attempts to cast its essence into a trustworthy parameterization.

Still, there is hope that numerical simulations will eventually help us in getting a better understanding and, indeed, considerable progress has been made in this field. Early studies have avoided an explicit description of the resulting small-scale turbulence by either excessive diffusion or a parameterization of the smallest scales (Winters and D’Asaro,

1994; Andreassen et al., 1994; Fritts et al., 1994; Isler et al., 1994; Lelong and Dunkerton, 1998a,b). Recent work, however, has employed direct numerical simulations (DNS) where all scales are properly resolved (Fritts et al., 2003, 2006). While such calculations, at Reynolds numbers in the range  $10^3 - 10^5$ , will certainly yield the least ambiguous results they also put a very high demand on presently available computer resources. Therefore, and also for the sake of systematic insight, good a priori knowledge of the developing scales and structures seems highly desirable. It thus appears important to have a very good understanding of the initial linear phase of the wave instability: It sets the stage for the nonlinear wave decay, and corresponding studies not only provide us with possible instability thresholds but also with perturbation patterns and wavelengths to be focussed on in the simulations.

Indeed much has already been learned in the past. A widespread misconception is that instability does not set in before the wave amplitude causes local vertical gradients of density (or potential temperature) and flow field allowing for static or dynamic instability. In the former case, one needs an overturning of density or potential-temperature layers, while in the latter case the local Richardson number  $Ri$  must fall due to sufficient vertical shear below a certain threshold. This picture rests on the work of Howard (1961) and Miles (1961) who have shown that in plane-parallel vertically stratified flow  $Ri < 1/4$  is a necessary condition for instability. Strictly speaking this only applies locally to monochromatic GWs with exactly vertical phase propagation. At least approximately this is the case for monochromatic inertia-gravity waves (IGWs) with nearly vertical propagation. A corresponding stability analysis has been done by Yau et al. (2004). At statically unstable wave amplitudes, rapidly growing normal modes (NMs) are found. At statically stable amplitudes NM growth is, even in the inviscid-nondiffusive limit, rather weak, unless the IGW inclination angle is extremely steep. In that case one gets an effect from the shear of the near-circularly polarized horizontal velocity field in the wave. In high-frequency gravity waves (HGWs) with slantwise phase propagation (i.e. at a non-vertical inclination angle to the horizontal) the static and dynamic instability criteria are not applicable. Indeed we know by now that such waves show instabilities at all amplitudes, unless damped by viscosity (Mied, 1976; Klostermeyer, 1982, 1983, 1991;

Lombard and Riley, 1996; Sonmor and Klaassen, 1997).

A limitation of these studies is that they had to rely on the monochromaticity of the wave, a condition seldom met in purity. Only in that case one can choose a reference system, i.e. the one moving with the phase velocity of the wave, within which the GW is time independent. This is a necessary condition for a rigorous NM analysis. In more general cases one can either try to neglect the time dependence of the wave, as has been done in the studies of IGW packets (Fritts and Yuan, 1989b; Yuan and Fritts, 1989; Dunkerton, 1997; Kwasniok and Schmitz, 2003), or the stability theory must be generalized. This leads to an additional aspect which is just beginning to get a systematic focus: Even for stationary reference states NM analyses only provide information about possible time-asymptotic wave instabilities at infinitely small perturbation level. It is however known from several other fields of fluid dynamics that under conditions when no growing NMs exist rapid transient growth of so-called optimal perturbations or singular vectors (SVs) can still be possible (Farrell, 1988a,b; Boberg and Brosa, 1988; Butler and Farrell, 1992; Trefethen et al., 1993). Provided a sufficiently high, but possibly yet small, initial perturbation level is available this can lead to the onset of turbulence even when such a result would not be expected from a NM analysis. Moreover, even if growing NMs exist, it may happen that they take much longer in their amplification so that the incipient instability is better characterized by transient growth leading directly into the nonlinear decay phase. Luckily, a SV analysis by which such possibilities are examined does not rely on the stationarity of the wave examined. A corresponding study of the GW stability problem thus seems to be in place.

The application of the results from such a linear analysis to wave breaking leads directly to another question of potential interest. In stressing the eventual three-dimensionality of the developing turbulent spectrum previous studies have typically perturbed a GW by small random disturbances, and described the hence ensuing wave decay process. Certainly this has already taught us a lot, but it still seems to be of conceptual interest what time development the GW and its perturbation will take if the latter is initially identical to a leading NM or SV. One might qualify this as a purely academic problem, but indeed there is hope that corresponding studies might highlight paradigm-



matic features which might be useful both for the interpretation of measurements and observations of GW breaking and for eventual progress in the parameterization of the impact of wave breaking and turbulence on the larger-scale flow.

This thesis therefore addresses the following two main sets of questions:

- What can we learn from an extension of the linear stability theory from NM analyses to the determination of characteristic optimal perturbations? Are SVs potential candidates for the triggering of wave breaking and turbulence onset where NMs cannot lead to such a development? How do NMs, if well-defined, and SVs compare to each other in their linear dynamics.?
- What nonlinear development do we get if a GW is perturbed by its leading NM or SV? What impact do different NMs have on the GW, and how does this compare to the corresponding results from a perturbation of the GW by a leading SV? Are the features observed comparable to available observations?

With this program the thesis is structured as follows:

In order to further prepare the ground, chapter 2 gives a short overview of the most important properties of GWs under the Boussinesq approximation. With the same intention chapter 3 reviews the concepts of NMs and SVs in linear instability theory so that the reader can follow the ensuing analyses. These start with a study of the generalized stability of IGW packets in chapter 4. Due to their near-vertical propagation they have a comparatively simple structure which allows two helpful levels of simplifications. In one of those the IGW packet is locally approximated as a stratified shear layer with reduced static stability. This even admits closed analytical solutions containing much comprehensive information on the parameter dependence of optimal growth. They also help understanding the responsible growth mechanisms. The second simplification of the IGW, by its vertical profile at the statically least stable horizontal location, further clarifies the role of the elliptically polarized horizontal flow field in the IGW in modifying and merging these mechanisms. The verification of the results follows in an examination of the non-simplified IGW packet. As one might have guessed from the applicability of the shear-layer theory it turns out that many results do not really hinge on the wave-packet

envelope. Thus the question arises how much of the results from chapter 4 can be transferred to monochromatic IGWs. At the same time one might ask about the generalized stability of monochromatic HGWs. This is done in chapter 5.

On the basis of the linear results the other major part of the thesis discusses the breaking of GWs initialized by NMs or SVs. For reasons of practicality and conceptual simplicity this is done for monochromatic waves. In chapter 6 this is first discussed for IGWs. In corresponding 2.5D DNS, where the possible impact of secondary perturbations with horizontal directions of propagation transverse to those of the primary NM or SV is neglected, it is found that indeed SVs extend the range of possibilities for turbulence onset. The chapter also profits from the previous linear analyses. Much of the nonlinear behavior observed can only be well understood on that basis. Specifically this also refers to the spatial distribution of the turbulent fields within the IGW, which turns out to be controlled by the elliptic polarization of the flow field in the wave. In order to complete the picture chapter 7 finally explores the dynamics of a HGW after a perturbation by its NMs or SVs. Although the DNS is again 2.5D, many results from more comprehensive 3D simulations in the literature are re-identified, pointing at the applicability of such an approach for further studies. Finally also here the characteristics of the nonlinear development of SV perturbations is studied, pointing at a possible relation to layering of turbulence as observed in the measurements. The thesis is concluded by a synthesis and discussion of all results in chapter 8

## Chapter 2

# Gravity waves in a rotating Boussinesq fluid

The problem is discussed in the simplest possible framework, i.e. the Boussinesq equations on an  $f$  plane

$$\nabla \cdot \mathbf{v} = 0 \quad (2.1)$$

$$\frac{\partial \mathbf{v}}{\partial t} + (\mathbf{v} \cdot \nabla) \mathbf{v} + f \mathbf{e}_z \times \mathbf{v} + \nabla p - \mathbf{e}_z b = \nu \nabla^2 \mathbf{v} \quad (2.2)$$

$$\frac{\partial b}{\partial t} + (\mathbf{v} \cdot \nabla) b + N^2 w = \mu \nabla^2 b \quad . \quad (2.3)$$

Here  $\mathbf{v} = (u, v, w)$  denotes the three-dimensional velocity field. The buoyancy  $b = g(\theta - \bar{\theta}(z))/\theta_0$  is a measure of the deviation of the potential temperature  $\theta$  from a merely vertically dependent reference profile  $\bar{\theta}(z)$ , normalized by a characteristic value  $\theta_0$ .  $g$  is the vertical gravitational acceleration. The squared background Brunt-Vaisala frequency is  $N^2 = (g/\theta_0)d\bar{\theta}/dz$ . An equivalent interpretation of buoyancy and Brunt-Vaisala frequency is  $b = -g(\rho - \bar{\rho}(z))/\rho_0$  and  $N^2 = -(g/\rho_0)d\bar{\rho}/dz$  where  $\rho$ ,  $\bar{\rho}(z)$ , and  $\rho_0$  are density, a corresponding reference field, and a characteristic value, respectively.  $p$  is the pressure field, normalized by a constant reference density,  $f$  the Coriolis parameter, and  $\mathbf{e}_z$  the vertical unit vector. The Boussinesq equations can be expected to give a reasonably good approximation of the full GW dynamics as long as the focus is on processes with vertical scales of the order or less than the atmospheric or oceanic scale height. This is the case throughout this study. For viscosity and thermal diffusivity the typical upper-mesospheric

values  $\nu = \mu = 1\text{m}^2/\text{s}$  are taken (unless stated otherwise). For better readability for a broader audience it has been decided not to nondimensionalize the equations. One should, however, keep in mind that a non-dimensionalization, using the GW wavelength  $\Lambda$  (specified below) and the Brunt-Vaisala period  $T = 2\pi/N$  as length and time scales, would leave as the only controlling parameters the ratio  $f/N$ , the Reynolds number  $\text{Re} = \Lambda^2/(\nu T)$ , and the Prandtl number  $\text{Pr} = \nu/\mu$ . For later reference also the energy density  $e = 1/2 \left( |\mathbf{v}|^2 + b^2/N^2 \right)$  is introduced which obeys

$$\frac{\partial e}{\partial t} + \nabla \cdot \left[ \mathbf{v}(e + p) - \nu \nabla \frac{|\mathbf{v}|^2}{2} - \mu \nabla \frac{b^2}{2N^2} \right] = -\nu \sum_{i=1}^3 |\nabla v_i|^2 - \mu \left| \nabla \frac{b}{N} \right|^2 \quad . \quad (2.4)$$

In the inviscid-nondiffusive limit with typical (e.g. periodic) boundary conditions the volume integral of energy density is obviously a conserved quantity.

The equations admit as exact solutions monochromatic GWs of the form

$$\begin{pmatrix} \mathbf{v} \\ b \end{pmatrix} = a \Re \left[ \begin{pmatrix} \tilde{\mathbf{v}} \\ \tilde{b} \end{pmatrix} e^{i\phi} \right] \quad . \quad (2.5)$$

The amplitudes  $(\tilde{\mathbf{v}}, \tilde{b})$  will be specified below. The phase is  $\phi = \mathbf{K} \cdot \mathbf{x} - \Omega t$ , with wavenumber  $\mathbf{K} = (K_x, K_y, K_z)$  and frequency  $\Omega$  satisfying the dispersion relation

$$\Omega = \pm \sqrt{N^2 \cos^2 \Theta + f^2 \sin^2 \Theta} \quad . \quad (2.6)$$

Here  $\Theta$  is the inclination angle of the GW vector with respect to the horizontal so that  $(\cos \Theta, \sin \Theta) = (K_x/\sqrt{K_x^2 + K_z^2}, K_z/\sqrt{K_x^2 + K_z^2})$ . Without loss of generality it is assumed that  $K_y = 0$ . Then the wave amplitudes are

$$(\tilde{\mathbf{v}}, \tilde{b}) = -c_x \left( 1, -i \frac{f}{\Omega}, -\cot \Theta, iN \frac{N}{\Omega} \cot \Theta \right) \quad , \quad (2.7)$$

where  $c_x = \Omega/K_x$  is the horizontal phase velocity. The nondimensional amplitude factor  $a$  is defined so that the wave is statically stable for  $a < 1$ , i.e. at these values one has  $N^2 + \partial b/\partial z > 0$  everywhere. In other words it is the amplitude relative to the overturning or static instability threshold. At  $K_z > 0$  the minus-branch of the dispersion relation represents a wave with upward directed group velocity  $\mathbf{c}_g = \nabla_{\mathbf{K}} \Omega$ , but downward directed phase velocity  $\mathbf{c} = (\Omega/K) (\mathbf{K}/K)$ , where  $K = |\mathbf{K}|$ .

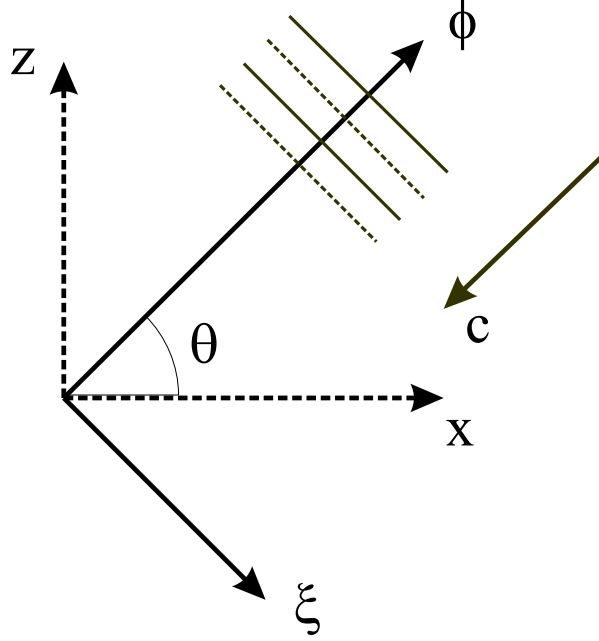


Figure 2.1: The rotated and translated coordinate system for the simplest representation of a monochromatic GW. The (orthogonal)  $\xi$ - and  $\phi$ -axes lie in the  $x - z$  plane. The  $y$ -axis points vertically into that plane. The new coordinate system moves with the phase velocity  $\mathbf{c}$  of the GW, rendering the latter stationary.

Following Mied (1976) and Drazin (1977) a coordinate system can be introduced for monochromatic GWs in which their representation is especially simple. It is obtained by a rotation about the  $y$ -axis so that the new vertical coordinate points in the direction of the wave number vector, a translation along this axis with the phase velocity, and a rescaling of the vertical axis in units of the wave phase (see also Fig. 2.1). The new coordinates are  $(\xi, y, \phi)$  with

$$\xi = x \sin \Theta - z \cos \Theta \quad (2.8)$$

$$\phi = K(x \cos \Theta + z \sin \Theta) - \Omega t \quad . \quad (2.9)$$

The rotated velocity components along the new axes being  $u_\xi$ ,  $v$ , and  $u_\phi$ , the GW takes in this representation the time-independent form

$$u_\xi = -a \frac{\Omega/K}{\sin \Theta \cos \Theta} \sin \phi \quad (2.10)$$

$$v = a \frac{f/K}{\cos \Theta} \cos \phi \quad (2.11)$$

$$u_\phi = 0 \quad (2.12)$$

$$b = -a \frac{N^2/K}{\sin \Theta} \cos \phi \quad . \quad (2.13)$$

For easier comparability to some of the literature (Klostermeyer, 1982; Yau et al., 2004) it is noted that there the nondimensional  $u_\xi$ -amplitude  $2A = -(a\Omega/N) / (\sin \Theta \cos \Theta)$  is used for a characterization of the wave. The phase convention (Yau et al., 2004, e.g.) is such that the buoyancy gradient minimizes (maximizes) at  $\phi = 3\pi/2$  ( $\pi/2$ ). The largest shear due to  $u_\xi$  occurs at  $\phi = 0, \pi$ , and the largest shear due to  $v$  (only relevant for IGWs where  $R = |f/\Omega|$  is not negligible) is at the extrema of the buoyancy gradient. The relationship of  $a$  to the amplitude of  $u_\xi$  and to energy density integrated over one wave train is given by

$$E = \int_0^{2\pi} d\phi e = \pi \frac{a^2 (f^2 \sin^2 \Theta + N^2 \cos^2 \Theta)}{K^2 \sin^2 \Theta \cos^2 \Theta} = \pi \left( 2A \frac{N}{K} \right)^2 \quad . \quad (2.14)$$

In view of its frequent application, the local Richardson number in the wave also deserves a short discussion. It appears in a NM analysis of a shear flow obtained by neglecting in the GW all vertical motions, its time dependence, and the horizontal dependence. The resulting Taylor-Goldstein equation (Howard, 1961; Miles, 1961; Fritts and Rastogi, 1985; Dunkerton, 1997) contains a height-dependent Richardson number which also depends on the horizontal direction of propagation of the NM with respect to that of the GW. A necessary condition for a NM to grow is that its respective Richardson number is anywhere less than  $1/4$  (Howard, 1961; Miles, 1961). Of most interest therefore is the minimum of the Richardson number, both over all horizontal directions of mode propagation and over all altitudes (or phases). At a given phase, the minimum over all directions of propagation is

$$\text{Ri}_m = \frac{N^2 + \partial b / \partial z}{(\partial u / \partial z)^2 + (\partial v / \partial z)^2} \quad . \quad (2.15)$$

Inserting the wave fields (2.10)–(2.13) and using the coordinate transformations (2.8)–(2.9) and the dispersion relation (2.6) one finds

$$\text{Ri}_m = \frac{1 - R^2}{a^2 (1 - \Omega^2/N^2)} \frac{1 + a \sin \phi}{1 - (1 - R^2) \sin^2 \phi} \quad . \quad (2.16)$$

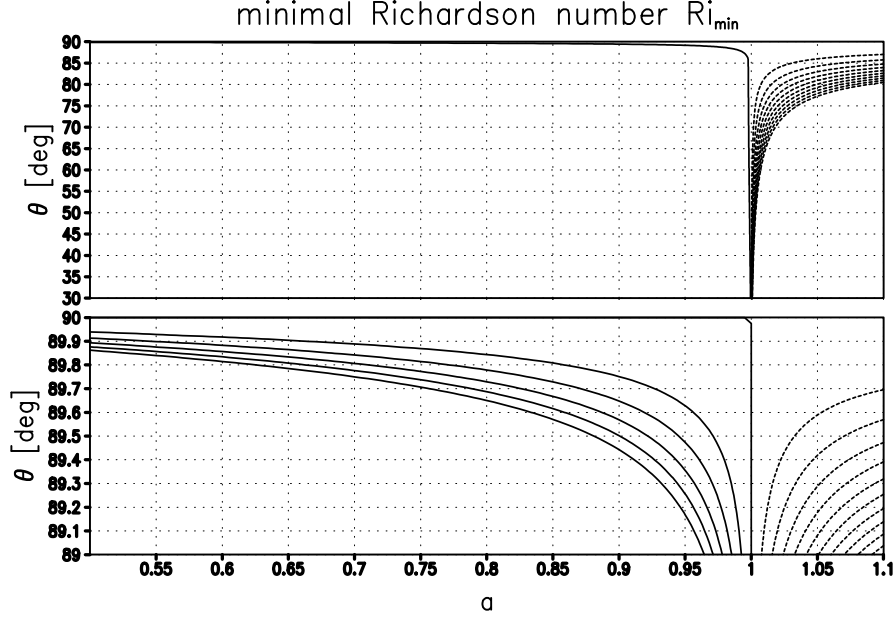


Figure 2.2: The minimal Richardson number  $Ri_{min}$  in a monochromatic GW in its dependence on the wave amplitude  $a$  with respect to static instability and its inclination angle  $\Theta$  with respect to the horizontal. The upper panel shows the range  $30^\circ \leq \Theta \leq 90^\circ$ . Isolines are between 0.25 (leftmost contour) and -50.25 in steps of 5. The lower panel shows the range  $89^\circ \leq \Theta \leq 90^\circ$ . Here contours are between 0.25 and -0.5 in steps of 0.05.

The minimum of  $Ri_m$  over all phases is at

$$\sin \phi = \begin{cases} -1 & \text{if } a > 2(1 - R^2) / (2 - R^2) \\ -1/a + \sqrt{1/a^2 - 1/(1 - R^2)} & \text{else} \end{cases} \quad (2.17)$$

This minimal value,  $Ri_{min}$ , is shown as a function of  $a$  and  $\Theta$  in Fig. 2.2. As is well known, only for IGWs the Richardson-number criterion  $Ri < 1/4$  for dynamic instability can be satisfied for  $a \ll 1$ .

## Part II

### Linear stability theory



## Chapter 3

# Basic instability concepts: Normal modes and optimal perturbations

In the linear stability analysis of some reference solution  $(\mathbf{V}_0, B_0)(\mathbf{x}, t)$  of the Boussinesq equations, here given by a monochromatic GW or a GW packet, one asks for the time development resulting from arbitrary perturbations at the initial time  $t = 0$ . For this purpose the decomposition  $(\mathbf{v}, b)(\mathbf{x}, t) = (\mathbf{V}_0, B_0)(\mathbf{x}, t) + (\mathbf{v}', b')(\mathbf{x}, t)$  with the perturbation  $(\mathbf{v}', b')$  is inserted into the Boussinesq equations which are then linearized about the reference solution. One then asks what initial perturbation leads within this linear approximation to the strongest perturbation growth. Here the concepts of NMs and SVs come into play. For reasons of practical simplicity it is assumed in the following discussion that, as is usually the case, the linear equations have been discretized in a suitable manner, so that the perturbation can be described by a (possibly complex, see below) state vector  $\mathbf{x}(t)$  containing as elements the values of  $\mathbf{v}'$  and  $b'$  at all model grid points. The dynamics of the linear model is then given by  $d\mathbf{x}/dt = \mathcal{A}(t)\mathbf{x}$  with some model operator  $\mathcal{A}$ . Within this framework the concepts of NMs and SVs are explained in the two sections below, while technical aspects are covered in the appendix A. An interested reader is advised to read the latter after this chapter.

### 3.1 Normal modes

NMs are strictly only defined for time-independent reference solutions, as e.g. a monochromatic GW in the transformed coordinate system (2.8) - (2.9). Under this condition they are the eigenvectors  $\mathbf{n}_\nu$  of the model operator, satisfying

$$\mathcal{A}\mathbf{n}_\nu = -i(\omega_\nu + i\gamma_\nu)\mathbf{n}_\nu \quad (3.1)$$

with an eigenvalue consisting of an eigenfrequency  $\omega_\nu$  and a growth rate  $\gamma_\nu$ . An initial state given up to an amplitude  $a_\nu$  by a NM, i.e.  $\mathbf{x}(0) = a_\nu\mathbf{n}_\nu$ , leads to a time-dependent solution

$$\mathbf{x}(t) = a_\nu e^{\gamma_\nu t} e^{i\omega_\nu t} \mathbf{n}_\nu \quad , \quad (3.2)$$

so that the existence of a growing NM with  $\gamma_\nu > 0$  implies linear instability. In addition, in typical cases where all NMs form together a complete set, every initial state can be written as a superposition of NMs behaving in time as given by (3.2) so that, *if an initial state projects even to the least onto the leading NM (if there is one, with largest  $\gamma_\nu$ ), this NM will be approached asymptotically as  $t \rightarrow \infty$ .*

### 3.2 Singular vectors

While a NM analysis searches perturbations growing exponentially in time, a SV analysis explores the possibility of rapid *transient* growth. For this one needs a definition of the strength of a perturbation, i.e. a norm  $\|\mathbf{x}\|^2 = \bar{\mathbf{x}}^t \mathcal{M} \mathbf{x}$  where the metric  $\mathcal{M}$  is positive definite and symmetric. The upper index  $t$  denotes transposition, the overbar taking the complex conjugate. Among the different possible choices the present study uses the discretized version of

$$\|\mathbf{x}\|^2 = \int_0^{2\pi} d\phi \varepsilon = \int_0^{2\pi} d\phi \frac{1}{2} (|\mathbf{v}|^2 + \frac{|b|^2}{N^2}) \quad , \quad (3.3)$$

with an integrand  $\varepsilon$  which is proportional to the average of energy density over one horizontal wavelength of the perturbation. The metric thus takes a simple diagonal form. Given a norm, a SV analysis asks what initial perturbation  $\mathbf{x}(0)$  would maximize for some given finite time  $\tau$  the ratio  $\|\mathbf{x}(\tau)\|^2 / \|\mathbf{x}(0)\|^2$ . For an answer one needs the propagator

matrix  $\Phi(\tau)$  mapping the initial perturbation to its state at  $t = \tau$  via  $\mathbf{x}(\tau) = \Phi(\tau)\mathbf{x}(0)$ . For time-independent reference states and  $\mathcal{A}$  one has  $\Phi(\tau) = \exp(\mathcal{A}\tau)$ . Variational analysis tells us that the desired perturbation initializing strongest growth is the leading eigenvector  $\mathbf{p}_\nu$  satisfying

$$\mathcal{M}^{-1}\overline{\Phi}^t(\tau)\mathcal{M}\Phi(\tau)\mathbf{p}_\nu = \sigma_\nu^2\mathbf{p}_\nu \quad (3.4)$$

with the largest possible eigenvalue  $\sigma_\nu^2$ , which is the squared growth factor  $\|\mathbf{x}(\tau)\|^2 / \|\mathbf{x}(0)\|^2$  if  $\mathbf{x}(0) = \mathbf{p}_\nu$ .  $\mathcal{M}$  being symmetric and positive definite there is a Cholesky factorization  $\mathcal{M} = \overline{\mathcal{N}}^t\mathcal{N}$  where  $\mathcal{N}$  is upper triangular (diagonal in the case here). Inserting the factorization into (3.4) and defining  $\mathbf{q}_\nu = \mathcal{N}\mathbf{p}_\nu$  the eigenvalue problem can be rewritten

$$\overline{\mathcal{L}}^t\mathcal{L}\mathbf{q}_\nu = \sigma_\nu^2\mathbf{q}_\nu \quad (3.5)$$

with  $\mathcal{L} = \mathcal{N}\Phi(\tau)\mathcal{N}^{-1}$ , showing that all eigenvalues are positive. The eigenvectors  $\mathbf{q}_\nu$  are orthogonal with respect to the euclidian metric, and henceforth also the optimal perturbations  $\mathbf{p}_\nu$  with respect to  $\mathcal{M}$ . The time-dependent state  $\Phi(\tau)\mathbf{p}_\nu$  developing from an optimal perturbation  $\mathbf{p}_\nu$  is the corresponding SV.

NMs and SVs differ in several regards. So one observes that NMs always have the same oscillating structure which is simply growing or decaying in time. This is not the case for SVs. Their structure can differ quite a lot between initialization and final time. As a consequence, the exchange processes between perturbation and background responsible for the change in amplitude are always the same for a NM, while they can vary considerably in the development of a SV. For a nonnormal model operator (where  $\overline{\mathcal{A}}^t\mathcal{A} \neq \mathcal{A}\overline{\mathcal{A}}^t$ ) it can also be shown that the leading SV and leading NM only agree as  $\tau \rightarrow \infty$ . For more details the reader is referred to Farrell and Ioannou (1996a,b) and Schmid and Henningson (2001)

# Chapter 4

## Linear stability of inertia-gravity wave packets

We begin with an analysis of the stability of IGWs. Due to their near-vertical phase propagation they allow under certain approximations an analytical treatment which clarifies important aspects of the dynamics of optimal perturbations of IGWs. These will also be helpful for an interpretation of significant features of the nonlinear wave-breaking process. The content of this chapter has also been published in Achatz and Schmitz (2006a,b).

### 4.1 The wave packet and its approximation in a model hierarchy

Having in mind an analysis of the stability of an IGW propagating from the lower atmosphere into the mesosphere, thereby gaining in amplitude due to the vertical ambient density gradient, this chapter focusses on the stability of an IGW packet. The other, conceptually interesting, case of a monochromatic IGWs is covered together with monochromatic HGWs in chapter 5. In all calculations in this chapter the Brunt-Vaisala frequency was assumed to be  $N = 10^{-2}\text{s}^{-1}$ , and the  $f$ -plane is centered at  $45^\circ$ .

The initial state of the wave packet is obtained from the solution (2.5) with upward

directed group velocity, convolved by a Gaussian envelope, i.e.

$$\begin{pmatrix} \mathbf{V}_0 \\ B_0 \end{pmatrix}(\mathbf{x}, 0) = a\Re \left[ \begin{pmatrix} \tilde{\mathbf{v}} \\ \tilde{b} \end{pmatrix} e^{i\mathbf{K}\cdot\mathbf{x} + \pi/2 - z^2/\sigma_z^2} \right], \quad (4.1)$$

where for convenience the phase has been shifted so that the statically least stable location comes to lie at  $(x, z) = (\Lambda_x/2, 0)$  with the horizontal wavelength given by  $\Lambda_x = 2\pi/K_x$ . As vertical extent  $\sigma_z$  of the packet one vertical wavelength  $\Lambda_z = 2\pi/K_z$  is used. For the wavelengths we have chosen typical observed values: The horizontal wavelength is 500km, whereas the vertical wavelength was varied between 3, 6, and 9km in order to get some information about the effect on the results here of varying the ratio  $R = f/|\Omega|$ . For the examined wavelengths it is  $R = 0.86, 0.65$ , and  $0.50$ , respectively. The time dependent wave packet was obtained by integrating from the specified initial state a nonlinear Boussinesq model, formulated in analogy to the model described in chapter 6. The linear dynamics of perturbations of the wave packet are analyzed on three levels of complexity.

#### 4.1.1 The linear model for the general IGW packet

The most general treatment is obtained by linearizing the Boussinesq equations about the general time dependent IGW packet. The latter is symmetric in  $y$  so that we can use the ansatz  $(\mathbf{v}', b', p') = (\mathbf{v}, b, p)(x, z) \exp(i ly)$  with an arbitrary wavenumber  $l$ , while  $p'$  denotes pressure. This yields

$$\nabla_2 \cdot \mathbf{v} = 0 \quad (4.2)$$

$$\frac{D\mathbf{v}}{Dt} + u \frac{\partial \mathbf{V}_0}{\partial x} + w \frac{\partial \mathbf{V}_0}{\partial z} + f \mathbf{e}_z \times \mathbf{v} + \nabla_2 p - \mathbf{e}_z b = \nu \nabla_2^2 \mathbf{v} \quad (4.3)$$

$$\frac{Db}{Dt} + u \frac{\partial B_0}{\partial x} + N_{tot}^2 w = \mu \nabla_2^2 b, \quad (4.4)$$

where  $\nabla_2 = (\partial/\partial x, il, \partial/\partial z)$ ,  $D/Dt = \partial/\partial t + \mathbf{V}_0 \cdot \nabla_2$ , and  $N_{tot}^2 = N^2 + \partial B_0/\partial z$ . The model equations have been discretized using second-order finite central differences on a staggered C grid (Tapp and White, 1976). The boundary conditions are periodic in  $x$  and  $z$ . It was always made sure that the boundaries are far enough from the instability in order not to affect the results. The pressure Poisson equation, obtained by taking the divergence

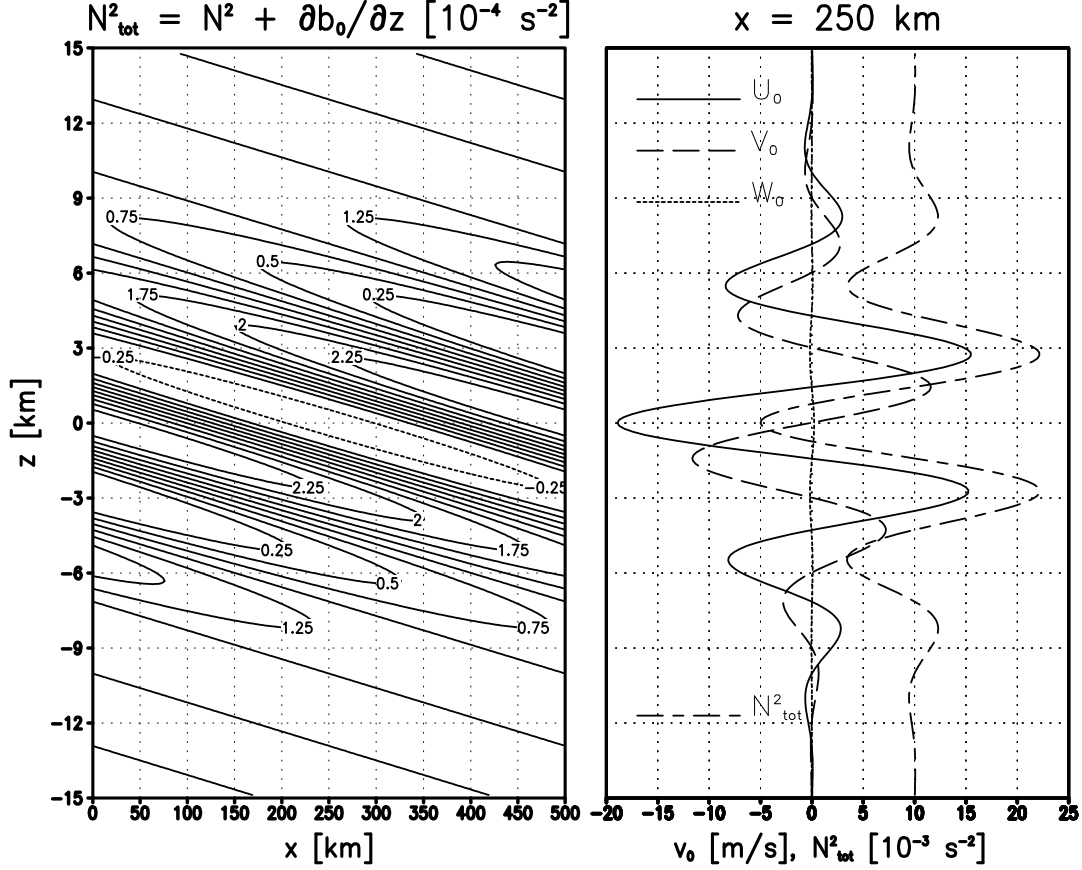


Figure 4.1: Squared total Brunt-Vaisala frequency in an IGW packet with  $a = 1.5$  (left panel, negative values are indicated by dashed contours), and at  $x = \Lambda_x/2$  its vertical dependence and that of the three-dimensional velocity field (right).

of (4.3) and using (4.2), is solved by standard techniques. The time integration is done by two initial fourth-order Runge-Kutta time steps and a third-order Adams-Bashforth scheme thereafter. These time-stepping schemes, as well as the solution of the Poisson equation are discussed in Durrán (1999). Further resolution details are given below.

#### 4.1.2 Approximation of the IGW by a one-dimensional profile

As will be seen much of the dynamics of an incipient instability of an IGW is controlled by the conditions near its statically least stable location. An interesting option simplifying the problem is therefore to approximate the IGW packet by its state at the location  $x = x_0 = \Lambda_x/2$  ( $= 250 \text{ km}$ ) where initially the strongest static instability is to be expected.

Vertical motion in the IGW is duely neglected since for IGW  $\cot \Theta \leq f/N \ll 1$ , i.e. we assume  $W_0 = 0$  (see also Fig. 4.1). Due to a corresponding symmetry in the basic wave packet, the resulting linear model does not couple different wave numbers in the horizontally parallel ( $x$ ) and transverse ( $y$ ) direction. Thus one can as well set  $(\mathbf{v}', b', p') = (\mathbf{v}, b, p)(x, z) \exp[i(kx + ly)]$  for arbitrary wavenumbers  $k$  and  $l$ . As others have done before (Dunkerton, 1997, e.g.) the horizontal wavenumbers are expressed in terms of parallel wavenumber  $k_{\parallel}$  and azimuth angle  $\alpha$  as  $(k, l) = k_{\parallel}(\cos \alpha, \sin \alpha)$ . For the further discussion it is also useful to introduce a modified coordinate system, obtained by rotating the horizontal axes so that in the new coordinates  $(x_{\parallel}, y_{\perp})$  the  $x_{\parallel}$ -axis points into the direction of the horizontal wave vector of the perturbation, i.e. one takes

$$x_{\parallel} = x \cos \alpha + y \sin \alpha \quad (4.5)$$

$$y_{\perp} = -x \sin \alpha + y \cos \alpha \quad . \quad (4.6)$$

With the corresponding horizontal velocity components in perturbation and IGW being denoted by  $(u_{\parallel}, v_{\perp})$  and  $(U_{\parallel}, V_{\perp})$  the model equations then become

$$ik_{\parallel}u_{\parallel} + \frac{\partial w}{\partial z} = 0 \quad (4.7)$$

$$\frac{Du_{\parallel}}{Dt} + w \frac{dU_{\parallel}}{dz} + ik_{\parallel}p - fv_{\perp} = \nu \nabla_1^2 u_{\parallel} \quad (4.8)$$

$$\frac{Dv_{\perp}}{Dt} + w \frac{dV_{\perp}}{dz} + fu_{\parallel} = \nu \nabla_1^2 v_{\perp} \quad (4.9)$$

$$\frac{Dw}{Dt} + \frac{\partial p}{\partial z} - b = \nu \nabla_1^2 w \quad (4.10)$$

$$\frac{Db}{Dt} + N_{tot}^2 w = \mu \nabla_1^2 b \quad , \quad (4.11)$$

where  $D/Dt = (\partial/\partial t + ik_{\parallel}U_{\parallel})$ ,  $\nabla_1 = (ik_{\parallel}, 0, \partial/\partial z)$ , and  $N_{tot}^2 = N^2 + dB_0/dz$ . Provided the coriolis effect is weak, which is the case here, one sees from (4.7)–(4.11) that  $v_{\perp}$  is coupled to the other model variables only passively.

Again the equations have been discretized using second-order finite central differences on a staggered grid with  $u_{\parallel}, v_{\perp}, b$  on full and  $w$  on intermediate half levels. Boundary conditions are periodic. Unless specified differently the model domain extension was  $L_z = 3\Lambda_z$  and the number of grid points (512 or 1024) was chosen large enough to ensure numerical convergence of all results.

As preparation for the constant-shear-layer approximation below it shall also be noted that there is, due to (4.7), a streamfunction  $\psi$  so that  $(u_{\parallel}, w) = (-\partial/\partial z, ik_{\parallel})\psi$ . With this the model equations can be written

$$\frac{D\zeta}{Dt} + ik_{\parallel}b = \nu \nabla_1^2 \zeta - ik_{\parallel} \frac{d^2 U_{\parallel}}{dz^2} \psi + f \left( \frac{\partial v_{\perp}}{\partial z} + ik_{\parallel} u_{\parallel} \right) \psi \quad (4.12)$$

$$\frac{Dv_{\perp}}{Dt} + ik_{\parallel} \frac{dV_{\perp}}{dz} \psi = \nu \nabla_1^2 v_{\perp} \quad (4.13)$$

$$\frac{Db}{Dt} + ik_{\parallel} N_{tot}^2 \psi = \mu \nabla_1^2 b, \quad (4.14)$$

where  $\zeta = (k_{\parallel}^2 - \partial^2/\partial z^2)\psi$  is the vorticity component in  $y_{\perp}$ -direction.

### 4.1.3 Approximation by a stratified constant-shear layer

Going one step further one can focus even more on the initial conditions near the statically least stable location by approximating (see also Fig. 4.1) the IGW fields by their tangents there at  $t = 0$ , i.e. by assuming

$$U_0 = u_0 = a\Omega/K \quad (4.15)$$

$$V_0 = \beta z \quad (\beta = afM/K) \quad (4.16)$$

$$N_{tot}^2 = N^2(1 - a), \quad (4.17)$$

so that  $U_{\parallel} = u_c + \beta_s z$  and  $dV_{\perp}/dz = \beta_c$ , where we write  $\beta_{s,c} = \beta(\sin \alpha, \cos \alpha)$  and  $u_c = u_o \cos \alpha$ . Optimal growth in a corresponding nonrotating stratified constant-shear layer with  $N_{tot}^2 = N^2$ , i.e. without locally reduced static stability, has been studied by Farrell and Ioannou (1993b) and Bakas et al. (2001) whose results are here used and expanded on. We neglect in (4.12)–(4.14), but not in the basic state, the coriolis effect and set

$$(\psi, \zeta, v_{\perp}, b)(z, t) = \int_{-\infty}^{\infty} dm (\psi_m, \zeta_m, v_m, b_m)(t) \exp [i(m_t z - k_{\parallel} u_c t) - D] \quad (4.18)$$

with  $m_t = m - k_{\parallel} \beta_s t$  a time dependent vertical wave number, and  $D = \nu \int_0^t d\tau K_t^2(\tau)$  the viscous-diffusive damping increment (assuming  $\mu = \nu$ ), while  $K_t^2 = k_{\parallel}^2 + m_t^2$ . Thus one obtains the independent three-component systems

$$\frac{d\zeta_m}{dt} = -ik_{\parallel} b_m \quad (4.19)$$



$$\frac{db_m}{dt} = -ik_{\parallel} N_{tot}^2 \psi_m \quad (4.20)$$

$$\frac{dv_m}{dt} = -ik_{\parallel} \beta_c \psi_m \quad (4.21)$$

with  $\zeta_m = K_t^2 \psi_m$ . Note that these equations conserve the quantity  $v_m/\beta_c - b_m/N_{tot}^2$ . One should also be aware that the stratified-shear-layer approximation is as well applicable to monochromatic IGWs as to IGW packets.

## 4.2 Analysis in the shear-layer approximation

Expressing kinetic energy in terms of  $\psi$  and  $v_{\perp}$  one finds that for the constant-shear-layer case total energy is given, up to an irrelevant constant factor, by  $E = \int_{-\infty}^{\infty} dk \int_{-\infty}^{\infty} dl \int_{-\infty}^{\infty} dm E_{klm}$  with

$$E_{klm} = \frac{e^{-2D}}{2} \left( K_t^2 |\psi_m|^2 + |v_m|^2 + \frac{|b_m|^2}{N^2} \right), \quad (4.22)$$

so that different  $k$  and  $l$ , i.e.  $k_{\parallel}$  and  $\alpha$ , and different initial vertical wavenumbers  $m$  are completely decoupled in the energy norm. Thus each of the subsystems (4.19)–(4.21) must be considered separately in a SV analysis. This can be done numerically for arbitrary azimuth angles, but the special advantage of the constant-shear-layer approximation is that it admits several closed analytical solutions helpful in getting an oversight of the dependence of optimal growth on the various parameters.

### 4.2.1 Normal modes and singular vectors

It is instructive to first neglect in (4.19)–(4.21) the time dependence of  $K_t$  and  $m_t$ , yielding a linear system with constant coefficients, and NM solutions

$$(\psi_m, b_m, v_m)_{\pm} = (1, \pm N_{tot} K_t, \pm \beta_c K_t / N_{tot}) / (K_t \sqrt{\epsilon_+}) \quad (4.23)$$

$$(\psi_m, b_m, v_m)_v = (0, 0, 1) \quad (4.24)$$

with eigenfrequencies  $\omega_{\pm} = \pm N_{tot} k_{\parallel} / K_t$  and  $\omega_v = 0$ , where  $\epsilon_+ = 1 + \beta_c^2 / |N_{tot}|^2 + |N_{tot}|^2 / N^2$ . The normalization has been chosen so that all three modes have the same initial unit energy  $E_{klm} = 1$ . For  $a > 1$  the convention is  $N_{tot} = i |N_{tot}|$  so that in this case

the first NM is growing exponentially, unless damped at small wavelengths by viscosity and diffusion, while at  $a < 1$  all three modes are damped. One sees that two possibilities for near-collinearity between the two first or all NMs arise. If  $\beta_c = 0$  and  $|N_{tot}|$  is small the two first modes are in structure very close to  $(1, 0, 0)$ , whereas for small  $|N_{tot}|$  and large  $\beta_c/|N_{tot}|$  they are approximately collinear with the third mode. This collinearity is the very reason for the strong optimal growth discussed below.

Getting back to the real case with time dependent  $K_t$  and  $m_t$  it is useful to exploit that the subsystem (4.19)–(4.20) always yields

$$\frac{d^2 \zeta_m}{dt^2} = -\frac{N_{tot}^2 k_{\parallel}^2}{K_t^2} \zeta_m \quad (4.25)$$

admitting for large enough  $|\omega_{\pm}|$  the WKB solution (Mathews and Walker, 1970; Farrell and Ioannou, 1993b)  $\zeta_m(t) \propto \sqrt{K_t} \exp(\pm i\phi)$  with  $\phi(t) = \int_0^t dt' N_{tot} k_{\parallel} / K(t')$ . Thus we use for the solution of the general initial-value problem the ansatz, validated a posteriori below,

$$\begin{pmatrix} \psi_m \\ b_m \\ v_m \end{pmatrix} (t) = a_+ e^{-i\phi} \begin{pmatrix} \psi \\ b \\ v \end{pmatrix}_+ + a_- e^{i\phi} \begin{pmatrix} \psi \\ b \\ v \end{pmatrix}_- + a_v \begin{pmatrix} \psi \\ b \\ v \end{pmatrix}_v \quad (4.26)$$

$$(\psi, b, v)_{\pm} = \frac{g^{3/4}}{K_0 \sqrt{\epsilon_+}} (1, \pm N_{tot} K_t, \pm \beta_c K_t / N_{tot}) \quad (4.27)$$

$$(\psi, b, v)_v = (0, 0, 1) \quad (4.28)$$

with  $K_0 = K_t(t = 0)$  and  $g = K_0^2 / K_t^2$ . Note that the WKB solution uses as basis time dependent generalizations of the NMs discussed above, which are exact for the case  $\beta_s = 0$ , i.e.  $\alpha = 0^\circ$ . As shown in appendix B the approximation yields analytical approximate optimal-growth factors which in the two limit cases of parallel or transverse propagation of the perturbation take an especially simple form.

### Parallel singular vectors

In the case  $\alpha = 0$  one has  $\beta_s = 0$ , i.e.  $m_t$  and  $K_t$  are constant, and thus the WKB solution is exact. The available basic shear is transverse to the wave vector, which corresponds to the situation where the so-called *roll mechanism* (Moffat, 1967; Ellingsen and Palm,

1975; Landahl, 1980) transfers kinetic energy from the basic state to a perturbation in which an initial vertical velocity induces a transverse wind component in the presence of a corresponding basic shear. The hence resulting growth factor for the leading optimal perturbation, given in the appendix B, can be approximated for  $\beta_c^2/|N_{tot}|^2 = 1/|\text{Ri}| \gg 1 \gg |N_{tot}|^2/N^2$  by

$$\sigma_1^2 \approx e^{-2D} \frac{4}{|\text{Ri}|} \frac{N^2}{|N_{tot}|^2} \begin{cases} \sin^4 \frac{\phi}{2} & \text{for } a < 1 \\ \sinh^4 \frac{|\phi|}{2} & \text{for } a > 1 \end{cases}. \quad (4.29)$$

Via an increase of the collinearity of the involved NMs both shear and reduced static stability act to enforce the transient growth, which is reduced by viscous-diffusive damping. Most notably, it can be strong even for  $a < 1$ , when all three NMs decay.

Given a vertical wavenumber  $m$  and an optimization time  $\tau$  one can ask oneself about the dependence of  $\sigma_1^2$  on  $k_{\parallel}$ , especially at which  $k_{\parallel}$  optimal growth maximizes. For  $a > 1$  one finds that due to  $|\phi| = |N_{tot}| k_{\parallel} \tau / \sqrt{k_{\parallel}^2 + m^2}$  the leading-term behavior is  $\sigma_1^2 = (4/|\text{Ri}|)(N^2/|N_{tot}|^2) \exp \left\{ 2\tau \left[ |N_{tot}| k_{\parallel} / \sqrt{k_{\parallel}^2 + m^2} - \nu (k_{\parallel}^2 + m^2) \right] \right\}$  so that growth maximizes, just as for the unstable NM, at  $k_{\parallel} = k_m$  where

$$0 = \frac{|N_{tot}| m^2 k_m}{(m^2 + k_m^2)^{3/2}} - 2\nu k_m^2, \quad (4.30)$$

i.e.  $k_m \approx m (|N_{tot}|/2\nu m^2)^{1/4}$  for  $\nu m^2 \ll |N_{tot}|/2$ , and  $k_m \approx m |N_{tot}|/2\nu m^2$  for  $\nu m^2 \gg |N_{tot}|/2$ . In this case the wavenumber location of optimal growth is independent of the optimization time.

The situation differs for  $a < 1$ . For  $N_{tot}\tau/2\pi > 1$  there are local maxima of  $\sigma_1^2$  where  $\phi \approx (2n+1)\pi$  for some positive integer  $n < (N_{tot}\tau/\pi - 1)/2$ , i.e. at  $k_{\parallel} \approx k_n$  where

$$k_n = \frac{m}{\sqrt{\left[ \frac{N_{tot}\tau}{(2n+1)\pi} \right]^2 - 1}}. \quad (4.31)$$

The number of extrema thus rises with increasing  $\tau$  where always the one at longest horizontal wavelength, i.e.  $k_{\parallel} = k_0$ , is least damped by diffusion and viscosity, so that there  $\sigma_1^2 \approx (4/|\text{Ri}|)(N^2/N_{tot}^2)$  for not too strong damping. For  $N_{tot}\tau/2\pi < 1$  only one maximum remains which is near

$$k_0 = m \left[ \frac{N_{tot}}{2\nu m^2 \tan(N_{tot}\tau/2)} \right]^{1/4}, \quad (4.32)$$

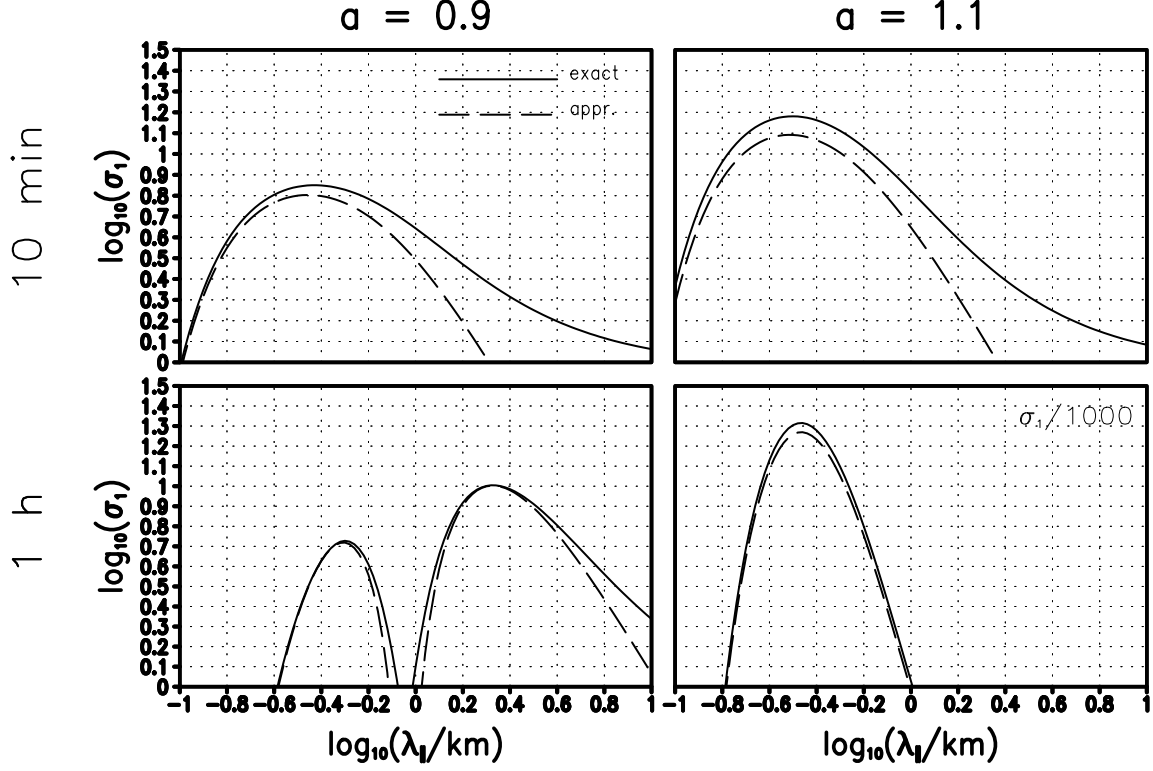


Figure 4.2: For the shear-layer approximation of optimal growth of parallel perturbations ( $\alpha = 0$ , vertical wavelength  $\lambda_z = 600\text{m}$ ) in an IGW packet ( $\Lambda_z = 6\text{km}$ ), for two different amplitudes  $a$  the leading growth factors for optimization times  $\tau = 10\text{min}$  and  $1\text{h}$ , in dependence of the horizontal wavelength  $\lambda_{||} = 2\pi/k_{||}$  of the perturbation. Shown are both the exact values and the approximation given by equation (4.29). In the case  $(a, \tau) = (1.1, 1\text{h})$  the growth factors have been divided by a factor 1000.

as long as in this approximation  $k_0 \gg m$ , reducing for  $N_{tot}\tau/2 \ll 1$  to  $k_0 = m/(\tau\nu m^2)^{1/4}$ , i.e. only slowly increasing with decreasing  $\nu$  and  $\tau$ . In contrast to the case  $a > 1$  one thus here has a dependence of the growth factor on optimization time. For  $\lambda_z = 0.1\Lambda_z = 600\text{m}$  and four representative combinations of  $a$  and  $\tau$  the leading growth factors are shown in Fig. 4.2, giving also a good confirmation of approximation (4.29).

The structure of the optimal perturbations is quite interesting. In appendix B it is also shown that under the same approximations as used for (4.29) one has for the strongest-growing structure

$$a_{\pm} \approx \mp \frac{1}{2} \frac{N_{tot}}{|N_{tot}|} \frac{\beta_c}{|\beta_c|} a_v \quad . \quad (4.33)$$

Inserting this into (4.26)–(4.28) yields for  $\beta_c/|N_{tot}| \gg 1$  and  $|N_{tot}|/N \ll 1$

$$\psi_m = \frac{a_v}{2K_0} \frac{|N_{tot}|}{|\beta_c|} \frac{N_{tot}}{|N_{tot}|} \frac{\beta_c}{|\beta_c|} (e^{i\phi} - e^{-i\phi}) \quad (4.34)$$

$$b_m = -\frac{a_v}{2} N \frac{|N_{tot}|}{|\beta_c|} \frac{N_{tot}}{N} \frac{N_{tot}}{|N_{tot}|} \frac{\beta_c}{|\beta_c|} (e^{i\phi} + e^{-i\phi}) \quad (4.35)$$

$$v_m = -\frac{a_v}{2} (e^{i\phi} + e^{-i\phi}) + a_v, \quad (4.36)$$

so that one sees that it is composed in such a way from the three NMs that both  $\psi_m$  and  $v_m$  are initially approximately cancelled, whence due to subsequent removal of this cancellation especially the latter quickly rises in amplitude. This case of transient growth is thus a clear example of the interference effect behind optimal growth in general, here acting to produce rapid growth in the transverse flow field.

### Transverse singular vectors

For  $\alpha = 90^\circ$  one has  $\beta_c = 0$  and thus the two first WKB NMs have no parallel-velocity component  $v_m$ . The leading optimal perturbation is composed from these so that optimal growth is restricted to  $\psi_m$  and  $b$ . Now the available shear is parallel to the horizontal wavenumber vector of the perturbation, so that the so-called *Orr mechanism* (Orr, 1907) can extract energy from the transverse flow-field component  $V_0$  of the shear layer. In this case the perturbation leans initially against the shear and intensifies as it is sheared over, thus producing strong vertical velocities.  $K_t$  is time dependent so that the variation of  $g$  has an important impact. As also shown in appendix B one has at  $|N_{tot}|^2/N^2 \ll 1$

$$\sigma_1^2 \approx e^{-2D} g^{1/2} \frac{N^2}{|N|_{tot}^2} \begin{cases} \sin^2 \phi & \text{for } a < 1 \\ \sinh^2 |\phi| & \text{for } a > 1 \end{cases}. \quad (4.37)$$

Also for this case both shear (via  $g$ ) and reduced static stability (via an enhanced collinearity of the involved NMs) act to enforce the transient growth, which is reduced by viscous-diffusive damping. Once again  $a = 1$  is no real instability threshold.

At fixed initial vertical wavenumber  $m$  the squared growth factor  $\sigma_1^2$  peaks at the maximum of  $g$  where  $K_t^2$  minimizes. This is at  $k_{\parallel} = m/\beta\tau$ . There

$$g = 1 + \beta^2 \tau^2 \quad (4.38)$$

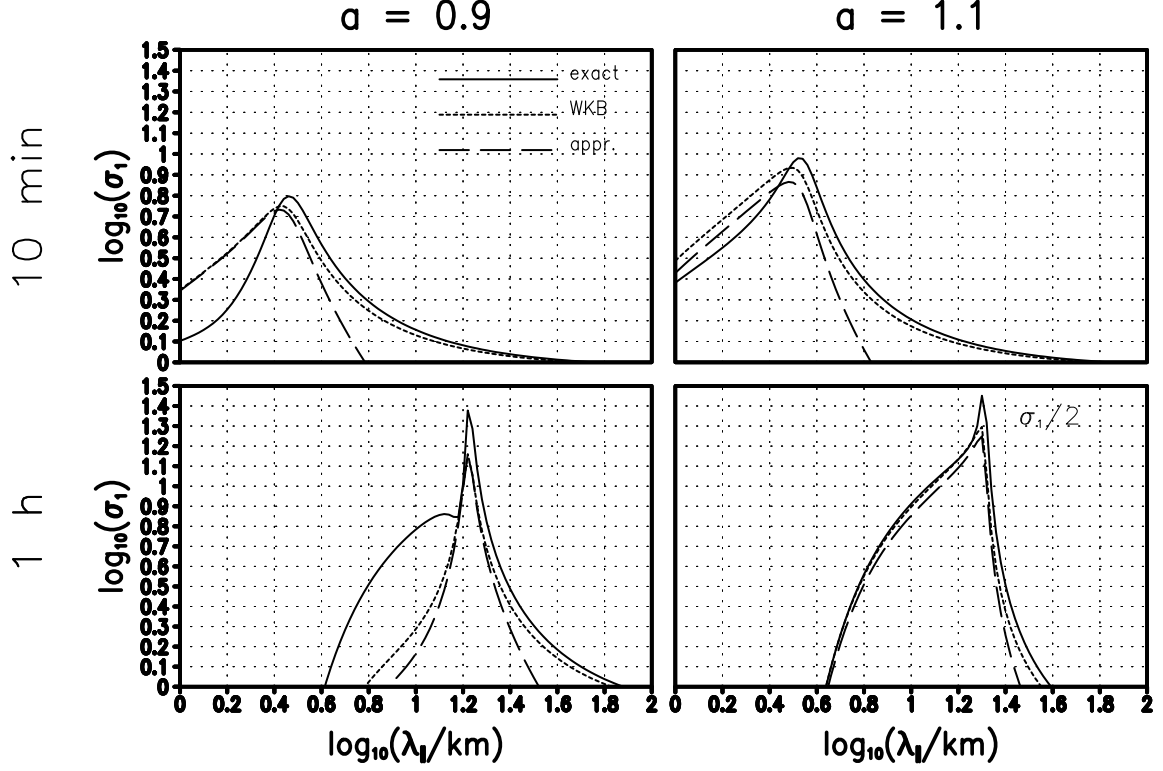


Figure 4.3: For the shear-layer approximation of optimal growth of transverse perturbations ( $\alpha = 90^\circ$ , vertical wavelength  $\lambda_z = 600\text{m}$ ) in an IGW packet ( $\Lambda_z = 6\text{km}$ ), for two different amplitudes  $a$  the leading growth factors for optimization times  $\tau = 10\text{min}$  and  $1\text{h}$ , in dependence of the horizontal wavelength  $\lambda_{\parallel} = 2\pi/k_{\parallel}$  of the perturbation. Shown are both the exact values, their WKB approximation by equation (B.5), and the approximation given by equation (4.37). In the case  $(a, \tau) = (1.1, 1\text{h})$  the growth factors have been divided by a factor 2.

$$D = \nu m^2 \tau \left( \frac{1}{\beta^2 \tau^2} + \frac{1}{3} \right) \quad (4.39)$$

$$\phi = -\frac{N_{tot}}{\beta} \ln \left( \sqrt{1 + \beta^2 \tau^2} - \beta \tau \right) \quad , \quad (4.40)$$

so that the growth factor is of the order  $N^2/|N_{tot}|^2$  for small  $\tau$ , and diverges for large  $\tau$  as long as viscous-diffusive damping is unimportant. This divergence is  $\propto \tau$  for  $a < 1$  and  $\propto \tau^{\sqrt{4/|\text{Ri}|}+1}$  for  $a > 1$ , i.e. in contrast to the parallel case algebraic and not exponential. For  $\lambda_{\parallel} = 0.1\Lambda_z = 600\text{m}$  and four representative combinations of  $a$  and  $\tau$  the leading growth factors are shown in Fig. 4.3, giving also a good confirmation of the WKB

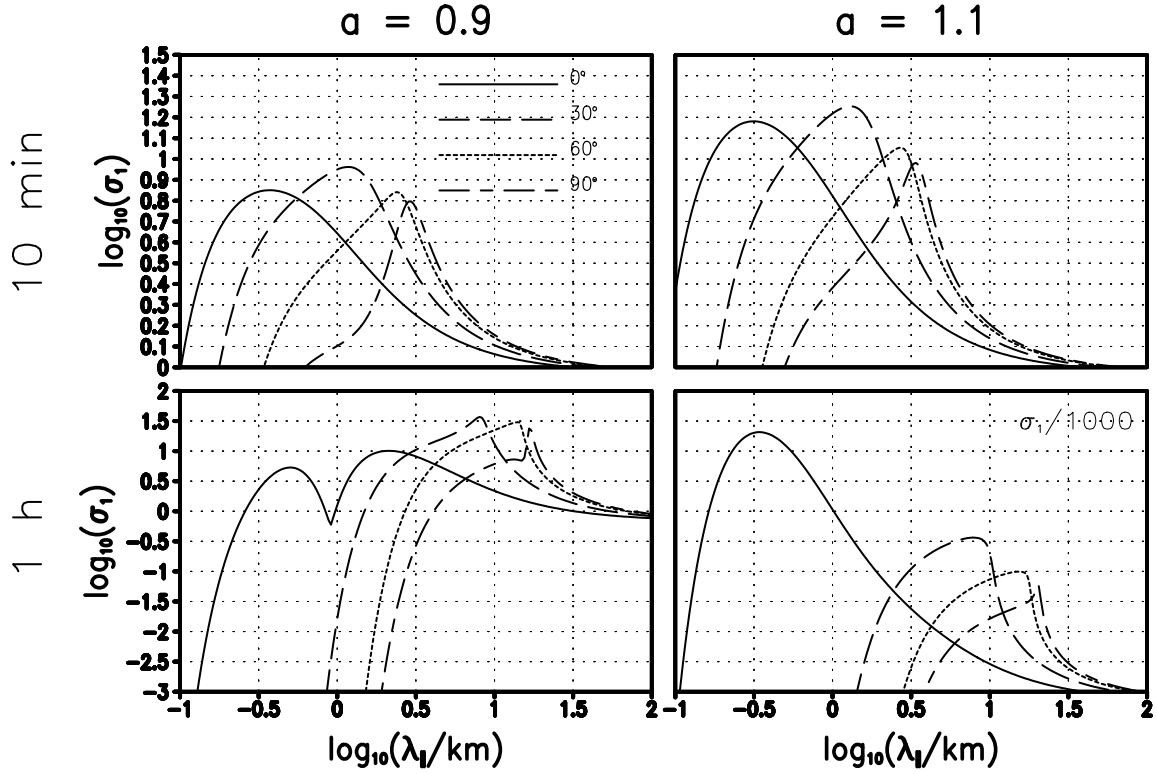


Figure 4.4: For the same four cases as shown in Figs. 4.2 and 4.3, the optimal growth factors for the azimuth angles  $\alpha = 0^\circ, 30^\circ, 60^\circ$ , and  $90^\circ$ .

approach and approximation (4.37). For the exact values the propagator matrix has been determined from numerical integration of (4.19)–(4.21), followed by a numerical solution of the eigenvalue problem (3.4).

The structure of the leading optimal perturbation reveals a similar interference effect as in the case above. To lowest approximation in  $|N_{tot}|^2/N^2 \ll 1$  one finds (appendix B)  $a_+ \approx -a_-$  so that

$$\psi_m = -a_+ \frac{g^{3/4}}{K_0} (e^{i\phi} - e^{-i\phi}) \quad (4.41)$$

$$b_m = a_+ N_{tot} g^{1/4} (e^{i\phi} + e^{-i\phi}) \quad , \quad (4.42)$$

i.e. there is initially near-cancellation in  $\psi_m$  after which it rapidly rises in amplitude due to removal of the destructive interference, so that this structure is dominated by growth in kinetic energy in  $\psi_m$ . For both cases, i.e. parallel and transverse propagation, one finds the buoyancy growth to be relatively weak.

### Dependence on azimuth angle

In order to give an impression of the general dependence of optimal growth in the shear-layer approximation Fig. 4.4 shows for the same four cases as in Figs. 4.2 and 4.3 the exact growth factors for the azimuth angles  $\alpha = 0^\circ, 30^\circ, 60^\circ$ , and  $90^\circ$ . In a comparison between the growth of parallel and transverse perturbations one finds the former to dominate for  $a > 1$ . This is a result of the exponential dependence on optimization time in the parallel case, while optimal growth of transverse perturbations only rises algebraically with  $\tau$ . At  $a < 1$  parallel optimal growth dominates for small  $\tau$ , due to the additional factor  $4/|\text{Ri}|$  in  $\sigma_1^2$ , while transverse optimal growth takes the lead for larger  $\tau$ , since the growth factors of parallel perturbations cannot be larger than  $(4/|\text{Ri}|)(N^2/N_{tot}^2)$ , while  $\sigma_1^2 \propto \tau$  in the other case. Interestingly for  $a < 1$  the growth factor gets largest for intermediate azimuth angles. This is in good agreement with the synergism between Orr mechanism and roll mechanism observed by Farrell and Ioannou (1993a) in unstratified shear layers. Only at larger  $a$  and  $\tau$  the growth of parallel perturbations dominates as a result of the strong exponential dependence of the corresponding growth factor on  $\tau$ . The dependence of the optimal wavenumber, at which optimal growth maximizes, on optimization time is for oblique SVs, due to the factor  $g$ , quite similar to the behavior in the transverse case, i.e. one finds optimal growth near  $k_{\parallel} = m/\beta_s \tau$ , so that the optimal wavelength rises in proportion with the optimization time. One also recognizes the dependence of the optimal wavelength of parallel optimal growth on  $\tau$  as predicted for  $a < 1$  by (4.31) ( $n = 0$  for  $\tau = 1\text{h}$ ) and (4.32) (for  $\tau = 10\text{min}$ ). The only case where the optimal wavenumber stays independent of  $\tau$  is for parallel SVs at  $a > 1$ .

### 4.2.2 Energetics and temporal development

The mechanism by which the identified patterns extract their energy from the basic shear layer deserves further attention. For this purpose it seems worthwhile to look explicitly at the relevant energy exchange terms in their time development and examine what they can teach us about the process. For each combination of  $k$  and  $l$ , i.e.  $k_{\parallel}$  and  $\alpha$ , and  $m$  in



the stratified shear layer one can derive from 4.19–4.21

$$\frac{dE_{klm}}{dt} = r_{\parallel} + r_{\perp} + r_b + r_d \quad (4.43)$$

$$r_{\parallel} = m_t k_{\parallel} \beta_s |\psi_m|^2 e^{-2D} \quad (4.44)$$

$$r_{\perp} = -k_{\parallel} \beta_c \Im(v_m \bar{\psi}_m) e^{-2D} \quad (4.45)$$

$$r_b = k_{\parallel} \left(1 - \frac{N_{tot}^2}{N^2}\right) \Im(b_m \bar{\psi}_m) e^{-2D} \quad (4.46)$$

$$r_d = -2\nu K_t^2 E_{klm} \quad , \quad (4.47)$$

containing successively the Reynolds exchange terms due to the fluxes of momentum in  $x_{\parallel}$ - and  $y_{\perp}$ -direction and of buoyancy against the respective gradients in the shear layer, and viscous-diffusive damping. Defining an instantaneous amplification rate  $\Gamma = (1/2E_{klm})(dE_{klm}/dt)$ , which for a NM is identical with its growth rate, one obtains the respective components  $\Gamma_{\parallel}, \Gamma_{\perp}, \Gamma_b$ , and  $\Gamma_d$ , so that  $\Gamma = \Gamma_{\parallel} + \Gamma_{\perp} + \Gamma_b + \Gamma_d$ . On the basis of these terms the time development of the leading optimal perturbations is analyzed, focussing on the two cases of parallel ( $\alpha = 0^\circ$ ) and transverse ( $\alpha = 90^\circ$ ) propagation where the simple closed analytical solutions of the initial-value problem exist.

### Parallel singular vectors

From  $\beta_s = 0$  follows  $r_{\parallel} = 0$ . Furthermore, in the limit  $\beta^2/|N_{tot}|^2 = 1/|\text{Ri}| \gg 1 \gg |N_{tot}|^2/N^2$  the approximations (4.34)–(4.36) apply, yielding for  $a < 1$ , under consistent assumptions,

$$E_{klm} = \frac{|a_v|^2}{2} e^{-2D} \left[ 4 \sin^4\left(\frac{\hat{\Omega}}{2}t\right) + |\text{Ri}| \frac{|N_{tot}|^2}{N^2} \right] \quad (4.48)$$

$$r_{\perp} = 2 \frac{k_{\parallel}}{K_0} |N_{tot}| |a_v|^2 e^{-2D} \sin(\hat{\Omega}t) \sin^2\left(\frac{\hat{\Omega}}{2}t\right) \quad (4.49)$$

$$r_b = |\text{Ri}| \frac{k_{\parallel}}{K_0} |N_{tot}| \left(1 - \frac{N_{tot}^2}{N^2}\right) \frac{|a_v|^2}{2} e^{-2D} \sin(2\hat{\Omega}t) \quad , \quad (4.50)$$

where it has been used that  $\phi = \hat{\Omega}t$  with  $\hat{\Omega} = N_{tot}k_{\parallel}/K_0$ . In (4.48) the small term  $|\text{Ri}| |N_{tot}|^2/N^2$  has been kept for consistency with the calculated growth factor, while in (4.50)  $N_{tot}^2/N^2$  has not been neglected in comparison with 1 in order to ensure that  $r_b = 0$  for  $N_{tot}^2 = N^2$ . For  $a < 1$  one thus sees the energy of the SVs to perform a damped

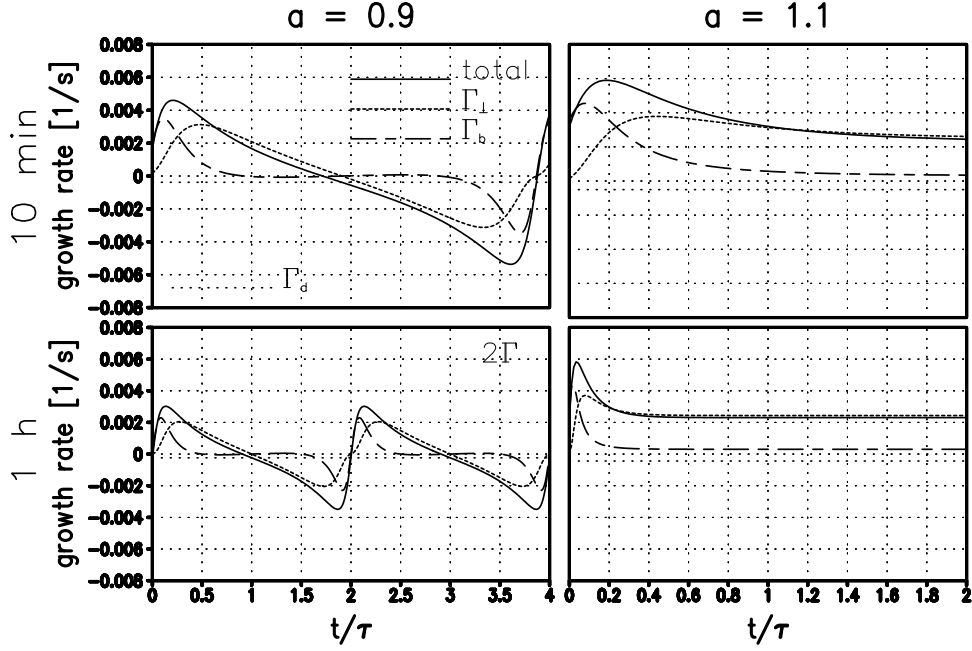


Figure 4.5: For the shear-layer approximation of optimal growth of parallel perturbations ( $\alpha = 0$ , vertical wavelength  $\lambda_z = 600\text{m}$ ) in an IGW packet ( $\Lambda_z = 6\text{km}$ ), for two different amplitudes  $a$  the time-dependent amplification-rate decomposition from an integration of the leading optimal perturbation (i.e. at optimal horizontal wavenumber) for optimization times  $\tau = 10\text{min}$  and  $1\text{h}$ . The contributing terms are the instantaneous amplification rates due to vertical counter-gradient fluxes of momentum in  $y_\perp$ -direction and buoyancy  $b$ , and viscous and diffusive damping. For the case  $(a, \tau) = (0.9, 1\text{h})$  twice the amplification rates are shown.

oscillation with period  $T = 2\pi/\hat{\Omega}$ . Note that for the perturbation growing at fixed  $m$  most strongly over the optimization time  $\tau$  one has for  $\tau > 2\pi/N_{tot}$  the identity  $\hat{\Omega}\tau = \pi$  and hence  $T = 2\tau$ . Similar oscillatory behavior is exhibited by the exchange terms. Generally  $r_\perp$  is the larger term besides near  $t = nT$  for some integer  $n$ , where both vanish but  $r_\perp$  has zero time derivative and thus the increase in  $r_b$  is steeper.

The corresponding relations for  $a > 1$  are obtained by the replacements  $\sin \rightarrow \sinh$  and  $\hat{\Omega} \rightarrow |\hat{\Omega}|$ . Then no oscillation results but a convergence of the total amplification rate towards the growth rate of the corresponding NM, i.e.  $\Gamma \rightarrow |N_{tot}k_\parallel/K_0|$ , which is due to the convergence of the optimal perturbation towards the structure of the NM. It is interesting to observe that as a result of the strong NM component in  $v_\perp$ , induced by the

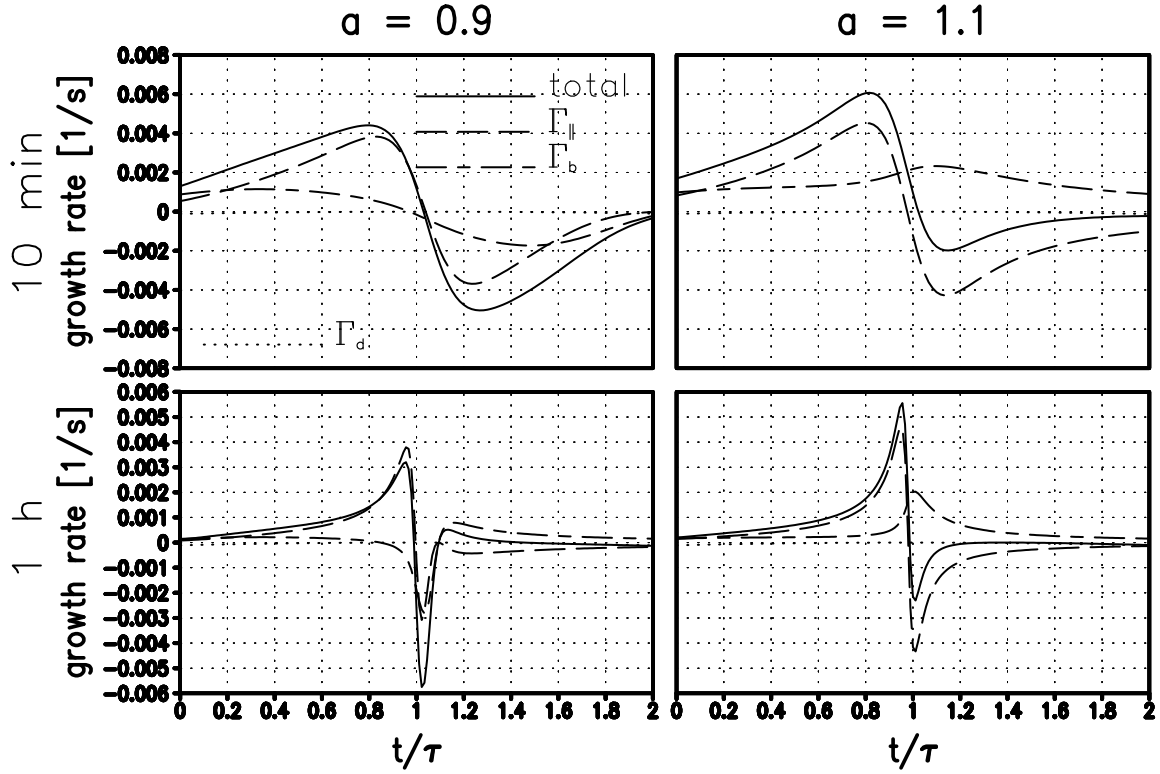


Figure 4.6: As Fig. 4.5, but now for the leading transverse perturbations ( $\alpha = 90^\circ$ ). Instead of the counter-gradient flux of momentum in  $y_\perp$ -direction one here has a contribution from the flux of momentum in  $x_\parallel$ -direction.

shear gradient,  $\Gamma_b/\Gamma_\perp = r_b/r_\perp \rightarrow |\text{Ri}|(1 - N_{\text{tot}}^2/N^2) \ll 1$  although the total growth rate of the NM is not influenced by the shear. The exact amplification-rate decomposition, obtained from an integration of the exact optimal perturbations (i.e. at optimal  $k_\parallel$ ) at  $\lambda_z = 2\pi/m = 0.1\Lambda_z = 600\text{m}$  and four representative combinations of  $a$  and  $\tau$ , is shown in Fig. 4.5. Note that in the case  $(a, \tau) = (0.9, 10\text{min})$  the optimal value of  $k_\parallel \approx 2\pi/380\text{m}$  yields  $T \approx 3.9\tau$ , which is in quite good agreement with the observed exact behavior.

### Transverse singular vectors

As discussed above the time-dependent leading transverse SV is a two-dimensional structure in the velocity field. One has  $v_m = 0$ , and in a WKB approximation in the limit  $|N_{\text{tot}}|^2/N^2 \ll 1$  the approximations (4.41) and (4.42) apply. One obtains generally  $r_\perp = 0$  (since  $\beta_c = 0$ ), and for  $a < 1$  under the assumptions above

$$E_{klm} = 2g^{1/2} |a_+|^2 e^{-2D} \left( \sin^2 \phi + \frac{|N_{tot}|^2}{N^2} \cos^2 \phi \right) \quad (4.51)$$

$$r_{\parallel} = 4g^{3/2} \frac{k_{\parallel} m_t}{K_0^2} \beta |a_+|^2 e^{-2D} \sin^2 \phi \quad (4.52)$$

$$r_b = 2g \frac{k_{\parallel}}{K_0} |N_{tot}| \left( 1 - \frac{N_{tot}^2}{N^2} \right) |a_+|^2 e^{-2D} \sin 2\phi \quad . \quad (4.53)$$

The corresponding relations for  $a > 1$  result from the replacements  $(\cos, \sin) \rightarrow (\cosh, \sinh)$  and  $\phi \rightarrow |\phi|$ . One sees that for  $|\text{Ri}| \ll 1$  growth and decay are generally dominated by  $r_{\parallel}$ . As discussed above, at fixed initial vertical wave number  $m$  largest growth over  $\tau$  is obtained at  $k_{\parallel} = m/\beta\tau$ , implying  $m_t = m(1 - t/\tau)$  so that decay sets in at  $t = \tau$ . Only near  $t = 0$ , when both  $r_{\parallel}$  and  $r_b$  approximately vanish, the latter dominates since the former there has zero time derivative. The large-time asymptotic behavior, incorrectly predicted by the WKB approximation, is best determined directly from the model equations (4.19)–(4.21) whence one finds, similarly to Farrell and Ioannou (1993b), that  $(\psi_m, b_m) \propto t^{\sqrt{1/4 - N_{tot}^2/\beta^2} - 1/2} (t^{-1}, 1)$  for  $t \rightarrow \infty$  so that  $E_{klm} \propto t^{\sqrt{1 - 4N_{tot}^2/\beta^2} - 1} \exp(-2D)$ . Thus even in the absence of viscosity and diffusion energy eventually decays for  $a < 1$ , while for  $a > 1$  a final decay is caused by viscous-diffusive damping. For the same four cases as used before the exact time-dependent amplification-rate decomposition of the optimally growing perturbation (i.e. with optimal  $k_{\parallel}$ ) is shown in Fig. 4.6. One sees that the relative importance of  $\Gamma_b$  decreases with increasing  $\tau$ , which can be understood by noting that, up to the phase factors, at the optimal wavenumber  $r_b/r_{\parallel} \propto \left( \sqrt{|\text{Ri}|}/2 \right) \left[ 1/\beta^2\tau^2 + (1 - t/\tau)^2 \right]^{1/2} / (1 - t/\tau)$  so that near  $t = 0$  the ratio decreases with increasing  $\tau$ .

### Dependence on azimuth angle

For general azimuth angles the behavior is a transition between the two cases discussed above. Fig. 4.7 shows for the same four combinations of  $a$  and  $\tau$  as above the exact time dependence of energy for four representative azimuth angles. One observes for  $\alpha = 0$  the damped oscillation at  $a < 1$ , and the exponential divergence at  $a > 1$  which only is obstructed by viscous-diffusive damping if  $D > |\hat{\Omega}|$ . For larger azimuth angles one sees at  $t = \tau$  the peak or sudden reduction of further growth as predicted by WKB theory. The

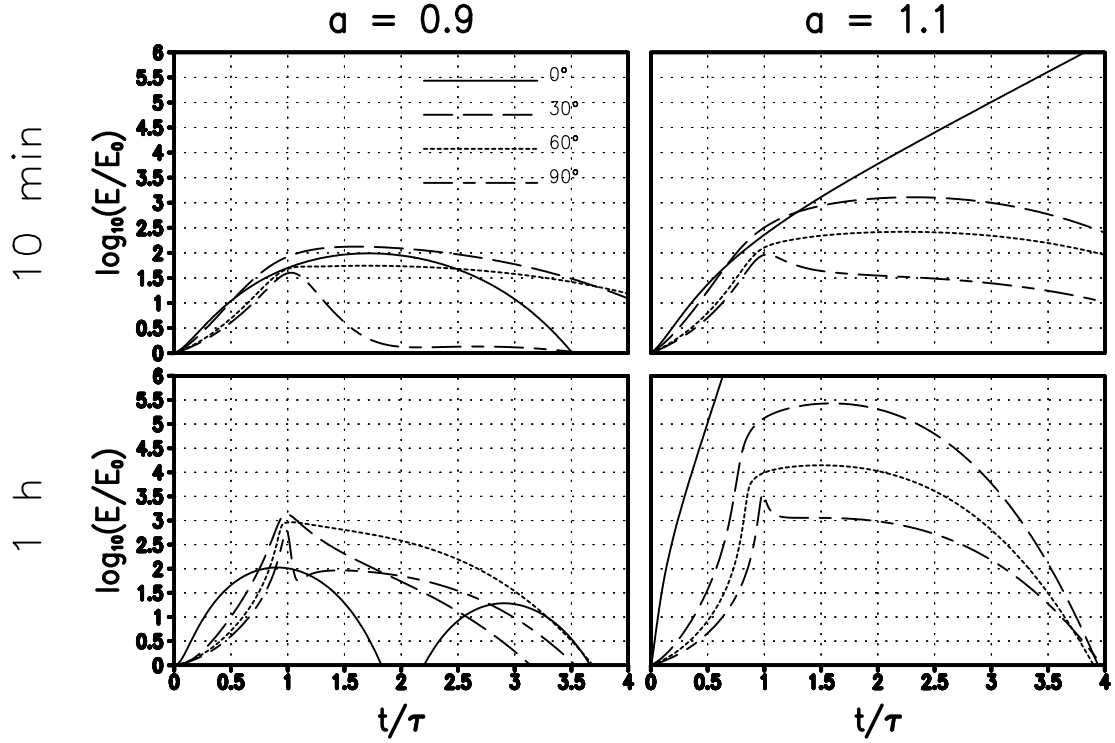


Figure 4.7: For the same four combinations of  $a$  and  $\tau$  and the same  $\lambda_z$  and  $\Lambda_z$  as in Fig. 4.5 the time-dependent energy in the integration of the leading optimal perturbations for the azimuth angles  $\alpha = 0^\circ, 30^\circ, 60^\circ$ , and  $90^\circ$ .

general large-time asymptotic behavior is similar to the transverse case, i.e.  $(\psi_m, b_m) \propto t^{\sqrt{1/4 - N_{tot}^2/\beta_s^2} - 1/2} (t^{-1}, 1)$  and  $v_m \rightarrow v_m(t=0) - \beta_c/N_{tot}^2 b_m(t=0) + o\left(t^{\sqrt{1/4 - N_{tot}^2/\beta_s^2} - 1/2}\right)$  for  $t \rightarrow \infty$  so that the energy in  $\psi_m$  and  $b_m$  is  $\propto t^{\sqrt{1 - 4N_{tot}^2/\beta_s^2} - 1} \exp(-2D)$  while that in  $v_m$  asymptotes towards a constant in the inviscid-nondiffusive limit (following from the conservation of  $v_m/\beta_c - b_m/N_{tot}^2$ , see also Bakas et al., 2001). In the general case viscous and diffusive damping eventually prevails since  $D \propto t^3$  for large times, but a transition phase of algebraic growth at  $a > 1$  for  $t > \tau$  is visible for the two intermediate azimuth angles.

### 4.3 Analysis of the 1D profile

In the approximation of an IGW by a one-dimensional vertical profile one obtains the independent subsystems (4.7)–(4.11), one for each combination of  $k$  and  $l$ , i.e.  $k_{\parallel}$  and

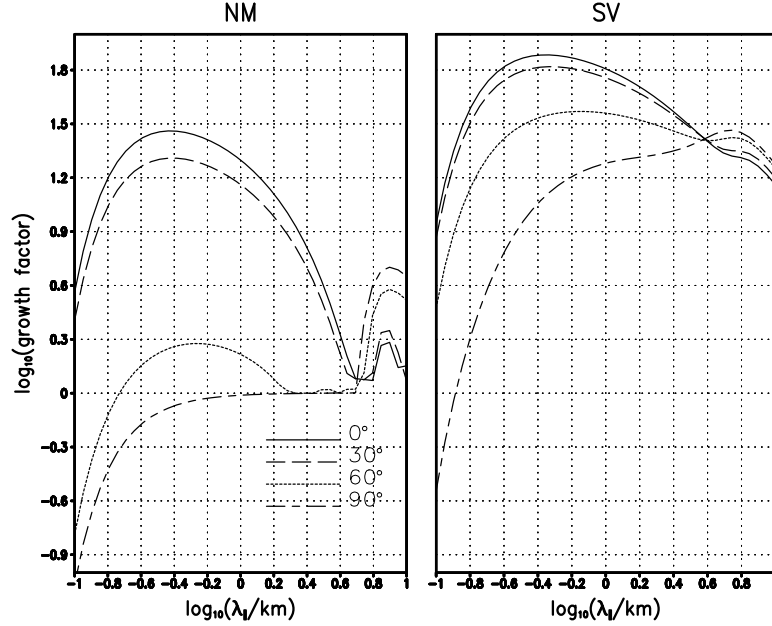


Figure 4.8: For the vertical profile at the horizontal location of maximal static instability, of a statically unstable ( $a = 1.5$ ) IGW packet with vertical wavelength  $\Lambda_z = 6\text{km}$ , the growth factors of the most unstable NMs (left panel) and leading SVs (right panel), propagating in the horizontal at various azimuth angles  $\alpha$  with respect to the basic wave, as a function of the parallel wave length  $\lambda_{\parallel} = 2\pi/k_{\parallel}$ . Integration time is  $\tau = 10\text{min}$ .

$\alpha$ . Moreover total energy can be written, up to an irrelevant constant factor, as  $E = \int_{-\infty}^{\infty} dk \int_{-\infty}^{\infty} dl E_{kl}$  with  $E_{kl} = |\mathbf{v}|^2/2 + |b|^2/2N^2$ , so that the energy norm also does not couple different horizontal wave vectors. Thus both the NMs and the SVs must be determined separately for each combination of  $k_{\parallel}$  and  $\alpha$ . This has been done using sparse-matrix techniques, as described in appendix A. Since the largest similarities to the results on SVs from the shear-layer approximation are to be expected for short optimization times, where the time-dependence of the 1D profile can be neglected, the analysis first focusses on that case. Longer optimization times are studied separately.

### 4.3.1 Normal modes and short-term singular vectors

#### Short-term normal-mode growth vs singular-vector growth

First a statically unstable IGW packet ( $a = 1.5$ ) is analyzed with vertical wavelength  $\Lambda_z = 6\text{km}$ . NMs are determined from the profile at  $t = 0$ . The development time

considered is  $\tau = 10\text{min}$ , i.e. approximately one Brunt-Vaisala period. The growth factors ( $\exp \gamma_\nu \tau$  for the NMs and  $\sigma_\nu$  for the SVs) of the leading patterns (with largest growth factors, i.e. for  $\nu = 1$ ) obtained in both analyzes are shown for different azimuth angles and parallel wavelengths in Fig. 4.8. Because of the Coriolis effect there is a weak asymmetry in the growth factors between (for any  $\beta$ )  $\alpha = 90^\circ \pm \beta$ . It is however so small that only results for  $0^\circ \leq \alpha \leq 90^\circ$  are shown. In comparing the NM growth curves to corresponding results by Dunkerton (1997) and Kwasniok and Schmitz (2003) minor differences are to be expected, since in those studies the impact of the Coriolis effect was taken into account as far as the shape of the basic wave is concerned, but not in the linear model itself. However, we actually find quite good agreement for this value of  $a$ . Thus, also two main features in the growth curves obtained there are reproduced. First, at parallel wavelengths of the order of the vertical wavelength of the basic wave one finds a local maximum which is especially pronounced for transverse propagation ( $\alpha = 90^\circ$ ). Secondly, towards shorter wavelengths the growth factors for non-transverse propagation rise again to an even higher level. Most pronounced here is the growth factor for parallel propagation ( $\alpha = 0^\circ$ ), maximizing at  $\lambda_\parallel = 2\pi/k_\parallel \approx 400\text{m}$  to a value near 30. At even shorter scales viscosity takes over and leads to weaker growth rates, and finally decay. This is in close correspondence to the strong growth of small-scale parallel NMs in the constant-shear layer discussed above.

The two peaks, as well as the general finding that instability exists at all azimuths, can also be interpreted via the local Richardson number  $\text{Ri} = N_{\text{tot}}^2/(\partial U_\parallel/\partial z)^2$ . As also noted above, motivation for the use of the local Richardson number is that for a purely  $z$ -dependent background without vertical wind the well-known Taylor-Goldstein equation can be derived from the linear equations (4.7) – (4.11) without rotation, which has been the basis of the analysis by Fritts and Yuan (1989b), Yuan and Fritts (1989), Dunkerton (1997), and Kwasniok and Schmitz (2003). This equation had previously been analyzed by Howard (1961) and Miles (1961) who showed that no NM growth can exist if  $\text{Ri} > 1/4$  everywhere. As a necessary condition for NM instability the local Richardson number should therefore be less than  $1/4$  anywhere in the domain. Neglecting viscosity and diffusivity, setting  $\mathbf{K} \cdot \mathbf{x} - \omega t = Kx_0 + Mz = \pi + \Phi$  with local phase  $\Phi = Mz$  one finds,

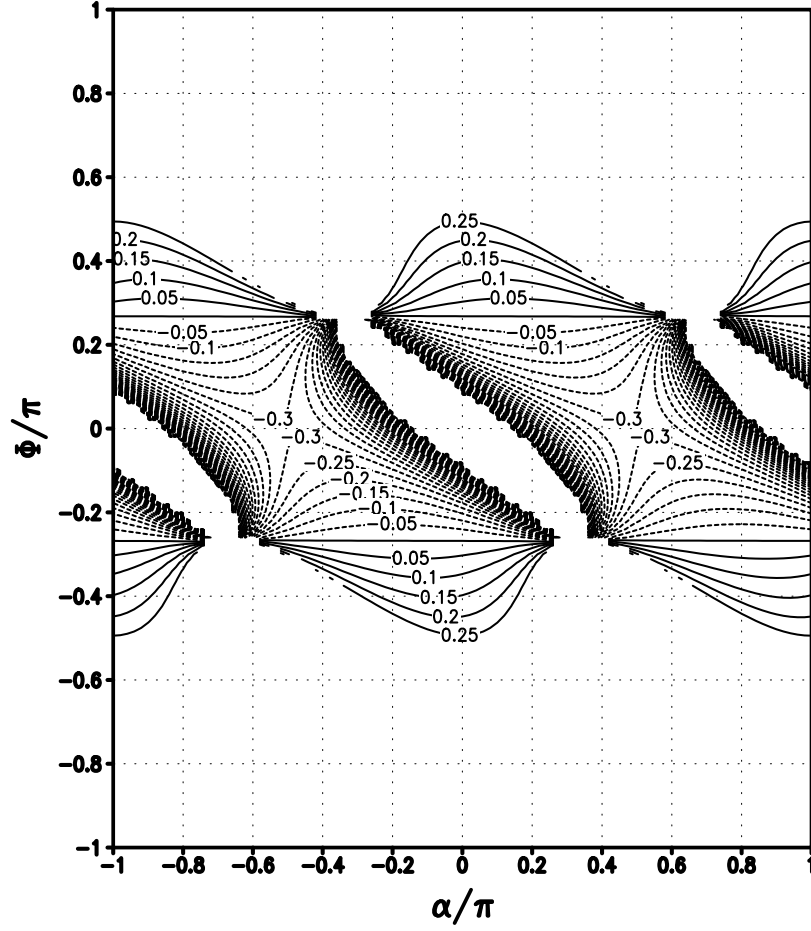


Figure 4.9: As a function of instability azimuth  $\alpha$  and wave phase  $\Phi$ , the local Richardson number in the vertical IGW profile used in the analysis shown in Fig. 4.8. Only values  $-2 \leq \text{Ri} \leq 1/4$  are shown.

in analogy to (2.16),

$$\text{Ri} = \frac{(1 - R^2)(1 - a \cos \Phi)}{a^2(R \sin \alpha \cos \Phi + \cos \alpha \sin \Phi)^2} \frac{1}{1 - \Omega^2/N^2} . \quad (4.54)$$

For  $(R, a) = (0.65, 1.5)$   $\text{Ri}(\alpha, \Phi)$  has been plotted in Fig. 4.9 (assuming  $\Omega^2 \ll N^2$ ). The instability at all azimuths is consistent with the observation that for all  $\alpha$  there is a wave phase where  $\text{Ri} < 1/4$ . Furthermore one finds at  $\Phi = 0$  negative singularities at  $\alpha = 0, \pm\pi$ , and saddle points at  $\alpha = \pm\pi/2$ , indicating the most pronounced instabilities to occur at parallel propagation. Lelong and Dunkerton (1998a) show a similar plot for  $a < 1$  where the minimum of  $\text{Ri}$  lies at  $\alpha = \pm\pi/2$ . It appears that the growth rate peaks found for transverse propagation are related to these minima which here at  $a > 1$  become



masked by the negative singularities at  $\alpha = 0, \pm\pi$ .

Now turning to the SVs (right panel of Fig. 4.8) one observes conspicuous similarities to the NMs. Again one finds the most intense growth at short scales and parallel propagation with a secondary peak at longer scales and transverse propagation. The peaks are less pronounced, and the azimuth dependence is also somewhat weaker. Furthermore, the most rapidly growing transverse SVs have smaller scales. Whereas the most rapid transverse NM growth is at  $\lambda_{\parallel} \approx 8\text{km}$ , the respective nonmodal growth maximizes at 5km. The most important difference, however, is that nonmodal growth within  $\tau = 10\text{min}$  is more rapid, by about a factor 3, than NM growth. At other wave amplitudes one gets the same result. Figure 4.10 shows the NM and SV growth curves for parallel and transverse propagation at  $a = 0.9$  and 0.5. At slightly subcritical amplitudes ( $a = 0.9$ ) optimal growth is still quite strong (nearly a factor 10 for parallel propagation) while the NMs grow only by an insignificant rate. The largest growth factor one finds is  $\exp(\gamma_1\tau) = 1.006$  at  $(\alpha, \lambda_{\parallel}) = (90^\circ, 8.9\text{km})$ . The slightly more intense NM instabilities found by Yau et al. (2004) for subcritical monochromatic IGWs seem to be due to their neglect of viscosity and diffusion, and their use of larger values for  $a$  and  $R$  than here. Even at rather small amplitudes ( $a = 0.5$ ) optimal growth still exists. This, however, should perhaps not be overrated, since growth by a factor 2 might usually not be sufficient for really destabilizing the basic wave packet. These results verify the prediction from the constant-shear-layer approximation that at short optimization times strong transient growth of nonmodal perturbations can exist, dominated by near-parallel propagation. This persists for  $a < 1$ , while there modal growth is basically suppressed. Also the scales of parallel and transverse optimal perturbations are reproduced, the former being considerably shorter than the latter. A major difference is that no synergism between the roll and Orr mechanisms is seen in the sense that it is always the parallel perturbations which grow most rapidly, while the shear layer would predict most rapid growth for slightly oblique directions of propagation, as also visible in Fig. 4.4.

The impact of the vertical wavelength of the basic wave on optimal growth can be seen in Fig. 4.11. There the leading growth factors (for parallel and transverse SVs) for different basic wave amplitudes and vertical wavelengths are shown. As  $R$  is increased

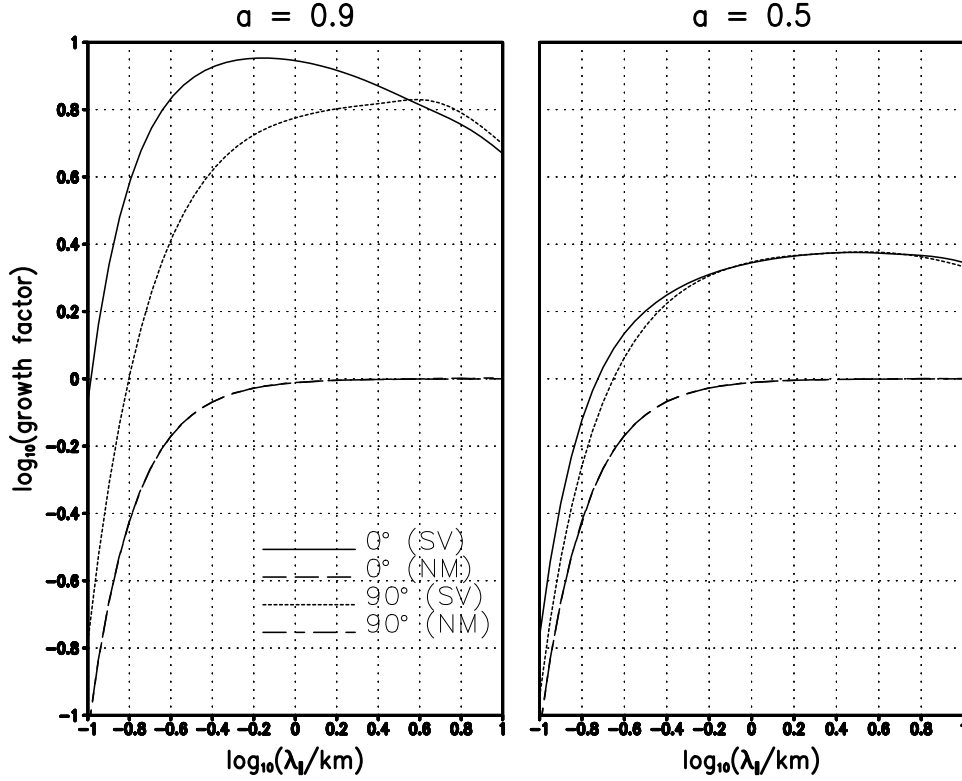


Figure 4.10: As Fig. 4.8, but just for transverse and parallel perturbations, and the basic wave amplitudes  $a = 0.9$  and  $0.5$ .

or  $\Lambda_z$  decreased ( $R = 0.86, 0.65$ , and  $0.50$ , for  $\Lambda_z = 3, 6$ , and  $9\text{km}$ , respectively) the SV growth gets stronger. It appears that the tendency for subcritical growth (at  $a < 1$ ) occurs mainly in IGWs with smaller vertical wavelengths (i.e. large  $R$ ). This is in close analogy to the predictions from NM theory (Fritts and Rastogi, 1985; Dunkerton, 1997). Once again one finds this also to be a prediction from the constant-shear-layer approximation where it is found that parallel optimal growth obeys the proportionality  $\sigma_1 \propto \sqrt{4/|\text{Ri}|} = 2\beta/|N_{\text{tot}}|$  while for transverse perturbations one has  $\sigma_1 \propto (1 + \beta^2\tau^2)^{1/4}$ . Thus smaller vertical wavelengths with larger shear in the transverse wind  $\beta = afM/K$  lead to stronger nonmodal instabilities. Furthermore, also here one finds for all examined waves stronger short-term growth for parallel SVs. One also sees a tendency for longer instability wavelengths  $\lambda_{\parallel}$  as  $\Lambda_z$  is increased. At least partially this might be explained as an effect of viscosity and diffusion since the shear-layer approximation would predict, due to the corresponding damping, strongest growth at smallest  $m$  which, however, is limited

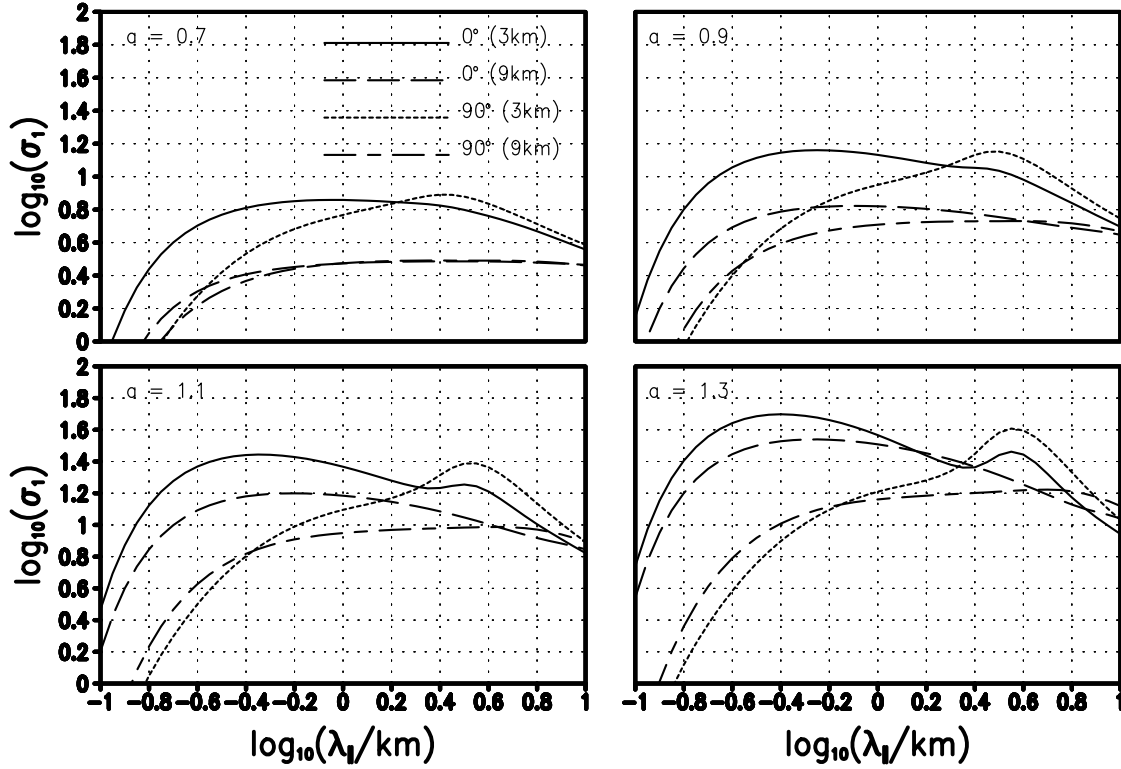


Figure 4.11: For the basic-wave vertical wavelengths  $\Lambda_z = 3\text{km}$  and  $9\text{km}$ , the wavelength-dependence of the leading SV growth factors ( $\tau = 10\text{min}$ ) for parallel and transverse perturbations, at basic-wave amplitudes  $a = 0.7, 0.9, 1.1$ , and  $1.3$ .

below by the vertical wavenumber of the wave packet. Smaller  $K_z$  thus allow smaller  $m$  not in contradiction to the basic assumption that the perturbative scales are smaller than those of the IGW, while the optimal  $k_{\parallel}$  scales roughly with  $m$ .

### 4.3.2 Singular vectors for long optimization times

In the analysis of SVs for longer optimization times the focus is on the subcritical case  $(a, \Lambda_z) = (0.9, 6\text{km})$ . For all calculations the model resolution used is 1024 grid points per  $5\Lambda_z$ , where the model domain size was always chosen large enough so that potentially radiating structures (see below) never reached the model boundaries. Examined optimization times are  $\tau = 1\text{h}, 2\text{h}, 5\text{h}$ , and  $10\text{h}$ . The last value approaches the IGW period  $T \approx 11\text{h}$ . The time dependence of the wave packet makes the results from the constant-shear-layer approximation the less applicable the larger  $\tau/T$  is. It is nice to see how much it can

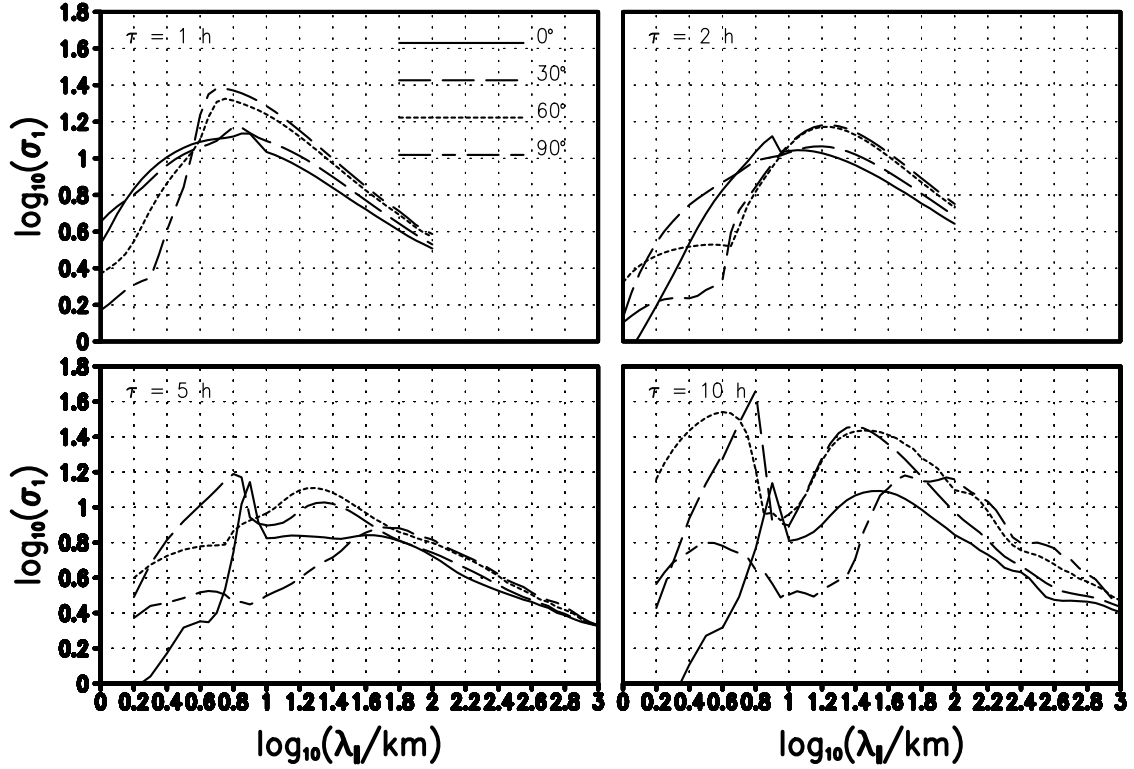


Figure 4.12: For the approximation of an IGW with  $(a, \Lambda_z) = (0.9, 6\text{km})$  by a one-dimensional profile, the wavelength dependence of the growth factors of the strongest growing optimal perturbations at azimuth angle  $\alpha = 0^\circ, 30^\circ, 60^\circ$ , and  $90^\circ$  for four different long optimization times  $\tau$ .

nonetheless still be used for qualitative explanations of SV behavior in these cases.

Figure 4.12 shows the wavelength dependent growth-factor curves. In agreement with the expectations from the constant-shear-layer theory the SVs are to be found at progressively increasing wavelengths as  $\tau$  is increased. At large  $\tau$ , however, for all azimuth angles an important growth-factor peak at rather short scales (of the order  $\Lambda_z$ ) appears with values as large as nearly 50 at  $\alpha = 30^\circ$  for  $\tau = 10\text{h}$ . Another prediction one finds verified is that the largest growth factor at  $\alpha = 0^\circ$  is approximately independent of  $\tau$ , i.e.  $\sigma_1^2 \approx (4/\text{Ri}) (N^2/N_{\text{tot}}^2) \approx 238$  as determined from the conditions at the statically least stable altitude. Also as expected, at least for intermediate  $\tau$  transverse optimal growth gets larger than its parallel counterpart. Most important at large  $\tau$  are, however, oblique azimuth angles, which dominate at nearly all scales. For these cases neither the statically

enhanced roll or Orr mechanisms act alone but always a combination of the two.

It is interesting that even for  $\tau = 10h$  the growth factor is near 50. The time the corresponding perturbations take for their amplification is quite large so that their appearance might be prevented by nonlinear modifications of the IGW under the influence of other perturbations rising in amplitude more quickly. The oblique directions of propagation of these SVs, however, suggest that they might be related to the diagonal shear modes found by Lelong and Dunkerton (1998a) in their simulations of a case with  $a = 0.95$  and a ratio between inertial frequency and IGW frequency  $R = 0.7$ , which is rather near to our combination  $(R, a) = (0.65, 0.9)$ . A one-two-one comparison is difficult since in that study an artificially increased ratio  $f/N = 0.1$  was used, but it is striking that there an asymmetry in perturbation growth about  $\alpha = 90^\circ$  was found, so that if the findings here were related to that work, we should also see a corresponding asymmetry in the growth factors. Indeed this is the case. So one finds that SV growth over  $\tau = 10h$  is not larger than by a factor 9 if determined for the azimuth angles  $\alpha = 120^\circ$  and  $150^\circ$  (not shown here). Moreover, those authors also found a vacillation of energy growth about a mean value. This seems to be related to a damped vacillation found here (see below) which is due to the movement of the perturbation through the periodic IGW fields.

### 4.3.3 Energetics and temporal development

As in the case of the shear-layer approximation the dynamics of the SVs is studied also here using energy considerations. From (4.7)–(4.11) one finds

$$\frac{\partial}{\partial t} \frac{|u_{\parallel}|^2}{2} + \Re \left( p \frac{\partial \bar{w}}{\partial z} \right) - \nu \frac{\partial^2}{\partial z^2} \frac{|u_{\parallel}|^2}{2} - f \Re(u_{\parallel} \bar{v}_{\perp}) = r_{\parallel} - \nu \left( k_{\parallel}^2 |u_{\parallel}|^2 + \left| \frac{\partial u_{\parallel}}{\partial z} \right|^2 \right) \quad (4.55)$$

$$\begin{aligned} \frac{\partial}{\partial t} \frac{|v_{\perp}|^2}{2} - \nu \frac{\partial^2}{\partial z^2} \frac{|v_{\perp}|^2}{2} + f \Re(u_{\parallel} \bar{v}_{\perp}) &= r_{\perp} \\ &\quad - \nu \left( k_{\parallel}^2 |v_{\perp}|^2 + \left| \frac{\partial v_{\perp}}{\partial z} \right|^2 \right) \end{aligned} \quad (4.56)$$

$$\frac{\partial}{\partial t} \frac{|w|^2}{2} + \Re \left( \bar{w} \frac{\partial p}{\partial z} \right) - \nu \frac{\partial^2}{\partial z^2} \frac{|w|^2}{2} = e_{bw} - \nu \left( k_{\parallel}^2 |w|^2 + \left| \frac{\partial w}{\partial z} \right|^2 \right) \quad (4.57)$$

$$\frac{\partial}{\partial t} \frac{|b|^2}{2N^2} - \mu \frac{\partial^2}{\partial z^2} \frac{|b|^2}{2N^2} = r_b - e_{bw}$$

$$-\frac{\mu}{N^2} \left( k_{\parallel}^2 |b|^2 + \left| \frac{\partial b}{\partial z} \right|^2 \right), \quad (4.58)$$

yielding for the energy density  $e_{kl} = 1/2 (|\mathbf{v}|^2 + |b|^2 / N^2)$

$$\frac{\partial e_{kl}}{\partial t} + \frac{\partial}{\partial z} \left[ \Re(\bar{w}p) - \nu \frac{\partial}{\partial z} \frac{|\mathbf{v}|^2}{2} - \mu \frac{\partial}{\partial z} \frac{|b|^2}{2N^2} \right] = r_{\parallel} + r_{\perp} + r_b - D_v - D_b \quad (4.59)$$

with

$$r_{\parallel} = -\Re(u_{\parallel} \bar{w}) \frac{\partial U_{\parallel}}{\partial z} \quad (4.60)$$

$$r_{\perp} = -\Re(v_{\perp} \bar{w}) \frac{\partial V_{\perp}}{\partial z} \quad (4.61)$$

$$r_b = -\Re(b \bar{w}) \frac{1}{N^2} \frac{\partial B_0}{\partial z} \quad (4.62)$$

$$e_{bw} = \Re(b \bar{w}) \quad (4.63)$$

$$D_v = \nu \left[ k_{\parallel}^2 |\mathbf{v}|^2 + \left| \frac{\partial \mathbf{v}}{\partial z} \right|^2 \right] \quad (4.64)$$

$$D_b = \frac{\mu}{N^2} \left[ k_{\parallel}^2 |b|^2 + \left| \frac{\partial b}{\partial z} \right|^2 \right]. \quad (4.65)$$

Integrating (4.59) in the vertical one sees that total energy  $E_{kl} = \oint_{L_z} dz e_{kl}$  is subject to changes by the flux of momentum in  $x_{\parallel}$ - and  $y_{\perp}$ -direction against the corresponding gradients in the IGW ( $r_{\parallel}$  and  $r_{\perp}$ ), the counter-gradient flux of buoyancy ( $r_b$ ), and viscous and diffusive damping ( $D_v$  and  $D_b$ ). In the same manner as above we calculate from these terms and energy an instantaneous amplification rate  $\Gamma = 1/(2E_{kl}) dE_{kl}/dt$  and its decomposition.

### Short optimization times

For the analysis of the dynamics of optimal perturbations at short optimization times we look at  $\tau = 10\text{min}$  and focus on the two exemplary cases  $\alpha = 0^\circ$  and  $\alpha = 90^\circ$ . Intermediate azimuth angles can be seen as a transition between these two cases.

**Parallel singular vectors** In the left column of Fig. 4.13 one sees for the leading parallel optimal perturbation (i.e. at optimal horizontal wavelength) the energy for  $a = 0.9$  and  $1.1$ , and the amplification-rate decomposition for  $a = 0.9$  from integrations over

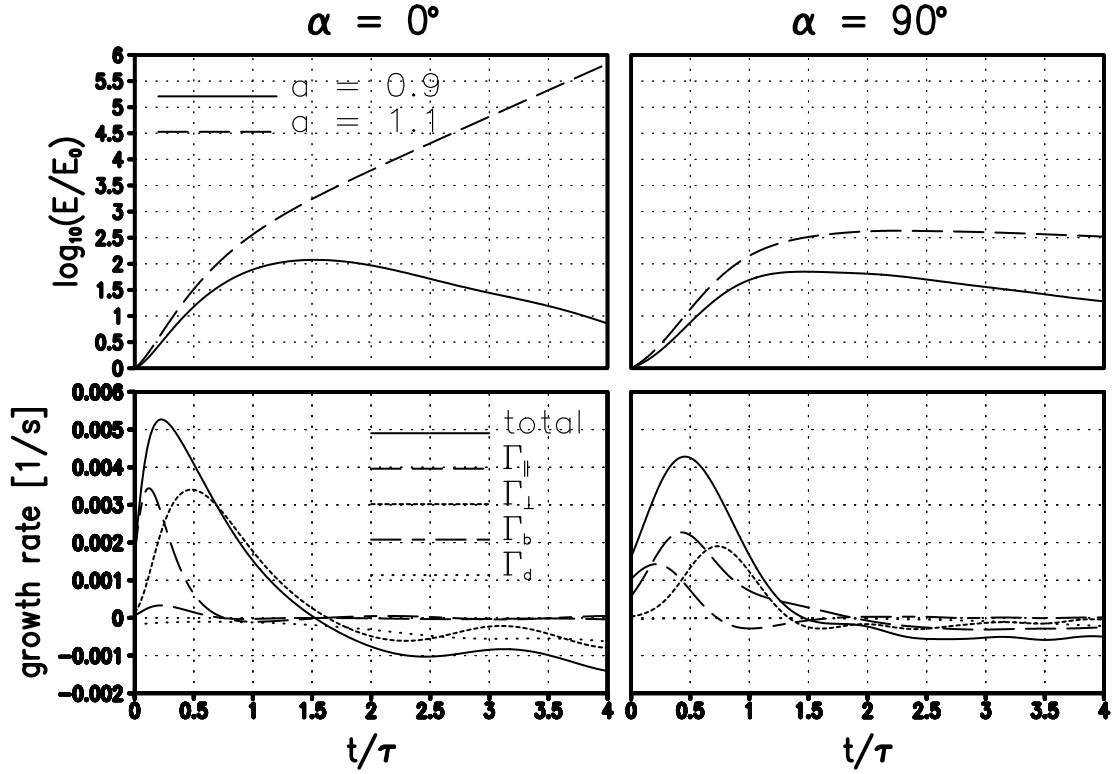


Figure 4.13: For the leading (i.e. at optimal horizontal wavelength) parallel SV (left column) and transverse SV (right column) in the approximation of the IGW with  $\Lambda_z = 6\text{km}$  by a 1D profile, time-dependent total energy for  $a = 0.9$  and  $a = 1.1$  (top row) and for  $a = 0.9$  the instantaneous amplification rate and its decomposition (bottom), from integrations over four optimization periods  $\tau = 10\text{min}$ .

four optimization periods. Because in the supercritical case  $a = 1.1$  at the horizontal wavelength of the leading SV also an unstable NM exists one sees the energy to eventually diverge exponentially, indicating that the structure of the SV has approached that of the NM. Figure 4.14 gives a comparison between the altitude dependent contributions to the total amplification rate at  $t = 0$  and  $t = \tau$  for the leading parallel optimal perturbation and NM (at the same horizontal wavelength) at  $a = 1.1$ , i.e. e.g.  $\gamma_{\parallel} = r_{\parallel} / \langle 2e_{kl} \rangle$  for the flux of parallel momentum so that  $\Gamma_{\parallel} = \langle \gamma_{\parallel} \rangle$  and likewise for all other terms (angle brackets indicate a vertical average multiplied by  $L_z/\Lambda_z$ ). Two aspects are notable there. First, the NM does not exhibit any time dependence in its amplification-rate decomposition. This is due to its time-independent structure which in turn precludes a dynamic development

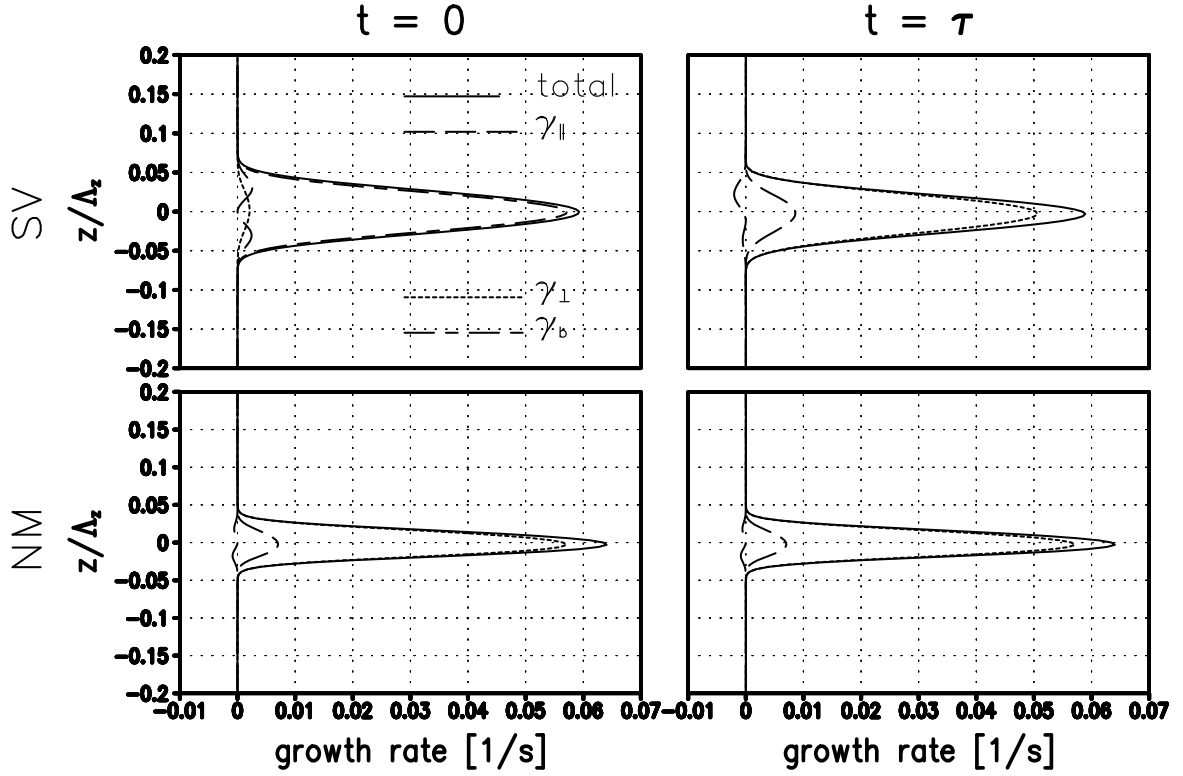


Figure 4.14: For the 1D-profile approximation of an IGW with  $(a, \Lambda_z) = (1.1, 6\text{km})$ , the altitude-dependent amplification-rate decomposition at  $t = 0$  (left column) and  $t = \tau$  (right) of the leading parallel SV (i.e. at the optimal horizontal wavelength) for the optimization time  $\tau = 10\text{min}$  (top row), and the leading parallel NM at the same horizontal wavelength (bottom).

as seen in the SV which can thereby extract energy from the basic wave in a much more efficient manner. Secondly, in the later stages the exchange processes do not differ any more between SV and NM, so that obviously the SV then has developed into the structure of the NM. Detailed comparisons between the SV and NM structure in the various dynamic fields further bear this out (not shown).

Details of the SV exchange processes for the subcritical case  $a = 0.9$  are shown in the lower panel of Fig. 4.13. At least in part these are in interesting correspondence to those seen in the constant-shear-layer approximation (Fig. 4.5). Buoyant energy exchange seems to trigger the energy growth. This is followed by a strong contribution  $\Gamma_{\perp}$ , indicating that also here the roll mechanism is the most important process at work by which



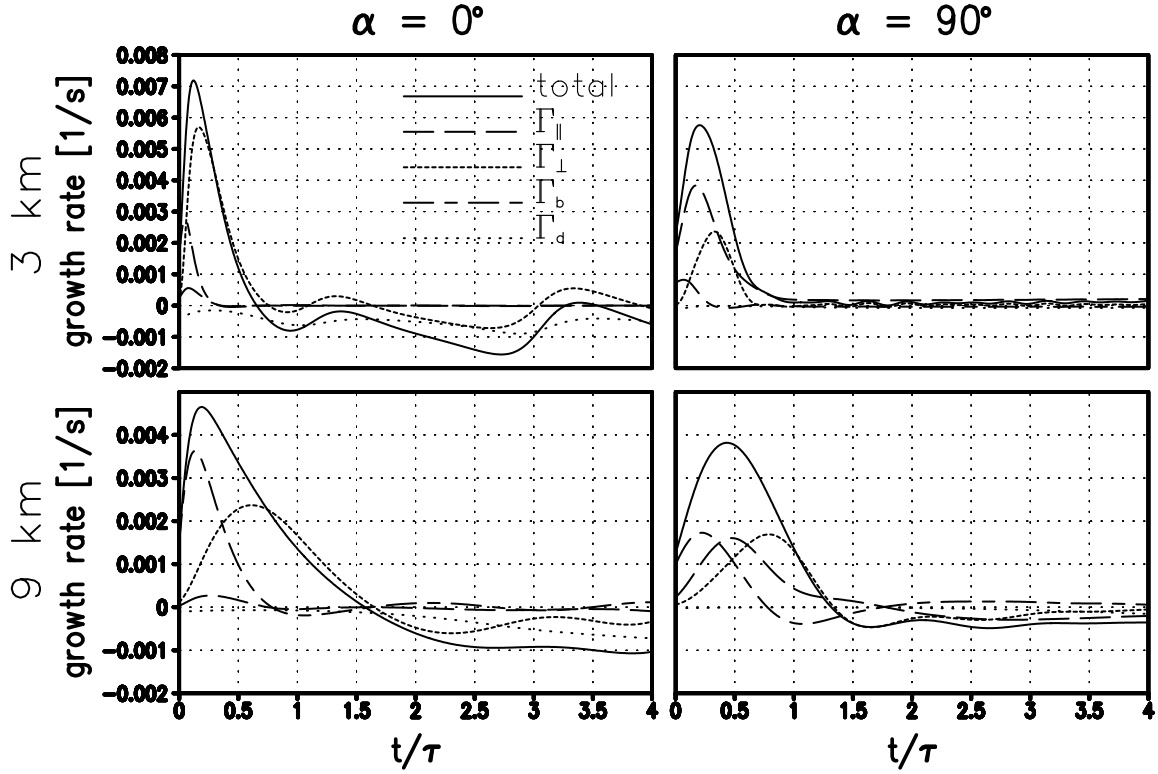


Figure 4.15: As the bottom row in Fig. 4.13, but now for  $\Lambda_z = 3\text{km}$  (top row here) and  $\Lambda_z = 9\text{km}$  (bottom).

energy is transferred from the shear in the transverse wind component in the IGW ( $V_0$ ) to the perturbation. In contrast to the predictions from the shear-layer approximation, however, there is no damped oscillation in the energy. This oscillation, a result of the repeated destructive and constructive interference between two damped NMs, seems to be obstructed by the probably more complex modal decomposition of the SV in the more general approximation. One growth cycle is followed by decay which to about equal parts results from along-gradient momentum flux ( $\Gamma_{\perp}$ ) and viscous-diffusive damping ( $\Gamma_d$ ).

For an impression of the impact of the ratio  $K_z/K_x$  in the IGW the left column of Fig. 4.15 shows for  $a = 0.9$  and the vertical wavelengths  $\Lambda_z = 3\text{km}$  and  $9\text{km}$ , but always  $\Lambda_x = 500\text{km}$ , the time dependent amplification-rate decomposition from integrations of the leading parallel SV. In the shear-layer picture larger  $K_z/K_x$  means larger  $\beta$  and thus a more important contribution from the shear-related exchange term  $\Gamma_{\perp}$  in comparison to  $\Gamma_b$ . Likewise one would expect an increase of the total growth factor and thus also the

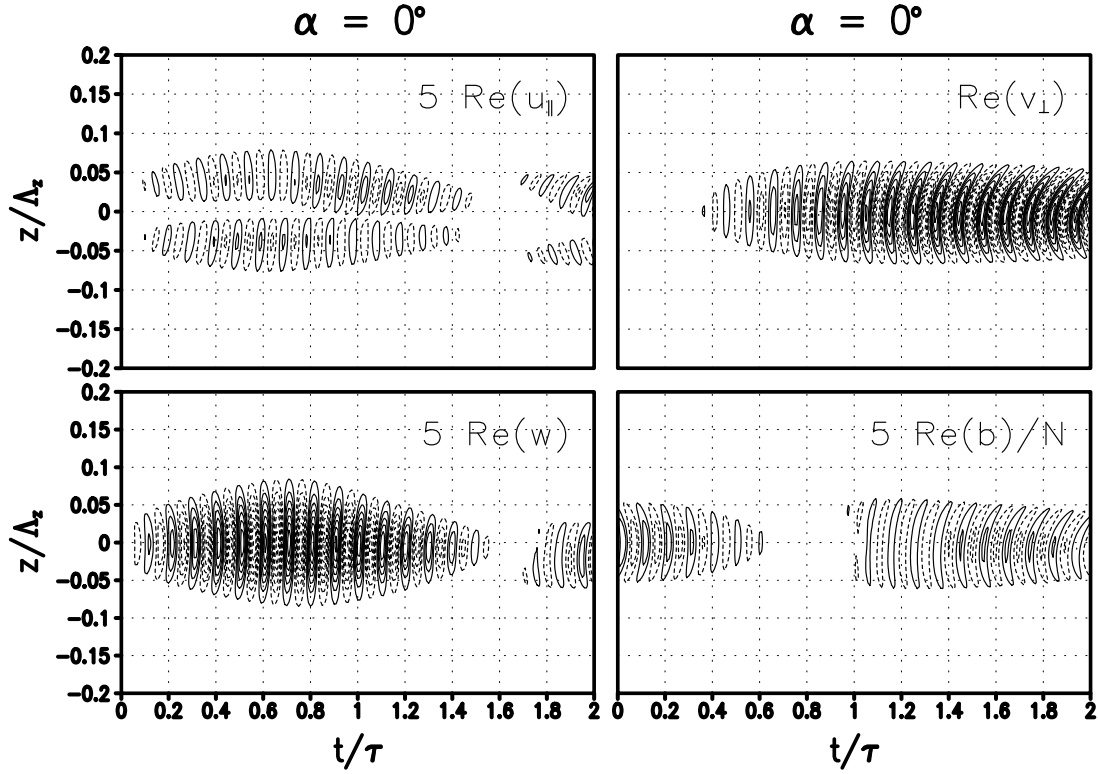


Figure 4.16: For the leading (i.e. at optimal horizontal wavelength) parallel SV in the approximation of the IGW with  $\Lambda_z = 6\text{km}$  and  $a = 0.9$  by a 1D profile, the time-dependent real parts of all four model variables from integrations over two optimization periods  $\tau = 10\text{min}$ . Contour intervals are in arbitrary units, but five times larger for  $v_\perp$  than for the other variables. The zero contour is not shown. Negative values are indicated by dashed contours.

instantaneous amplification rate. Both expectations are verified here while also in these cases no damped energy oscillation is observed.

The space-time dependence of the leading parallel SV for  $(a, \Lambda_z) = (0.9, 6\text{km})$  is shown in Fig. 4.16 where one can see the time development (between  $t = 0$  and  $t = 2\tau$ ) of the real parts of all four model variables. At all stages the structure is extremely confined to the statically least stable altitude region, which might be an explanation why for this case the constant-shear-layer approximation works so reasonably. Notable is also the dominance of growth in  $v_\perp$  (note the different contour intervals), resulting from the exchange via the roll mechanism, while the buoyancy perturbation is initially losing energy. The rapid time-

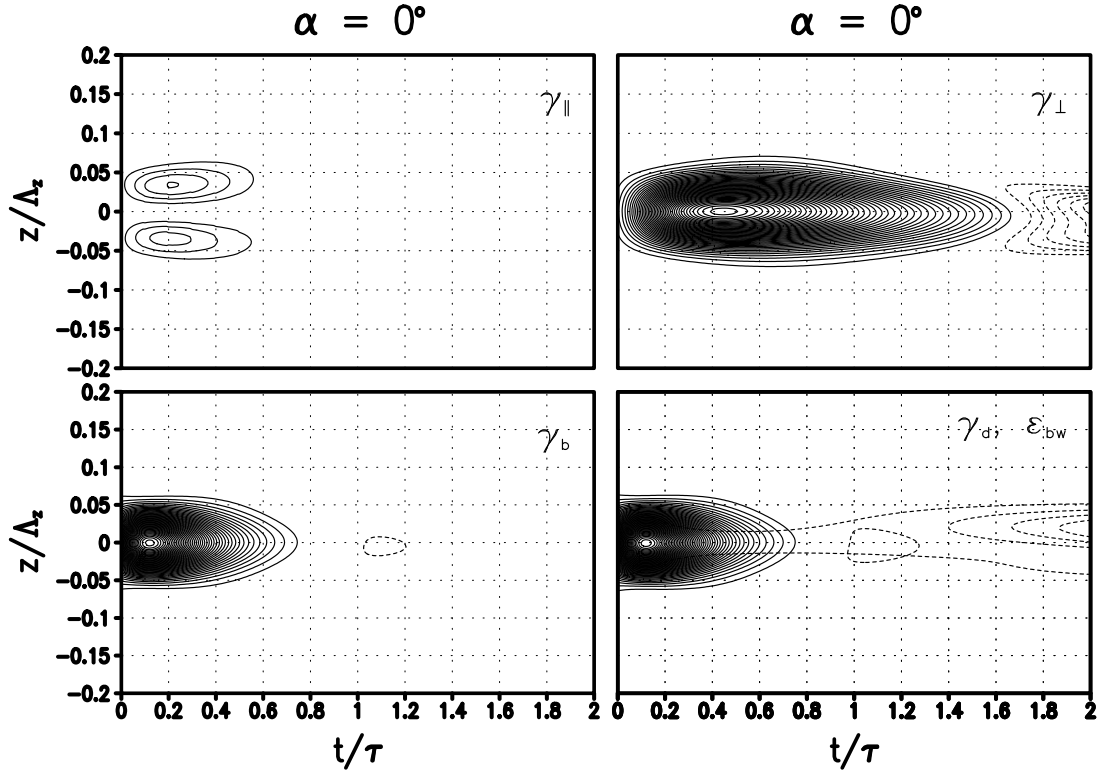


Figure 4.17: From the same integration as shown in Fig. 4.16 the corresponding altitude-dependent amplification-rate contributions. The contour interval is  $2 \cdot 10^{-4} \text{s}^{-1}$ . The zero contour is not shown. Negative values are indicated by dashed contours. In the lower right panel the viscous-diffusive damping is recognizable from its negative values throughout.

oscillation is due to the advection of the small-scale structure ( $\lambda_{\parallel} \approx 660 \text{m}$ ) in the parallel wind in the IGW which reaches a minimum  $U_0 \approx -11 \text{m/s}$  at  $z = 0$ , also in agreement with the shear-layer picture (i.e. all variables are  $\propto \exp(ik_{\parallel} U_{\parallel} t)$ ). The corresponding time development of the amplification-rate contributions can be seen in Fig. 4.17, showing the strong exchange  $\gamma_{\perp}$  due to the roll mechanism. It is interesting to see that the energy in  $b$  decays while  $\gamma_b$  is positive initially. This is a result of a buoyant exchange  $\epsilon_{bw} = e_{bw} / \langle e_{kl} \rangle$  between the perturbation energy in  $b$  and  $w$ , while the latter then leads via  $\gamma_{\perp}$  to the growth in  $v_{\perp}$ , showing how in this chain both reduced static stability (via  $\gamma_b$ ) and the transverse wind shear (via  $\gamma_{\perp}$ ) together lead to the strong overall growth of the perturbation in  $v_{\perp}$ . Note that  $r_b = (1 - N_{\text{tot}}^2 / N^2) e_{bw}$ , implying that near the initially statically least stable altitude  $z = 0$  buoyancy must necessarily decay via  $e_{bw}$  for  $a < 1$  if

$r_b > 0$ . In fact Fig. 4.16 clearly shows that the energy in  $w$  increases if that in  $b$  decreases and vice versa.

**Transverse singular vectors** Now turning to the leading transverse SVs one sees in the right column of Fig. 4.13 the energy for  $a = 0.9$  and  $1.1$ , and the amplification-rate decomposition for  $a = 0.9$ , also from integrations over four optimization times. In contrast to the parallel case, at the respective horizontal wavelength no unstable NM exists so that, as in the constant-shear-layer approximation, energy eventually decays. Details of the SV exchange processes for the subcritical case  $a = 0.9$  are shown in the lower panel of Fig. 4.13. At least in part these are again in interesting correspondence to those seen in the constant-shear-layer approximation. Buoyant energy exchange seems to trigger the energy growth, followed by another contribution from  $\Gamma_{\parallel}$ , indicating the Orr mechanism to be at work, in which the counter-gradient flux of  $u_{\parallel} = v$  interacts with the corresponding shear  $dU_{\parallel}/dz = dV_0/dz$  in the IGW. In contrast to the shear-layer approximation, however, there also is a final important contribution from  $\Gamma_{\perp}$ , so that also here the roll mechanism seems to be active. The impact of the ratio  $K_z/K_x$  in the IGW (right column in Fig. 4.15) is again in reasonable correspondence to the predictions from the constant-shear-layer approximation. Larger  $K_z/K_x$ , and hence larger  $\beta$  lead to a more important contribution from  $\Gamma_{\parallel}$  in comparison to  $\Gamma_b$ , and also stronger overall growth. In all examined cases, however, we also see a significant contribution from the roll mechanism, as not predicted in the shear-layer picture.

The space-time dependence of the SV together with its energetics are shown in Figs. 4.18 and 4.19. Since  $U_{\parallel} = V_0$  vanishes near  $z = 0$  no corresponding high-frequency advection is visible as in the case of the parallel SV. A strong contribution from  $\gamma_{\parallel}$  at  $z = 0$  shows the Orr mechanism to work near the strongest gradient of  $U_{\parallel} = V_0$ . Similarly to the case of the parallel SV one finds, however, also a large initial  $\gamma_b$  while  $b$  decays, indicating that  $e_{bw}$  is immediately transferring buoyant energy into kinetic energy in  $w$ , thereby enforcing the roll mechanism which via  $\gamma_{\perp}$  leads to a considerable increase in the energy in  $v_{\perp}$ . Note that the latter process here works at some distance from  $z = 0$  where it would be forbidden due to  $\partial V_{\perp}/\partial z = -\partial U_0/\partial z = 0$ . The remaining behavior looks more

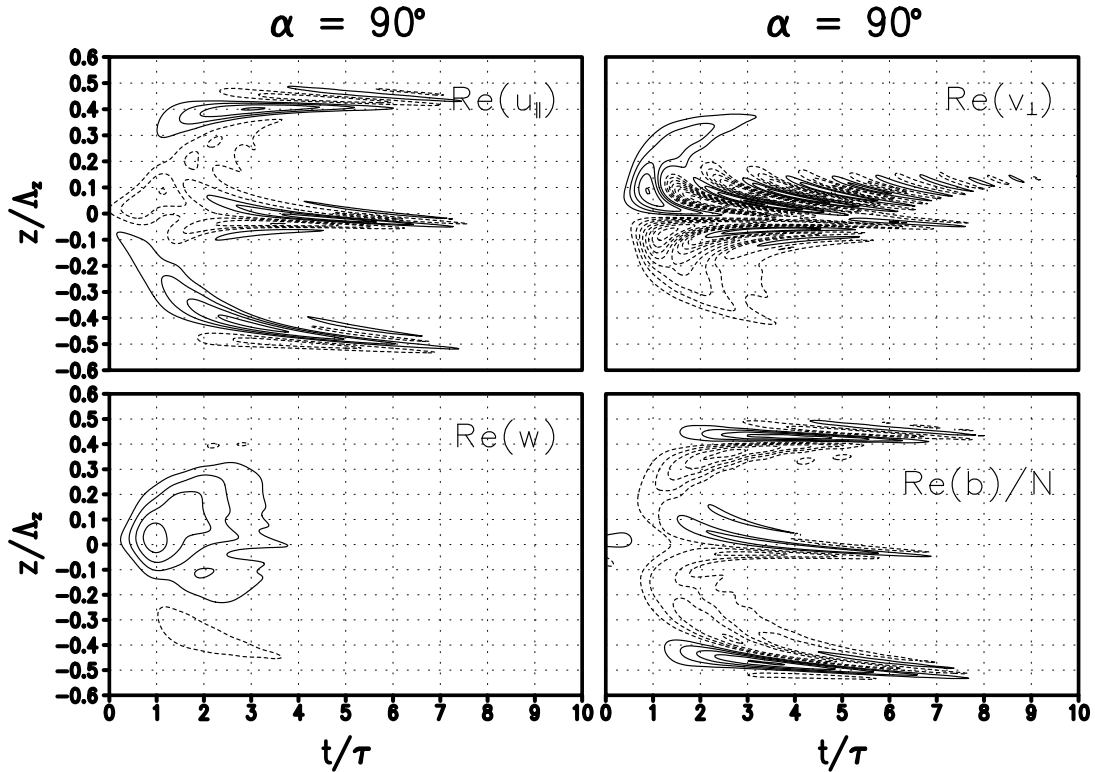


Figure 4.18: As Fig. 4.16, but now from an integration of the leading transverse SV over ten optimization periods  $\tau = 10\text{min}$ . Here all variables are shown with identical contours.

complex, with apparent vertical radiation from the statically least stable altitude, ending in small-scale structures near  $z = \pm\Lambda_z/2$  and  $z = 0$ . We also note that the vertical scales of the developing structures are progressively decreasing, leading to strong viscous-diffusive decay in the late stages of the development, and that they are considerably shorter than the ones set by the IGW packet. While the behavior near  $z = 0$  is consistent with the picture of an Orr mechanism leading to diverging vertical wavenumber in the source region, one might speculate that the development near  $z = \pm\Lambda_z/2$  is related to the approach of a small-scale wave towards a critical layer, as first described via WKB theory by Bretherton (1966). This is a hypothesis which shall be tested here in a quantitative manner.

We observe that in comparison to the perturbation the spatial and time dependence of the basic wave is weak. In the case of a constant background one would obtain from the model equations plane gravity waves with no component in  $v_\perp$ . Therefore a scaling

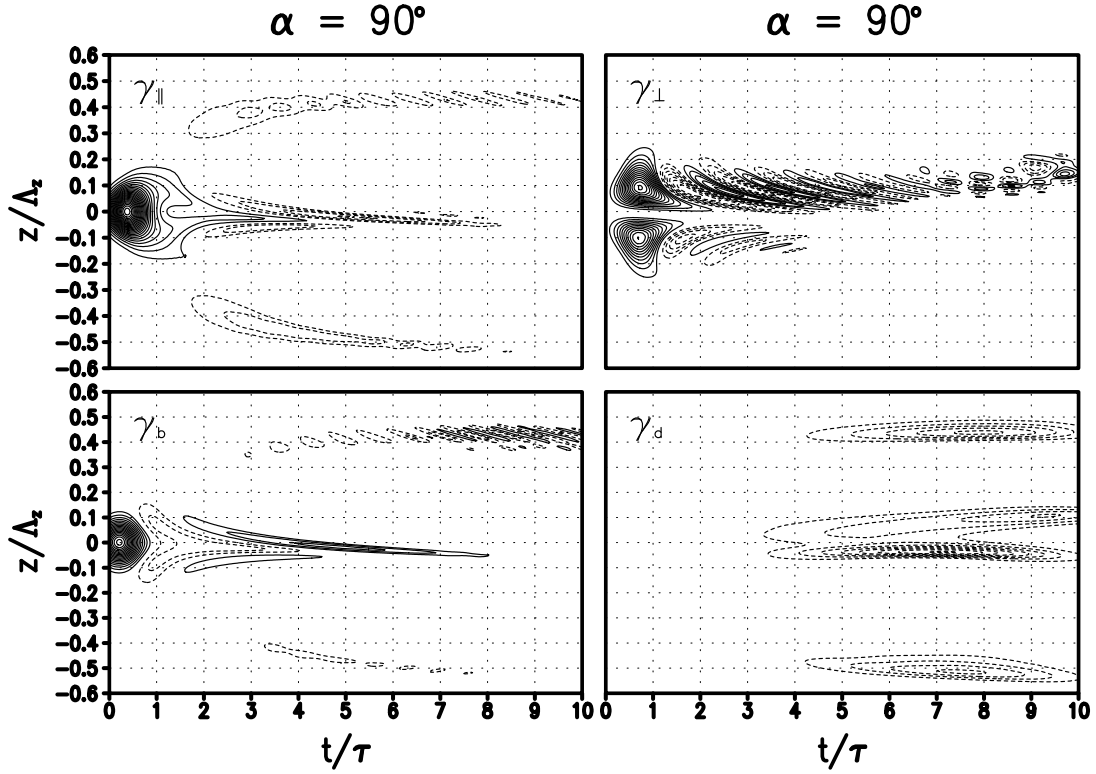


Figure 4.19: From the same integration as shown in Fig. 4.18 the corresponding altitude-dependent amplification-rate contributions. The contour interval is  $2 \cdot 10^{-4} s^{-1}$ . The zero contour is not shown. Negative values are indicated by dashed contours.

parameter  $\varepsilon$  is introduced and we use the modified WKB ansatz

$$\left( U_{\parallel}, V_{\perp}, N_{tot}^2 \right) (z, t) = \left( \tilde{U}_{\parallel}, \tilde{V}_{\perp}, \tilde{N}_{tot}^2 \right) (\varepsilon z, \varepsilon t) \quad (4.66)$$

$$\left( u_{\parallel}, v_{\perp}, w, b, p \right) (z, t) = \left( \tilde{u}_{\parallel}, \varepsilon \tilde{v}_{\perp}, \tilde{w}, \tilde{b}, \tilde{p} \right) (\varepsilon z, \varepsilon t) e^{i\eta(\varepsilon z, \varepsilon t)/\varepsilon} \quad (4.67)$$

We define

$$\omega = -\frac{1}{\varepsilon} \frac{\partial \eta}{\partial t} \quad (4.68)$$

$$m = \frac{1}{\varepsilon} \frac{\partial \eta}{\partial z} \quad , \quad (4.69)$$

while the model equations (neglecting the Coriolis effect) yield to lowest order in  $\varepsilon$

$$u_{\parallel} = -i \frac{\hat{\omega}}{N_{tot}^2} \frac{m}{k_{\parallel}} b \quad (4.70)$$

$$v_{\perp} = \frac{b}{N_{tot}^2} \frac{\partial V_{\perp}}{\partial z} \quad (4.71)$$

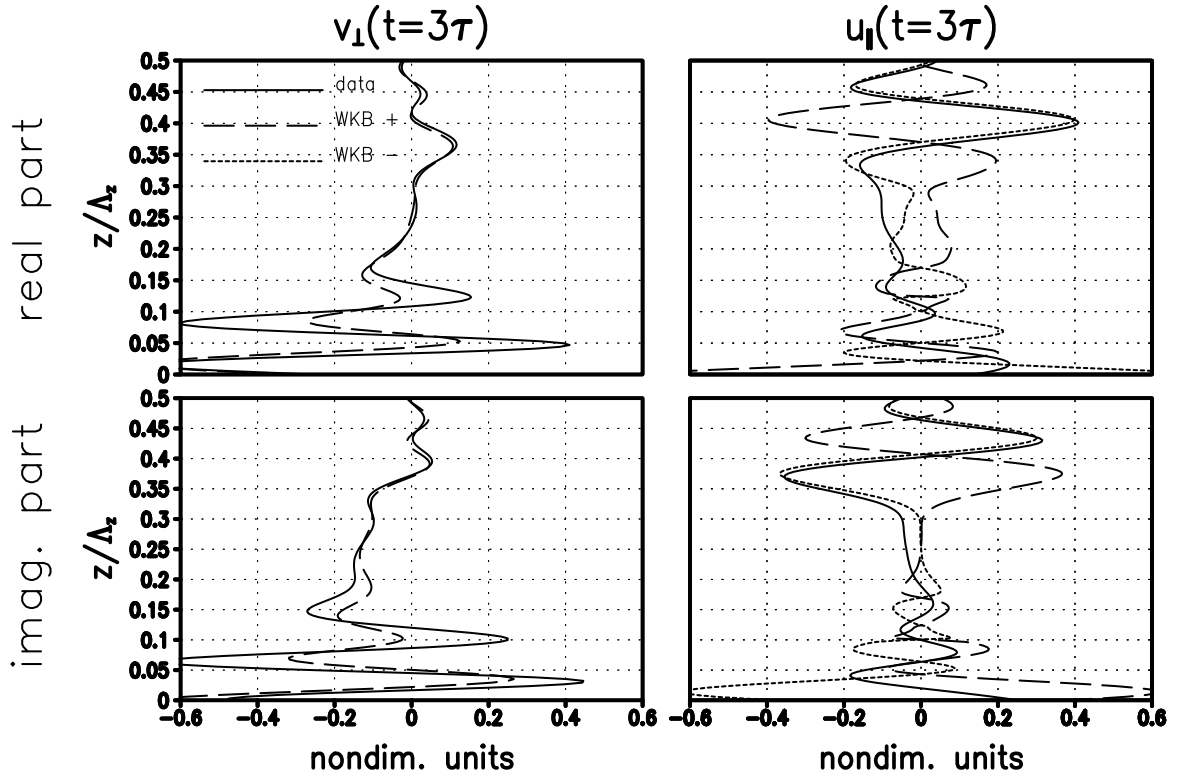


Figure 4.20: From the same integration as shown in Fig. 4.18 the real parts (top row) and imaginary parts (bottom) for  $v_{\perp}$  (left column) and  $u_{\parallel}$  (right) at  $t = 3\tau = 30\text{min}$ , as well as the prediction of these fields from WKB theory using the two branches  $\delta = \pm 1$ .

$$w = i \frac{\hat{\omega}}{N_{tot}^2} b \quad (4.72)$$

$$\hat{\omega} = \omega - k_{\parallel} U_{\parallel} = \delta \sqrt{\frac{N_{tot}^2 k_{\parallel}^2}{k_{\parallel}^2 + m^2}} \quad , \quad \delta = \pm 1 \quad . \quad (4.73)$$

(4.68) – (4.69) can be combined with (4.73) to give a predictive equation for the local vertical wavenumber

$$\frac{\partial m}{\partial t} = -c_{gz} \frac{\partial m}{\partial z} - \frac{\partial \Omega}{\partial z} \quad (4.74)$$

with the vertical group velocity  $c_{gz} = \partial \Omega / \partial m = -\hat{\omega} m / (k_{\parallel}^2 + m^2)$  and the frequency function  $\Omega(k_{\parallel}, m, z, t) = k_{\parallel} U_{\parallel} + \hat{\omega}(k_{\parallel}, z, t)$ . Once buoyancy  $b$  and the vertical wavenumber  $m$  have been diagnosed from the linear model one can examine whether  $u_{\parallel}$ ,  $v_{\perp}$ , and  $w$  are for any  $\delta$  consistent with the WKB theory via (4.70) – (4.72). Having verified this, it is then possible to go to (4.74) and identify the process responsible for the apparent increase

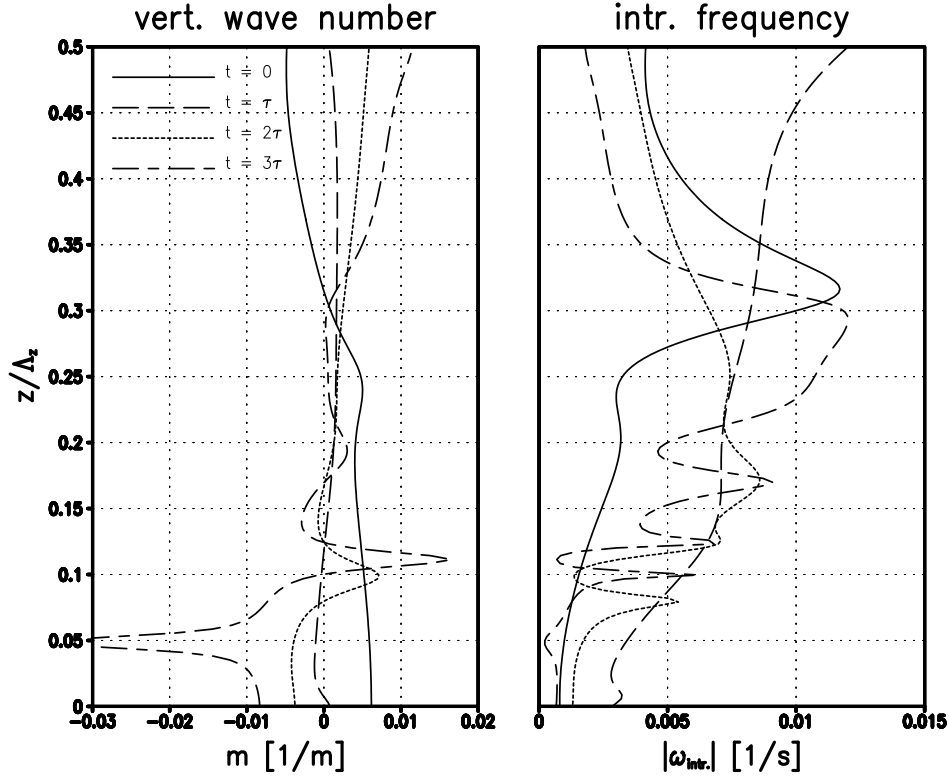


Figure 4.21: From the same integration as shown in Fig. 4.18 the vertical wavenumber (left panel) and the absolute value of the intrinsic frequency according to WKB theory (right) at four characteristic times.

of the vertical wavenumber in the layer formation. This is what has been done here. The vertical wavenumber has been determined from the buoyancy fields by first determining  $\exp(i\eta/\varepsilon) = b/|b|$  and hence  $m = \Im[\exp(-i\eta/\varepsilon)\partial/\partial z \exp(i\eta/\varepsilon)]$ .

For illustration some results for  $z > 0$  are shown, while in the other altitude range they support at the same accuracy the final conclusions. For  $t = 3\tau$  Fig. 4.20 shows the real and imaginary parts of the two horizontal wind components, as well as the prediction of these quantities from the basic-wave fields,  $b$ , and  $m$ , for both cases  $\delta = \pm 1$ . The time dependent vertical wave number and intrinsic frequency are shown in Fig. 4.21. One sees that  $m < 0$  near  $z = 0$  and  $m > 0$  else. The agreement between the horizontal wind in the perturbation and the prediction from WKB theory is very good for  $\delta = -1$  near  $z = \Lambda_z/2$  and reasonable for  $\delta = 1$  near  $z = 0$ . This indicates that the data can be interpreted by the WKB model as resulting from small-scale GWs radiating away from the statically



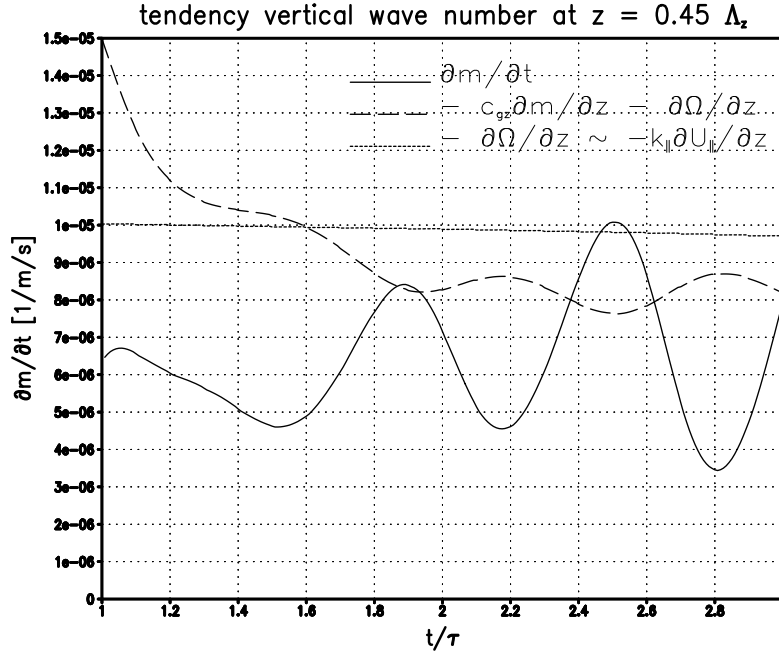


Figure 4.22: From the same integration as shown in Fig. 4.18 the tendency of vertical wavenumber at  $z = 0.45\Lambda_z$ , its prediction by WKB theory (long-dashed), and the part of the latter due to the transverse-wind gradient in the IGW  $\partial U_{\parallel}/\partial z = \partial V_0/\partial z$  (short-dashed).

least stable location.

Returning now to the critical-layer hypothesis we first note that the local frequency  $\omega(z, t) = \Omega[m(z, t), z, t]$  satisfies

$$\frac{\partial \omega}{\partial t} = -c_{gz} \frac{\partial \omega}{\partial z} + \frac{\partial \Omega}{\partial t} \quad , \quad (4.75)$$

i.e. for a time-independent background the frequency would be conserved along rays defined by the local group velocity. Under such circumstances a critical layer arises as in the course of propagation along a ray  $k_{\parallel} U_{\parallel} \rightarrow \omega$ , and hence  $\hat{\omega} \rightarrow 0$  and  $|m| \rightarrow \infty$ . In (4.74) this should express itself in a dominance of  $\partial \Omega / \partial z \approx k_{\parallel} \partial U_{\parallel} / \partial z$  on the right-hand side. Here we have a time-dependent background so that this picture can only be satisfied approximately. Still, however, one finds the layer near  $z = \Lambda_z/2$  to be characterized by an increase of vertical wavenumber and corresponding decrease of intrinsic frequency  $\hat{\omega}$ , as visible in Fig. 4.21. In passing we also note the sign change in  $m$  near  $z = 0$  from  $t < \tau$  to  $t > \tau$ , as predicted from the shear-layer theory. Finally Fig. 4.22 shows for the altitude

$z = 0.45\Lambda_z$  the diagnosed tendency of vertical wavenumber (estimated from central 10-sec differences), the prediction of this by WKB theory, and the contribution to the latter by the vertical shear in the transverse wind of the basic IGW. Indeed WKB theory seems to give a useful approximation of the complete wavenumber dynamics during the formation of the small-scale layer. It slightly overestimates the wavenumber increase but the basic effect is reproduced, where it is mostly the vertical shear in  $U_{\parallel} = V_0$  which causes the scale collapse observed at the shear layer. In summary, although the time-dependence of the background precludes a robust critical layer (Broutman and Young, 1986, e.g.), one sees a strongly related effect due to the propagation of the excited perturbation towards the zero lines  $z = \pm\Lambda_z/2$  of the transverse wind in the basic IGW packet.

### Long optimization times

For  $\tau = 2\text{h}$  one sees in Fig. 4.23 the time dependent amplification-rate decomposition of the optimally growing structure at each of the four examined azimuth angles (see above). The behavior of the parallel optimal perturbation is still very similar to the one at short optimization times, albeit on a longer time scale. Again one sees the statically enhanced roll mechanism at work, with an initial trigger by buoyancy related energy exchange with the IGW.  $\Gamma_{\parallel}$  rises at larger  $\alpha$  in importance over  $\Gamma_{\perp}$ , while the initial contribution from  $\Gamma_b$  is always there, giving an indication of a statically enhanced Orr mechanism. Again one does not find the damped energy oscillation from the constant-shear-layer picture at  $\alpha = 0^\circ$ . At  $\alpha > 0^\circ$  damped oscillatory behavior is visible, but from the next two figures one can see that the process behind this is not the same as in the shear-layer approximation.

In Fig. 4.24 one can see for all azimuth angles the development of the real part of the vertical wind in the perturbation, while Fig. 4.25 shows for  $\alpha = 60^\circ$  the space-time dependence of the four amplification-rate contributions. One sees that for all  $\alpha < 90^\circ$  the SVs radiate small-scale GWs into the far field where the IGW does not influence the propagation conditions any more. In Fig. 4.25 one can recognize that the damped oscillatory behavior of the amplification-rate contributions results from the movement of the radiated waves through the IGW. In the course of this propagation it gets successively into contact

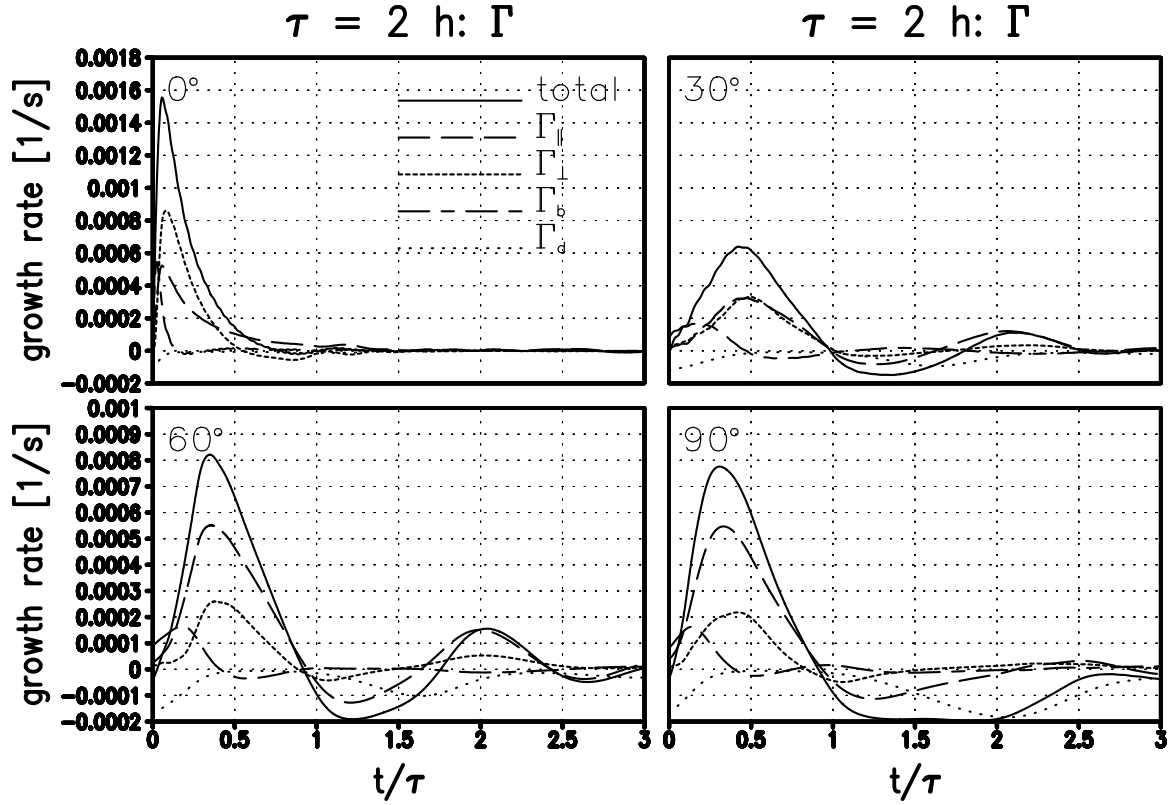


Figure 4.23: From an integration of the leading SVs (i.e. at most rapidly growing parallel wavelength), at azimuth angle  $\alpha = 0^\circ, 30^\circ, 60^\circ$ , and  $90^\circ$  and optimization time  $\tau = 2\text{h}$ , in an approximation of an IGW with  $(a, \Lambda_z) = (0.9, 6\text{km})$  by a one-dimensional profile, the instantaneous amplification rate and its decomposition.

with differing shear and stratification conditions. As the static energy exchange  $\Gamma_b$  is only important initially it is concentrated in the packet center, but the shear-related exchange terms  $\gamma_{||}$  and  $\gamma_{\perp}$  are correlated with the respective gradients  $\partial U_{||}/\partial z$  and  $\partial V_{\perp}/\partial z$ . The corresponding oscillation in the energy exchange (Fig. 4.23) gets weaker as the radiated waves move away from the center of the IGW packet into regions where the IGW gradients are negligible.

It is interesting to note that the fact that we here find wave radiation by the SVs, while this is not visible for the shorter optimization time  $\tau = 10\text{min}$  (see Figs. 4.16 and 4.18), can be understood in terms of simple linear GW dynamics. As shown above, but also visible in Fig. 4.24, all but the transverse SVs show a rapid time oscillation

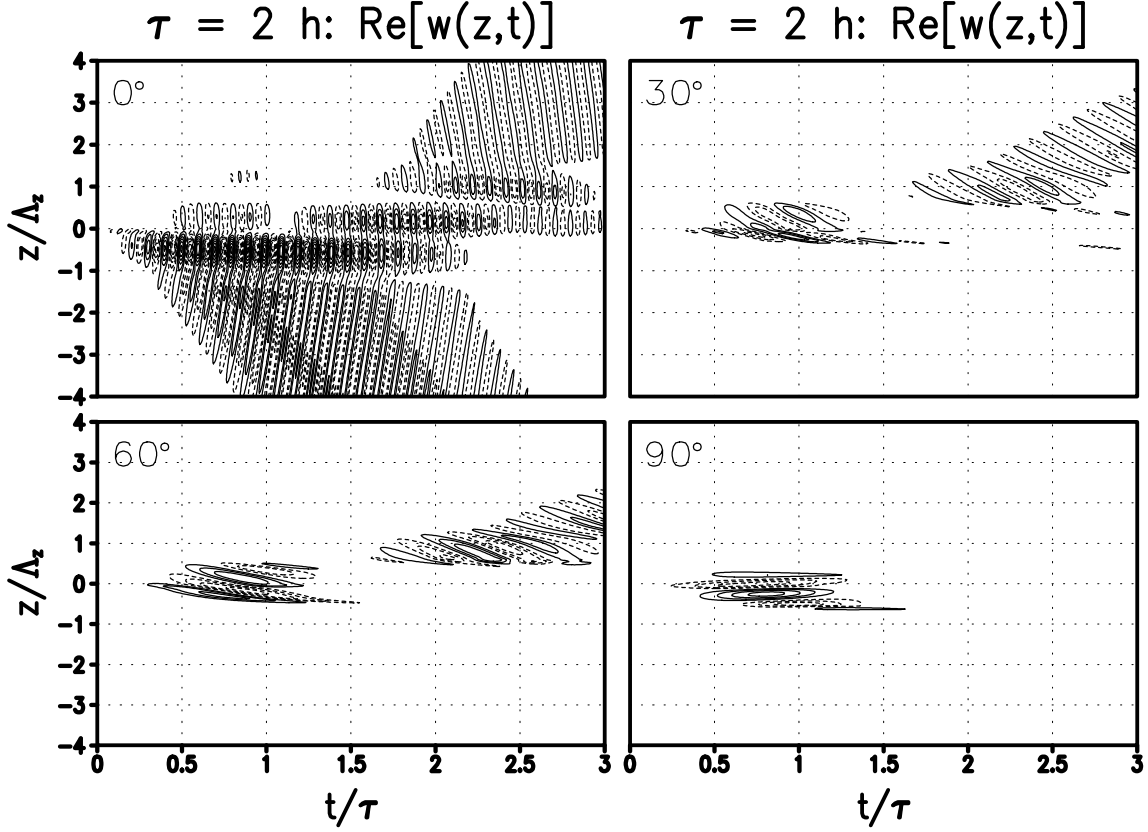


Figure 4.24: From the same integrations as shown in Fig. 4.23, the space-time dependent real part of the vertical wind in the perturbation. The contour intervals are in nondimensional units. Negative values are indicated by dashed contours. The zero contour is not shown.

in all fields with a period determined by advection of their small-scale structure in the wind  $U_{\parallel}$  in the IGW near the statically least stable location, i.e. their frequency is  $\omega \approx k_{\parallel} U_{\parallel}$ . In the external region (where the IGW fields are essentially zero) GWs at such a frequency can only propagate if  $|\omega| < N$  so that non-evanescent wavenumbers are limited to  $k_{\parallel} < N/|U_{\parallel}|$ . Since the scales of SVs at short optimization times are too small for this (e.g.  $\lambda_{\parallel} \approx 660\text{m}$  for  $\alpha = 0^\circ$  and  $\tau = 10\text{min}$ , see above) they cannot radiate, while the opposite holds for longer  $\tau$ . The same rationale can also explain the vertical scales of the radiated structures themselves. From the far-field GW dispersion relation  $\omega = \pm N k_{\parallel} / \sqrt{k_{\parallel}^2 + m^2}$  follows for  $\alpha < 90^\circ$  (neglecting the Coriolis effect)

$$m = \sqrt{\frac{N^2}{u_0^2 \cos^2 \alpha} - k_{\parallel}^2} \quad , \quad (4.76)$$

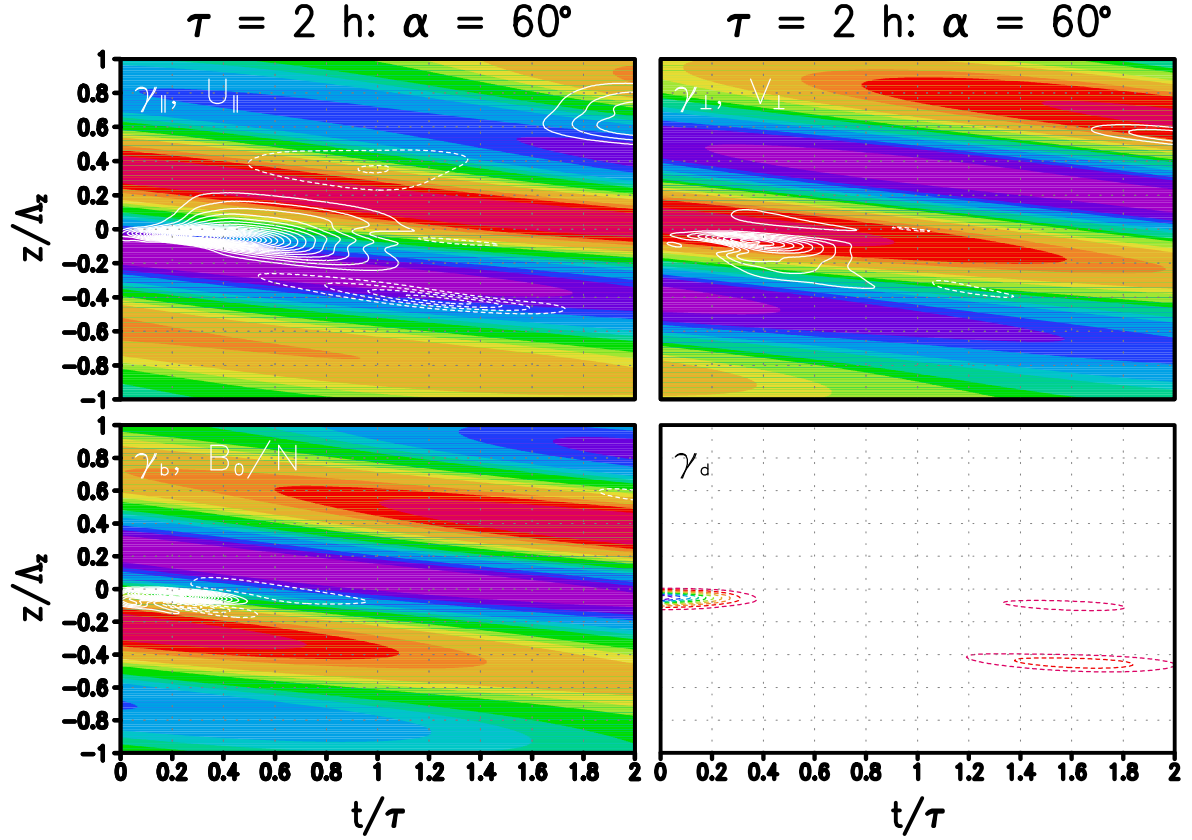


Figure 4.25: From the integration for  $\alpha = 60^\circ$  shown in Figs. 4.23 and 4.24, the space-time dependent IGW fields (shaded with shading interval 1m/s), and the respective contributions to the instantaneous amplification rate, as well as that of viscous-diffusive damping. For the amplification-rate contributions the contour interval is  $2 \cdot 10^{-4} \text{s}^{-1}$ . Negative values are indicated by dashed contours. The zero contour is not shown.

since near the statically least stable location  $U_{\parallel} = u_0 \cos \alpha$ . From this relation one finds for the radiated structures in Fig. 4.25 the predicted vertical scales  $2\pi/m \approx 2.7\Lambda_z, 1.1\Lambda_z, 0.61\Lambda_z$  for  $\alpha = 0^\circ, 30^\circ, 60^\circ$ , where the optimal wavelengths are 7.9km, 16km, and 16km, respectively (see Fig. 4.12). These are in quite good agreement with the numerical results shown here. As a consequence one can expect as far-field behavior of slightly subcritical IGW the radiation of high-frequency GWs with increasingly shorter periods and longer vertical wavelengths as the azimuth angle decreases. From the same reasoning one can also expect transverse radiation to be basically obstructed, since the resulting waves will always be evanescent.

## 4.4 General inertia-gravity wave packets

Dropping all simplifications we finally get to the most general SVs in the IGW packet with complete time and space dependence. As discussed above these are of the form  $(\mathbf{v}', b', p') = (\mathbf{v}, b, p)(x, z) \exp(i l y)$  with an arbitrary wavenumber  $l = 2\pi/\lambda_y$  in  $y$ -direction. One would expect that in a survey of the SV dependence on  $\lambda_y$  the parallel SVs from above leave their traces among the general SVs for  $\lambda_y = \infty$ , whereas oblique and transverse SVs are to be found among  $\lambda_y < \infty$ . For illustration here the two cases  $\tau = 10\text{min}$  and  $1\text{h}$ , for  $a = 0.9$  each, are discussed.

Expecting the resulting features to be located near the location of least static stability the IGW packet, from a nonlinear integration in a periodic box with dimensions  $(L_x, L_z) = (\Lambda_x, 5\Lambda_z) = (500\text{km}, 30\text{km})$ , was stored for greater numerical efficiency for the analyzes of  $\lambda_y < \infty$  in the inner sub-domains with  $(L_x, L_z) = (\Lambda_x/2, 3\Lambda_z)$  and tapered to zero with a cosine profile in the outer regions therefrom with horizontal extent  $\Lambda_x/8$  and vertical extent  $\Lambda_z$ . For  $\tau = 10\text{min}$  and  $l = 0$  the stored inner sub-domain is of extent  $(L_x, L_z) = (\Lambda_x/2, \Lambda_z)$  with tapering over the horizontal extent  $\Lambda_x/8$  and over the vertical extent  $\Lambda_z/8$ , while for  $\tau = 1\text{h}$  and  $l = 0$  the stored inner sub-domain is of extent  $(L_x, L_z) = (\Lambda_x/2, 5\Lambda_z)$  with tapering over the horizontal extent  $\Lambda_x/8$ . In each case the chosen resolution was made sure to well resolve all essential resulting features. In several experiments it was also made sure that the limitation to the central least stable region was of no effect on the results.

For the wavelength range between  $\lambda_y = 1\text{km}$  and  $6\text{km}$  the growth factors found for the leading SVs are shown in Fig. 4.26. One sees for  $\tau = 10\text{min}$  a local optimum with growth by  $\sigma_1 = 6.8$  at  $\lambda_y = 3.9\text{km}$ . This seems to be related to optimal transverse growth, i.e. at  $\alpha = 90^\circ$ , in the 1D profile by  $\sigma_1 = 7.0$  at  $\lambda_{\parallel} = 3.8\text{km}$  (see above). For the same  $\tau$  the general SV at  $l = 0$  grows by  $\sigma_1 = 8.9$ , just as the leading parallel SV, i.e. for  $\alpha = 0^\circ$ , found for the 1D profile. The wavelength  $\lambda_{\parallel} = 660\text{m}$  of that pattern also is in good agreement with the scales of the general SV (see below). For  $\tau = 1\text{h}$  an optimum at  $(\lambda_y, \sigma_1) = (5.5\text{km}, 26.3)$  is found which seems to correspond to optimal transverse growth in the 1D approximation at  $(\lambda_{\parallel}, \sigma_1) = (5.0\text{km}, 24.1)$ . At  $l = 0$  optimal growth by  $\sigma_1 = 14.7$  is found, seemingly corresponding to the leading parallel SV in the

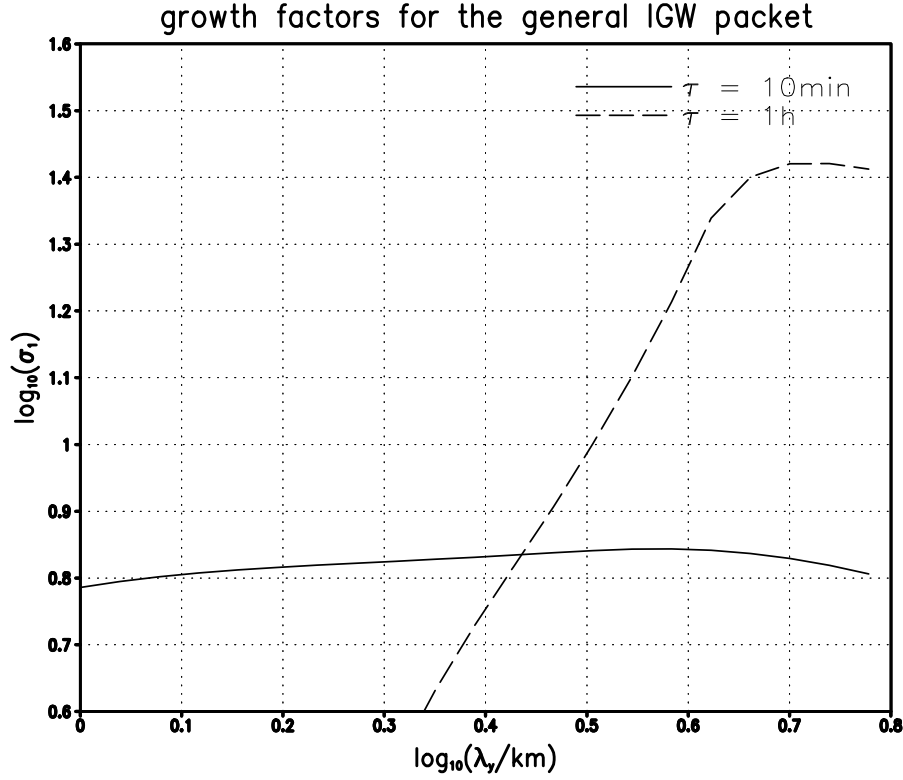


Figure 4.26: For the general IGW packet at  $(a, \Lambda_z) = (0.9, 6\text{km})$  with complete time and space dependence, the growth factors of the leading SVs for optimization times  $\tau = 10\text{min}$  and  $1\text{h}$ , in their dependence of the wavelength  $\lambda_y$  in  $y$ -direction.

1D approximation at  $(\lambda_{\parallel}, \sigma_1) = (7.1\text{km}, 13.7)$ . Also here the scales of the general SV and the one from the 1D approximation are in good agreement (not shown).

Also the energetics of the identified patterns indicates their relation to the SVs from the 1D approximation. In general one can derive for the energy density  $e_l = 1/2 (|\mathbf{v}|^2 + |b|^2 / N^2)$

$$\frac{\partial e_l}{\partial t} + \nabla_y \cdot \left[ \mathbf{V}_0 e_l + \Re(\bar{\mathbf{v}} p) - \nu \nabla_y \frac{|\mathbf{v}|^2}{2} - \mu \nabla_y \frac{|b|^2}{2N^2} \right] = r_u + r_v + r_w + r_b - D_v - D_b \quad (4.77)$$

with

$$r_u = -\Re(u \bar{\mathbf{v}}) \cdot \nabla_y U_0 \quad (4.78)$$

$$r_v = -\Re(v \bar{\mathbf{v}}) \cdot \nabla_y V_0 \quad (4.79)$$

$$r_w = -\Re(w \bar{\mathbf{v}}) \cdot \nabla_y W_0 \quad (4.80)$$

$$r_b = -\Re(b \bar{\mathbf{v}}) \cdot \frac{1}{N^2} \nabla_y B_0 \quad (4.81)$$

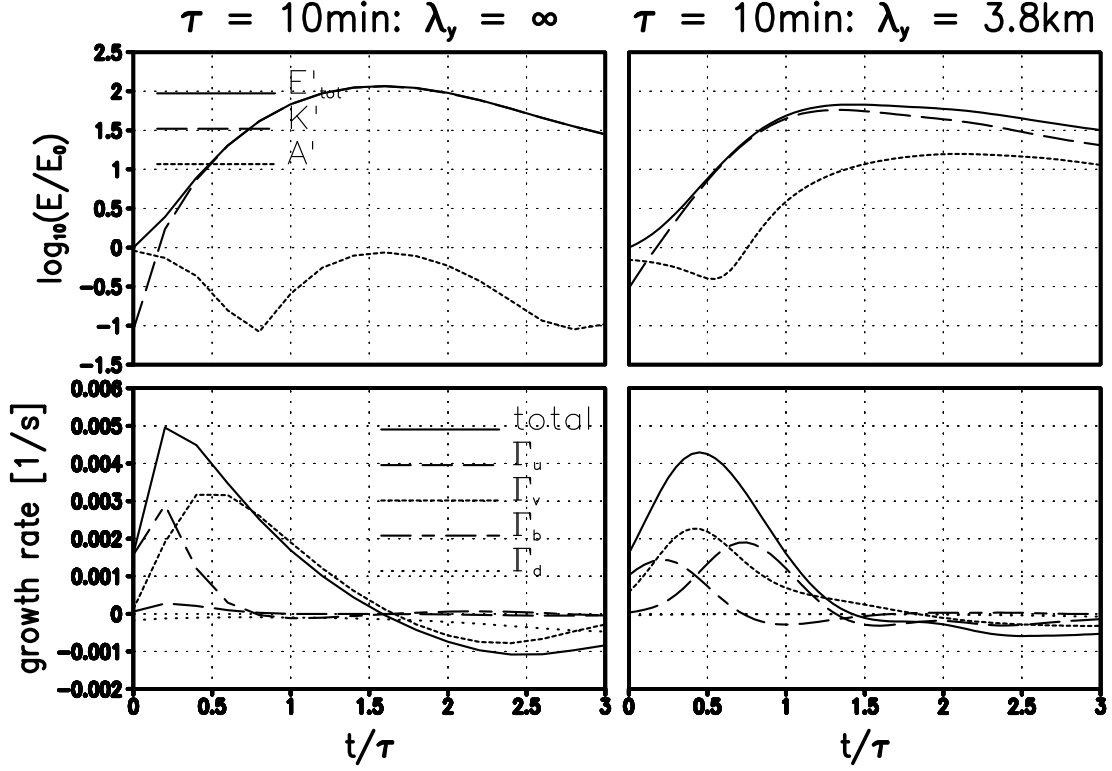


Figure 4.27: From integrations of the leading SVs, for  $\tau = 10\text{min}$  and at  $\lambda_y = \infty$  (left column) or  $3.8\text{km}$  (right), of the general IGW packet at  $(a, \Lambda_z) = (0.9, 6\text{km})$  with complete time and space dependence, the time dependence of kinetic, potential, and total energy (top row), and the corresponding instantaneous amplification-rate decomposition (bottom).

$$D_v = \nu \left[ l^2 |\mathbf{v}|^2 + \sum_{i=1}^3 |\nabla_y v_i|^2 \right] \quad (4.82)$$

$$D_b = \frac{\mu}{N^2} \left[ l^2 |b|^2 + |\nabla_y b|^2 \right] \quad , \quad (4.83)$$

where  $\nabla_y = (\partial/\partial x, 0, \partial/\partial z)$ . Energy exchange between  $w$  and  $b$  is given by the same term  $e_{bw}$  as in (4.63). As before one can calculate from the exchange terms corresponding instantaneous amplification rate contributions  $\Gamma_u$  etc. For  $\tau = 10\text{min}$  and  $a = 0.9$  the time-dependence of these and the total energy in the identified SVs is shown in Fig. 4.27. The latter is split into the kinetic energy  $K' = \int dxdz |\mathbf{v}|^2/2$  and the available potential energy  $A' = \int dxdz |b|^2/2N^2$ . The negligible contribution from  $\Gamma_w$  is not shown. Comparison with Fig. 4.13 further stresses the similarity between the general SVs and the



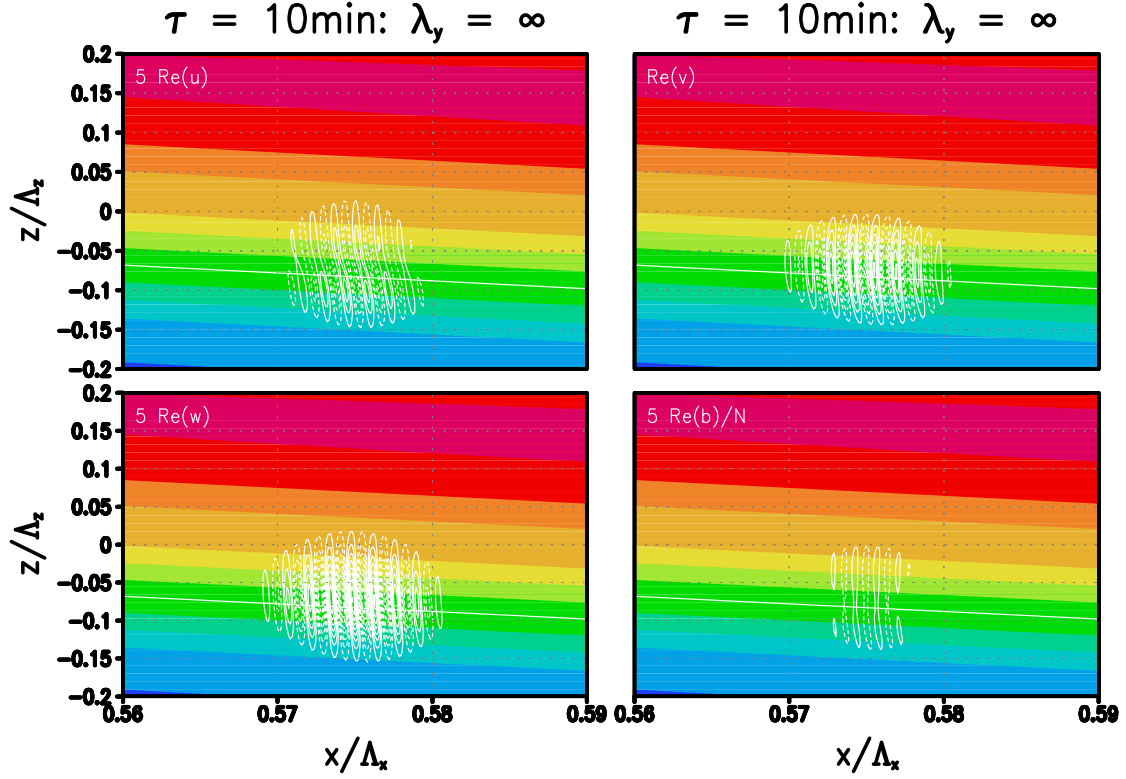


Figure 4.28: For the leading SV at  $\tau = 10\text{min}$  and  $\lambda_y = \infty$ , of the general IGW packet at  $(a, \Lambda_z) = (0.9, 6\text{km})$  with complete time and space dependence, the four dynamic fields at  $t = \tau$  (identical isolines in arbitrary units for  $u, w$  and  $b/N$ , but five times contour interval for  $v$ , zero contour not drawn), together with the transverse-wind field  $V_0$  of the IGW packet (shaded with interval  $1\text{m/s}$ , for better orientation the zero contour is indicated by a solid line), in the central region where the SV has significant amplitude.

ones from the analysis of the 1D profile, where for the case  $\lambda_y = \infty$  or  $\alpha = 0^\circ$  one obviously has to compare  $\Gamma_u$  with  $\Gamma_{\parallel}$  and  $\Gamma_v$  with  $\Gamma_{\perp}$ , while in the case  $\lambda_y = 3.8\text{km}$  or  $\alpha = 90^\circ$  the corresponding pairs are  $\Gamma_u$  and  $\Gamma_{\perp}$ , and  $\Gamma_v$  and  $\Gamma_{\parallel}$ . It thus is also no surprise that closer inspection also shows that in the general case the gradients in  $x$ -direction do not contribute to the energy budget in any significant way (not shown). Similar conclusions also hold for the case  $\tau = 1\text{h}$  (also not shown).

Of largest remaining interest therefore is the horizontal distribution of the general SVs, since the horizontal limitation of the statically weakly stable location should be expected to have some impact. Indeed this is found to be the case. Figure 4.28 shows for  $\tau = 10\text{min}$

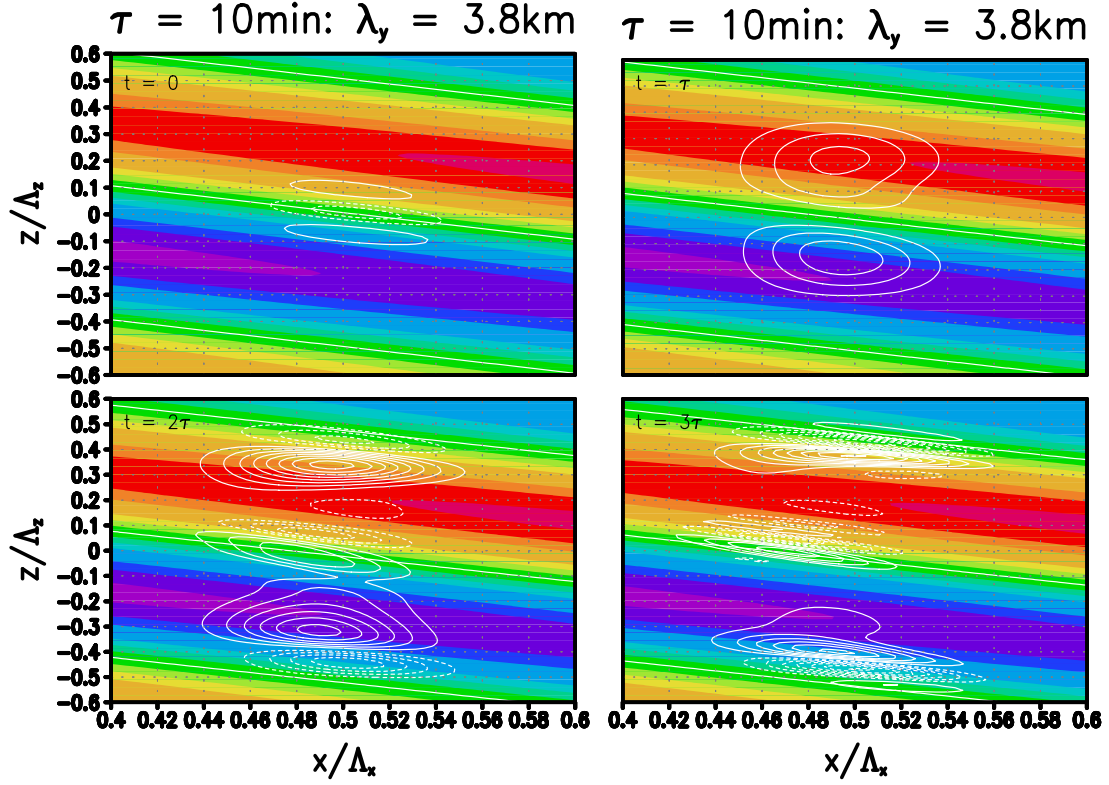


Figure 4.29: For the leading SV at  $\tau = 10\text{min}$  and  $\lambda_y = 3.8\text{km}$ , of the general IGW packet at  $(a, \Lambda_z) = (0.9, 6\text{km})$  with complete time and space dependence, the buoyancy field at four characteristic time instances (identical isolines in arbitrary units, zero contour not drawn), together with the transverse-wind field  $V_0$  of the IGW packet (shaded with interval  $1\text{m/s}$ , for better orientation the zero contour is indicated by a solid line), in the central region where the SV has significant amplitude.

the leading SV at  $l = 0$  and at  $t = \tau$  in the region where it has significant amplitude. One observes that it is a wave packet both vertically and horizontally closely confined near the location of least static stability. In the course of the time integration one observes its rapid leftwards advection to smaller  $x$  by the  $U_0$ -wind in the IGW (not shown). Note that near  $a = 1$  this advection is approximately at the horizontal phase velocity of the IGW so that the SV follows the movement of the statically least stable location, thereby enabling longer transient growth. Also here the overwhelming contribution to this growth is from the amplification of  $v$ . For  $\tau = 10\text{min}$  and  $\lambda_y = 3.8\text{km}$  Fig. 4.29 shows the time development of buoyancy in the leading SV between  $t = 0$  and  $t = 3\tau$ . Once again one

finds it to be confined to the location of least static stability, but of larger extent than the patterns at  $l = 0$ . This is consistent with the expectation, from the 1D picture, of a structure with comparatively weaker dependence on  $x$  than on  $y$ . Clearly visible is also the critical-layer behavior near the zero lines of  $V_0$ .

Observations for  $\tau = 1h$  are quite analogous (not shown). Also these patterns are closely confined to the region of least static stability. The structure at  $l = 0$  is advected by  $U_0$  towards smaller  $x$ , thereby following the least stable location. As was to be expected from the previously said it is also found to radiate small-scale GWs into the exterior range not affected by the IGW where they can propagate freely. Also as expected, the more strongly growing structure at  $\lambda_y = 5.5km$  cannot radiate but exhibits similar critical-layer behavior near the zero-lines of  $V_0$  as visible in Fig. 4.29.

## 4.5 Summary

This chapter works itself upwards through a hierarchy of three models with increasing complexity, each of them providing instructive pieces of information to the whole picture of modal and nonmodal growth in IGW packets. The most important result is that for statically and dynamically stable IGWs near the instability limit, where no NMs can grow, SVs can exhibit a temporary energy growth by nearly two orders of magnitude.

Beyond that, however, it is also pleasing to recognize that many features, especially of SVs for optimization times considerably shorter than the IGW period, can already be understood on the basis of a stratified constant-shear-layer approximation where only the initial local stratification  $N_{tot}^2$  and transverse-wind gradient  $\beta = \partial V_0 / \partial z$  near the statically least stable location of the IGW packet enter. Based on previous related work by Farrell and Ioannou (1993b,a) and Bakas et al. (2001) it is found that the two cases of perturbations most accessible to closed analytical treatment, i.e. propagating in the horizontal parallel (i.e. at azimuth angle  $\alpha = 0^\circ$ ) or transverse ( $\alpha = 90^\circ$ ) with respect to the IGW, can be understood in terms of a roll or Orr mechanism, respectively, both controlled by the shear, however significantly amplified by the locally reduced static stability. The latter serves as a catalyst for buoyant energy exchange between IGW and vertical

wind in the perturbation, thus further enforcing the shear-related exchange processes. In addition, both parallel and transverse optimal growth can be explained explicitly via a simple interference effect between contributing NMs.

Going more into the details, the scale-difference between the two types of optimal perturbations is reproduced correctly by the shear-layer theory, i.e. at a given vertical wavenumber the growth of parallel optimal perturbations maximizes at shorter wavelengths than that of transverse perturbations. Also the relative amplitudes of the respective growth factors can be understood based on the simple theory. One finds that the energy amplification of parallel perturbations in the statically stable case ( $a < 1$ ) has an upper limit  $(4/|\text{Ri}|)(N^2/N_{tot}^2)$ , with  $\text{Ri} = N_{tot}^2/\beta^2$ , while that of transverse perturbations increases algebraically with optimization time, as long as viscosity and diffusion are of weaker importance.

The short-term SV energetics in an approximation of the IGW by its time dependent vertical profile at the horizontal location with initially least static stability basically is in agreement with the findings from the stratified shear-layer theory. It further highlights a basic distinction between NMs and SVs that the former are structurally fixed while the latter can adjust their fields instantaneously so that over a finite time a more efficient energy exchange with the IGW is possible than in the NM case, thus giving a further explanation of the more rapid transient growth of SVs than admitted for NMs.

The 1D approximation of the IGW fields also shows a close initial confinement of the optimal perturbation to the altitude of least static stability. The leading parallel SV, having an intrinsic short time scale set by the advection of its small-scale fields by the parallel horizontal wind in the IGW, stays there as it is prevented from outwards radiation by a linear wave duct. Similar observations hold for oblique SVs which, however, have at fixed optimization time progressively larger intrinsic time scales as the azimuth angle increases.

The leading transverse SV therefore is not affected by the wave duct. In contrast to the shear-layer picture it is driven by a mixed statically enhanced Orr and roll mechanism. Its early development, when the statically enhanced Orr mechanism is at work (via the gradient of the transverse horizontal wind component  $V_0$ , as also in the stratified shear

layer), is characterized by radiation away from the statically least stable location. At the time when the SV has moved into regions of strong gradients in the parallel horizontal wind component  $U_0$ , a corresponding roll mechanism takes over, and further enhances the growth of the structure. Finally, its further vertical propagation is blocked by a critical-layer interaction at the zero line of the transverse wind in the IGW.

As predicted from the shear-layer theory, for larger optimization times oblique and transverse SVs prevail. Simply the time scale of the long-term transient growth behavior of all SVs, ending in algebraic or viscous-diffusive decay when no growing NM exists, but exhibiting asymptotic convergence towards the leading unstable NM if there is any, is to the most part set by  $\tau$ . Also the spatial scale of long-term SVs turns out to be proportional to  $\tau$ . Subject to these modifications, for a wide range of optimization times considerable optimal growth is allowed, even without any unstable NMs. For optimization times approaching the IGW period transient growth by an amplitude factor as large as 50 is still observed. The oblique SVs found there might be related to the diagonal shear modes diagnosed by Lelong and Dunkerton (1998a) in their simulations of the breakdown of a statically stable IGW.

An interesting result is the observation that SVs for longer optimization times tend to radiate GWs into the exterior field where the IGW has no direct impact any more. This offers an alternative mechanism for a mesospheric GW source to the excitation of gravity waves by ageostrophic body forcing resulting from GW breakdown (Vadas and Fritts, 2001; Zhou et al., 2002) or by normal-mode instabilities of statically unstable IGWs (Kwasniok and Schmitz, 2003). Specific features of the radiation mechanism identified here are that it does not require the basic IGW to be unstable in the normal-mode sense and that the vertical wavelength and the frequency of the radiated waves get larger the more parallel the direction of propagation of the radiated waves is with respect to the IGW.

Similar behavior is also found in the most general treatment of the problem where also the horizontal spatial dependence of the IGW is taken into account. The SVs from the 1D approximation are basically reproduced, then however with a horizontal modulation of their amplitude so that they tend to be confined to the statically least stable horizontal

location. From this one can expect a certain patchiness in the turbulence onset in an IGW packet propagating upwards through the mesosphere, as would be consistent with turbulence measurements from rocket soundings (Müllemann et al., 2003, e.g.).

The parameter dependence of the results seems worth some discussion. Since the value of the Brunt-Vaisala frequency used here is actually a bit low for the middle atmosphere, although it has e.g. also been employed by Fritts et al. (2003, 2006), also calculations with  $N = 2 \cdot 10^{-2} \text{s}^{-1}$  at  $70^\circ$  latitude have been done. The results there have been very similar to the ones reported here, with the major difference that the overall instability time scale was shorter by a corresponding factor 2. As noted in chapter 2, after a non-dimensionalization of the Boussinesq equations, with the Brunt-Vaisala period as time scale, the main controlling parameter at zero viscosity and diffusion is the ratio  $f/N$ . Thus, at fixed  $f/N$  and spatial IGW scales, varying  $N$  simply implies a proportional variation of the inverse time scale of the problem, thus explaining the above mentioned factor 2. The remaining influence of the different ratio  $f/N$  found in the second set of calculations is due to a corresponding variation of the ratio  $R = f/|\Omega|$  between the inertial frequency and that of the IGW. As a result of that the identified growth factors (within 5min now) are slightly weaker, while the results described here would strictly rather apply to a basic wave with longer horizontal wavelength, i.e. approximately 650km.

# Chapter 5

## General monochromatic gravity waves

The previous chapter has shown that a generalization of the stability problem for IGW packets towards the inclusion of optimal growth leads to a larger scope of possible instability scenarios. The identified mechanisms, however, do not seem to hinge on the wave packet envelope given the examined IGWs. One might assume that similar findings can also be made for monochromatic IGWs. In addition, the question arises what the generalized stability theory implies for HGWs. These questions shall be answered in the present chapter where monochromatic GWs of arbitrary inclination angles are analyzed. Its content has also been published by Achatz (2005).

### 5.1 The linear model

For the stability analysis the Boussinesq equations are linearized about the GW fields (2.10)–(2.13), henceforth denoted by  $(\mathbf{V}, B)$ . Due to the symmetry of the problem in  $\xi$  and  $y$  different perturbation wavenumbers in the corresponding plane are not coupled by the linear equations. It therefore makes sense to use for the perturbations the ansatz (Mied, 1976; Drazin, 1977; Klostermeyer, 1982)  $(\mathbf{v}', b') = \Re \{ (\mathbf{v}, b) (\phi, t) \exp [i (\kappa \xi + \lambda y)] \}$  so that the componentwise equations in the rotated and translated coordinate system

become with  $\mathbf{v} = (u_\xi, v, u_\phi)$

$$i\kappa u_\xi + i\lambda v + K \frac{\partial u_\phi}{\partial \phi} = 0 \quad (5.1)$$

$$\frac{Du_\xi}{Dt} + K u_\phi \frac{dU_\xi}{d\phi} + i\kappa p + b \cos \Theta - \sin \Theta f v = \nu \nabla^2 u_\xi \quad (5.2)$$

$$\frac{Dv}{Dt} + K u_\phi \frac{dV}{d\phi} + i\lambda p + f (\sin \Theta u_\xi + \cos \Theta u_\phi) = \nu \nabla^2 v \quad (5.3)$$

$$\frac{Du_\phi}{Dt} + K \frac{\partial p}{\partial \phi} - b \sin \Theta - \cos \Theta f v = \nu \nabla^2 u_\phi \quad (5.4)$$

$$\frac{Db}{Dt} + K u_\phi \frac{dB}{d\phi} + N^2 (\sin \Theta u_\phi - \cos \Theta u_\xi) = \mu \nabla^2 b \quad , \quad (5.5)$$

using the shortcuts  $D/Dt = \partial/\partial t - \Omega \partial/\partial \phi + i(\kappa U_\xi + \lambda V)$  and  $\nabla^2 = -(\kappa^2 + \lambda^2) + K^2 \partial^2/\partial \phi^2$ . Unless specified differently the Brunt-Vaisala frequency is  $N = 2 \cdot 10^{-2} \text{s}^{-1}$ , and the  $f$  plane is centered at  $70^\circ \text{N}$ .

Since the coefficients of the equations (5.1)–(5.5) are periodic in  $\phi$  with period  $2\pi$ , Floquet theory (Bender and Orszag, 1978; Lombard and Riley, 1996) tells us that it is possible to consider independently solutions of the form  $(\mathbf{v}, b) = \exp(i\eta\phi) (\tilde{\mathbf{v}}, \tilde{b})(\phi, t)$  with  $(\tilde{\mathbf{v}}, \tilde{b})(\phi + 2\pi, t) = (\tilde{\mathbf{v}}, \tilde{b})(\phi, t)$  and  $-1/2 \leq \eta \leq 1/2$ . In line with Lombard and Riley (1996) the present analysis is restricted to  $\eta = 0$ , so that it is assumed that  $(\mathbf{v}, b) = (\tilde{\mathbf{v}}, \tilde{b})$  with a periodicity of  $2\pi$  in  $\phi$ . At least for IGWs Yau et al. (2004) have shown that this generally captures the leading NM. Obvious respective generalizations are left to future studies.

For a numerical treatment (5.1)–(5.5) have, as above, been discretized on a standard staggered grid in  $\phi$  ( $u_\xi, v, p$ , and  $b$  on full levels, and  $u_\phi$  on intermediate half levels) with periodic boundary conditions. The model domain extends from 0 to  $2\pi$ . Pressure is obtained by applying the divergence on the momentum equations, using (5.1), and solving the resulting Poisson equation by a Fourier transform technique. The time integration is done by two initial fourth-order Runge-Kutta time steps, followed by third-order Adams-Bashforth time steps. The number of grid points used in the model discretization, usually 1024, was always chosen so as to well resolve all relevant scales.



$\Theta/^\circ$	$a$	A	R	$\text{Ri}_{min}$
89.5	0.71	0.45	0.62	0.88
70	0.85	0.45	$2.0 \cdot 10^{-2}$	1.2
50	0.69	0.45	$1.1 \cdot 10^{-2}$	3.1
30	0.45	0.45	$7.9 \cdot 10^{-3}$	19
89.5	0.87	0.55	0.62	0.28
70	1.0	0.55	$2.0 \cdot 10^{-2}$	0
50	0.84	0.55	$1.1 \cdot 10^{-2}$	1.9
30	0.55	0.55	$7.9 \cdot 10^{-3}$	12
89.5	1.2	0.76	0.62	-0.23
70	1.4	0.76	$2.0 \cdot 10^{-2}$	$-5.8 \cdot 10^2$
50	1.2	0.76	$1.1 \cdot 10^{-2}$	$-2.1 \cdot 10^3$
30	0.76	0.76	$7.9 \cdot 10^{-3}$	5.7

Table 5.1: For all examined GWs, their inclination angle  $\Theta$  with respect to the horizontal, their amplitude  $a$  with respect to the overturning threshold, the nondimensional amplitude  $A$  of the  $u_\xi$ -wind, the ratio  $R = f/|\Omega|$  between Coriolis parameter and wave frequency, and the smallest Richardson number in the whole phase range and among all directions of propagation of a perturbation,  $\text{Ri}_{min}$ .

## 5.2 Growth factors

In the following a comparison is given between the NMs and SVs for typical GW scales. The wavelength of the GW has been chosen to be  $\Lambda = 2\pi/K = 6\text{km}$ , implying a Reynolds number  $\text{Re} = 1.1 \cdot 10^5$ . In comparing the results for different inclination angles a choice had to be made about how to treat the wave amplitude  $a$  with respect to static instability. One option would be keeping  $a$  fixed. This, however, leads to infinite energy, and correspondingly infinite gradients, at  $\Theta = 0^\circ$  and  $\Theta = 90^\circ$ . This study therefore follows Yau et al. (2004) and keeps in comparisons between different inclination angles the amplitude

in  $U_\xi$  (or equivalently the energy) fixed so that, using (2.14),

$$a(\Theta) = \frac{2A \sin \Theta}{\sqrt{1 + (f/N)^2 \tan^2 \Theta}} \quad . \quad (5.6)$$

For an overview of the effects of the wave amplitude and the inclination angle on the intensity of the respective NM and SV instabilities the study focusses on the representative inclination angles  $\Theta = 89.5^\circ$ ,  $70^\circ$ ,  $50^\circ$ , and  $30^\circ$ . This way an IGW is included ( $\Theta = 89.5^\circ$ ) with not too extreme a value for  $R$  (0.62), as well as three HGWs with periods  $2\pi/\Omega = 920\text{s}$ ,  $490\text{s}$ , and  $360\text{s}$ . The examined amplitudes  $A = 0.45$ ,  $0.55$ , and  $0.76$  have been chosen so that the IGW is either well below ( $a = 0.71$ ), slightly below ( $a = 0.87$ ), or above ( $a = 1.2$ ) the overturning threshold. For the reader's convenience the most important parameters of all examined waves are also listed in table 5.1.

As described before, again a separate set of NMs or SVs belongs to each horizontal perturbation wave vector, which will in the following be defined by its wavelength  $\lambda_\parallel$  (or wavenumber  $k_\parallel = 2\pi/\lambda_\parallel$ ) and the azimuth angle  $\alpha$  between wave vector and  $\xi$ -axis, so that

$$(\kappa, \lambda) = k_\parallel (\cos \alpha, \sin \alpha) \quad . \quad (5.7)$$

In a complete analysis it is not necessary to survey the whole  $\kappa - \lambda$  plane. Due to the invariance of the equations (5.1)–(5.5) under the simultaneous transformations  $(\kappa, \lambda) \rightarrow -(\kappa, \lambda)$  and complex conjugation  $(\mathbf{v}, b) \rightarrow (\bar{\mathbf{v}}, \bar{b})$  it is sufficient to consider the subrange  $0 \leq \alpha \leq 180^\circ$ . In addition, in the absence of rotation, so that both  $f$  and  $V$  vanish, one would also have invariance under the transformations  $\lambda \rightarrow -\lambda$  and  $v \rightarrow -v$ . It turned out that, although this symmetry is broken by rotation, there is not much difference in the results between  $\alpha = 90^\circ \pm \beta$ . Therefore here only the subrange  $0 \leq \alpha \leq 90^\circ$  is discussed.

Since optimal growth should show the largest differences from NM behavior at short optimization times this study mainly focusses on  $\tau = 300\text{s}$ , which is approximately one Brunt-Vaisala period. Longer optimization times are discussed briefly in order to give a rough overview of the various possibilities. Note, however, that here NMs are well defined for all time scales since in the chosen reference system the basic GW is time independent.

### 5.2.1 Short optimization times

Looking first at the shorter optimization time  $\tau = 300\text{s}$ , the reader will find many results for the IGW highly reminiscent of the findings from chapter 4. Figure 5.1 shows for  $A = 0.45$  the growth factors  $\sigma_1 = e^{\gamma_1 \tau}$  of the leading NMs of the four GWs, as a function of the wavelength (or wavenumber) and the azimuth angle of the horizontal wavenumber vector of the mode. A glance at table 5.1 shows that in none of the four cases an instability would have to be expected from an (inappropriate) application of the theory of Howard (1961) and Miles (1961). Indeed the IGW case, best approaching the conditions examined by these authors, has no growing NM. It might be that in the inviscid-nondiffusive limit weak instabilities like the ones published by Yau et al. (2004) exist, but as in the IGW-packet case (chapter 4) these seem to be damped by viscosity and diffusion. The other three cases are in agreement with previous findings on waves with slantwise phase propagation (Lombard and Riley, 1996, e.g.). All three examined GWs are unstable. While parallel perturbations (i.e. with  $\alpha = 0^\circ$ ) grow most rapidly, there also is a second important azimuth-angle range  $50^\circ \leq \alpha \leq 70^\circ$ . Moreover, the instability increases with decreasing inclination angle  $\Theta$ .

A quite different picture is presented by the most rapidly growing SVs. Their growth factors  $\sigma_1$  are shown in Fig. 5.2. Although it has no unstable NM at all, even the IGW admits optimal growth by nearly a factor 4. In agreement with the results in chapter 4 the most rapidly amplifying SVs propagate parallel to the IGW, but at a somewhat larger wavelength transverse perturbations ( $\alpha = 90^\circ$ ) also amplify. From the NM analysis it does not come as a surprise that the three HGWs exhibit stronger instabilities. The ratio between optimal growth and growth of the leading NM increases with increasing inclination angle, ranging between 2 for  $\Theta = 30^\circ$  and 4 for  $\Theta = 70^\circ$ . The most active wavelengths and azimuth angles are quite different from those for the NMs. In all HGW cases transverse instabilities are favored over parallel ones. At intermediate inclination angles they are the most vigorous ones in the whole azimuth-angle range, but for  $\Theta = 30^\circ$  a propagation at  $\alpha = 70^\circ$  with respect to the  $\xi$ -axis is favored. Another difference is that here it is not the smallest inclination angle which leads to the strongest instability. The strongest transient instabilities are found for  $\Theta = 50^\circ$ . Finally, the leading SVs tend to

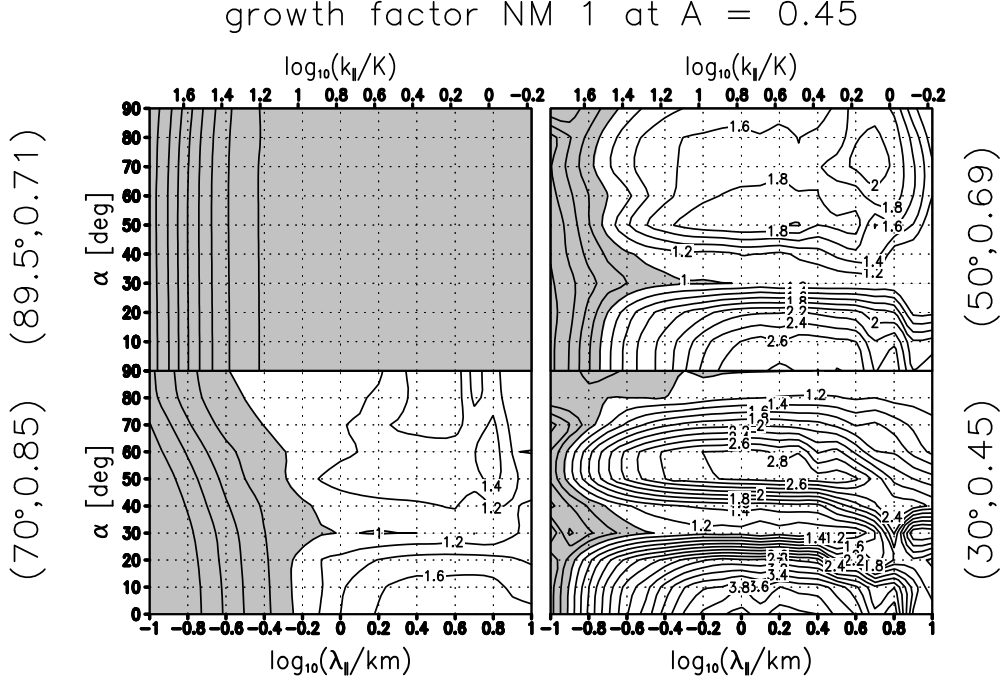


Figure 5.1: The growth factors  $\sigma_1 = \exp(\gamma_1 \tau)$  (integration time  $\tau = 300s$ ) of the leading NMs of four GWs with different inclination angles but identical energy or  $u_\xi$ -amplitude (in nondimensional units  $A = 0.45$ ), as a function of the wavelength  $\lambda_\parallel$  (or the corresponding wavenumber normalized by that of the basic wave, see the top axis) and the azimuth angle  $\alpha$  of the horizontal wave vector of the mode with respect to the  $\xi$ -axis. Inclination angle and wave amplitude with respect to the static overturning threshold of the four waves are  $(\Theta, a) = (89.5^\circ, 0.71)$  (top-left panel),  $(70^\circ, 0.85)$  (bottom-left),  $(50^\circ, 0.69)$  (top-right), and  $(30^\circ, 0.45)$  (bottom-right). The contour interval is 0.2, values less than 1, i.e. the regions without NM growth, are indicated by shading. In the graph for  $\Theta = 89.5^\circ$  the contour range is between 0.2 (leftmost contour) and 0.9 (rightmost) in steps of 0.1.

be at smaller wavelengths (between a few 100m and 1km) than the most unstable NMs which have scales more of the order of the wavelength of the basic wave.

Increasing the wave energy so that  $A = 0.55$ , i.e.  $a = 0.87$  at  $\Theta = 89.5^\circ$ , leads to the NM and SV growth factors shown in Figs. 5.3 and 5.4. The main effect is to intensify the instabilities while leaving the favored scales and azimuth angles the same. Still the IGW case shows no growing NM. Its optimal perturbations, however, amplify by nearly an order of magnitude. The growth-factor ratio between leading SV and NM for the

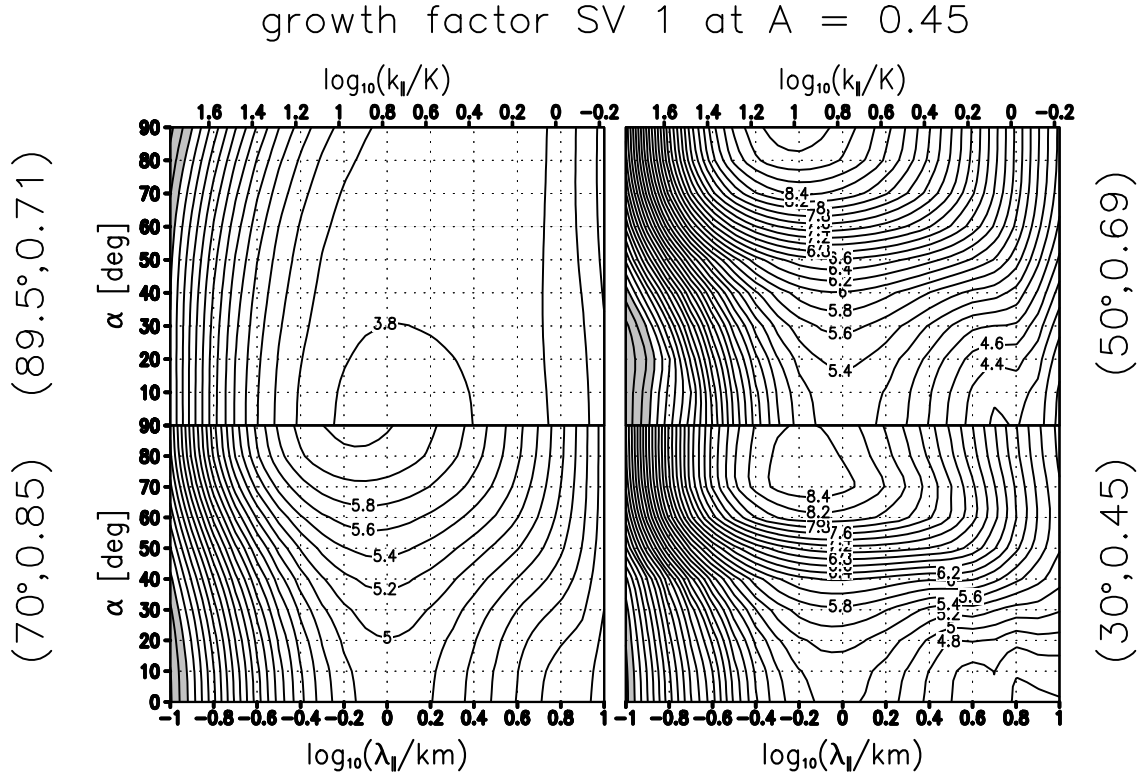


Figure 5.2: As Fig. 5.1, but now the growth factors  $\sigma_1$  of the leading SVs (optimization time  $\tau = 300$ s). The contour interval is 0.2 everywhere.

HGWs ranges between 2 at  $\Theta = 30^\circ$  and 6 at  $\Theta = 70^\circ$ .

An essential modification is caused by a further increase of the wave energy to a value  $A = 0.76$ , corresponding for the IGW to  $a = 1.2$ . The growth factors for these cases can be seen in Figs. 5.5 and 5.6. Due to a considerable static and dynamic instability the IGW now has unstable NMs (see also Yau et al., 2004). The distribution of the instabilities over the  $\alpha - \lambda_{\parallel}$  plane is very similar to the one of optimal growth for the two IGWs with smaller amplitudes, favoring parallel propagation over a secondary maximum at transverse propagation. The SV growth factors for this IGW are, however, still larger than those for the NMs by a factor 5. In addition, the wavelengths of the leading SVs are smaller than those of the most rapidly growing NMs. With regard to the HGWs, the NM growth maximum for  $\Theta = 70^\circ$  now has shifted to transverse propagation, but at a wavelength which is about an order of magnitude larger than the one of the leading, also transverse, SV. In a comparison between the different inclination angles the NM instability still is

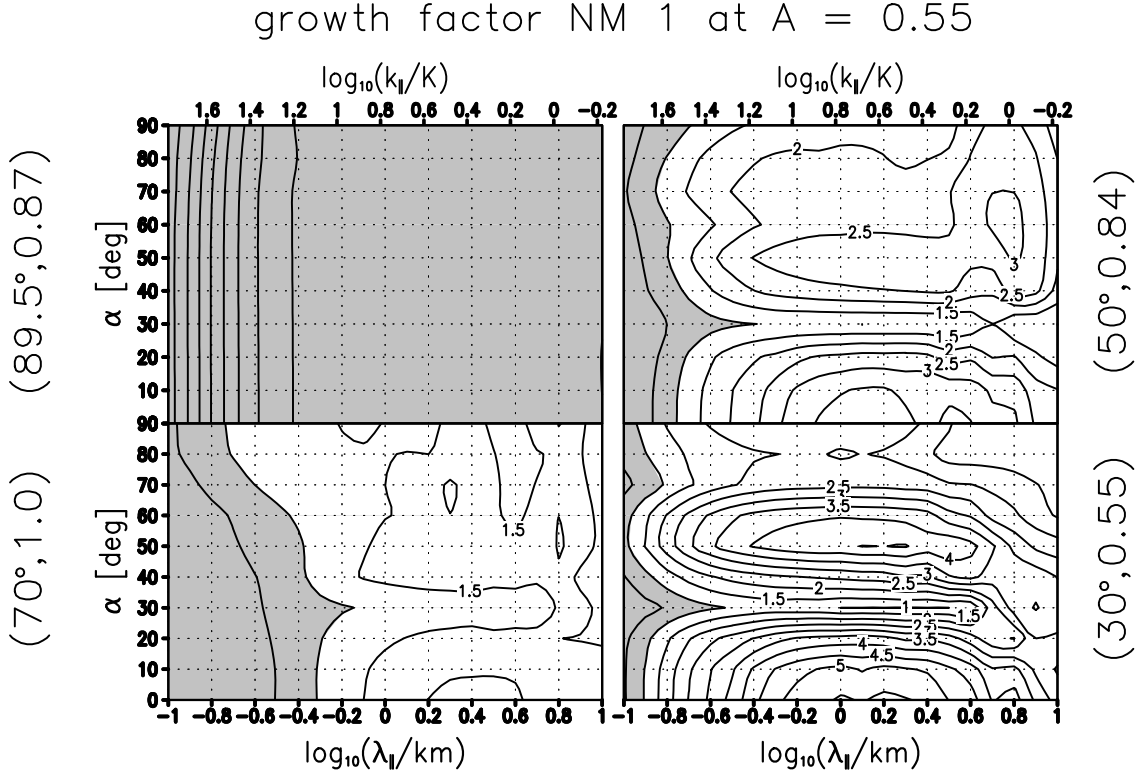


Figure 5.3: As Fig. 5.1, but now with an increased wave energy so that  $A = 0.55$ . For the IGW ( $\Theta = 89.5^\circ$ ) the leftmost contour is at 0.2, the rightmost contour at 0.9, and the contour interval 0.1. For the other cases the contour interval is 0.5

most intense at the smallest inclination angle  $\Theta = 30^\circ$ , although this is the only case not satisfying the instability criteria of Howard (1961) and Miles (1961) (see table 5.1). In contrast to the other two weaker wave amplitudes now, however, oblique propagation at  $\alpha = 50^\circ$  is favored there over parallel propagation. At all inclination angles the optimal perturbations are found to amplify by more than an order of magnitude, with the most intense instability encountered at  $\Theta = 70^\circ$ . The growth-factor ratio between SVs and NMs ranges between 2.5 at  $\Theta = 30^\circ$  and 10 at  $\Theta = 70^\circ$ .

### 5.2.2 Longer optimization times

For longer optimization times one must distinguish between the two main cases where either growing NMs exist or not. In the latter case, one typically searches for the so-called global optimal, i.e. one attempts to find a value for  $\tau$  where optimal growth

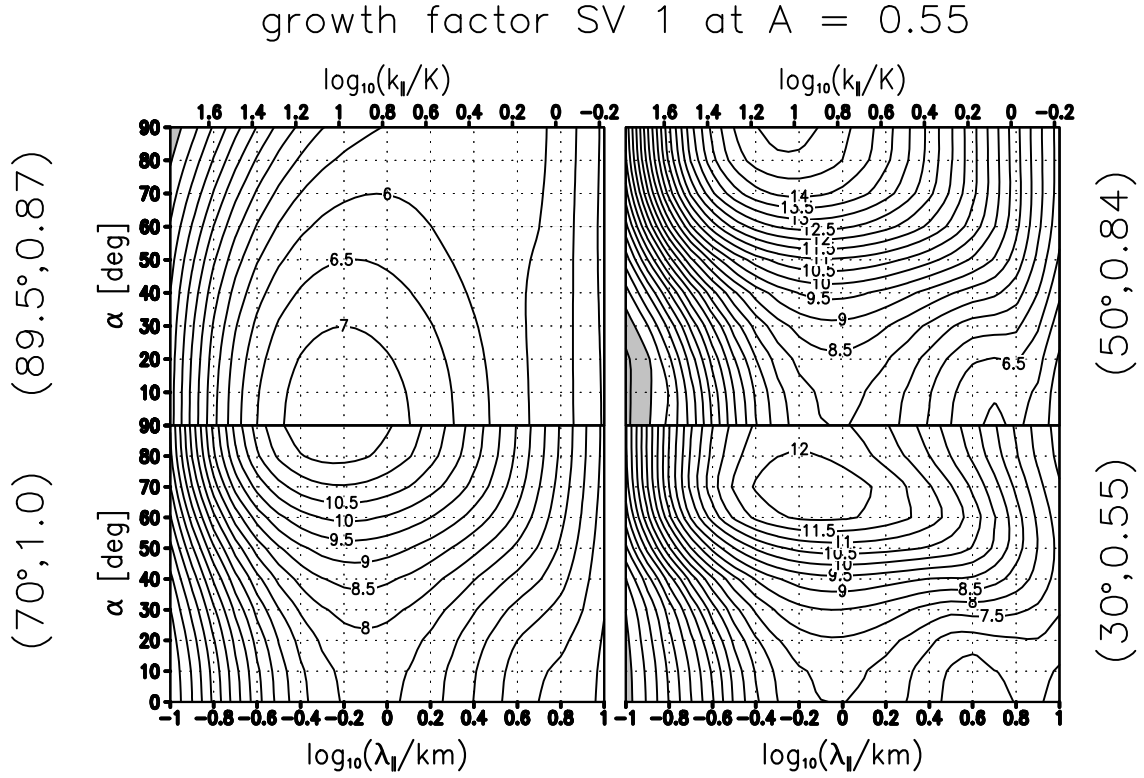


Figure 5.4: As Fig. 5.3, but now for the leading SVs.

maximizes. Such an analysis suggests itself for the subcritical ( $a < 1$ ,  $\text{Ri} > 1/4$ ) IGW examined here. In the former case nearly all initial perturbations eventually converge towards the set of leading NMs so that within the linear approximation perturbation growth usually is not limited. This is the case for all HGWs examined here. Instead of searching for a global optimal it seems for these to be more meaningful to consider the longest time scale of dynamical relevance within the model framework. In the present context this could be the time needed by the basic wave to cover one atmospheric scale height, after which its amplitude would have changed by a factor  $e^{1/2}$ , an effect not described within the Boussinesq approximation. Another interesting time scale is the HGW period  $P = 2\pi/|\Omega|$ . Since it is here also not too far from the time needed by the wave to cover one atmospheric scale height, it has instead been chosen as examined long optimization time.

The SV growth factors for the slightly subcritical IGW ( $a = 0.87$ ) are shown in Fig. 5.7 for  $\tau = 15\text{min}$ ,  $30\text{min}$ ,  $1\text{h}$ , and  $2\text{h}$ . Three aspects are interesting. First, at longer

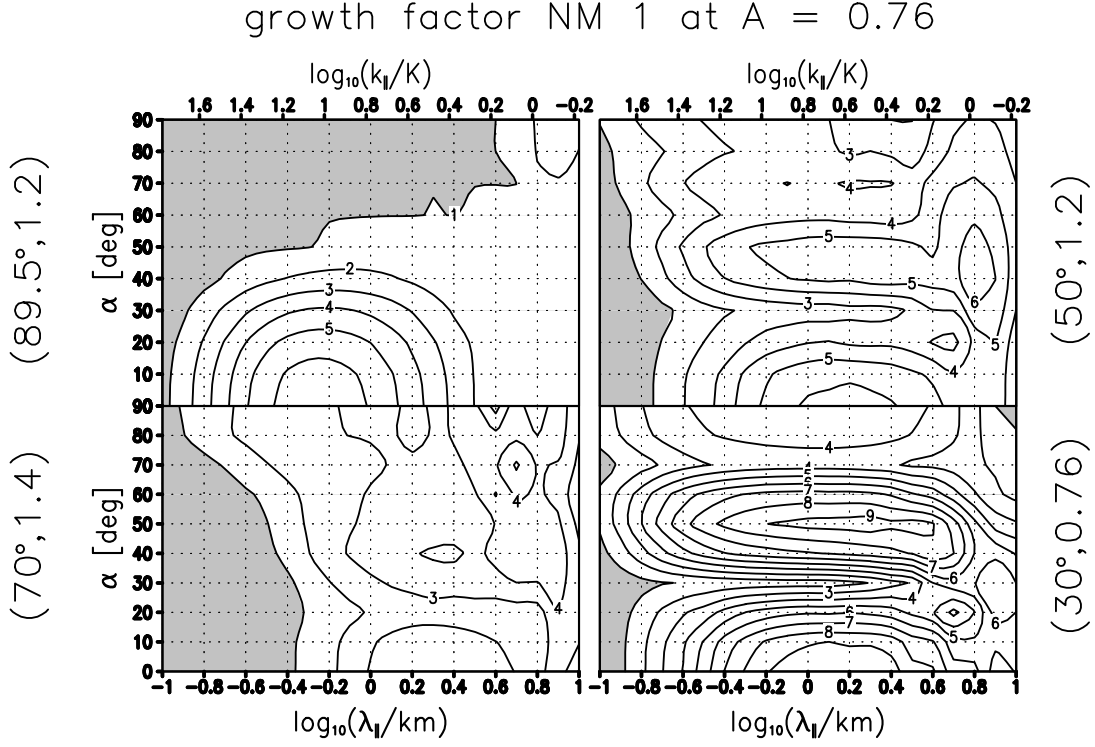


Figure 5.5: As Fig. 5.1, but now with an increased wave energy so that  $A = 0.76$ . The contour interval is 1.0 everywhere

optimization times transverse SVs are favored. Secondly, optimal growth is strongest around  $\tau = 30\text{min}$ , with a value near 20. Thirdly, the dominant scales generally increase with  $\tau$ . For the IGW packet case the increase in the growth factors for longer  $\tau$  (here between 5min and 30min), as well as the increase in horizontal wavelength and the tendency of transverse perturbations to grow most rapidly at larger  $\tau$ , is analyzed in detail in chapter 4. Under the assumption that only the local conditions near the statically least stable location  $\phi = 3\pi/2$  enter, it is found that the roll mechanism responsible for optimal growth at  $\alpha = 0$  allows a maximal growth, approached for large  $\tau$ , of  $\sigma_1^2 = 4/\text{Ri}_l N^2/N_{tot}^2$ , where  $\text{Ri}_l = N_{tot}^2/\beta^2$  is the local Richardson number, determined by the local vertical gradient of the transverse velocity in the IGW  $\beta = af \tan \Theta$  and the local total squared Brunt-Vaisala frequency  $N_{tot}^2 = (1 - a)N^2$ . At fixed vertical scale the horizontal scale is  $\lambda_{||} \propto \tau$ . Transverse perturbations, on the other hand, are amplified by a mixed roll and Orr mechanism which allows optimal growth to increase without bounds over a wider span of  $\tau$  (before viscous-diffusive effects become important). For these one has the rough



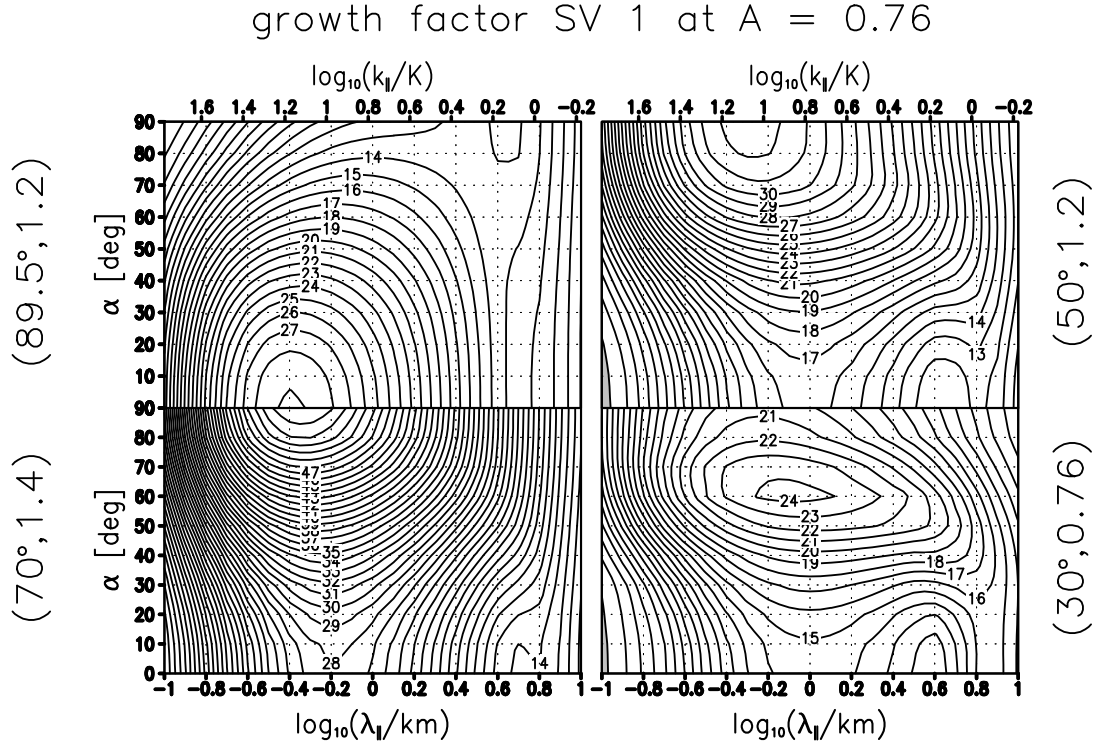


Figure 5.6: As Fig. 5.5, but now for the leading SVs. The contour interval is 1 everywhere.

identity  $\tau = m_0/(\beta k_{||})$ , where  $m_0$  is an initial typical vertical scale of the perturbation. Indeed it is found that e.g. the structure of the leading transverse optimal perturbation for  $\tau = 15\text{min}$  is that of a wave packet near the statically least stable location with vertical scale about twice that of the corresponding structure for  $\tau = 30\text{min}$  (not shown), which fits well since the horizontal scale of both optimal perturbations is about the same. The present calculations thus seem to reproduce the behavior described in chapter 4. There also a local optimum in SV growth near the same nondimensional  $\tau N$  has been found as here, however with the modification that at very long  $\tau$  of the order of the IGW period optimal growth seems to rise again to even larger values (in an approximation of the IGW packet by its vertical profile at the initially statically least stable horizontal location). Corresponding calculations (not shown) indicate no such effect for the monochromatic IGW. The reason for this discrepancy could be either in the slightly different wave parameters, the packet envelope, or the 1D approximation used in chapter 4 for the longest  $\tau$ .

Figure 5.8 shows for the two HGWs at  $\Theta = 70^\circ$  and  $50^\circ$  and  $A = 0.55$  the SV growth

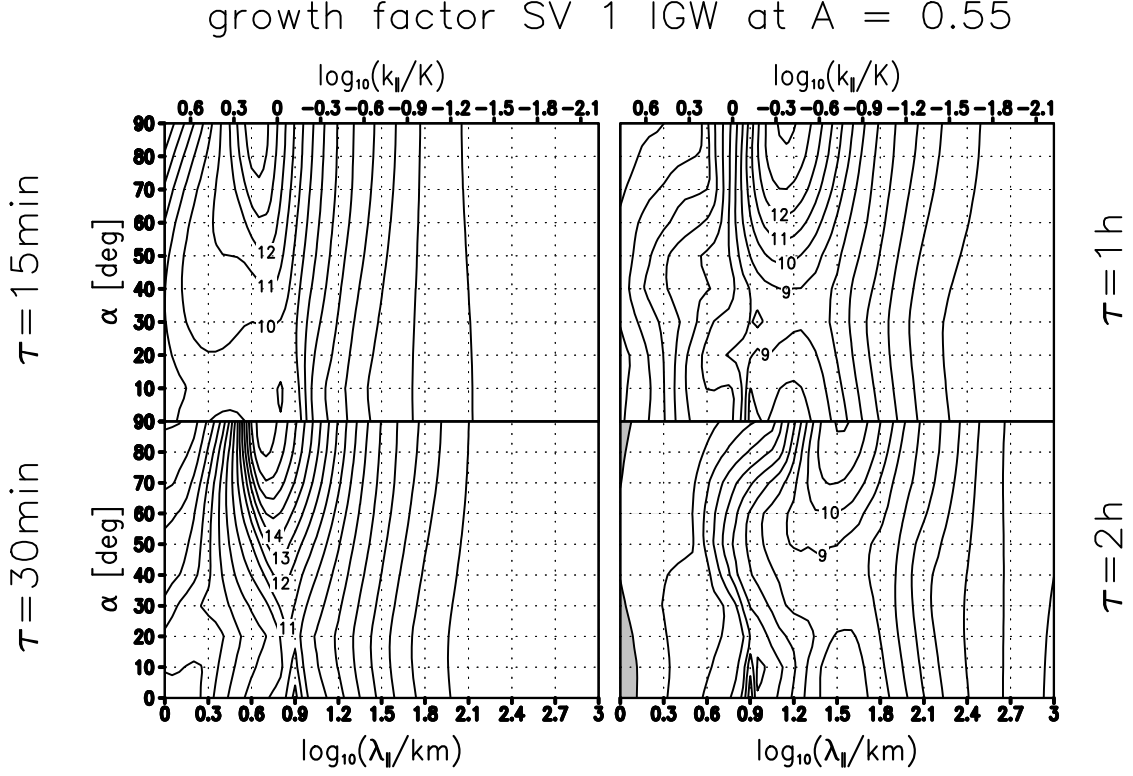


Figure 5.7: As function of the parallel wavelength  $\lambda_{||}$  (or wavenumber  $k_{||}$ , top axis) and the azimuth angle  $\alpha$ , the growth factors of the leading SVs of the slightly subcritical IGW ( $\Theta = 89.5^\circ$  and  $(a, A) = (0.87, 0.55)$ ), for the optimization times  $\tau = 15\text{min}$ ,  $30\text{min}$ ,  $1\text{h}$ , and  $2\text{h}$ . The contour interval is 1, and values less than 1, i.e. the regions without SV growth, are indicated by shading.

factors, along with those of the NMs, for  $\tau = P$ . As expected, one observes a greater similarity between NM and SV growth than at  $\tau = 300\text{s}$ , especially with regard to the  $\lambda_{||} - \alpha$  distribution. SV growth maximizes near the locations of largest NM growth. Thus the SVs also have much larger horizontal scales than the SVs at shorter optimization times. Still, however one finds about the same ratio between the growth factors as for smaller  $\tau$

### 5.3 Energetics and time development

For an analysis of the growth and decay behavior of the respective identified perturbations it is again helpful to resort to energy considerations. For this purpose it is noted, in close



$$D_b = -\frac{\mu}{N^2} \left[ (\kappa^2 + \lambda^2) |b|^2 + K^2 \left| \frac{\partial b}{\partial \phi} \right|^2 \right] . \quad (5.13)$$

Integrating (5.8) over a wave period in  $\phi$  removes, due to the periodic boundary conditions, the phase derivative on the left-hand side so that growth and decay can be attributed to contributions from integrals over the right-hand side terms over the wave phase  $\phi$ . These describe the shear-related energy exchange with the basic wave due to counter-gradient fluxes of  $u_\xi$  and  $v$  ( $r_\xi$  and  $r_y$ ), convective exchange by counter-gradient buoyancy fluxes ( $r_b$ ), and viscous and diffusive losses ( $D_v$  and  $D_b$ ). This decomposition is again represented in terms of contributions to the instantaneous amplification rate  $\Gamma(t) = 1/(2\langle e_{\kappa\lambda} \rangle) d\langle e_{\kappa\lambda} \rangle/dt$ , which takes the time-independent value  $\Gamma = \gamma_\nu$  for a NM. Here angle brackets denote an average over a wave phase. Using the instantaneous amplification rate and its decomposition

$$\begin{aligned} \Gamma &= \Gamma_\xi + \Gamma_y + \Gamma_b + \Gamma_d \\ &= \langle \gamma_\xi \rangle + \langle \gamma_y \rangle + \langle \gamma_b \rangle + \langle \gamma_d \rangle \quad , \end{aligned} \quad (5.14)$$

where  $\gamma_\xi = r_\xi/\langle 2e_{\kappa\lambda} \rangle$ , likewise for the  $\gamma_\perp$  and  $\gamma_b$ , and  $\gamma_d = (D_v + D_b)/\langle 2e_{\kappa\lambda} \rangle$ , the following gives an analysis of the processes responsible for the growth and decay of the leading NMs or SVs.

With respect to NMs a caveat shall be mentioned concerning a possible misinterpretation of the amplification-rate decomposition. It can happen that one of the amplification-rate contributions introduced above is large and still the corresponding gradient in the basic-wave field does not cause the NM growth behavior. To show this the further coordinate transformation is applied in which the axes in the  $\xi - y$  plane are rotated so that the axes for the new coordinates, denoted by  $x_\parallel$  and  $y_\perp$ , point in the direction of the horizontal wavenumber vector of the perturbation and orthogonal to it, i.e.  $x_\parallel = \xi \cos \alpha + y \sin \alpha$  and  $y_\perp = -\xi \sin \alpha + y \cos \alpha$ . The corresponding velocity components of  $\mathbf{v}$  and  $\mathbf{V}$  are  $(u_\parallel, v_\perp)$  and  $(U_\parallel, V_\perp)$ . One obtains from (5.1)–(5.5)

$$ik_\parallel u_\parallel + K \frac{\partial u_\phi}{\partial \phi} = 0 \quad (5.15)$$

$$\frac{Du_\parallel}{Dt} + Ku_\phi \frac{dU_\parallel}{d\phi} + ik_\parallel p + b \cos \alpha \cos \Theta + f (\sin \alpha \cos \Theta u_\phi - \sin \Theta v_\perp) = \nu \nabla^2 u_\parallel \quad (5.16)$$

$$\frac{Dv_{\perp}}{Dt} + Ku_{\phi} \frac{dV_{\perp}}{d\phi} - b \sin \alpha \cos \Theta + f \left( \sin \Theta u_{\parallel} + \cos \alpha \cos \Theta u_{\phi} \right) = \nu \nabla^2 v_{\perp} \quad (5.17)$$

$$\frac{Du_{\phi}}{Dt} + K \frac{\partial p}{\partial \phi} - b \sin \Theta - f \cos \Theta \left( \sin \alpha u_{\parallel} + \cos \alpha v_{\perp} \right) = \nu \nabla^2 u_{\phi} \quad (5.18)$$

$$\frac{Db}{Dt} + Ku_{\phi} \frac{dB}{d\phi} + N^2 \left[ \sin \Theta u_{\phi} - \cos \Theta \left( \cos \alpha u_{\parallel} - \sin \alpha v_{\perp} \right) \right] = \mu \nabla^2 b \quad (5.19)$$

where here  $D/Dt = \partial/\partial t - \Omega \partial/\partial \phi + ik_{\parallel} U_{\parallel}$ . Note the close relationship of these equations to (4.7) – (4.11). It thus turns out that  $v_{\perp}$  is coupled to the other variables only passively provided that the Coriolis terms are negligible for the perturbation dynamics, which seems always to be the case here, and  $\cos \Theta \sin \alpha \approx 0$ . The latter implies either the IGW case or parallel horizontal propagation of the perturbation with respect to the GW. Then  $u_{\parallel}$ ,  $u_{\phi}$  and  $b$  can be considered independently from  $v_{\perp}$ , and taking all these to be proportional to  $\exp(-i\omega_{\nu}t + \gamma_{\nu}t)$  the eigenfrequencies and growth rates of all NMs can be determined from the equations (5.15), (5.16), (5.18), and (5.19) alone. Thus, in the IGW case they do not depend on  $V_{\perp}$ . A contribution of the corresponding shear term to the amplification rate indicates something different: Since in a NM up to the oscillating phase factor all fields grow or decay in strict proportion one also has for IGWs ( $\cos \Theta \approx 0$ ), with the obvious transformations  $(r_{\xi,y}, \Gamma_{\xi,y}) \rightarrow (r_{\parallel,\perp}, \Gamma_{\parallel,\perp})$ , and neglecting for the moment the generally weak impact from viscosity and diffusion, the identity  $\langle r_{\parallel} + r_w + r_b \rangle / \langle |u_{\parallel}|^2 + |w|^2 + |b|^2 / N^2 \rangle \approx r_{\perp} / \langle |v_{\perp}|^2 \rangle$  so that

$$\frac{\Gamma_{\perp}}{\Gamma_{\parallel} + \Gamma_w + \Gamma_b} \approx \frac{\langle |v_{\perp}|^2 \rangle}{\langle |u_{\parallel}|^2 + |w|^2 + |b|^2 / N^2 \rangle} \quad (5.20)$$

Thus a large contribution from  $\Gamma_{\perp}$  tells us that the NM contains a correspondingly large part of its energy in the flow field  $v_{\perp}$  which indeed is extracted from the wave via a momentum flux against the shear in  $V_{\perp}$ , but at a rate independent from this gradient.

In the case of SVs the interpretation of the amplification-rate decomposition must be somewhat different. In some way it turns out to be less subtle. There the dynamical fields do not grow in strict proportion. A single growth rate, characterizing the identical rate at which energy is transferred from the basic wave into the various perturbative fields, does not exist. On the contrary the energetics of the perturbation is determined by the sum of all the contributions listed above which can be highly time-dependent not only

in their magnitude but also in their relative importance. This time dependence must be traced in order to comprehend the full dynamics. Still, in the IGW case one finds that  $v_\perp$  reacts only passively to changes in the other perturbative fields. In contrast to the NM case, however, a large  $\Gamma_\perp$  does not simply tell us that much energy is in  $v_\perp$ , which yet grows at a rate determined by all fields in the basic wave except  $V_\perp$ . It rather indicates that the growth or decay of the energy in the SV is to a large part to be attributed to a corresponding growth or decay in the energy in  $v_\perp$ , which indeed is induced by the gradient in  $V_\perp$  and a corresponding momentum flux  $\Re(\bar{v}_\perp u_\phi)$  in the perturbation. In fact, this is the essence of the roll mechanism described in chapter 4, and widely differing values in the amplification-rate contributions are often a sign of considerably disproportionate amplifications of the energy content in the various dynamical fields.

### 5.3.1 Inertia-gravity waves

In the investigation of the dynamics of the identified perturbations the beginning shall be made by a discussion of those found in the stability analysis of the IGW ( $\Theta = 89.5^\circ$ ). Basically most results from chapter 4 are retrieved.

#### Short optimization times

To begin with the case of  $\tau = 300\text{s}$ , Fig. 5.9 shows for the statically unstable case ( $a = 1.2$ ) the spatial dependence of energy density  $e_{\kappa\lambda}$  and the IGW-phase dependent amplification-rate decomposition (i.e. the RHS terms of (5.8), normalized by  $2\langle e_{\kappa\lambda} \rangle$ ) of the leading parallel ( $\alpha = 0^\circ$ ) and transverse ( $\alpha = 90^\circ$ ) NM. The structures are quite different. The parallel mode is highly confined to the region of strongest static instability due to the wave-related negative buoyancy gradient. The main contribution to its positive growth rate is apparently from  $\gamma_\perp$ , with another one from  $\gamma_b$ . However, since we are looking at the stability problem of an IGW the caveat from above applies, and thus its growth rate is only determined by the gradients of  $U_\parallel = U_\xi$  and  $B$ . Therefore the convective exchange seems to dominate the dynamics of this mode while much of its energy turns out to be in  $v_\perp = v$ . In comparison to this NM, the leading transverse mode is much broader, but it also obtains its energy to an important part via the convective exchange

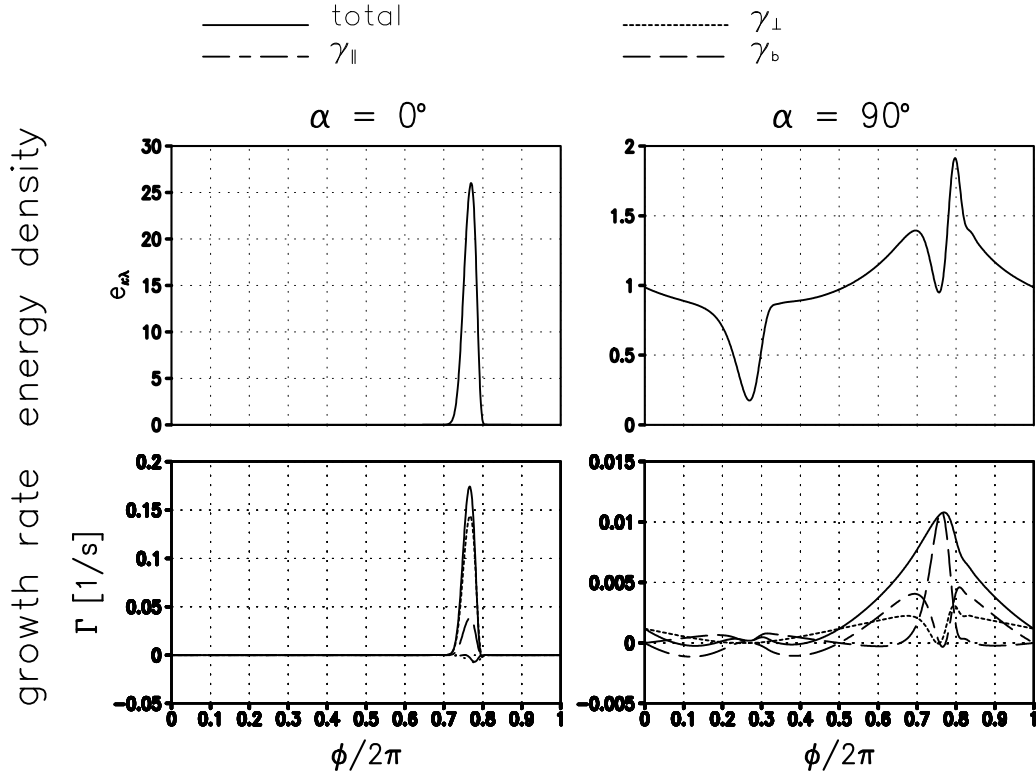


Figure 5.9: IGW-phase dependence of energy density (top row) and growth-rate decomposition (bottom) of the leading parallel and transverse NM for the statically unstable IGW ( $a = 1.2$ ,  $\Theta = 89.5^\circ$ ). The IGW-phase average of the sum of all growth-rate parts yields the total growth rate  $\Gamma = \gamma_1$ . The unimportant contribution from viscous and diffusive losses is indicated by a dotted line. The amplitude of the NM (in meaningless units) has been chosen to normalize the IGW-phase average of energy density ( $\langle e_{\kappa\lambda} \rangle = 1$ ).

term  $\gamma_b$  in the region of strongest static instability (near  $\phi = 3\pi/2$ ). As is seen in table 5.2, where the IGW-phase averaged amplification-rate decomposition is listed,  $\Gamma_u = \Gamma_\perp$  makes the largest contribution, but also here in reality  $\Gamma_v = \Gamma_\parallel$  and  $\Gamma_b$  are the essential terms in determining (to about equal contributions) the growth rate of the NM. The large contribution from  $\Gamma_u = \Gamma_\perp$  indicates that much of the energy of the mode is contained in  $u = -v_\perp$ .

In comparison to NMs, the IGW-phase dependence of energy density and amplification-rate decomposition in a SV is time dependent. Figure 5.10 shows for the optimal perturbation ( $t = 0$ ) and the resulting SV at the optimization time ( $t = 300s$ ) these fields for

$\Theta/^\circ$	$a$	$\alpha/^\circ$	$\Gamma_\xi/10^{-3}\text{s}^{-1}$	$\Gamma_y/10^{-3}\text{s}^{-1}$	$\Gamma_b/10^{-3}\text{s}^{-1}$	$\Gamma_d/10^{-3}\text{s}^{-1}$
89.5	0.87	0	-0.15	5.4	1.4	-0.31
89.5	0.87	90	1.1	0.76	0.83	-0.01
70	1.0	0	-1.1	0.01	3.1	-0.65
70	1.0	90	1.1	0.0	0.26	-0.17
50	0.84	0	0.7	0.0	3.9	-0.21
50	0.84	90	1.6	0.0	0.33	-0.30
30	0.55	0	1.2	0.0	4.6	-0.11
30	0.55	70	1.4	0.0	1.6	-0.23

Table 5.2: For  $A = 0.55$ , the growth-rate decomposition of the leading NMs for GW inclination angle  $\Theta$ , amplitude  $a$ , and mode azimuth angle  $\alpha$  at the perturbation wavelength of strongest NM growth for the IGW ( $\Theta = 89.5^\circ$ ), and strongest SV growth else.

the leading parallel perturbation ( $\alpha = 0$ ). At first sight it looks similar to the leading NM, since it is also highly confined to the statically most unstable phase region. The amplification-rate contributions are, however, quite different. At initialization virtually all of the energy transfer from the basic wave to the SV is done convectively, while by  $t = \tau$  the state of the NM has been approached, where the shear-related exchange  $\gamma_y = \gamma_\perp$  is largest, followed by the convective contribution. In Fig. 5.11 one can see the leading transverse SV ( $\alpha = 90^\circ$ ). This perturbation is much more confined to the statically most unstable region than the corresponding NM. Also here the convective energy exchange makes the largest contribution at the initialization, followed by another important one from  $\gamma_v = \gamma_\parallel$ , while by the optimization time  $\gamma_u = \gamma_\perp$  also contributes significantly, and  $\gamma_v = \gamma_\parallel$  has become rather unimportant. It is to be noted that in this case at the perturbation wavelength where SV growth maximizes no growing NM exists (see Figs. 5.5 and 5.6) so that by  $t = \tau$  the SV structure cannot be explained in terms of a related NM.

This distinction gets even clearer as one looks at the time-dependent amplification-rate decomposition, according to (5.14), and energy density  $e_{\kappa\lambda}$  from somewhat longer integrations. These are shown for an integration over  $6\tau = 30\text{min}$  in Fig. 5.12. The



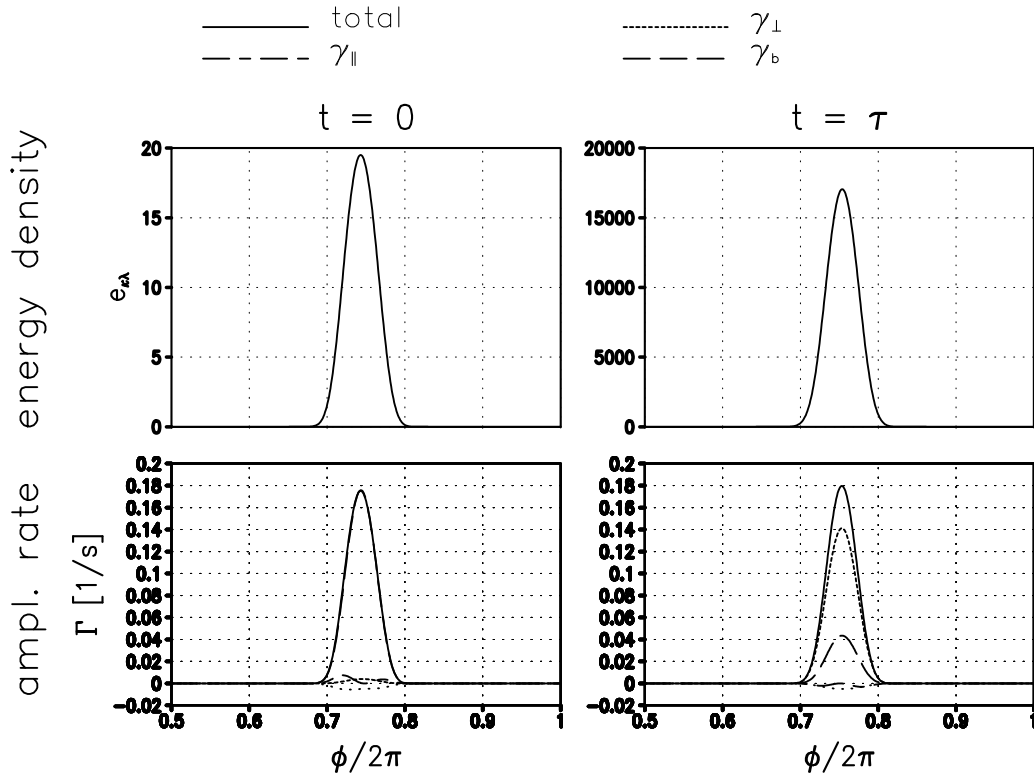


Figure 5.10: IGW-phase dependence of energy density (top row) and amplification-rate decomposition (bottom) of the leading short-term parallel singular vector ( $\alpha = 0$ ) for the statically unstable IGW ( $a = 1.2$ ,  $\Theta = 89.5^\circ$ ) at initialization ( $t = 0$ ) and optimization time ( $t = \tau = 300\text{s}$ ). The IGW-phase average of the sum of all amplification-rate parts yields the total instantaneous amplification rate  $\Gamma$ . The unimportant contribution from viscous and diffusive losses is indicated by a dotted line. The amplitude of the perturbation (in meaningless units) has been chosen to normalize the IGW-phase average of energy density ( $\langle e_{\kappa\lambda} \rangle = 1$ ) at  $t = 0$ . Only the IGW-phase range  $\pi \leq \phi \leq 2\pi$  is shown where the SV has a significant amplitude. At  $t = 0$  the total effective amplification rate is nearly identical to the convective contribution  $\gamma_b$ .

parallel SV exhibits a time-dependent amplification-rate decomposition with a maximum total value around  $t = 0.2\tau$ , when the initially dominant contribution from convective energy exchange is supplemented by that from the counter-gradient flux in  $v = v_\perp$ . By  $t = 2\tau$  a state is reached where the amplification rate does not vary anymore, both in its total value and in its decomposition in the various contributions (a leading contribution

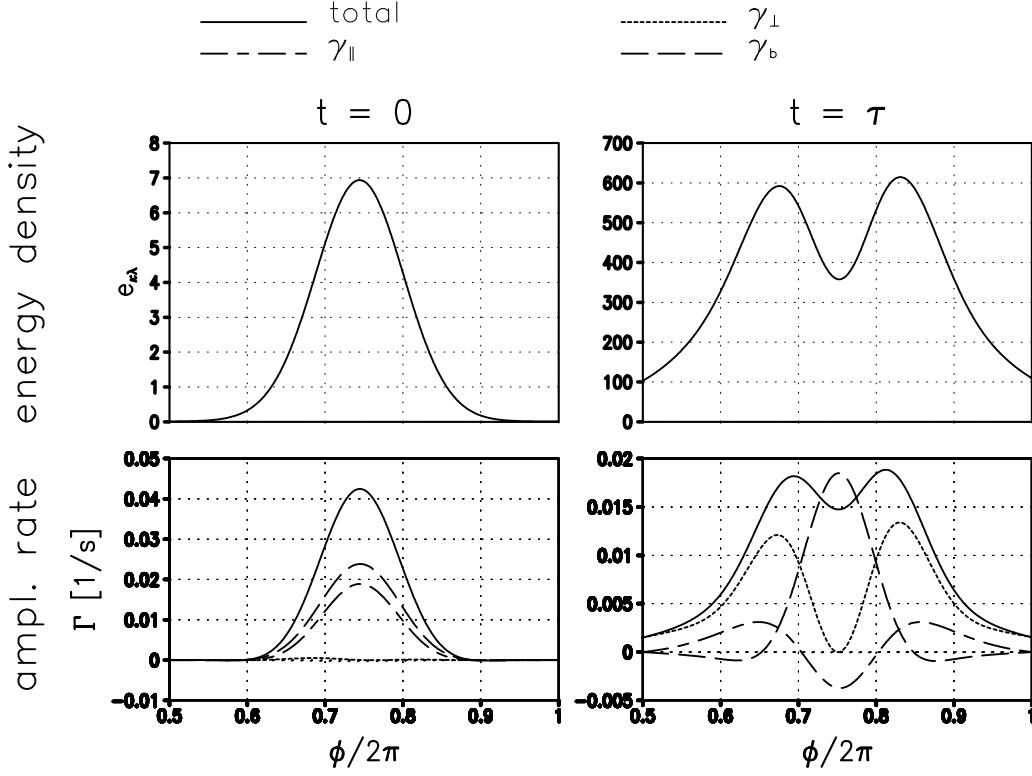


Figure 5.11: As Fig. 5.10, but now for the leading transverse SV ( $\alpha = 90^\circ$ ).

from shear in  $V = V_{\perp}$  with an additional weaker term from convective energy exchange). This indicates that the perturbation has assumed the structure of the leading NM and keeps on growing from there on. The energy density supports this picture. One sees a perturbation basically invariant in structure which is simply growing exponentially in time. The leading transverse SV, on the other hand, does not approach such an asymptotic behavior. Its amplification rate maximizes around  $t = 0.4\tau$ , then decreases until decay sets in at about  $t = 1.8\tau$  which at late times is dominated by viscous and diffusive losses ( $\Gamma \approx \Gamma_d$ ). But even then the amplification-rate decomposition stays time dependent. The energy density shows that the SV is split up into two main substructures, one of these at the original location of the initial perturbation, i.e. near the strongest static instability, and the other one near the other zero-line of the transverse wind in the IGW ( $\phi = \pi/2$ ). As is also discussed in chapter 4 for a similar case the SV radiates GWs which are approaching a quasi-critical layer near the transverse-wind zero-line, where their propagation is blocked and very small scales develop, thus explaining the observed

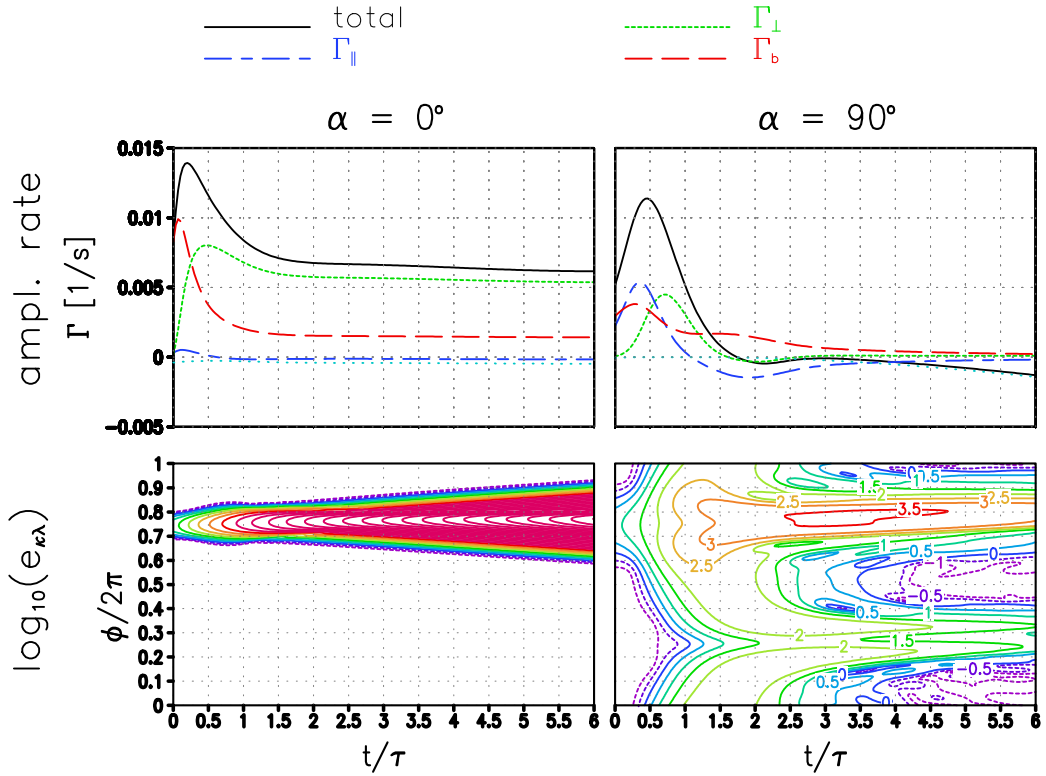


Figure 5.12: Time-dependent amplification-rate decomposition (top row) and energy density (bottom) from 30-min integrations of the leading short-term parallel (left column) or transverse (right) SV for the statically unstable IGW ( $a = 1.2$ ,  $\Theta = 89.5^\circ$ ). The optimization time is  $\tau = 5\text{min}$ . Viscous and diffusive losses are indicated by a dotted line. The contour interval in the lower panels is 0.5 in  $\log_{10}(e_{\kappa\lambda})$  (starting at -1). Negative contours are dashed.

behavior. A further short discussion of this effect is given in appendix C.2.

At a weaker IGW amplitude ( $a = 0.87$ ), where NMs can no longer grow, basically the same type of parallel and transverse SVs are found. Their time-dependent behavior is plotted in Fig. 5.13. Now one sees both eventually decaying in time, with a maximum in energy around  $t = 1.4\tau$ . The time-dependent decomposition of the instantaneous amplification rate is very similar to the one seen at the stronger IGW amplitude. In both cases static instability seems to act as a trigger of the instability, while later shear-related exchange plays an important, if not even dominant, role, as in the parallel SV. Although only nonmodal growth is possible the gain in energy covers about two orders of magnitude, indicating that at a suitable initial perturbation level SVs might be able

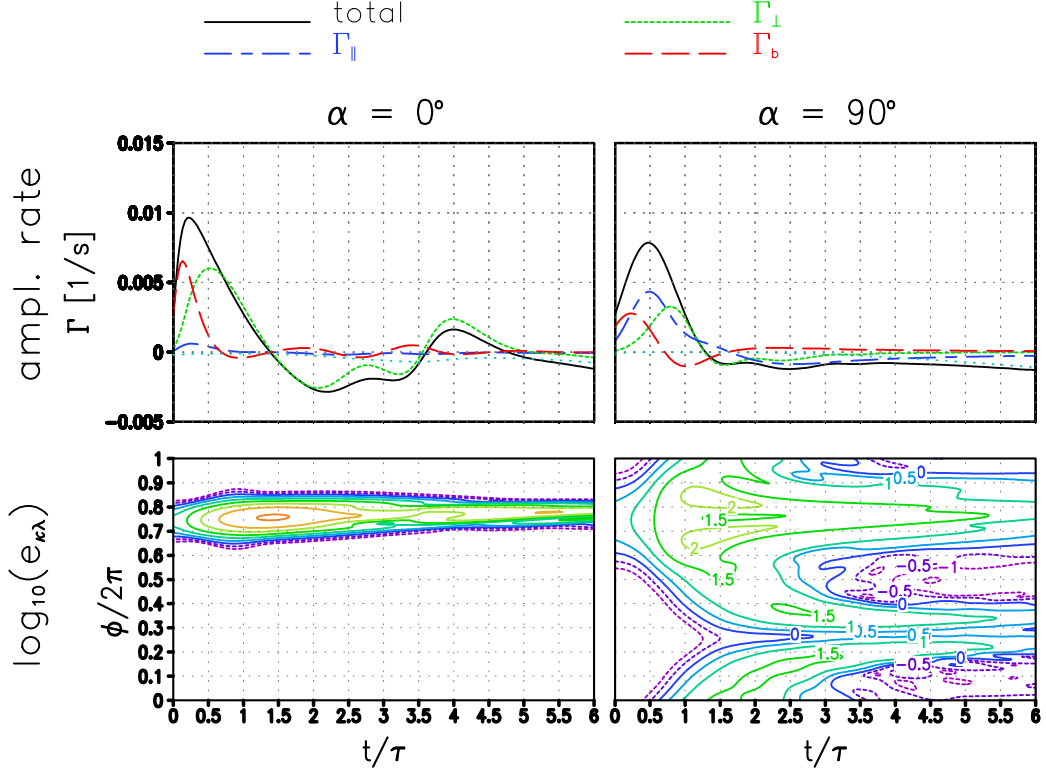


Figure 5.13: As Fig. 5.12, but now for an IGW amplitude  $a = 0.87$  excluding the possibility of NM instabilities.

to initialize nonlinear behavior and onset of turbulence. Another interesting observation is that also here in all cases the shear in  $V_{\perp}$  plays an important role, indicating that the amplification of the SVs is to a large part due to energy growth in  $v_{\perp}$ , and thus the roll mechanism discussed in chapter 4.

### Longer optimization times

Getting to the case of the longer optimization times the focus shall be on the global optimal  $\tau = 30\text{min}$  for  $a = 0.87$ . The time dependent amplification-rate decomposition and energy density of the leading parallel and transverse SV for  $a = 0.87$  are shown in Fig. 5.14. Similarly to the results in chapter 4 the time-dependence scales with  $\tau$ , i.e. energy growth persists until  $t = \tau$ , after which decay sets in (the same behavior is also seen for all other  $\tau$ , not shown). Also here convective exchange acts as a trigger, followed by the action of the counter-gradient fluxes in the horizontal velocity field. In comparison to the

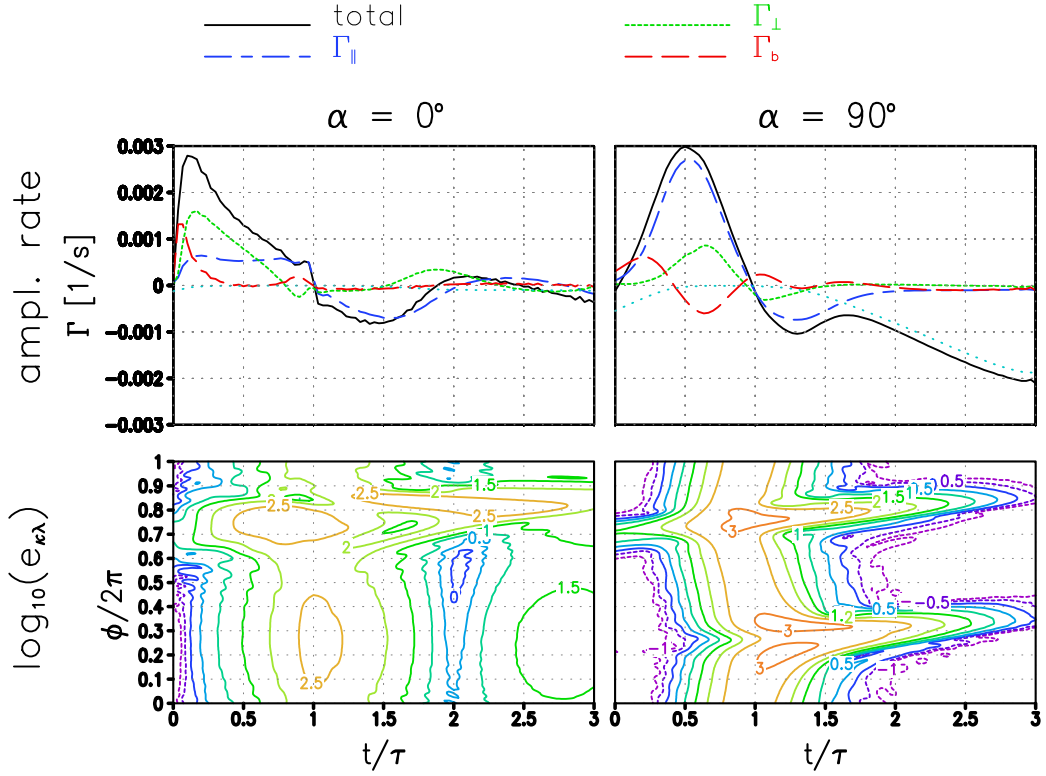


Figure 5.14: As Fig. 5.12, but now for an IGW amplitude  $a = 0.87$  excluding the possibility of NM instabilities (as in Fig. 5.13), and optimization time  $\tau = 30\text{min}$ .

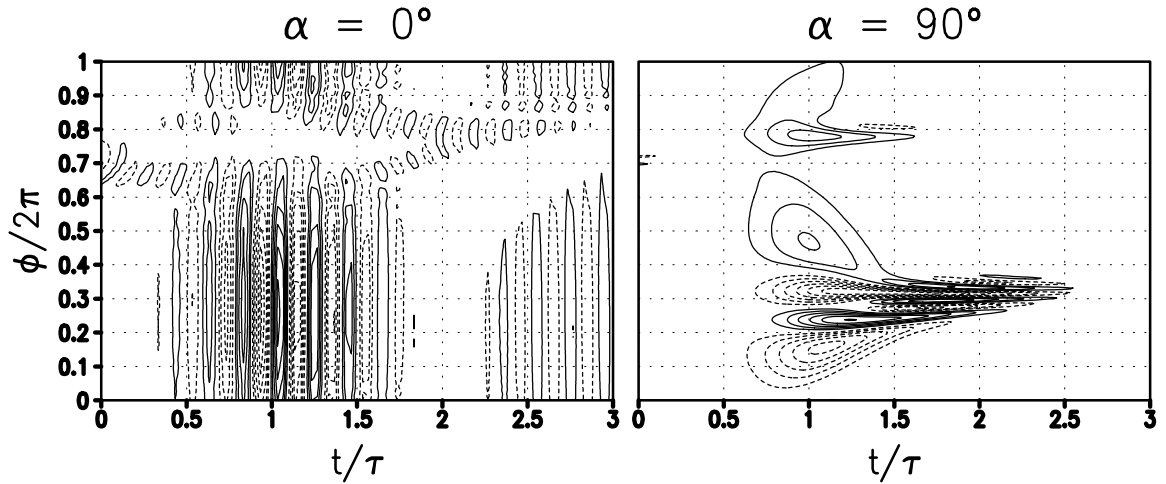


Figure 5.15: Corresponding to Fig. 5.14, the development of the buoyancy field in the respective SVs. Contour intervals are constant in arbitrary units. The zero contour has not been drawn.

short optimization time, the flux in  $v$  takes a less prominent role for the leading parallel SV (where  $v = v_\perp$ ). In the transverse case (where  $v = u_\parallel$ ) its role is dominant, indicating a main impact from the Orr mechanism. The energy density indicates in the latter case similar critical-layer interactions as for  $\tau = 300$ s. Indeed the time dependent buoyancy field in Fig. 5.15 shows this behavior, i.e. a tendency towards increasingly smaller scales near the zero-lines of  $V$ , a behavior which has been analyzed in depth in chapter 4 (but see also appendix C.2). For the leading parallel SV a quite different behavior can be seen. In contrast to the transverse SV the vertical scales progressively increase near  $\phi = \pi/2$ . This is different to the behavior seen in chapter 4, where the wave-packet envelope allowed the outwards radiation of high-frequency GWs. Here one sees a dynamics modified essentially by the periodic flow field in the basic IGW, leading to a ducting effect, where the SV, oscillating at a frequency  $\omega = \kappa U_\xi(\phi = 3\pi/2)$ , is prevented from radiating through the maximum of  $U_\xi$ . Details are also given in the appendix C.2.

A comparison of the relevance of the SVs for short and long optimization times, although desirable, must remain incomplete on the level of the present linear analysis. Note that, although showing larger overall growth, the long-optimization-time SVs grow at a smaller growth rate than the SVs for shorter  $\tau$ . This makes cases conceivable where, at sufficiently large initial perturbation level, the latter SVs lead the IGW into nonlinear behavior, before the ones for longer  $\tau$  have fully developed. More on this below.

### 5.3.2 High-frequency gravity waves

In contrast to the two subcritical IGW cases examined here, i.e. with  $a < 1$  and  $\text{Ri} > 0.25$  (see table 5.1), HGWs show NM activity at virtually all amplitudes. Thus after nearly every initialization of the linear model eventually the set of most unstable NMs will emerge as the final asymptotic state. The question only is how long it takes until this state is reached. As will be seen below, this time can be quite long.

#### Short optimization times

The focus shall first be on the short optimization time  $\tau = 300$ s. At least qualitatively the different HGW cases turn out to be very similar in the comparative dynamics of NMs

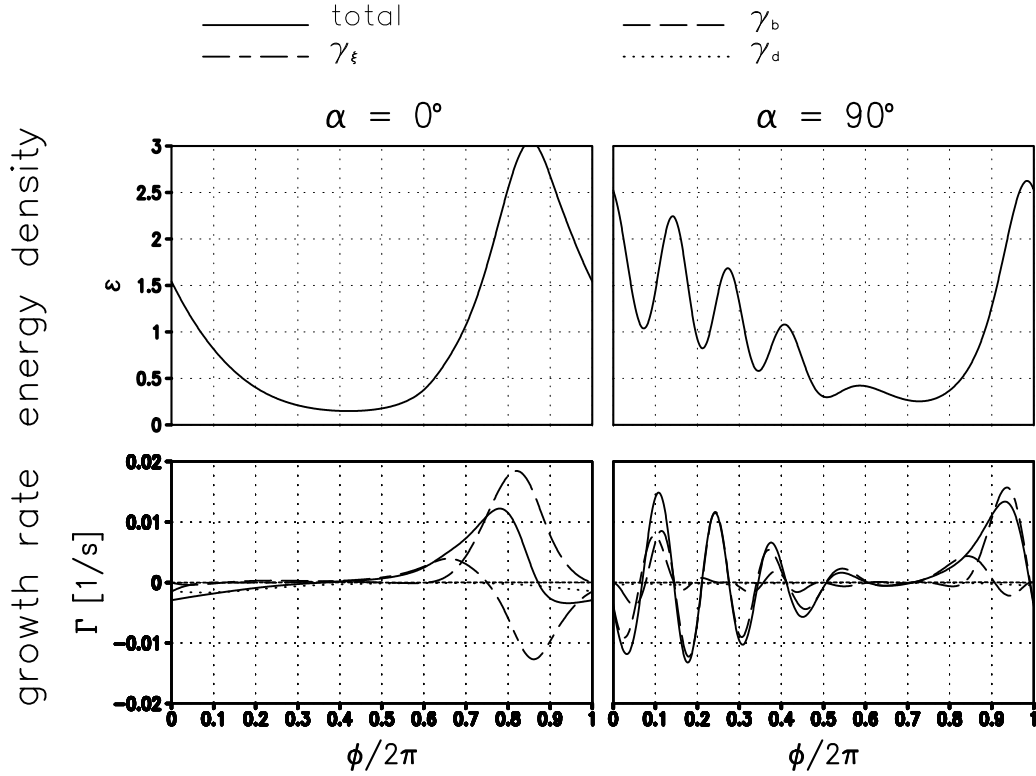


Figure 5.16: HGW-phase dependence of the energy density (top row) and the growth-rate decomposition (bottom) of the leading parallel (left column) and transverse (right) NM for the HGW with  $(\Theta, a) = (70^\circ, 1)$ , at the perturbation wavelength where optimal growth over  $\tau = 300$ s maximizes. The HGW-phase average of the sum of all growth-rate parts yields the total growth rate  $\Gamma = \gamma_1$ . The negligible contribution to the growth rate from shear in the transverse wind of the wave is indicated by a short-dashed line. The amplitude of the NM (in meaningless units) has been chosen to normalize the HGW-phase average of energy density, i.e.  $\langle e_{\kappa\lambda} \rangle = 1$ .

and SVs. As an example here the case  $\Theta = 70^\circ$  and  $a = 1$  (i.e.  $A = 0.55$ ) is discussed in some detail. Figure 5.16 shows for these parameters the HGW-phase dependence of energy density and amplification-rate decomposition for the leading parallel and transverse NM, each for the wavelength at which optimal growth maximizes (see Fig. 5.4). In addition, table 5.2 also lists the HGW-phase integral of the growth-rate decomposition. The results agree with those from Lombard and Riley (1996) in that the parallel mode is mainly excited convectively, while the transverse mode extracts its energy from the GW

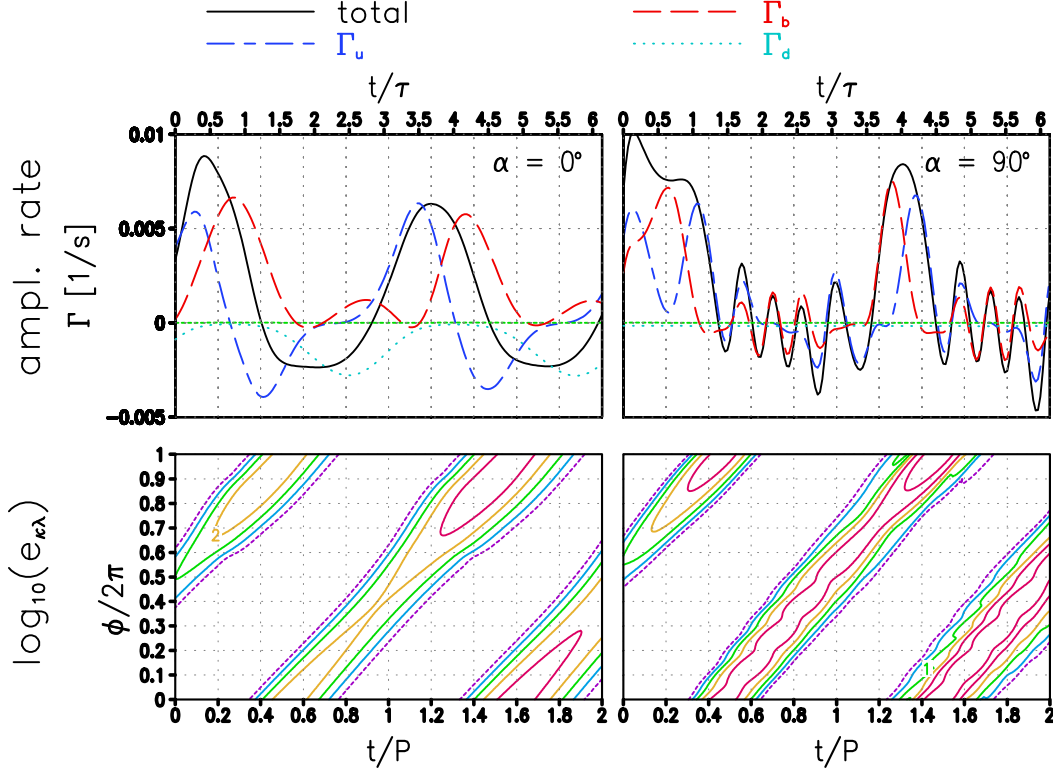


Figure 5.17: Time-dependence of the amplification-rate decomposition (top row) and energy density (bottom) from integrations of the leading parallel ( $\alpha = 0$ ) and transverse ( $\alpha = 90^\circ$ ) short-term ( $\tau = 300s$ ) SV, for a HGW with  $(\Theta, a) = (70^\circ, 1)$ , over two HGW periods  $P = 920s$ . The initial amplitudes in the patterns (in meaningless units) have been chosen to normalize the HGW-phase average of energy density, i.e.  $\langle e_{\kappa\lambda} \rangle = 1$ . Contouring starts at  $\log_{10}(e_{\kappa\lambda}) = -1$ . The contour interval is 1. Negative contours are dashed. For better orientation the time axis is shown both normalized by  $\tau$  (top) and  $P$  (bottom).

predominantly via shear-related exchange. Only  $dU_\xi/d\phi$  enters the latter since the GW amplitude in  $V$  is negligible. The HGW-phase dependence of the leading exchange terms is consistent with the wave structure: For the parallel mode the convective exchange is strongest near  $\phi = 3\pi/2$  where  $dB/d\phi$  is most negative, and the shear exchange for the transverse mode peaks near  $\phi = 2\pi$  where the wave shear reaches one of its two extrema. As for the complementary exchange terms, one sees wave shear near  $\phi = 2\pi$  to act against the growth of the parallel mode, while the transverse mode experiences convective excitation at  $\phi = \pi/2$ , where  $dB/d\phi$  becomes largest, an effect which is however quite



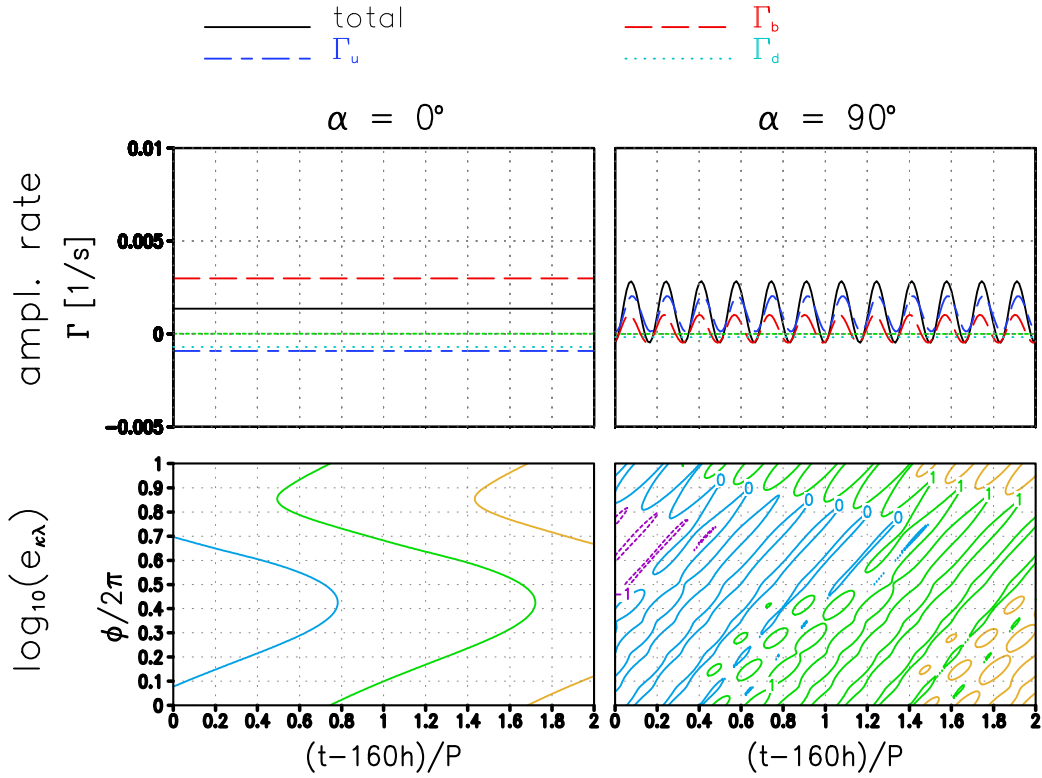


Figure 5.18: As Fig. 5.17, but for a later phase  $160h \leq t \leq 160h + 2P$ .  $e_{\kappa\lambda}$  has been normalized so that its phase average  $\langle e_{\kappa\lambda} \rangle = 1$  at  $t = 160h$ .

eliminated by strong negative contributions near the flanks of this region so that there is no essential net convective impact on the transverse mode. The respective dominance of the different exchange terms is also reflected in the HGW-phase distribution of the energy density of the NM: The parallel NM is concentrated near  $\phi = 3\pi/2$ , where the convective exchange is largest, and the transverse mode peaks in energy density near  $\phi = 2\pi$  where the shear-related exchange also maximizes.

The time dependence of the amplification-rate decomposition, according to (5.14), and the energy density  $e_{\kappa\lambda}$  are shown in Fig. 5.17 for integrations of the corresponding SVs over two HGW periods. If a single leading NM exists, the final asymptotic behavior can be expected as a time-independent amplification-rate decomposition identical to that of that NM (table 5.2) and an energy density growing in time but not moving with respect to the wave. One notes a slow approach towards this state in two regards: The amplification-rate contributions oscillate with slowly decaying amplitude about the NM values (see

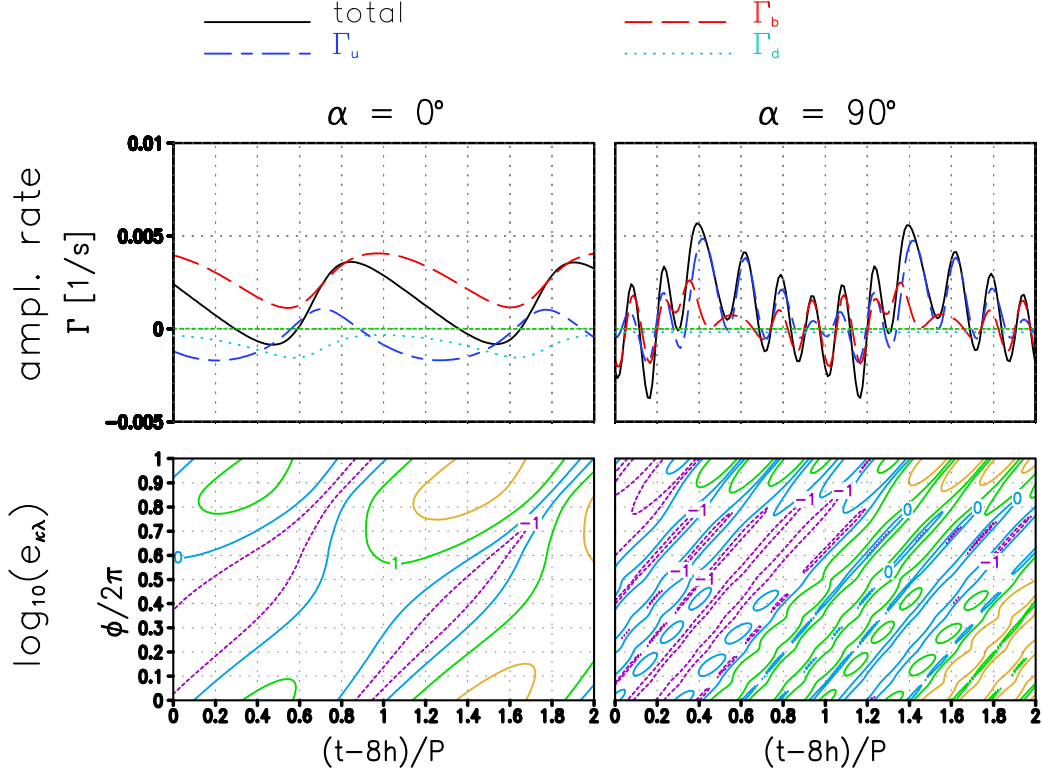


Figure 5.19: As Fig. 5.17, but for a later phase  $8h \leq t \leq 8h+2P$ .  $e_{\kappa\lambda}$  has been normalized so that its phase average  $\langle e_{\kappa\lambda} \rangle = 1$  at  $t = 8h$ .

table 5.2), and the energy densities of the two SVs, which indicate highly peaked pulses propagating upwards through the wave, are slowly broadening. As expected from the growth factors, the transverse SV shows more intensive growth than the parallel SV (note the logarithmic color and contour scale). The corresponding behavior after a long time (160h) is shown in figure 5.18. Indeed the parallel SV has approached the structure of the leading NM, while the transverse SV has split up into finer pulses still moving through the wave, however with an amplification-rate decomposition seemingly oscillating about the corresponding values of the leading NM. The difference between the two cases arises from the fact that for  $\alpha = 0^\circ$  a single leading NM exists, while for  $\alpha = 90^\circ$  two leading NMs are found which are very close to each other in growth rate ( $\exp(\gamma_1\tau) = 1.4494$  and  $\exp(\gamma_2\tau) = 1.4491$ ) and in their growth-rate decomposition (not shown). Seemingly those two together constitute the basis of the late stage of the development of the corresponding SV. In any case it seems interesting that the eventual approach of the leading NM is rather

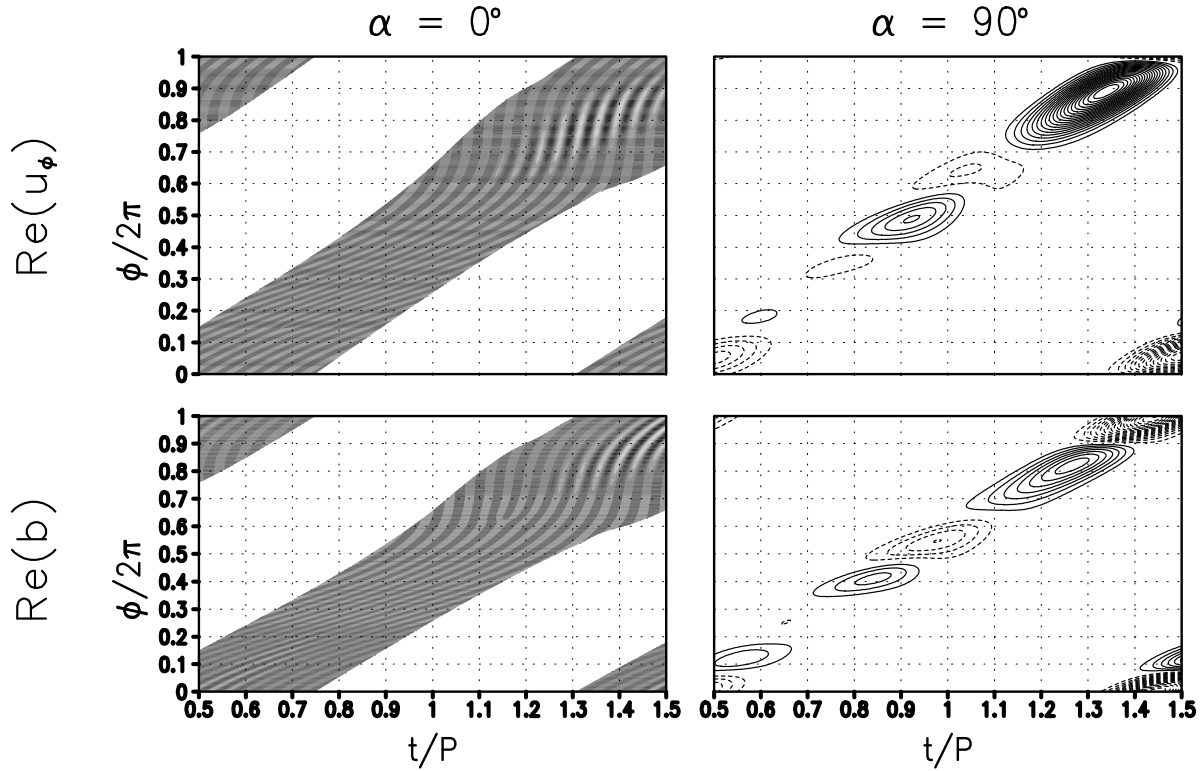


Figure 5.20: As Fig. 5.17, but now showing for one sub-cycle, corresponding to one passage of the GW over the perturbation, the time-dependent structure of the real parts of  $u_\phi$  (upper row) and  $b$  (bottom). Both the shading scale for the parallel perturbation and the contour intervals for the transverse perturbation are linear in arbitrary units. In the latter case the zero contour has not been drawn, and negative values are indicated by a dashed contour.

slow (e.g. by  $t = 8h$  the NM state has by far not been reached yet, see Fig. 5.19) so that the transition from SV to NM might take longer than one can expect the linear approximation to hold before nonlinear effects become important. Another main feature one also notes is that the time both SVs need for once covering the distance  $\Delta\phi = 2\pi$  agrees with the period of the GW, which means that the perturbation actually does not move in the original reference system, while the GW passes over it, at the same time repeatedly invigorating and damping the SV. In the case of a transition to the leading NM one would see the wave gradually picking up the slowly broadening perturbation until its energy-density distribution no longer moves in the translated coordinate system, and is basically swept along with the wave, as observable for the parallel SV.

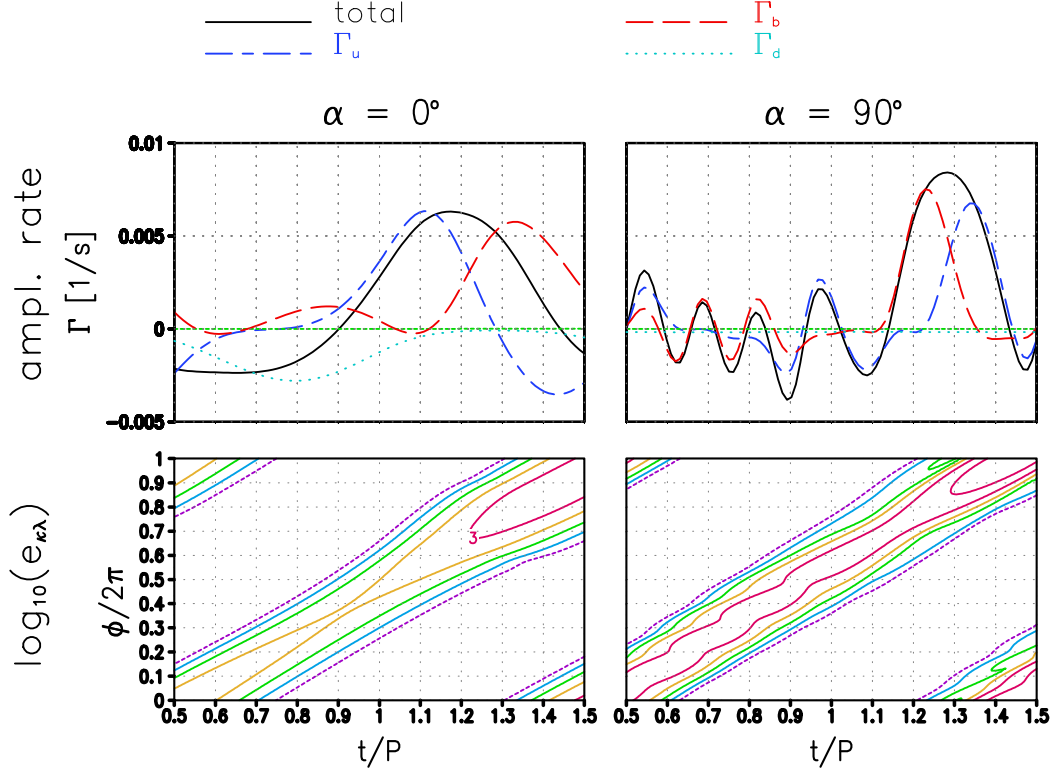


Figure 5.21: As Fig. 5.17, but now for one sub-cycle corresponding to one passage of the GW over the perturbation.

Besides this general observation the details of the two time series are also interesting, especially as they reveal impacts from the structures of both the NM and the basic wave. Although the parallel NM grows due to convective exchange the corresponding optimal perturbation is triggered by shear-related exchange. Initially  $\Gamma \approx \Gamma_u$  which is consistent with the perturbation being concentrated at  $\phi = \pi$  where the wave shear maximizes. By  $t \approx 0.8\tau$  convective exchange takes over, which is the time when the SV passes the statically most unstable HGW-phase  $\phi = 3\pi/2$ . Shortly later, when  $\phi = 2\pi$  is reached where  $dU_\xi/d\phi$  is largest, shear-related exchange is strong again, now however damping the perturbation. As the perturbation passes  $\phi = \pi/2$  strong viscous and diffusive damping sets in. This is due to a scale contraction of the SV which for one sub-cycle in the movement between  $\phi = 0$  and  $\phi = 2\pi$  is shown in Fig. 5.20. This behavior can be explained in terms of a WKB-type propagation of the perturbation in the flow field of the GW (see appendix C.3). The succession of processes sketched above is repeated many

times as the wave repeatedly passes over the perturbation (not shown). An interesting feature also becomes visible in a comparison of the time-dependent amplification rate of the parallel SV (Fig. 5.17) with the HGW-phase dependent analogue in the parallel NM (Fig. 5.16): It appears that in its moving from  $\phi = 0$  to  $\phi = 2\pi$  the SV experiences the same exchange processes as the NM exhibits at the respective HGW phase. This goes as far as even expressing itself in the HGW-phase dependent energy density, i.e. the NM peaks at  $\phi = 3\pi/2$  while the SV also shows a local maximum in energy density as it passes this HGW phase. So in some sense the SV already follows the NM energetics in its development towards that structure.

Very similar observations can also be made for the transverse perturbations ( $\alpha = 90^\circ$ , right columns in Figs. 5.16 – 5.20). Also the transverse SV is triggered by shear instability at  $\phi = \pi$ . As it passes  $\phi = 3\pi/2$  convective exchange takes over, followed by another peak of  $\Gamma_u$  as  $\phi = 2\pi$  is reached. This double peak in  $\Gamma_u$ , responsible for the stronger overall growth of the transverse SV between  $t = 0$  and  $t = \tau$  than that of the parallel SV, occurs only once. In the following cycles it is not repeated. Then growth due to shear is only observed at  $\phi = 2\pi$ , preceded by convective growth at  $\phi = 3\pi/2$ , just as observed in the NM. One conspicuous difference between the parallel and transverse SV is that, while the former is a rather small-scale wave packet in its dependence on  $\phi$ , the latter is a larger-scale pulse changing its sign several times in its apparent movement through the HGW. This is the reason (see Fig. 5.20) why viscosity and diffusion are of less importance for the transverse SV than for the parallel SV. Besides this, as the transverse SV moves from  $\phi = 0$  to  $\phi = 3\pi/2$  the instantaneous amplification rate undergoes rapid oscillations which are once again a good copy of corresponding behavior in the NM, as is also the phase distribution of the energy density. In order to facilitate a better comparison a cycle between  $\phi = 0$  and  $\phi = 2\pi$  has been redrawn for each SV in Fig. 5.21.

### **Longer optimization times**

As seen above, the parallel wavelength  $\lambda_{\parallel}$  of the SVs for longer optimization times ( $\tau = P$ ) is larger than for  $\tau = 300s$ , and their growth-factor distribution in the  $\lambda_{\parallel} - \alpha$  plane is more similar to that of the corresponding NMs. Interestingly however, it turns out that

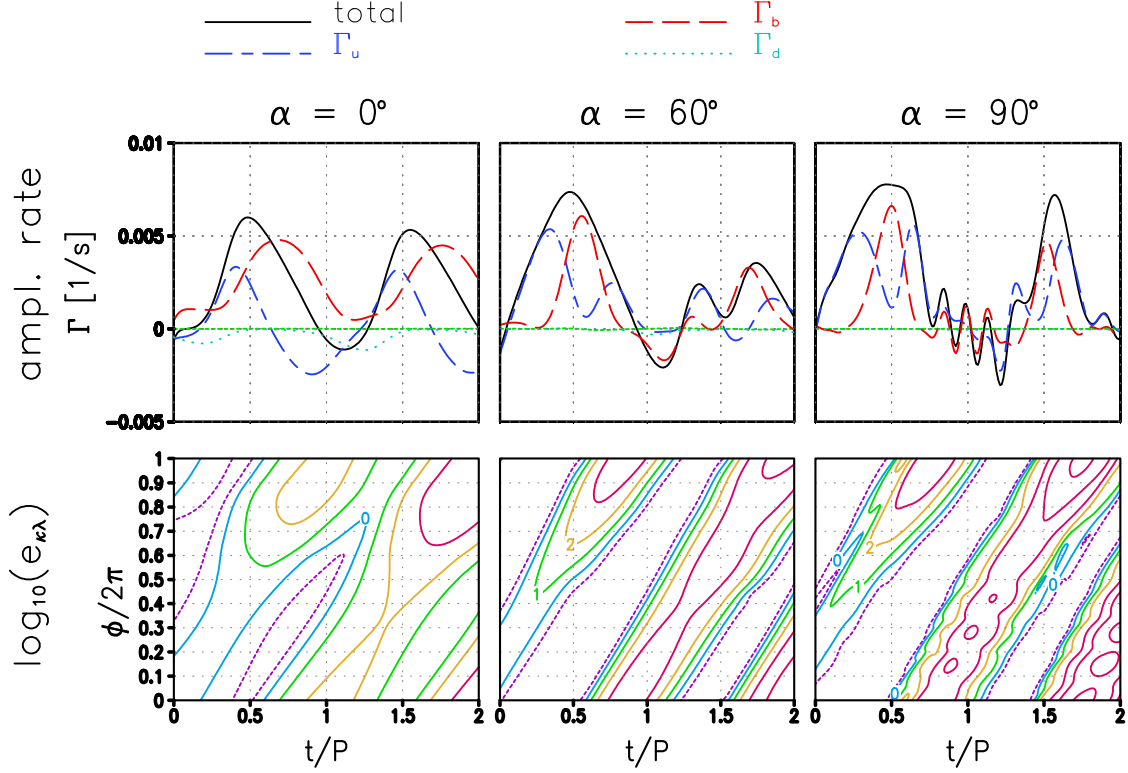


Figure 5.22: As Fig. 5.17, but now for the leading SVs for  $\tau = P = 920$ s and azimuth angles  $\alpha = 0^\circ, 60^\circ$ , and  $90^\circ$ .

their dynamics is still quite similar to that of the SVs for  $\tau = 300$ s. Being once again, at least qualitatively, representative for all cases, here the SVs for the HGW with  $(\Theta, a) = (1.0, 70^\circ)$  are discussed shortly. Figure 5.22 shows the time-dependent amplification-rate decomposition and energy-density distribution for the leading SVs at azimuth angles  $0^\circ$ ,  $60^\circ$  (the case of strongest optimal growth), and  $90^\circ$ . The similarity of the behavior of the leading parallel and transverse SV to that seen in Fig. 5.17 is obvious. As a major difference, in comparison to there the initial amplification rates are smaller, so that initial growth is not as rapid. Also the patterns are broader in structure, and thus nearer to the structure of the corresponding NMs. Remarkably, however, also here the transition to the NM is far from complete after two HGW periods.

As discussed in the comparison between short- and long-optimization-time SVs for IGWs, also for HGWs the respective relevance of the corresponding SVs can be expected to depend on the properties of the available perturbation spectrum. Mainly its overall

intensity will probably be of importance, but also the scales available in it, since the various SVs differ not only in optimization time but also in their intrinsic wavelengths.

## 5.4 Impact of the controlling parameters

For a complete picture one also needs an overview of what happens as the chosen external model parameters are varied. In the atmosphere, e.g., the inverse proportionality of kinematic viscosity and diffusivity with the background density implies that at fixed wavelength of the GW the Reynolds number decreases from the surface of the earth to the mesopause (at about 90km altitude) by nearly six orders of magnitude. Likewise varying at fixed altitude the basic-wave wavelength would also imply a variation of the Reynolds number. Another external parameter deserving some examination is the factor  $f/N$ . While here  $f$  has been chosen to be the Coriolis parameter at 70°N and  $N = 2 \cdot 10^{-2}\text{s}^{-1}$ , which is typical for the middle atmosphere, in the tropics, where  $f \approx 0$ , or in the lower atmosphere, where  $N = 1 \cdot 10^{-2}\text{s}^{-1}$  is more appropriate a choice, a different dynamics might occur. Without going into too great depth corresponding effects shall be estimated here.

### 5.4.1 Reynolds number

In varying the Reynolds number the above-mentioned six orders of magnitude are not covered. Instead, for reasons of computational economy, viscosity and diffusion have been increased to  $\nu = \mu = 5\text{m}^2/\text{s}$ , or decreased to  $\nu = \mu = 0.1\text{m}^2/\text{s}$  (corresponding to a mid-mesospheric altitude near 70km), and then the optimal growth over  $\tau = 300\text{s}$  has been determined for  $A = 0.55$ . Figures 5.23 and 5.24 show the results. The main effect is as expected: Larger Reynolds numbers mean stronger instabilities. Concerning the  $(\lambda_{\parallel}, \alpha)$ -dependence one finds that there is not much of an effect on the azimuth angles where optimal growth is most vigorous. However, in agreement with similar findings by Lombard and Riley (1996) on the dependence of the leading NMs for  $f = 0$  on the Reynolds number, the scales are affected so that the wavelength of strongest optimal growth gets smaller as the Reynolds number is increased. For IGWs the results from the

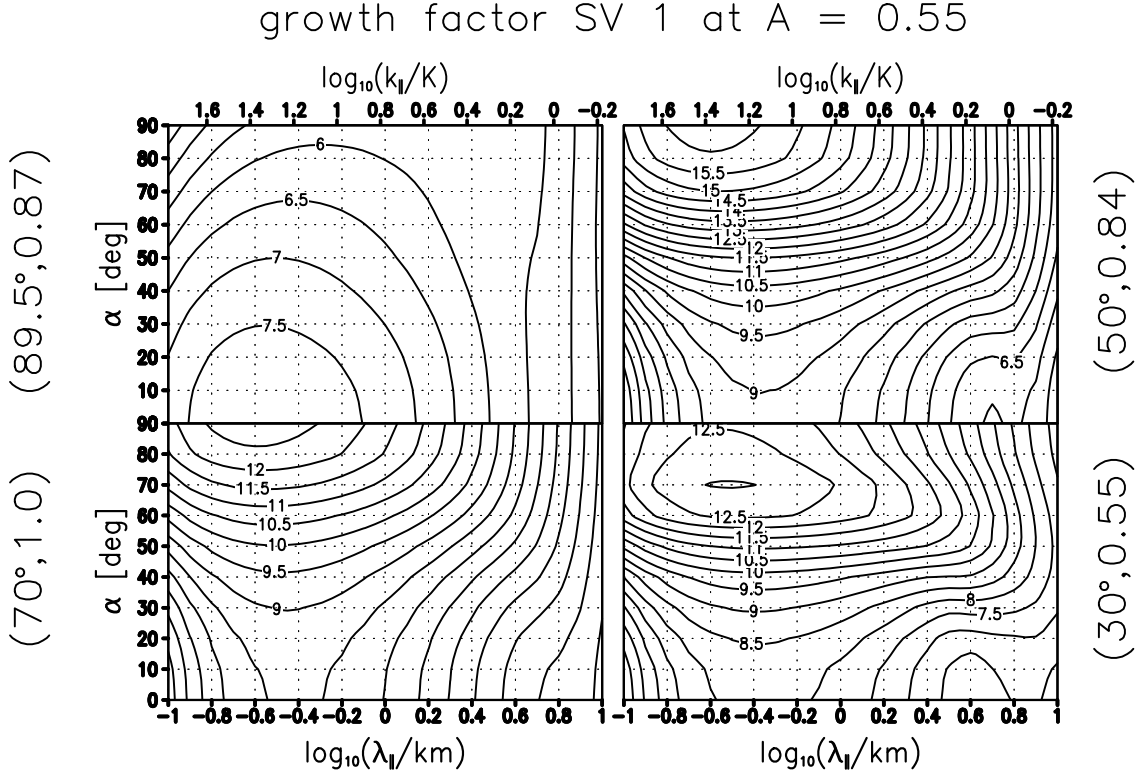


Figure 5.23: As Fig. 5.4, but now with decreased values of viscosity and diffusivity  $\nu = \mu = 0.1\text{m}^2/\text{s}$ .

shear-layer theory in chapter 4 suggest for parallel SVs a dependence as  $\lambda_{\parallel} \propto \text{Re}^{-1/4}$ . This is consistent with the results here. An exception to the Reynolds-number dependence of the wavelengths is the leading transverse SV of the IGW. For this one both the growth factor and its wavelength are found to be basically the same for all three Reynolds numbers examined. This is consistent with the identification of a comparable NM growth-rate peak for  $a > 1$  by others (Dunkerton, 1997; Kwasniok and Schmitz, 2003) in calculations for IGW packets with infinite Reynolds number. The main effect here is that, as is visible from a cut at  $\alpha = 90^\circ$  which is not shown here, while the Reynolds number is increased slowly, a secondary growth-factor peak at a shorter wavelength emerges which is at  $\lambda_{\parallel} \approx 600\text{m}$  for  $\nu = \mu = 0.1\text{m}^2/\text{s}$ . One might expect that this one gets stronger and moves to smaller scales as the Reynolds number is increased even further, while the one at the larger wavelength stays unaffected. Decreasing the Reynolds number would at some stage, however, also damp the growth of that branch. Similarly one also finds for



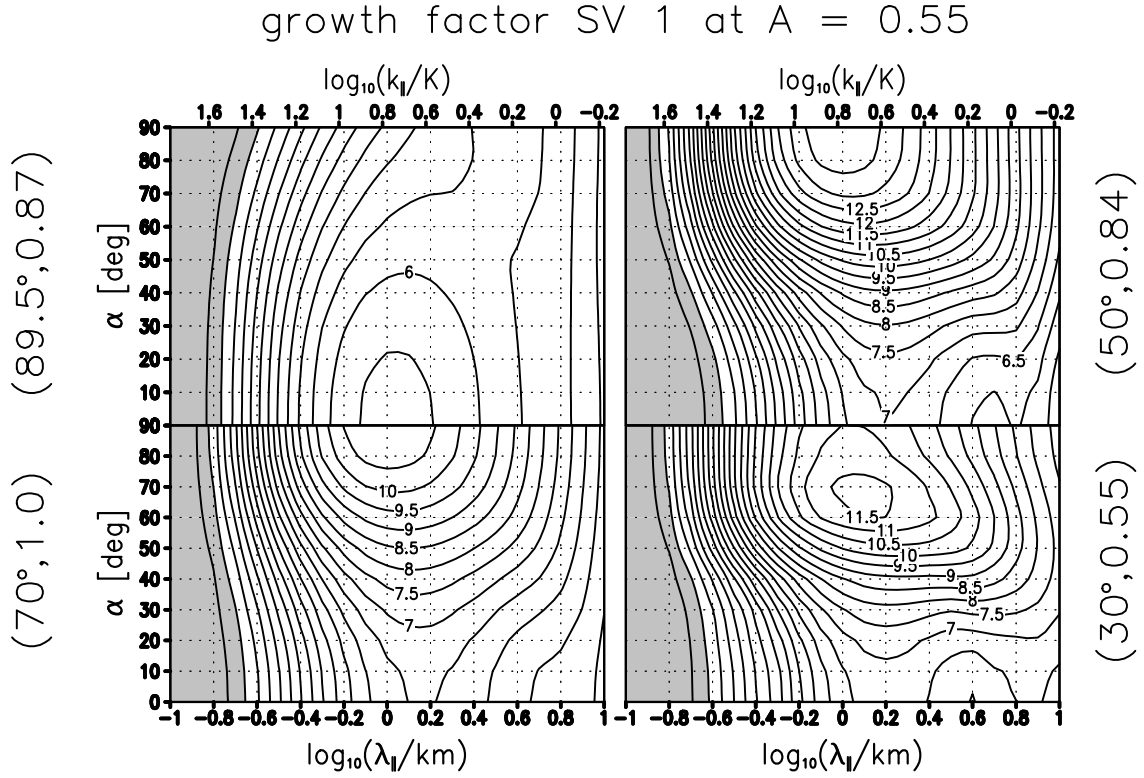


Figure 5.24: As Fig. 5.4, but now with increased values of viscosity and diffusivity  $\nu = \mu = 5\text{m}^2/\text{s}$ .

$\Theta = 30^\circ$  at  $\lambda_{\parallel} \approx \Lambda$  a parallel SV which is not much affected by viscosity and diffusion, but also here at even smaller Reynolds numbers the SV will probably be damped. For the high-Reynolds-number case NM growth factors (not shown) are found to slightly increase in comparison to Fig. 5.3 (maximal growth factors 2.2, 4.0, and 5.8, at  $\Theta = 70^\circ, 50^\circ$ , and  $30^\circ$ , with an overall  $\lambda_{\parallel} - \alpha$  dependence as before). This case, however, still shows no NM instabilities of the IGW.

### 5.4.2 Rotation

For an estimation of the impact of variations in  $f/N$  the determination of the SVs for  $A = 0.55$  has been redone for different latitudes. As expected only the IGW case showed an impact so that only this one shall be given some attention. Figure 5.25 shows the  $(\lambda_{\parallel}, \alpha)$ -dependence of the growth factors of the leading SVs obtained for the latitudes  $0^\circ, 30^\circ, 50^\circ$ , and  $90^\circ$ , to be compared to the upper left panel in Fig. 5.4. One sees two

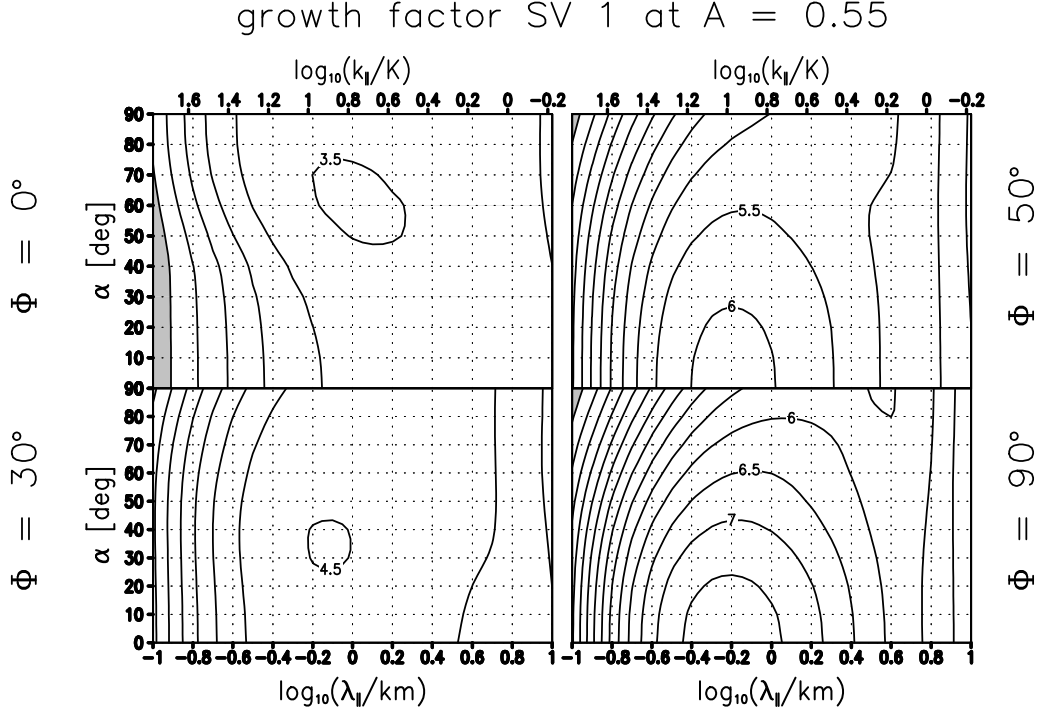


Figure 5.25:  $(\lambda_{||}, \alpha)$ -dependence of the growth factors of the leading SVs for a slightly subcritical 'IGW'  $((\Theta, a) = (89.5^\circ, 0.87))$  at the latitudes  $\Phi = 0^\circ, 30^\circ, 50^\circ$ , and  $90^\circ$ , determining the magnitude of the Coriolis parameter. The contour interval is 0.5. Values less than one are indicated by shading.

main effects: As rotation becomes smaller optimal growth gets weaker and the leading azimuth angle moves from parallel to  $\alpha = 60^\circ$ . The former is consistent with the previous observation that the energy exchange with the IGW via shear in  $V$  plays an important role. As rotation gets less the strength of this wind component in the wave is reduced so that the energy reservoir its kinetic energy provides for the SVs is reduced. In time integrations (not shown) the SVs are found to finally decay in all cases, as also follows from the absence of growing NMs. It seems that optimal growth is rather less important for subcritical IGWs in the tropics.

## 5.5 Mean growth from random initial conditions

A critical question one might ask about rapid transient growth from optimal perturbations is how relevant they are for realistic circumstances where a GW will encounter perturba-

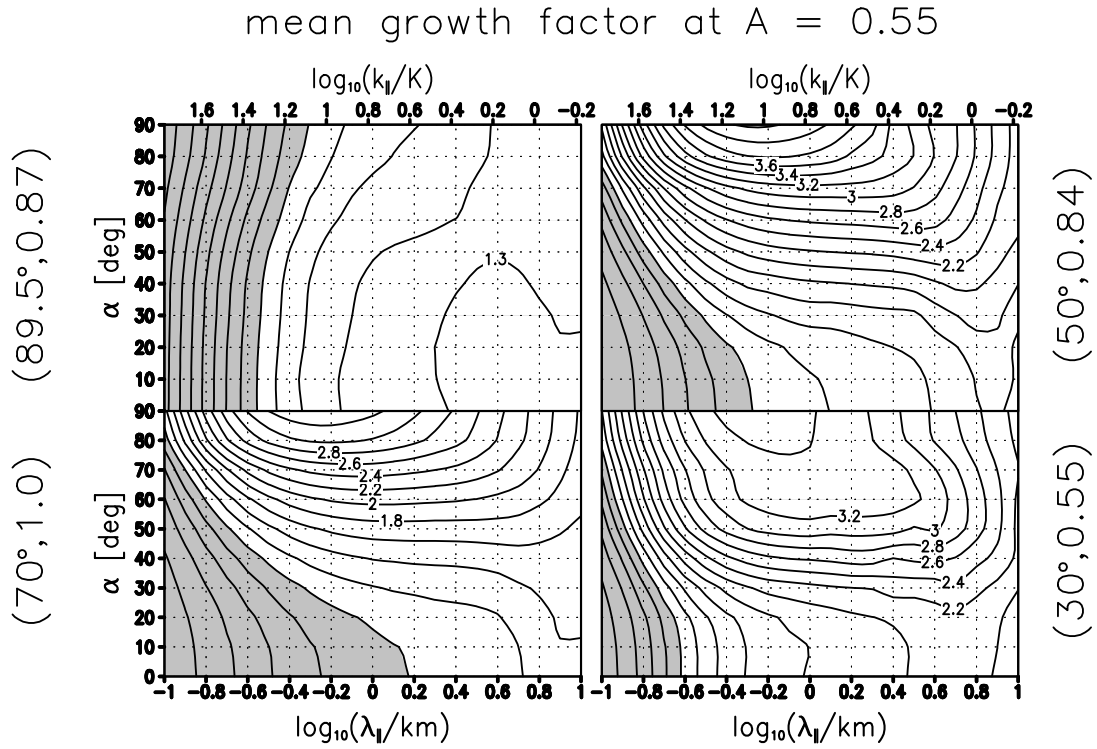


Figure 5.26: Similar to Fig. 5.4, but now showing the mean growth (within 300s) in the square root of energy from initial random perturbations with a 5/3 power law in the wavenumber in  $\phi$ -direction. The contour interval is 0.1 for the IGW case ( $\Theta = 89.5^\circ$ ) and 0.2 everywhere else. Values less than one are indicated by shading.

tions from ambient fluctuations which most probably will not project to the largest part onto a single optimal perturbation (Lott, 1997). If there is only one SV structure having rapid growth, it may not be sufficient to compete with the leading normal mode (if there is any). If, however, the number of growing optimal perturbations is large enough, and if these are similar enough to each other, optimal growth might play a role in explaining observed behavior of turbulence onset in its linear phase.

In order to get some insight into this problem the linear model has been integrated over 300s from random initial conditions. A possible option for a source spectrum would be just white noise, but this would not be overly realistic. Rather it is to be expected that a gravity wave will encounter fluctuations with a typical turbulent spectrum, as observed (Lübken, 1997) and modelled (Werne and Fritts, 1999; Fritts et al., 2003) by others. It has therefore been attempted to mimic a spectrum in the wavenumber in  $\phi$ -direction

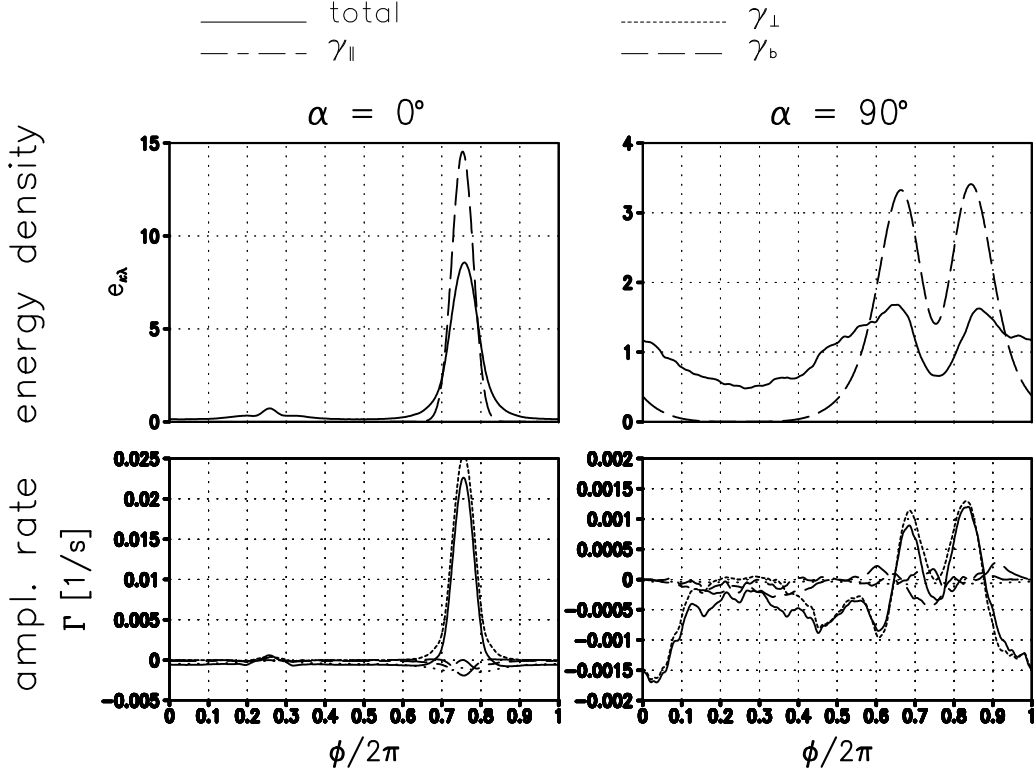
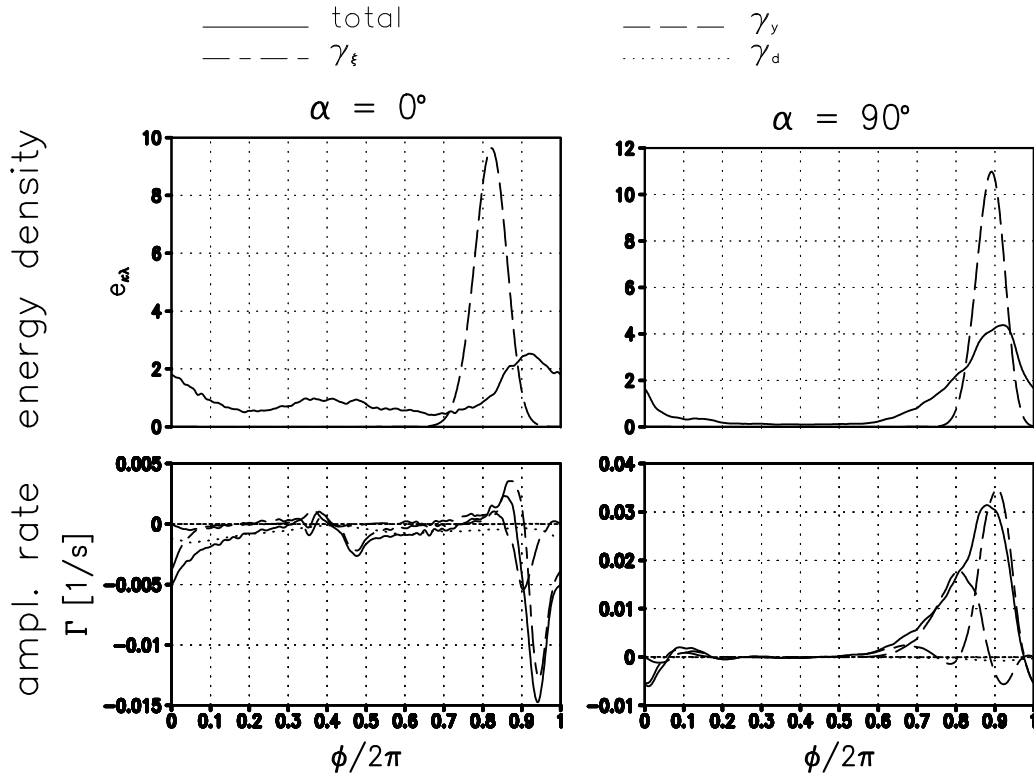


Figure 5.27: Corresponding to Fig. 5.26, the mean energy density (top row) and IGW-phase dependent amplification-rate decomposition (bottom) at  $t = 300$ s for parallel and transverse perturbations at the wavelength of strongest optimal growth for  $(\Theta, a) = (89.5^\circ, 0.87)$ . In the upper panels the mean energy density is indicated by the solid line while the dashed line shows the same field for the corresponding SV. Both are normalized to have a unit IGW-phase average.

with a typical  $5/3$  power law. For this energetically equipartitioned flow and buoyancy fields have been obtained from a random number generator. The Fourier transforms of these have then been modified to follow a  $5/3$  power law, and the resulting random initial states have then been used in the model. For each pair of azimuth angle and perturbation wavelength in the  $\xi - y$  plane the number of integrations has been doubled, starting at a minimum of 16, until the observed mean growth or decay in the square root of energy changed by less than a percent.

For  $A = 0.55$  the resulting mean growth is shown in Fig. 5.26. This is to be compared to Fig. 5.4. It is not surprising to find that, in comparison to the optimal growth factors,

Figure 5.28: As Fig. 5.27, but now for  $(\Theta, a) = (70^\circ, 1)$ .

these mean growth factors are smaller. On the other hand one also finds even mean growth of random perturbations to be possible for the IGW case, although this one does not have a single growing NM. Moreover, in all cases one sees a reasonable reproduction of the dependence of the growth factors on azimuth angle and horizontal wavelength. So also here the strongest mean growth is observed in the IGW case for parallel perturbations. The HGW cases show transverse perturbations to extract most of the energy from the wave. For  $\Theta = 70^\circ$  and  $\Theta = 50^\circ$  this is in agreement with the optimal-growth results. In these cases also the scale of the strongest growth matches quite well that of strongest optimal growth. In the case  $\Theta = 30^\circ$  the leading optimal perturbation is at  $\alpha = 70^\circ$ , while strongest mean growth is found at  $\alpha = 90^\circ$ , but also here one finds a trace of the optimal-growth results in that at the respective azimuth angle no maximum exists but a plateau which is not found at the other inclination angles. This is to be seen in contrast to Fig. 5.3, where the corresponding NM growth factors are shown, with no instability in the IGW case, and strongest growth for parallel perturbations in the HGW cases.

For the IGW case one sees in Fig. 5.27 for  $t = 300$ s the mean energy density and amplification-rate decomposition of parallel and transverse perturbations at the wavelength of strongest optimal growth. A comparison with the energy density of the SV, indicated by the dashed line in the upper row, suggests that many of the features seen can be explained in terms of optimal growth. This is further supported by the fact that NMs cannot be used here, since they all decay. For the case  $(\Theta, a) = (70^\circ, 1)$  the same fields are shown in Fig. 5.28. For the transverse perturbations once again optimal-perturbation theory seems to give a useful explanation. The energy density is much more strongly peaked near the location of the SV than in the NM (see Fig. 5.16). The same disparity between NM and mean structures is also found for the HGW-phase dependent amplification-rate decomposition. On the other hand, the parallel perturbations do not indicate SV behavior. This is probably an effect of the small-scale structure of the corresponding SV (see also Fig. 5.20 and appendix C.3). By using a source spectrum with suppressed small-scale activity such a perturbation is prevented to appear. Indeed, in a parallel calculation with random initial states with a white spectrum the parallel SVs can be identified (not shown).

## 5.6 Summary

As an extension to the investigation in chapter 4 on SVs of IGW packets, here optimal perturbations of monochromatic GWs, including HGWs, have been determined and compared to the corresponding NMs. The viscous-diffusive parameters have been chosen so as to agree with the conditions in the middle to upper mesosphere (between 70 and 90km altitude). Among the results the most important ones are the following.

First, the findings from chapter 4 are reproduced that IGWs can support rapid transient growth by several orders of magnitude (in energy) when no NM instability exists. This is the case for IGWs slightly below the overturning threshold ( $a = 0.87$ , say), where NM instabilities are prevented by viscous-diffusive effects. For such cases, optimal perturbation theory suggests, in contrast to the predictions from NM analyses, the possibility of turbulence onset, certainly subject to the condition that the ambient perturbations

encountered by such an IGW are already sufficiently strong so that a further amplitude growth by at most a factor 20 can lead into nonlinear development. The most important growth mechanisms are the same as described in chapter 4: The parallel SVs growing most rapidly for short optimization times are driven by the roll mechanisms. The leading transverse short-term SVs, with larger scale than the parallel SVs, are subject to a mixed Orr and roll mechanism. A global optimal at an optimization time of 30min is found, certainly conditioned on the specific wave parameters. At such longer optimization times the transverse SVs grow most strongly, as can also be understood based on the shear-layer theory in chapter 4.

Secondly, the leading SVs of all examined HGWs with weak to moderate amplitude, if determined for optimization times shorter than a wave period, show propagation characteristics with respect to the gravity wave, which differ from that of the leading NMs. The latter propagate preferentially in the  $x - z$  plane while the former generally favor transverse propagation. Calculations of mean growth from random perturbations indicate just this behavior, which could not be explained with the help of NMs.

Thirdly, the leading SVs of the examined HGWs differ structurally in an interesting manner from the identified NMs. Initially, they have the form of sharply peaked pulses which are nearly immobile in the geostationary reference frame. In its passage over its SVs a HGW repeatedly invigorates the perturbations as they get into contact with suitable buoyancy and velocity gradients in the wave. In the long run the SV structure is often transformed into the broader structure of the leading NM, which moves with the wave phase, but this transition is typically a very long process. Thus, although eventually the leading NM might take over, SVs seem to highlight the possibility of rapid growth of *local* perturbations, which might get strong enough to initialize turbulence onset before the leading broader NM has had time to develop from a SV. Certainly this does depend on the specific initial perturbation encountered by a HGW in the real atmosphere (or ocean).

## Part III

### Nonlinear dynamics



# Chapter 6

## Monochromatic inertia-gravity waves

Chapters 4 and 5 seem to support the view that SVs might be a relevant factor in the dynamics of turbulence excitation by GWs. A conclusive statement, however, is not possible on the linear level. For a full assessment one needs investigations of the nonlinear dynamics of these perturbations. Also the turbulence impact on the basic GW must to be estimated. Related numerical studies of the nonlinear GW breaking process have traditionally resorted to simulations with either excessive viscosity or a sub-grid-scale scheme for the parameterization of the smallest turbulent scales. (Winters and D’Asaro, 1994; Andreassen et al., 1994; Fritts et al., 1994; Isler et al., 1994; Lelong and Dunkerton, 1998a,b). Direct numerical simulations (DNS) with their least ambiguous results on the corresponding turbulence dynamics have only recently become possible (Fritts et al., 2003, 2006). While a DNS of wave breaking initialized by purely random perturbations, as done in these studies, sheds light on some aspects of the process, an alternative, conceptually as interesting, approach seems to be the direct study of the nonlinear interaction between a gravity wave and its leading NMs or SVs. Such studies might promote additional insight into the process by identifying its most paradigmatic features. Corresponding DNS are discussed in the following two chapters. Given their obviously different dynamics, IGWs and HGWs are examined separately. This chapter looks at the IGW case, while HGWs perturbed by their leading NMs or SVs are discussed in chapter 7.

A study of the nonlinear dynamics of an IGW packet would have to deal with especially large model volumes encompassing the whole wave packet. The computational

costs of such calculations would be especially high. Moreover, the comparative conceptual simplicity of a monochromatic IGW in itself also argues for first studying the nonlinear dynamics of such a wave after being perturbed by its leading SVs or NMs. The present chapter therefore focuses on this type of scenario. Interestingly, the corresponding nonlinear development has not really been looked at yet in a DNS. Among the three studies coming nearest to this, Lelong and Dunkerton (1998a,b), on the one hand, have simulated IGW breaking in a large-eddy simulation without explicit treatment of the turbulent scales. In addition, they have used a ratio  $f/N$  between inertial and Brunt-Vaisala frequency which exceeds typical values for the MLT by about an order of magnitude. Fritts et al. (2003), on the other hand, have treated either the case of HGW breaking or the instability of a simple shear layer, thus not including possible effects of the elliptic polarization of the IGW velocity field. The study in this chapter has the intent of going a step farther towards the simulation of the nonlinear development of an IGW perturbed by either NMs or SVs. Major points of interest are the change of the IGW amplitude, the energy exchange between IGW and perturbation, the distribution of perturbation energy between the various dynamical fields in question, its spatial distribution, and the strength and distribution of the occurring turbulent dissipation rates.

## 6.1 Model setup

As above the equations used are the Boussinesq equations (2.1) – (2.3) on an  $f$  plane. For viscosity and thermal diffusivity the typical upper-mesospheric values  $\nu = \mu = 1\text{m}^2/\text{s}$  are taken. The  $f$  plane is located at  $70^\circ$  latitude. The Brunt-Vaisala frequency is  $N = 2 \cdot 10^{-2}\text{s}^{-1}$ . Again following Mied (1976) and Drazin (1977) a coordinate system is introduced in which the representation of the basic GW is especially simple. It is obtained by a rotation about the  $y$ -axis so that the new vertical coordinate points in the direction of the wavenumber vector, a translation along this axis with the phase velocity, and a rescaling of the vertical axis in units of the wave phase (see also Fig. 2.1). The new coordinates  $(\xi, \phi)$  are determined from  $x$ ,  $z$ , and  $t$  via (2.8) and (2.9), while  $y$  is not modified.

Since the GW is symmetric with respect to the "horizontal" directions  $\xi$  and  $y$ , we

obtained in chapter 5 NMs and SVs for each combination of corresponding wavenumbers. These perturbations have the form  $(\mathbf{v}', b') = \Re \left\{ \left( \hat{\mathbf{v}}, \hat{b} \right) (\phi, t) \exp [i (\kappa \xi + \lambda y)] \right\}$  with  $(\kappa, \lambda) = k_{\parallel} (\cos \alpha, \sin \alpha)$  being the horizontal wave-vector components.  $\lambda_{\parallel} = 2\pi/k_{\parallel}$  and  $\alpha$  are the corresponding horizontal wavelength and the azimuth angle between  $(\kappa, \lambda)$  and the  $\xi$ -axis. In the simulations reported here the initial state for the nonlinear model is always obtained by a superposition of the GW and the state of one of the linear NMs or SVs at  $t = 0$ . It is symmetric with respect to the direction in the  $\xi - y$  plane transverse to the direction of propagation of the perturbation, and the model equations conserve this symmetry. It therefore makes sense to introduce a horizontally rotated system of coordinates (see also chapter 5)

$$(x_{\parallel}, y_{\perp}) = (\xi \cos \alpha + y \sin \alpha, -\xi \sin \alpha + y \cos \alpha) \quad (6.1)$$

respectively pointing in the directions parallel and transverse to the direction of the horizontal wavenumber vector of the perturbation. In this representation the Boussinesq equations take the form

$$\frac{\partial u_{\parallel}}{\partial x_{\parallel}} + \frac{\partial v_{\perp}}{\partial y_{\perp}} + K \frac{\partial u_{\phi}}{\partial \phi} = 0 \quad (6.2)$$

$$\frac{Du_{\parallel}}{Dt} - f (\sin \Theta v_{\perp} - \sin \alpha \cos \Theta u_{\phi}) + \frac{\partial p}{\partial x_{\parallel}} + b \cos \alpha \cos \Theta = \nu \nabla^2 u_{\parallel} \quad (6.3)$$

$$\frac{Dv_{\perp}}{Dt} + f (\sin \Theta u_{\parallel} + \cos \alpha \cos \Theta u_{\phi}) + \frac{\partial p}{\partial y_{\perp}} - b \sin \alpha \cos \Theta = \nu \nabla^2 v_{\perp} \quad (6.4)$$

$$\frac{Du_{\phi}}{Dt} - f (\sin \alpha \cos \Theta u_{\parallel} + \cos \alpha \cos \Theta v_{\perp}) + K \frac{\partial p}{\partial \phi} - b \sin \Theta = \nu \nabla^2 u_{\phi} \quad (6.5)$$

$$\frac{Db}{Dt} + N^2 \underbrace{\left( -\cos \alpha \cos \Theta u_{\parallel} + \sin \alpha \cos \Theta v_{\perp} + \sin \Theta u_{\phi} \right)}_w = \mu \nabla^2 b \quad , \quad (6.6)$$

where  $(u_{\parallel}, v_{\perp})$  are the velocity components corresponding to  $(x_{\parallel}, y_{\perp})$ , and  $D/Dt = \partial/\partial t + \mathbf{v} \cdot \nabla - \Omega \partial/\partial \phi$ . This representation, up to the last rotation (6.1) identical to the one also used by Fritts et al. (2003, 2006), seems to be best suited for a study of the breaking of a monochromatic gravity wave, so that it provides the framework for the simulations reported here.

For a numerical treatment the model equations have been discretized, as above in the linear studies, on a standard staggered C-grid, as discussed e.g. in Durran (1999), with

$\Theta/^\circ$	$a$	$\Lambda/\text{km}$	perturbation type	$\tau/\text{min}$	$\alpha/^\circ$	$\lambda_{\parallel}/\text{km}$	$n_{\parallel}$	$n_{\phi}$
89.5	1.20	6	SV	5	0	0.398	144	2304
89.5	1.20	6	SV	5	90	3.981	2304	2304
89.5	1.20	6	NM	–	0	0.501	288	2304
89.5	1.20	6	NM	–	90	7.943	4608	2304
89.5	0.87	6	SV	5	0	0.631	288	2304
89.5	0.87	6	SV	5	90	3.162	1152	2304
89.5	0.87	6	SV	30	0	7.943	4608	2304
89.5	0.87	6	SV	30	90	5.012	2304	2304

Table 6.1: Model extent  $\lambda_{\parallel}$  in the horizontal and  $\Lambda$  in IGW-phase direction, as well as the corresponding number of grid points  $n_{\parallel}$  and  $n_{\phi}$ , for all discussed integrations of an IGW (with an amplitude  $a$  with respect to the overturning limit) perturbed by either its leading SV (for optimization time  $\tau$ ) or NM at the azimuth angle  $\alpha$ .  $\Lambda$  is also the IGW wavelength, while  $\lambda_{\parallel}$  agrees with the horizontal wavelength of the respective perturbations.  $\Theta$  is the inclination angle between the IGW wave vector and the horizontal.

periodic boundary conditions. The model domain extends from 0 to  $2\pi$  in  $\phi$  and 0 to  $\lambda_{\parallel}$  in  $x_{\parallel}$ . Consistent with the here chosen initial states there is no dependence on  $y_{\perp}$ . The model might be called 2.5D since it describes buoyancy and a 3D velocity field depending on two spatial coordinates. It also differs from standard 2D simulations in that it can also handle cases with  $\alpha \neq 0$ . Pressure is obtained by applying the divergence to the momentum equations and solving the resulting Poisson equation by a Fourier transform technique. The equations are integrated using a third-order Runge-Kutta time step (Durrant, 1999). The model resolution was always chosen fine enough to resolve both the inertial and the viscous subrange of the resulting turbulence spectra. As in chapter 5, the wavelength and the inclination angle of the considered IGW are  $(\Lambda, \Theta) = (6\text{km}, 89.5^\circ)$ . Details are provided in table 6.1.

## 6.2 Energetics

Since the basic IGW is horizontally symmetric (i.e. with respect to  $x_{\parallel}$  and  $y_{\perp}$ ) it seems helpful to analyze the interaction between IGW and perturbation in terms of the energy exchange between the horizontal mean  $(\bar{\mathbf{v}}, \bar{b})$  and the horizontally-dependent deviations  $(\mathbf{v}', b') = (\mathbf{v}, b) - (\bar{\mathbf{v}}, \bar{b})$  (for simplicity henceforth called "eddy" part). It is a standard procedure to derive from (6.2)–(6.6) the following budget equations for the kinetic energy densities  $\bar{K} = |\bar{\mathbf{v}}|^2/2$  and  $K' = |\mathbf{v}'|^2/2$  and the densities of available potential energy  $\bar{A} = \bar{b}^2/2N^2$  and  $A' = b'^2/2N^2$ :

$$\frac{\partial \bar{K}}{\partial t} + K \frac{\partial}{\partial \phi} \left[ (\bar{u}_{\phi} - c) \bar{K} + \bar{\mathbf{v}} \cdot \overline{u'_{\phi} \mathbf{v}'} + \bar{u}_{\phi} \bar{p} - \nu K \frac{\partial \bar{K}}{\partial \phi} \right] = \bar{w} \bar{b} - P_S - \bar{\epsilon} \quad (6.7)$$

$$\frac{\partial K'}{\partial t} + K \frac{\partial}{\partial \phi} \left[ (\bar{u}_{\phi} - c) K' + \overline{u'_{\phi} \frac{|\mathbf{v}'|^2}{2}} + \overline{u'_{\phi} p'} - 2\nu \overline{v'_i S'_{i3}} \right] = \overline{w' b'} + P_S - \epsilon' \quad (6.8)$$

$$\frac{\partial \bar{A}}{\partial t} + K \frac{\partial}{\partial \phi} \left[ (\bar{u}_{\phi} - c) \bar{A} + \frac{\bar{b}}{N^2} \overline{u'_{\phi} b'} - \mu K \frac{\partial \bar{A}}{\partial \phi} \right] = -\bar{w} \bar{b} - C - \bar{D} \quad (6.9)$$

$$\frac{\partial A'}{\partial t} + K \frac{\partial}{\partial \phi} \left[ (\bar{u}_{\phi} - c) A' + \overline{u'_{\phi} \frac{b'^2}{2N^2}} - \mu K \frac{\partial A'}{\partial \phi} \right] = -\overline{w' b'} + C - D'. \quad (6.10)$$

The equations are obviously related to (5.8), but they split up the eddy energy tendencies into those of kinetic and available potential energy, see also (4.55) – (4.65), and also describe the energetic eddy feedback on the horizontal mean. The contributing terms on the right-hand sides are the shear production of eddy kinetic energy  $P_S = -\overline{u'_{\phi} \mathbf{v}} \cdot (K \partial \bar{\mathbf{v}} / \partial \phi)$ , the convective production of eddy available potential energy  $C = -\overline{u'_{\phi} b'} (K/N^2) \partial \bar{b} / \partial \phi$ , the dissipation of horizontal-mean kinetic energy  $\bar{\epsilon} = 2\nu \bar{S}_{ij} \bar{S}_{ij}$  (summing as usual over all double indices), the eddy dissipation  $\epsilon' = 2\nu \overline{S'_{ij} S'_{ij}}$ , the diffusive losses of horizontal-mean available potential energy  $\bar{D} = (\mu/N^2) K^2 |\partial \bar{b} / \partial \phi|^2$ , and the diffusive losses of the eddy available potential energy  $D' = (\mu/N^2) \overline{|\nabla b'|^2}$ . With the notations  $(x_1, x_2, x_3) = (x_{\parallel}, y_{\perp}, \phi/K)$  and  $(v_1, v_2, v_3) = (u_{\parallel}, v_{\perp}, u_{\phi})$  the shear-stress tensors are defined as  $\bar{S}_{ij} = (\partial \bar{v}_i / \partial x_j + \partial \bar{v}_j / \partial x_i) / 2$  and  $S'_{ij} = (\partial v'_i / \partial x_j + \partial v'_j / \partial x_i) / 2$ . The divergence terms on the left-hand sides of (6.7)–(6.10) serve to redistribute energy between different GW-phase locations, but they do not contribute to the budget of the mean of all reservoirs in phase direction. In fact even many of the results below on the development of the  $\phi$ –dependence of the four energies can be understood without resorting to these

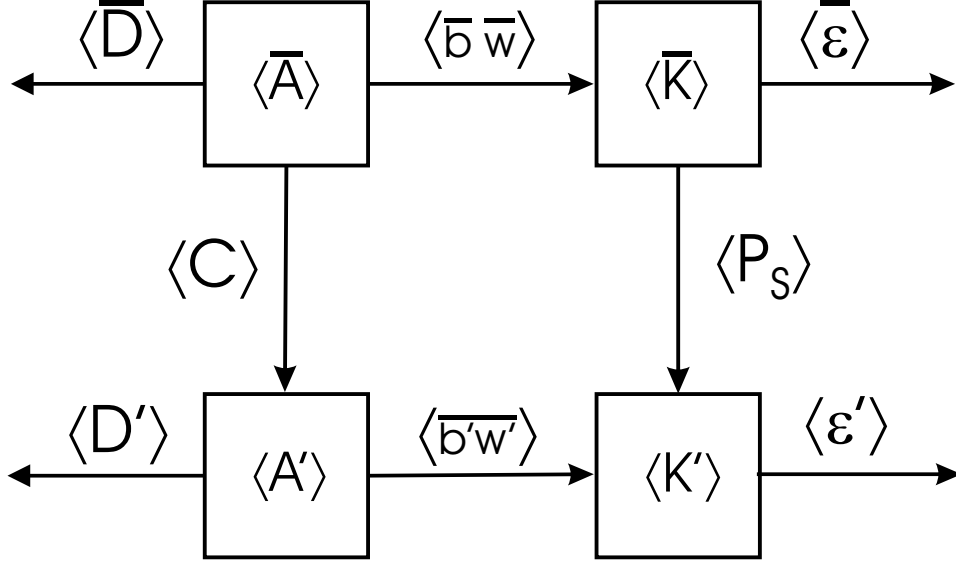


Figure 6.1: The budget for the exchange between the GW-phase averaged available potential energy  $A$  and kinetic energy  $K$  of the "horizontal" mean (denoted by an overbar, "vertical" meaning parallel to the direction of the GW wave vector) and the deviations from this mean (the eddies, denoted by a prime). For an explanation of the contributing terms see the main text.

terms. A graphic visualization of the energy cycle is given in Fig. 6.1. There  $\langle \bar{K} \rangle$  denotes e.g. the mean of  $\bar{K}$  over  $\phi$ , and likewise for all other quantities.

From the definitions of  $P_S$  and  $C$  one can derive for the total eddy energy  $E' = A' + K'$  the tendency  $\partial \langle E' \rangle / \partial t = 2\Gamma \langle E' \rangle$  with an instantaneous amplification rate  $\Gamma = \Gamma_{\parallel} + \Gamma_{\perp} + \Gamma_b + \Gamma_d$  where the amplification-rate parts

$$\begin{aligned} (\Gamma_{\parallel}, \Gamma_{\perp}, \Gamma_b, \Gamma_d) &= \langle \gamma_{\parallel}, \gamma_{\perp}, \gamma_b, \gamma_d \rangle \\ &= -\langle \overline{u'_{\phi} u'_{\parallel}} K \frac{\partial \bar{u}_{\parallel}}{\partial \phi}, \overline{u'_{\phi} v'_{\perp}} K \frac{\partial \bar{v}_{\perp}}{\partial \phi}, \overline{u'_{\phi} b'} \frac{K}{N^2} \frac{\partial \bar{b}}{\partial \phi}, D' + \epsilon' \rangle / 2\langle E' \rangle, \end{aligned} \quad (6.11)$$

as in the in the linear dynamics (chapter 5), describe consecutively the impact of the eddy fluxes of momentum in  $x_{\parallel}$ - and  $y_{\perp}$ -direction against the corresponding gradients in the horizontal mean, as well as the effect of the counter-gradient buoyancy fluxes and of diffusive and viscous damping. The relative strengths of  $\Gamma_{\parallel}$ ,  $\Gamma_{\perp}$ , and  $\Gamma_b$  tell us, in close analogy to the linear case, which part of the gain (or loss) of  $\langle E' \rangle$  can be attributed to respective direct changes in  $\langle K'_{\parallel} \rangle = \langle \bar{u}_{\parallel}^2 / 2 \rangle$ ,  $\langle K'_{\perp} \rangle = \langle \bar{v}_{\perp}^2 / 2 \rangle$ , and  $\langle A' \rangle$ . The

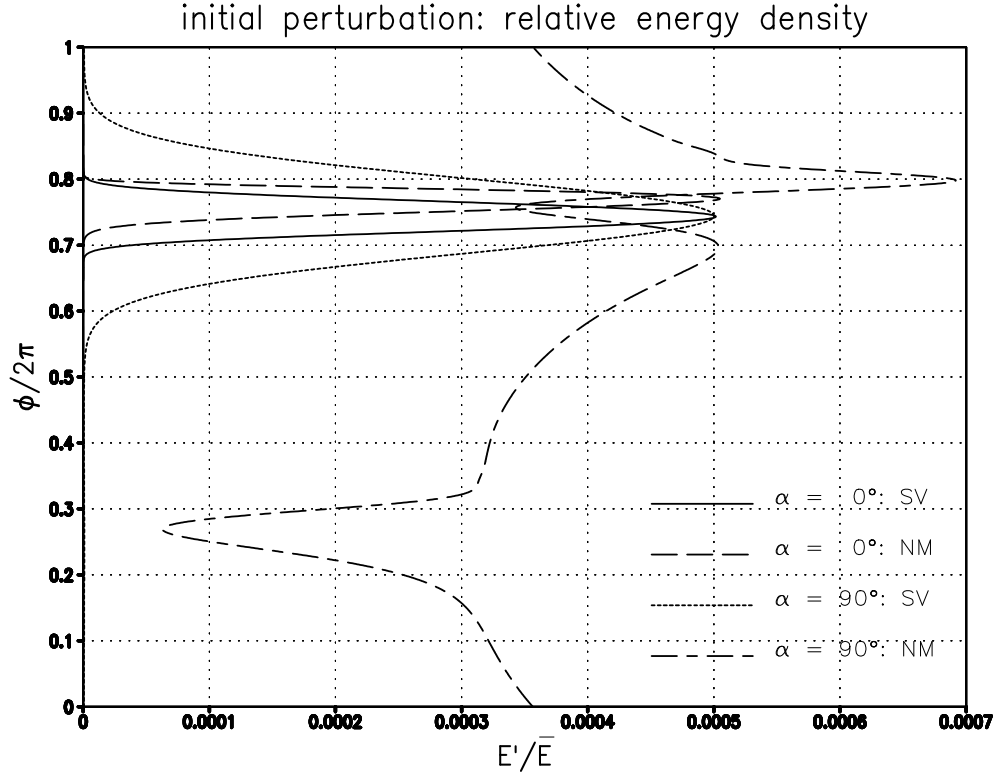


Figure 6.2: For the statically unstable IGW ( $a = 1.2$ ) with  $(\Theta, \Lambda) = (89.5^\circ, 6\text{km})$ , the initial perturbation energy density of the leading NMs and short-term SVs at azimuth angles  $\alpha = 0, 90^\circ$ , normalized by the spatially independent energy density  $\bar{E}$  of the IGW. All four perturbations have a local peak energy density  $\max_{x_\parallel, \phi} e' = 10^{-3}\bar{E}$ .

respective contributions to  $\overline{b'w'}/\langle 2E' \rangle$ , i.e.  $-\cos \alpha \cos \Theta \overline{u'_\parallel b'}/\langle 2E' \rangle$ ,  $\sin \alpha \cos \Theta \overline{v'_\perp b'}/\langle 2E' \rangle$ , and  $\sin \Theta \overline{u'_\phi b'}/\langle 2E' \rangle$ , indicate buoyant transfer from  $\langle A' \rangle$  to  $\langle K'_\parallel \rangle$ ,  $\langle K'_\perp \rangle$ , and  $\langle K'_\phi \rangle = \langle \overline{u_\phi^2}/2 \rangle$ . In the IGW case where  $(\cos \Theta, \sin \Theta) \approx (0, 1)$  buoyant exchange occurs mainly between  $A'$  and  $\langle K'_\phi \rangle \approx \langle \overline{w'^2}/2 \rangle$ .

### 6.3 NMs and SVs of a statically unstable IGW

The first set of experiments is meant to give an overview of the dynamics of modal and nonmodal perturbations of statically unstable IGWs. For this the NMs and short-term SVs ( $\tau = 300\text{s}$ ) of an IGW with  $a = 1.2$  were used to perturb that wave. The IGW period is  $P = 2\pi/\Omega \approx 7.87\text{h} \approx 94\tau$ . Among the multitude of possible NMs and SVs the

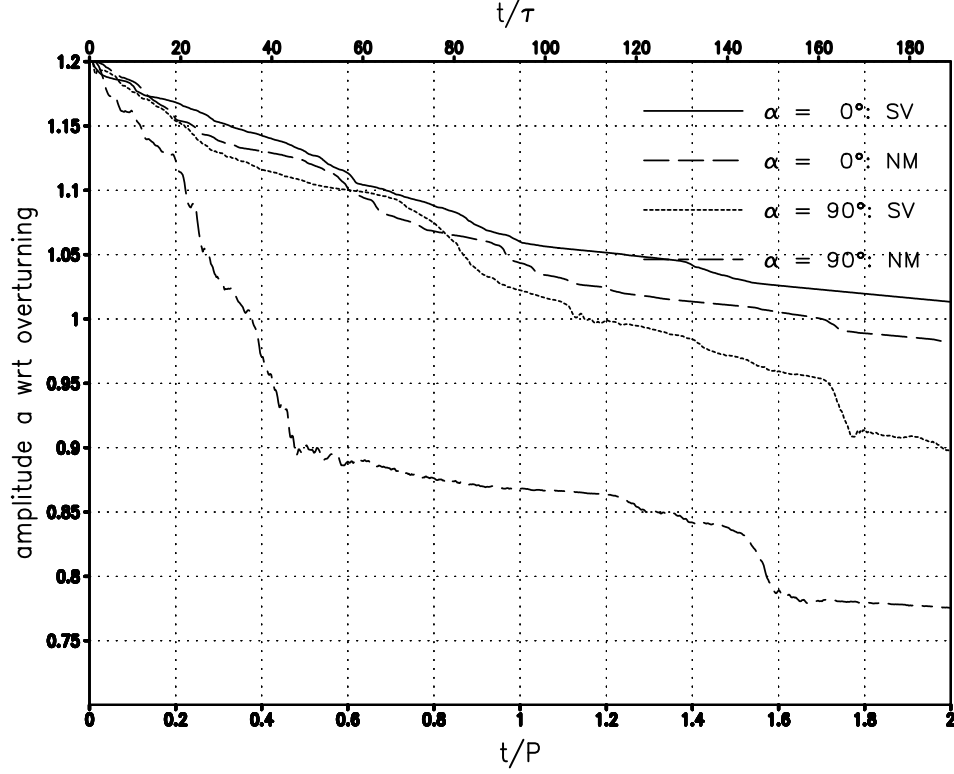


Figure 6.3: For the statically unstable IGW ( $a = 1.2$ ) with  $(\Theta, \Lambda) = (89.5^\circ, 6\text{km})$ , perturbed by the leading NMs and short-term SVs (optimization time  $\tau = 300\text{s}$ ) at azimuth angles  $\alpha = 0, 90^\circ$  with an initial local peak energy density  $\max_{x_{\parallel}, \phi} e' = 10^{-3} \bar{E}$  (see also Fig. 6.2), the time-dependent IGW amplitude  $a$  with respect to the overturning threshold. The IGW period is  $P = 7.87\text{h}$ .

leading structures at azimuth angle  $\alpha = 0, 90^\circ$  were taken since, as shown in chapters 4 and 5, they represent limit cases of the range of possible angles, while the NMs and SVs at intermediate azimuth angles ( $0^\circ < \alpha < 90^\circ$ ) show a kind of transitional behavior between these two. A choice had to be made concerning the perturbation amplitudes. The final decision was to choose an amplitude characterizing the peak strength of the energy density  $e'(x_{\parallel}, \phi) = (u_{\parallel}^2 + v_{\perp}^2 + u_{\phi}^2 + b^2/N^2)/2$  in relation to the corresponding energy density of the IGW. From (2.10) – (2.13) one can see that the latter is uniform and identical to  $\bar{E} = \bar{K} + \bar{A}$  at  $t = 0$ , which is  $\bar{E}(t = 0) = (a^2/2) c^2 / (\sin \Theta \cos \Theta)^2$ .  $c = \Omega/K$  is the IGW phase velocity. In all cases reported here the initial ratio  $\max_{x_{\parallel}, \phi} (e') / \bar{E}$  is  $10^{-3}$ , ensuring an initial behavior in agreement with the linear theory.



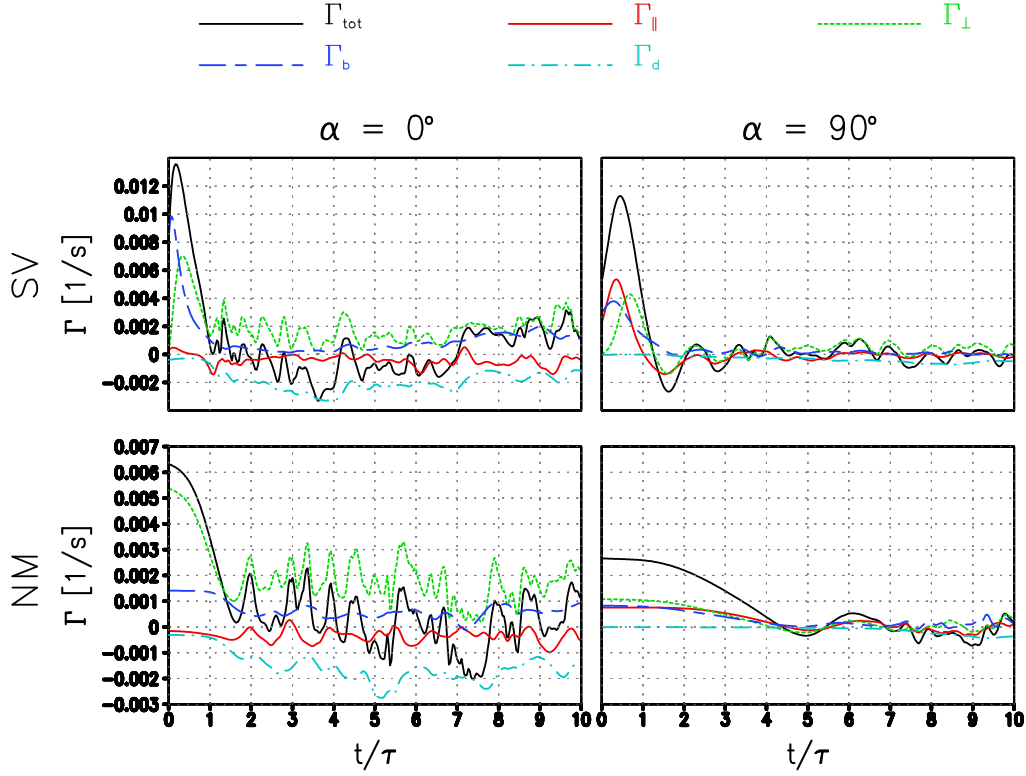


Figure 6.4: For the initial time span  $0 \leq t \leq 10\tau$  of the integrations shown in Fig. 6.3 (left and right column for  $\alpha = 0^\circ$  and  $90^\circ$ , top and bottom row for SV and NM), the time development of the instantaneous amplification-rate decomposition.

Figure 6.2 shows the corresponding ratios  $E'/\bar{E}$  at  $t = 0$ . While the three other perturbations are confined to the phase range near  $\phi = 3\pi/2$ , i.e. the statically most unstable region, the leading NM at  $\alpha = 90^\circ$  is quite smoothly spread over the whole range of IGW phases and, although it has the same peak energy as the other SVs and NM, its horizontal-mean energy  $E'$  is larger. As a consequence this pattern exhibits the largest fluxes and thus also the strongest interaction with the IGW. For an analysis of the eddy impact on the IGW the horizontal mean has been projected onto that wave via the procedure described in appendix D. Figure 6.3 shows for all four integrations the decay in the IGW amplitude  $a$  with respect to the overturning threshold. By far the fastest decay is obtained after a perturbation by the leading transverse NM. This has to be put into contrast with the growth factors the four patterns have according to the linear theory between  $t = 0$  and  $t = \tau$ , where the NM at  $\alpha = 90^\circ$  shows the least vigorous behavior.

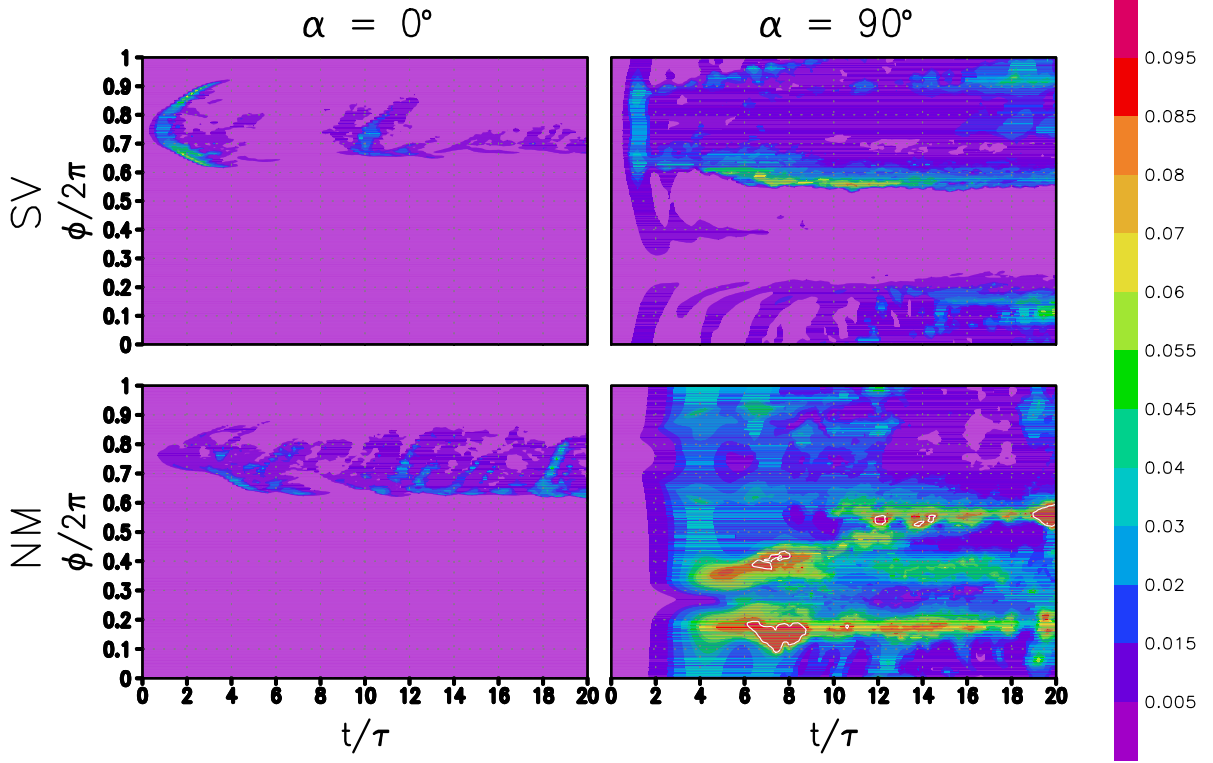


Figure 6.5: For the initial time span  $0 \leq t \leq 20\tau$  of the integrations shown in Figs. 6.3 and 6.4, the time development of the dependence of the eddy energy on the IGW phase. All plots show normalized values  $E'/\overline{E}(t=0)$ . The shading scale in all four panels is identical. The contour interval is 0.1, starting at 0.1.

An interesting feature in the development of the contributions to the total eddy energy, i.e.  $\langle K'_\perp \rangle$ ,  $\langle K'_\parallel \rangle$ ,  $\langle K'_\phi \rangle$ , and  $\langle A' \rangle$  (not shown), is that in all cases but the one of the NM at  $\alpha = 90^\circ$  the dominating term is  $\langle K'_\perp \rangle$ . This is consistent with the time dependence of the amplification-rate decomposition shown in Fig. 6.4 for  $0 \leq t \leq 10\tau$ . For the three cases one sees the later phase to be dominated by a balance between energy gain due to the counter-gradient flux of  $v_\perp$  and viscous-diffusive losses. This is in agreement with predictions from the linear theory in chapters 4 and 5 where the corresponding statically enhanced roll mechanism always shows up as a strong energy source. A further agreement with the linear theory is visible in the energetics for  $0 \leq t \leq \tau$  where the transient behavior with strong peak amplification rates is visible for the SVs, and a nearly constant amplification-rate decomposition for the NMs. Also the details agree with those

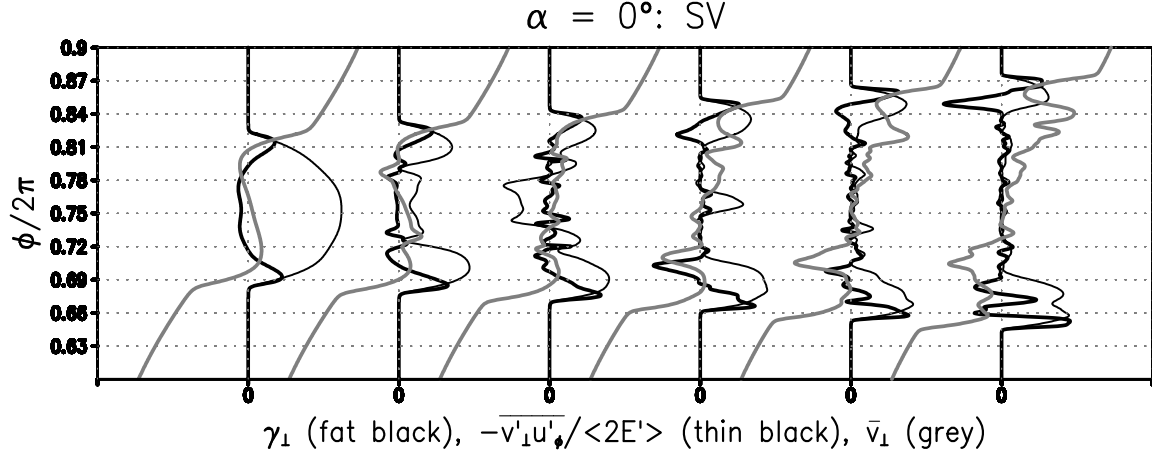


Figure 6.6: From the integration of the statically unstable IGW ( $a = 1.2$ ) perturbed by its leading short-term SV at  $\alpha = 0^\circ$ , for the time between (from left to right)  $t = \tau$  and  $t = 2\tau$  in steps of  $0.2\tau$ , the instantaneous IGW-phase-dependent amplification-rate contribution  $\gamma_\perp$  (fat black line) from eddy fluxes  $\overline{v'_\perp u'_\phi}$  (normalized negative, thin black line) of  $v_\perp$  against the phase-gradient in the horizontal-mean  $\bar{v}_\perp$  (grey line). All quantities have been re-scaled to make them fit into one graph. Only the relevant phase range  $0.6 \leq \phi/2\pi \leq 0.9$  is shown.

predictions: Initially the growth of both SVs is triggered by the buoyant exchange, later followed by growth due to  $\Gamma_\perp$  (statically enhanced roll mechanism) for  $\alpha = 0^\circ$  and growth due to  $\Gamma_\parallel$  for  $\alpha = 90^\circ$ , as in a statically enhanced Orr mechanism. In the latter case finally the roll mechanism also takes over, as is also in agreement with the linear theory.

### 6.3.1 Parallel modes ( $\alpha = 0^\circ$ )

Consistent with the initial distribution (Fig. 6.2) the eddy energy density in the two cases for  $\alpha = 0^\circ$  (left column of Fig. 6.5) stays more or less confined to the most unstable phase range, while splitting up into two peaks which are gradually moving away from  $\phi = 3\pi/2$ . The mechanism behind this is illustrated for the SV at  $\alpha = 0^\circ$  in Fig. 6.6. One sees there  $\gamma_\perp$  and its two contributors, i.e. the counter-gradient flux  $-\overline{u'_\phi v'_\perp}$  and  $\bar{v}_\perp$  (the latter entering into  $\gamma_\perp$  via its phase gradient). By  $t = \tau$  the fluxes have reversed the gradient of the horizontal mean, leading to a damping of the perturbation in the innermost part of the active region. The reversal of the internal gradient, however, has also led to an

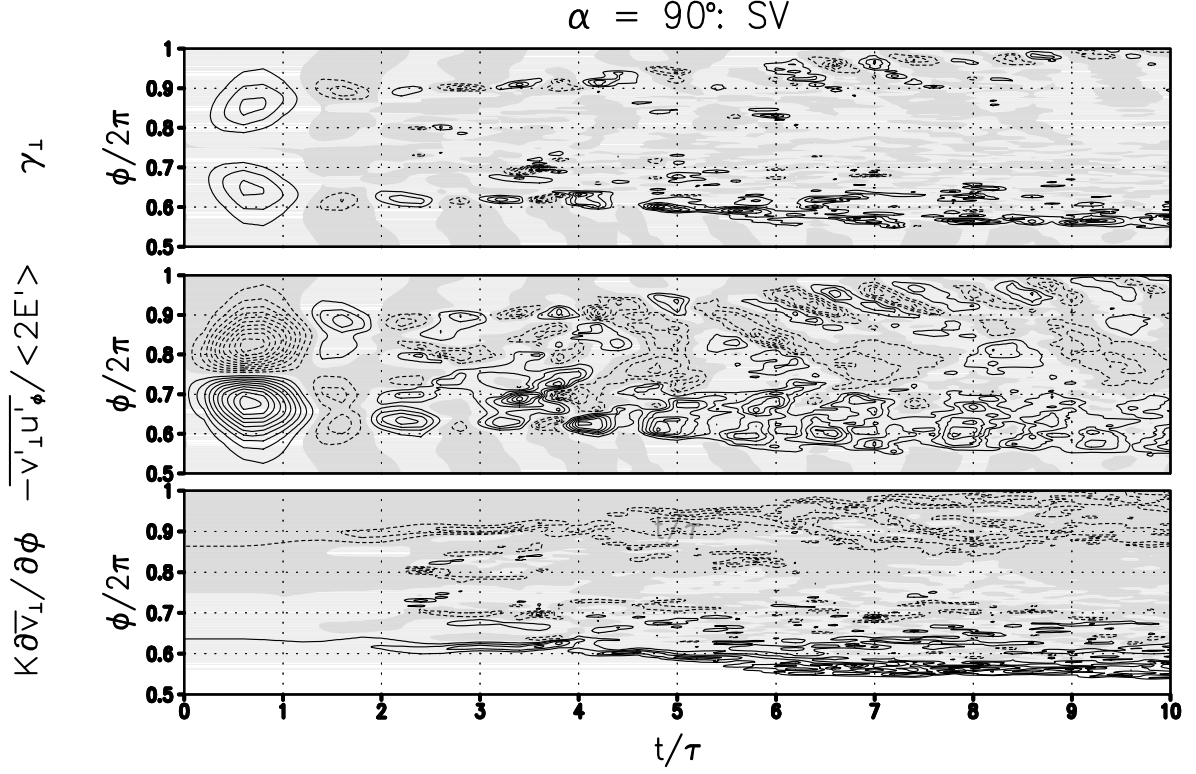


Figure 6.7: From the integration of the statically unstable IGW ( $a = 1.2$ ) perturbed by its leading short-term SV at  $\alpha = 90^\circ$ , the time dependence of  $\gamma_\perp$  (top panel, contour interval  $5 \cdot 10^{-3} \text{s}^{-1}$ ) and its contributing factors, i.e. the normalized counter-gradient flux  $-\overline{u'_\phi v'_\perp} / \langle 2E' \rangle$  (middle, contour interval 0.1) and the phase-gradient  $K \partial \bar{v}_\perp / \partial \phi$  (bottom, contour interval  $2 \cdot 10^{-2} \text{s}^{-1}$ ). In all panels negative values are indicated by dashed contours and shading, and the zero contour has not been drawn. Only the phase range  $0.5 \leq \phi/2\pi \leq 1$  is shown.

increased gradient at the edges of the active region, so that there the perturbation can continue to grow. By  $t = 1.2\tau$  it has thus led to small subregions on the internal side of the edges of the active regions where the same repeats itself on a smaller scale. At the same time the momentum fluxes, damped in the internal region, but further excited on the outside, push the increased gradients at the edges farther out. This process continues, and thus leads to the energy-density distribution observed in Fig. 6.5. At a later phase the fluxes have reduced the gradients in  $\bar{v}_\perp$  enough so that the growth in eddy energy is stalled. Even later, however, it bursts up again (near  $t = 9\tau$ , e.g.). A closer analysis can

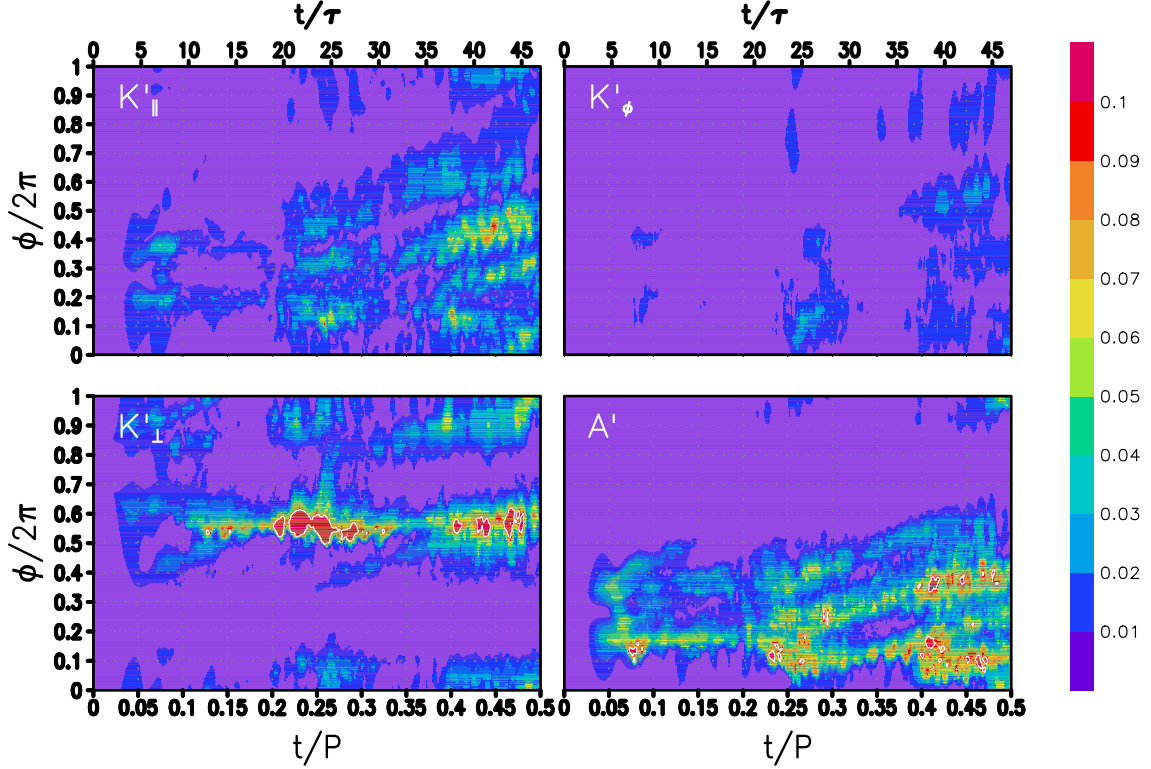


Figure 6.8: From the integration of the statically unstable IGW ( $a = 1.2$ ) and its leading NM at  $\alpha = 90^\circ$ , the time dependence of the four eddy energy densities  $K'_{||}$ ,  $K'_\perp$ ,  $K'_\phi$ , and  $A'$ . Shown are relative values with respect to the initial IGW energy density. The shading scale in all four panels is the same. The contour indicates regions where the relative energy density is larger than 0.1.

explain this in terms of partially reorganized gradients  $\partial \bar{v}_\perp / \partial \phi$  allowing stronger transient (i.e. optimal) growth of perturbations there (not shown). The NM at  $\alpha = 0^\circ$  turns out to be similar in behavior.

### 6.3.2 Transverse modes ( $\alpha = 90^\circ$ )

As already in its linear dynamics the SV at  $\alpha = 90^\circ$  shows in its early development a behavior as in a statically enhanced Orr mechanism, where a combination of static instability and counter-gradient fluxes of  $u_{||}$  in the statically most unstable phase region triggers its growth. Later the perturbations radiate away into regions where  $\partial \bar{v}_\perp / \partial \phi \neq 0$  (see Fig. 6.5). As visible in Fig. 6.7, there a statically enhanced roll mechanism takes over

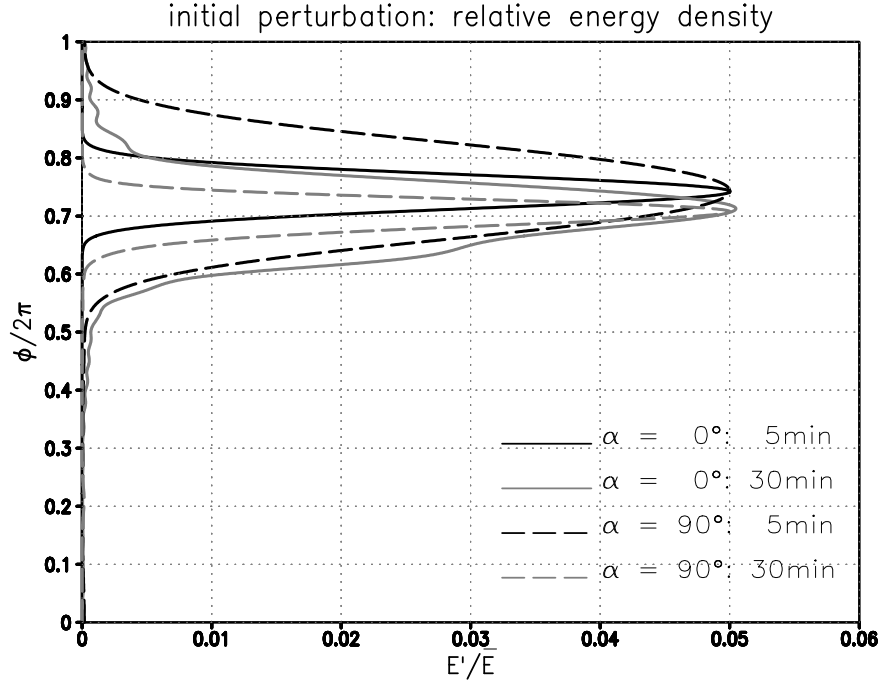


Figure 6.9: For the statically and dynamically stable IGW ( $a = 0.87$ , no unstable NM) at  $(\Theta, \Lambda) = (89.5^\circ, 6\text{km})$ , the initial perturbation energy density of the leading SVs at azimuth angles  $\alpha = 0, 90^\circ$  for the optimization times  $\tau = 5\text{min}$  and  $30\text{min}$ , normalized by the spatially independent energy density  $\bar{E}$  of the IGW. All four perturbations have a local peak energy density  $\max_{x_\parallel, \phi} e' = 10^{-1}\bar{E}$ .

and further amplifies the perturbation by the action of counter-gradient fluxes in  $v_\perp$ . Also here edges of increased gradients  $K\partial\bar{v}_\perp/\partial\phi$  form where the perturbation can experience further transient growth. Roughly between  $t = \tau$  and  $t = 5\tau$  one sees the fluxes  $\overline{u'_\phi v'_\perp}$  oscillating about a zero mean. This is consistent with a roll mechanism without feedback on the horizontal mean (see chapter 4). Seemingly in this phase the impact on  $\bar{v}_\perp$  is not strong enough to prevent this oscillation which later, at least at the lower edge, dies down in favor of a permanently positive  $\gamma_\perp$ . In the linear dynamics that mode also shows a critical-layer behavior near  $\phi = \pi/2$ . Although weakly discernible, it is not that important a process in the nonlinear development of the SV at the given initial amplitude.

At equal peak energy density the most vigorous, but also the most complex mode is the NM at  $\alpha = 90^\circ$ . This one is somewhat less dominated by the statically enhanced roll mechanism than the others. Figure 6.8 shows for  $0 \leq t \leq P/2$  the time and phase

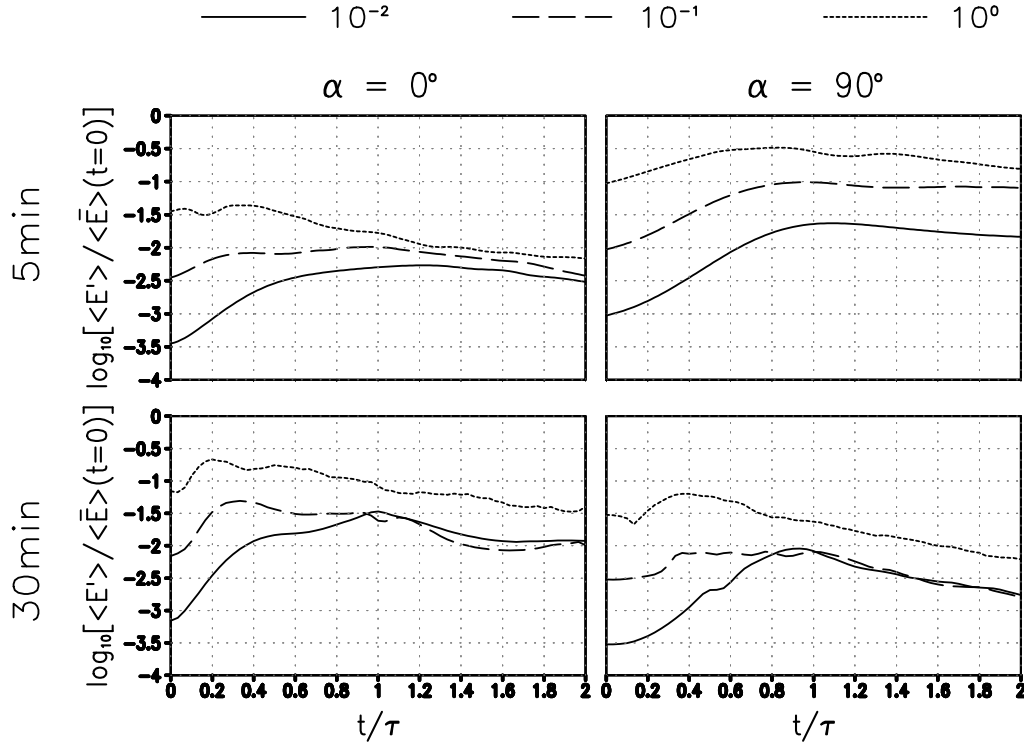


Figure 6.10: For the statically and dynamically stable IGW ( $a = 0.87$ , no unstable NM) at  $(\Theta, \Lambda) = (89.5^\circ, 6\text{km})$ , the time dependence of the eddy energy  $\langle E' \rangle$ , normalized by the initial IGW energy, from integrations after a perturbation by the leading SVs at azimuth angles  $\alpha = 0, 90^\circ$  (left and right column, respectively) for the optimization times  $\tau = 5\text{min}, 30\text{min}$  (top and bottom row, respectively), with initial relative perturbation amplitudes  $A_{\text{SV}}^2 = \max_{x_{\parallel}, \phi} e' / \bar{E} = 10^{-2}, 10^{-1}$ , and  $10^0$ .

dependence of the four contributing eddy energy densities, while Fig. 6.5 shows the total. Still, however, much of the eddy energy is in  $v'_\perp$  which maximizes near  $\phi = \pi$ . This is the region where for  $\alpha = 90^\circ$  the gradient  $\partial \bar{v}_\perp / \partial \phi$  in the original IGW is largest, so indeed also here one seems to see the roll mechanism at work. Another important term is the eddy available potential energy  $A'$  which gets large near  $\phi = \pi/2$ . This seems to be a case of a critical-layer interaction similar to the one found in the linear dynamics of the leading SV at  $\alpha = 90^\circ$  (see also chapters 4 and 5). This is further borne out by a comparison of the divergence terms in (6.10) with  $\partial A' / \partial t$  which exhibit a considerable resemblance (also not shown), indicating that radiation and thus nonlocal effects seem to play a role here.

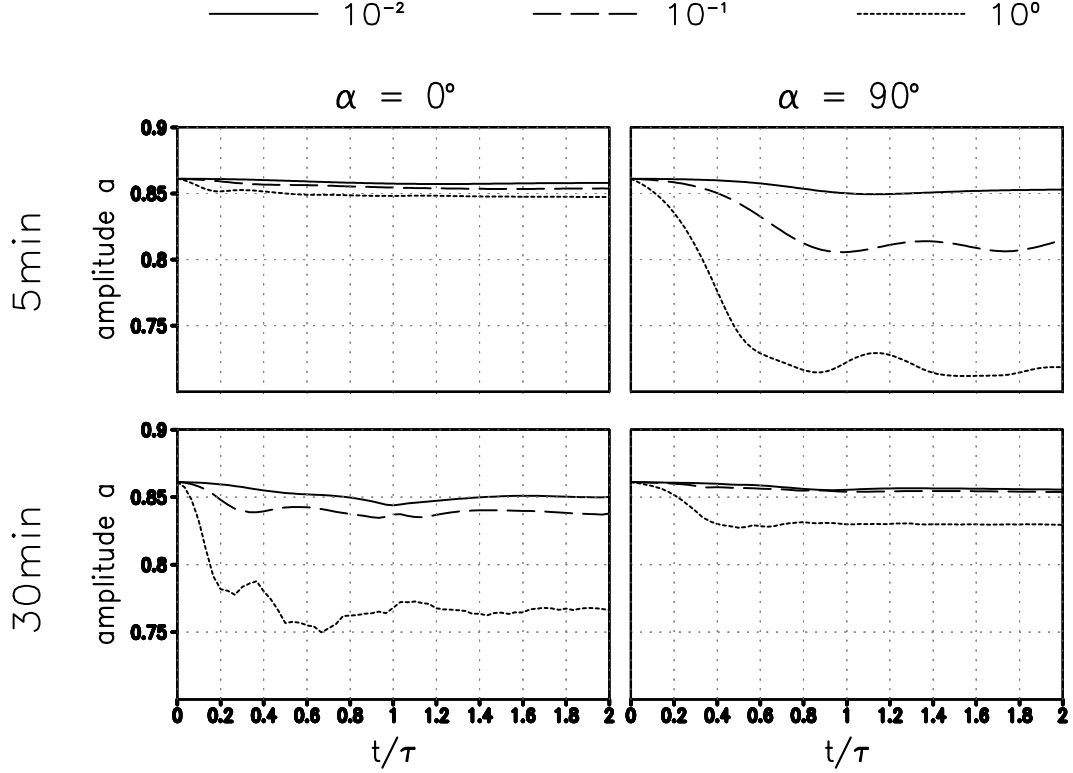


Figure 6.11: As Fig. 6.10, but now showing the time dependence of the IGW amplitude  $a$  with respect to the overturning threshold.

## 6.4 SVs of a statically stable IGW

The second set of experiments addresses the nonlinear dynamics of SVs for an IGW amplitude ( $a = 0.87$ ) precluding the existence of unstable NMs. Chapter 5 describes the linear dynamics of these SVs. It is shown that at an optimization time  $\tau = 5\text{min}$  the most strongly growing SV is at  $\alpha = 0^\circ$ , with a growth factor near 10, while the so-called global optimal, i.e. the most strongly growing SV for all optimization times, is found to be the SV for  $(\tau, \alpha) = (30\text{min}, 90^\circ)$ , with a growth factor near 20. Based on these results, here simulations are discussed where the IGW has been perturbed by its leading parallel ( $\alpha = 0^\circ$ ) and transverse ( $\alpha = 90^\circ$ ) SVs for  $\tau = 5\text{min}$  and  $30\text{min}$ . Given the finite growth factors one expects a purely linear behavior of these at very small initial amplitude but possibly nonlinear dynamics with feedback on the IGW at larger initial amplitude. For an overview integrations have been done with ratios between initial peak energy density and IGW energy density  $A_{\text{SV}}^2 = \max_{x_{\parallel}, \phi} (e') / \bar{E} = 10^{-2}, 10^{-1}$ , and  $10^0$ .



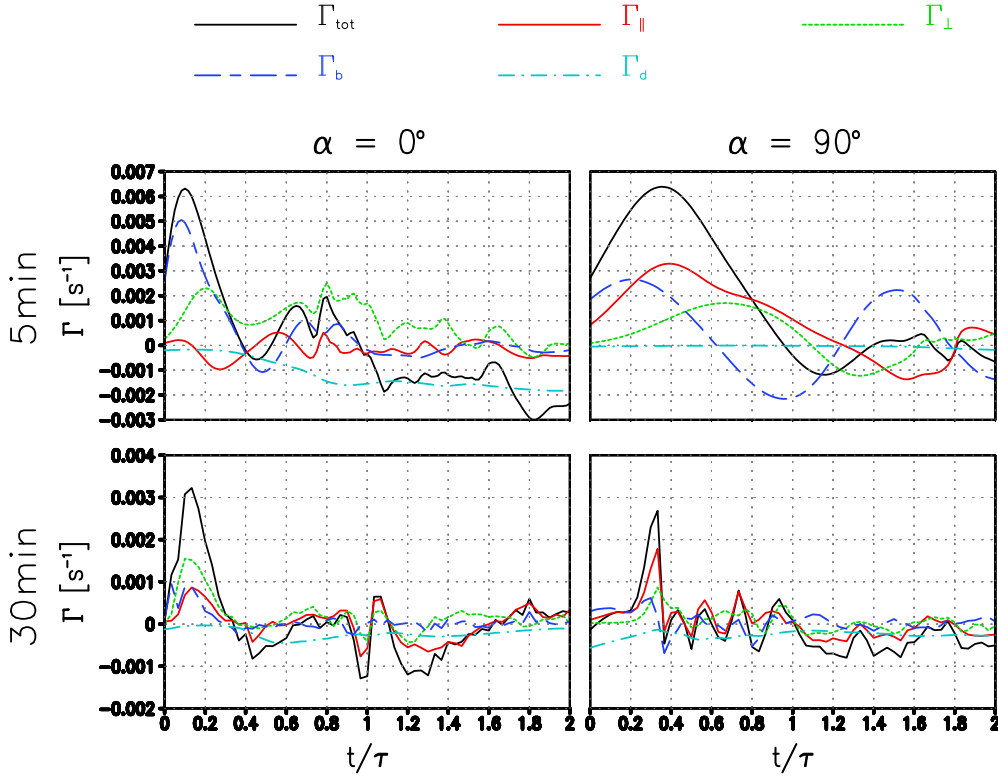


Figure 6.12: From to the integrations of the statically and dynamically stable IGW ( $a = 0.87$ , no unstable NM) perturbed by its leading SVs ( $\alpha = 0, 90^\circ$ ,  $\tau = 5\text{min}, 30\text{min}$ , in all cases the initial  $A_{\text{SV}}^2 = 10^{-1}$ ), the time development of the instantaneous amplification-rate decompositions.

For  $A_{\text{SV}}^2 = 10^{-1}$  the initial horizontal-mean energy density  $E'$  (normalized by  $\bar{E}$ ) of the SVs is shown in Fig. 6.9. As one sees they are all located near  $\phi = 3\pi/2$ . The broadest and most energetic structure is the SV for  $(\tau, \alpha) = (5\text{min}, 90^\circ)$ . Consistent with this, that SV has the strongest effect on the IGW. Figs. 6.10 and 6.11 show the time dependence of  $\langle E' \rangle$  and the IGW amplitude  $a$  for all integrations. One sees that larger  $A_{\text{SV}}^2$  imply a stronger decay in  $a$ , which can go as far down as 0.7, for the case of the SV for  $(\tau, \alpha) = (5\text{min}, 90^\circ)$  with an initial amplitude  $A_{\text{SV}}^2 = 10^0$ . That case also shows a sustained initial rise of  $\langle E' \rangle$  indicating linear behavior. For the other SVs such a strong initial amplitude leads, however, rather quickly to a decay of the eddy energy, showing that for these cases the initial SV amplitude is too large to allow an initial dynamics in agreement with the linear theory. One also sees that the initial growth phase gets longer

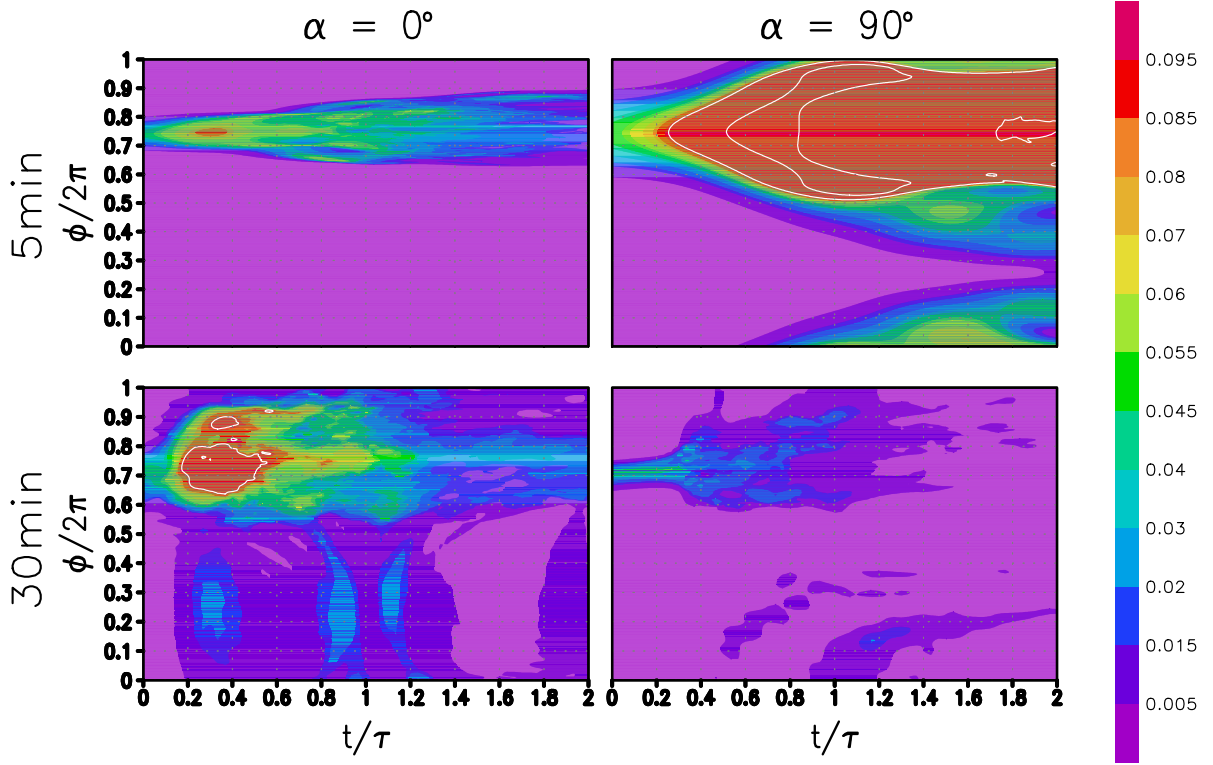


Figure 6.13: From the integrations shown in Fig. 6.12, the time development of the dependence of the eddy energy on the IGW phase. All plots show normalized values  $E'/\bar{E}(t=0)$ . The shading scale in all four panels is identical. The contour interval is 0.1, starting at 0.1.

as the initial SV amplitude is decreased, since a larger initial eddy energy leads to an earlier impact of nonlinearity. Finally, as a major difference to the case of the statically unstable IGW, the development is more rapid in the sense that the eddies have no more than two optimization periods time to interact with the IGW before their energy decays again.

The amplification-rate decompositions for the four integrations with initial  $A_{SV}^2 = 10^{-1}$  are shown in Fig. 6.12. The initial development is as in the linear theory, with an initial energy gain due to  $\Gamma_b$ , leading via  $\overline{b'w'}$  to a growing energy in  $u'_\phi$ , thus enabling a statically enhanced roll mechanism for  $\alpha = 0^\circ$  (i.e. growth of  $\langle K'_\perp \rangle$  via  $\Gamma_\perp$ ) and a statically enhanced Orr mechanism for  $\alpha = 90^\circ$  (growth of  $\langle K'_\parallel \rangle$  via  $\Gamma_\parallel$ ). In the case of  $(\tau, \alpha) = (5\text{min}, 90^\circ)$  in the late phase  $\langle K'_\perp \rangle$  gains by the same roll mechanism as described in chapter 5 and

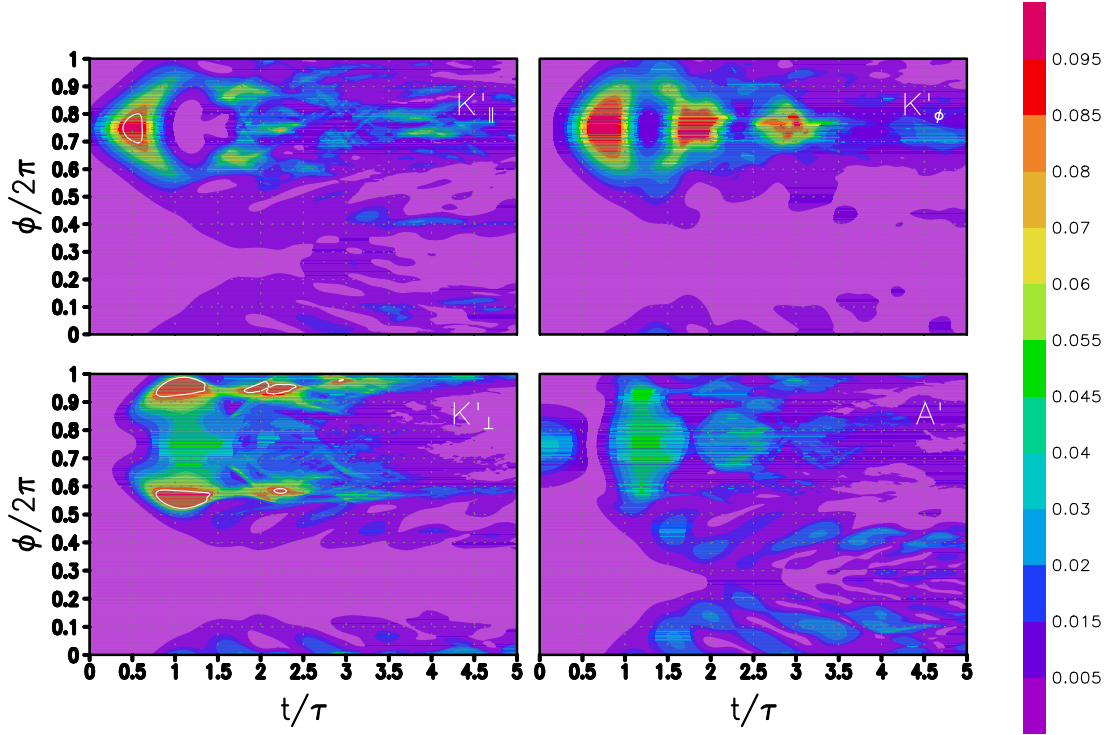


Figure 6.14: From the integration of the statically and dynamically stable IGW ( $a = 0.87$ ) perturbed by its leading SV for  $(\tau, \alpha) = (5\text{min}, 90^\circ)$  with initial amplitude  $A_{\text{SV}}^2 = 10^{-1}$ , the time dependence of the four eddy energy densities  $K'_{||}$  (upper left panel),  $K'_{\perp}$  (lower left),  $K'_{\phi}$  (upper right), and  $A'$  (lower right). Shown are relative values with respect to the initial IGW energy density. The shading scale in all four panels is the same. The contour indicates regions where the relative energy density is larger than 0.1.

also above for  $a = 1.2$ , but in the case of  $\tau = 30\text{min}$  this is blocked by a rapid decrease of the amplification rate around  $t = 0.3\tau$ , an effect which is also visible in the two cases for  $\alpha = 0^\circ$ . Seemingly nonlinear interactions stall any further growth of the eddy energy to be expected from the linear theory. This is followed by a rise of viscous-diffusive damping indicating an increased role from turbulent dissipation. The spatial distribution of the eddy energy is shown in Fig. 6.13.

#### 6.4.1 Short optimization time $\tau = 5\text{min}$

From the two SV cases for  $\tau = 5\text{min}$  the one for  $\alpha = 0^\circ$  is less spectacular. Closer inspection shows its initial dynamics to be quite related to the corresponding case discussed

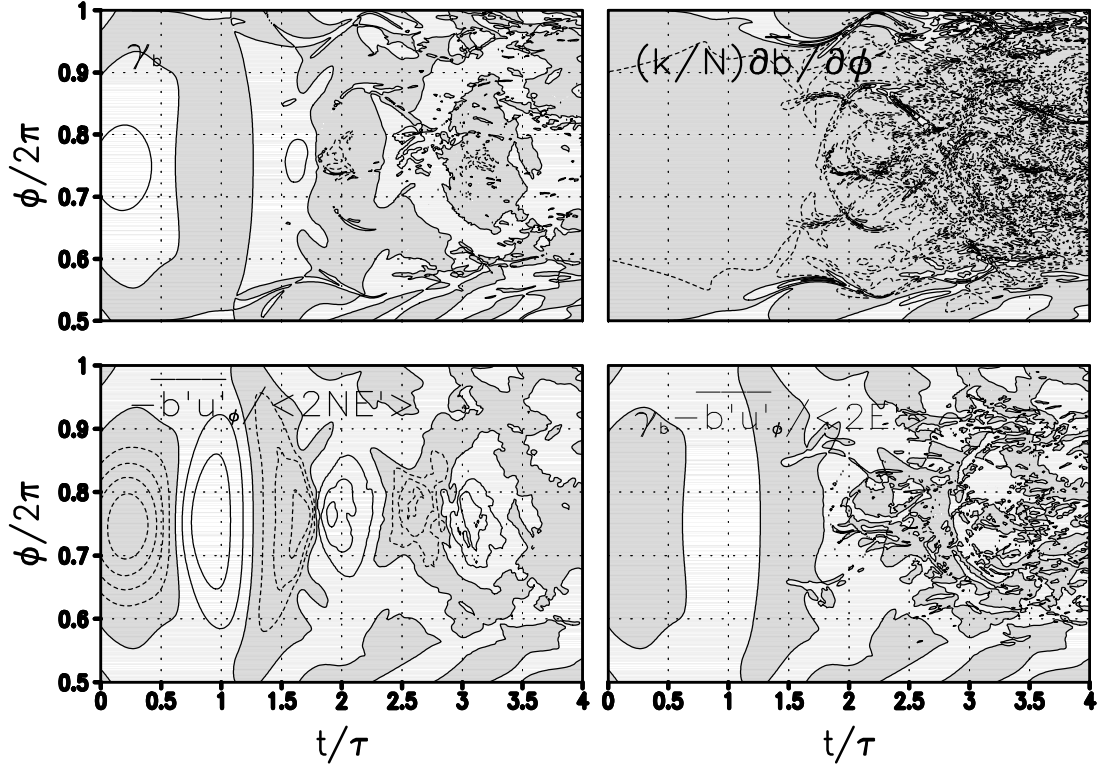


Figure 6.15: From the same integration as shown in Fig. 6.14, the time dependence of the IGW-phase dependent amplification-rate contribution  $\gamma_b$  (upper left panel, contour interval  $0.01\text{s}^{-1}$ ) from the buoyancy flux in phase direction (lower left panel, negative shown normalized by  $2N\langle E'\rangle$ , contour interval 0.2) against the corresponding gradient of the horizontal mean (upper right, normalized by  $N$ , contour interval  $0.01\text{s}^{-1}$ ). The lower right panel shows the difference  $\gamma_b - \overline{b'u'_\phi}/\langle 2E'\rangle$  characterizing the net growth and decay of  $A'$  (contour interval  $0.01\text{s}^{-1}$ ). In all panels negative values are indicated by shading. Only the phase range  $0.5 \leq \phi/2\pi \leq 1$  is shown.

above for  $a = 1.2$ , with the same leading contribution from  $K'_\perp$  (not shown). As seen from Fig. 6.14, the SV for  $\alpha = 90^\circ$  also shows behavior related to the corresponding structure for  $a = 1.2$ , however with a stronger contribution from the statically enhanced Orr process whose role in the present nonlinear integration shall be shortly documented here. First comes a decrease in  $A'$ . As visible in Fig. 6.15, this results from a contribution  $\gamma_b > 0$  in the statically least stable region, which for  $a < 1$  automatically leads to a contribution  $\gamma_b - \overline{b'u'_\phi}/\langle 2E'\rangle < 0$  there so that the eddy energy ends up in  $K'_\phi$  (see also chapters 4

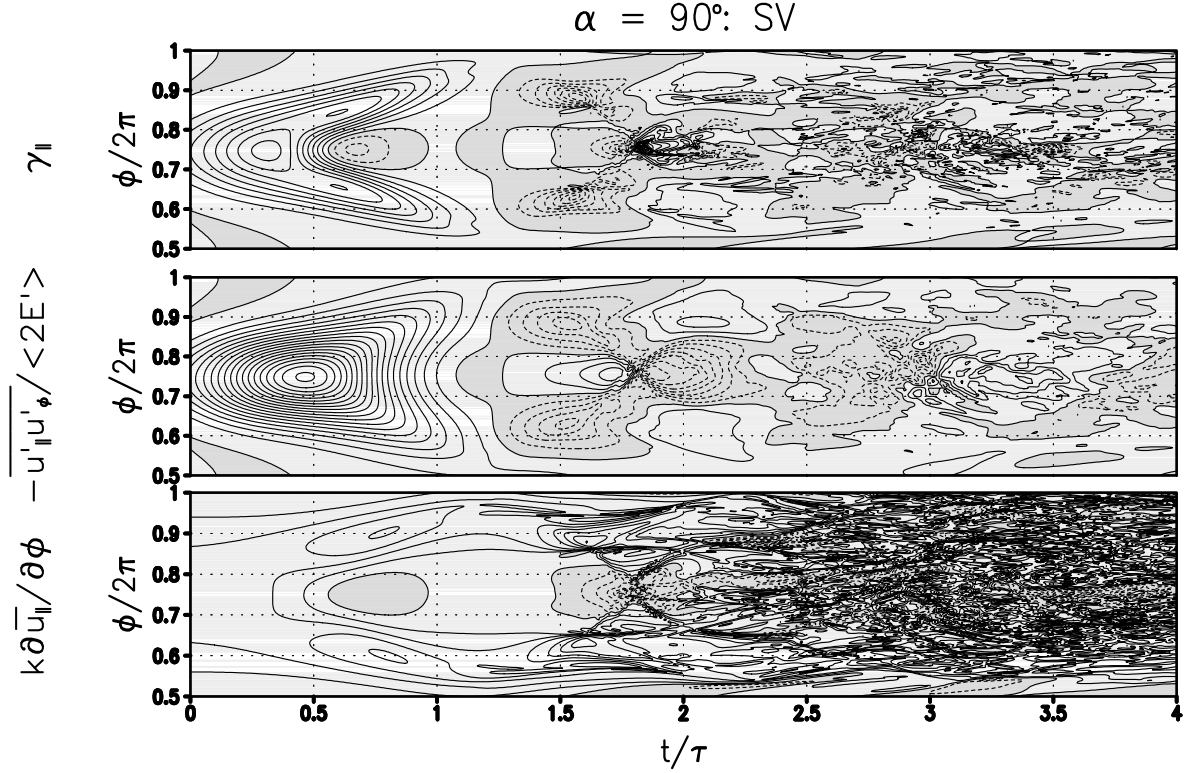


Figure 6.16: From the same integration as shown in Figs. 6.14 and 6.15, the time dependence of the IGW-phase dependent amplification-rate contribution  $\gamma_{\parallel}$  (top panel, contour interval  $0.002\text{s}^{-1}$ ) from the flux of  $u'_{\parallel}$  in phase direction (middle, negative shown normalized by  $2\langle E' \rangle$ , contour interval 0.1) against the corresponding gradient of the horizontal mean (bottom, contour interval  $0.005\text{s}^{-1}$ ). In all panels negative values are indicated by shading. Only the phase range  $0.5 \leq \phi/2\pi \leq 1$  is shown.

and 5). As in the classic Orr process this swings back after some time, here followed by a second similar oscillation with opposite tendencies in  $A'$  and  $K'_{\phi}$ . Accompanying this is an enhanced counter-gradient flux of  $u'_{\parallel}$  (Fig. 6.16), leading to transient growth of  $K'_{\parallel}$ . As visible in Fig. 6.16, the effect of the eddies is to invert the gradient  $K\partial\bar{u}_{\parallel}/\partial\phi$  near  $\phi = 3\pi/2$ , thus weakening the further growth of  $K'_{\parallel}$ . Simultaneously the gradient is increased at the outer edges, so that there an enhanced eddy growth is possible. Similar to the classic Orr process the growth in eddy energy is stopped near  $t = \tau$ , followed by a decay and a weaker second oscillation of a similar kind, after which the horizontal mean shows an increasingly turbulent structure. Also here, however, the gain in  $K'_{\perp}$  is consider-

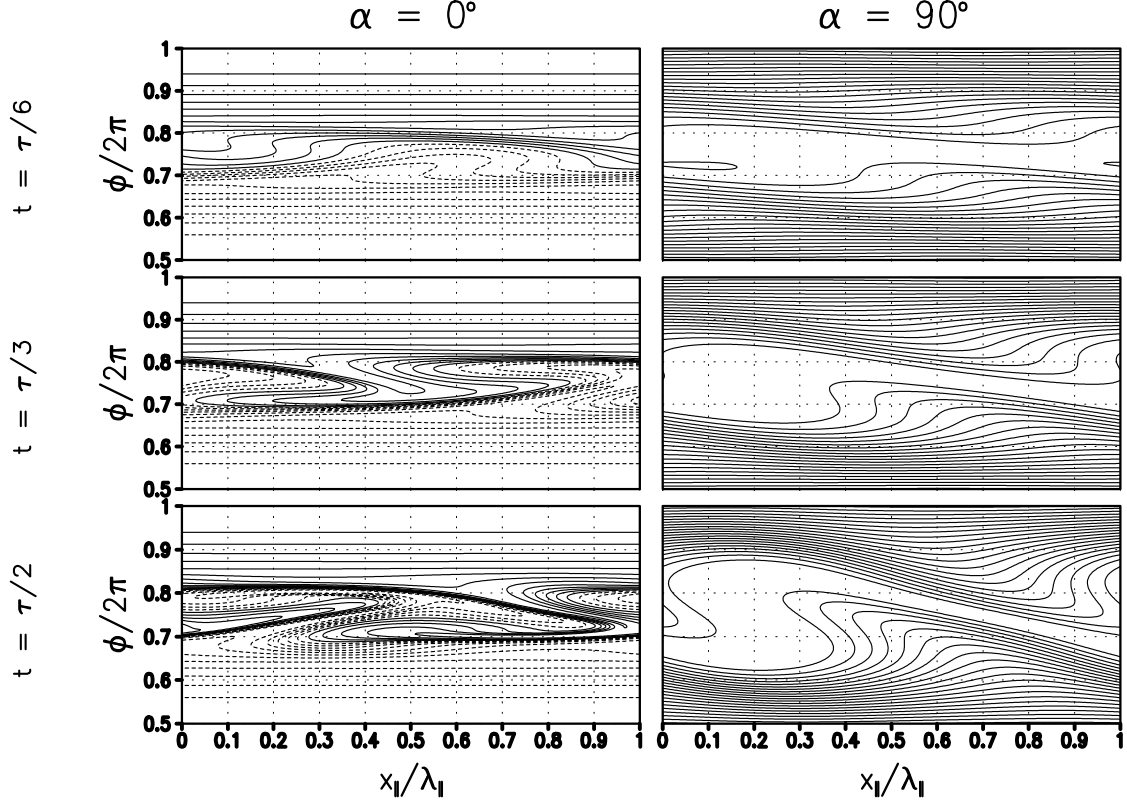
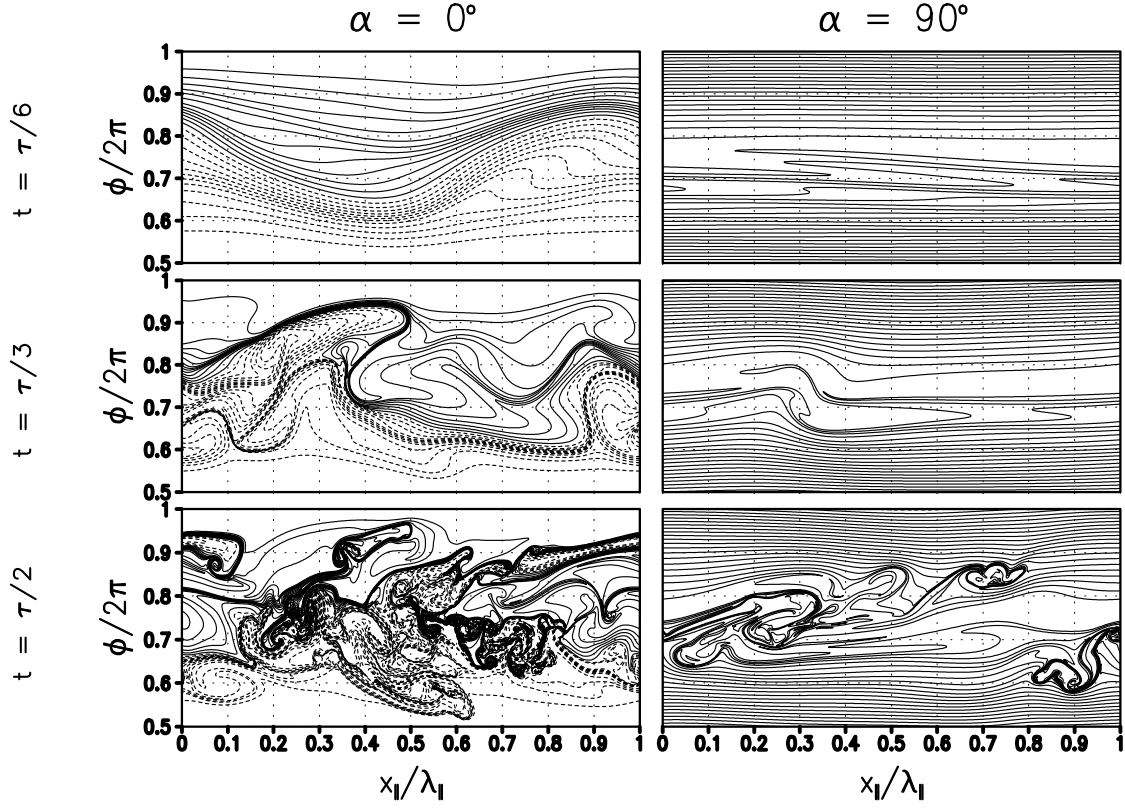


Figure 6.17: From the integrations of the statically and dynamically stable IGW ( $a = 0.87$ ) perturbed by its leading SVs for  $\tau = 5\text{min}$  (left column  $\alpha = 0^\circ$ , right column  $\alpha = 90^\circ$ ), the spatial dependence of  $v_\perp$  at  $t = \tau/6$  (top row),  $t = \tau/3$  (middle) and  $t = \tau/2$  (bottom). Only the phase range  $0.5 \leq \phi/2\pi \leq 1$  is shown. The contour interval is 1m/s. The maximum value in the right column is between 20 and 21 m/s (all panels). Negative values are indicated by dashed contours.

able, once again after the eddies have radiated outwards into regions where  $\partial \bar{v}_\perp / \partial \phi \neq 0$ . Another feature visible in the later phase is an accumulation of  $A'$  near  $\phi = \pi/2$ , which is a visible consequence of the critical-layer interaction predicted by the linear theory (see Fig. 6.14).

An interesting question is why the leading transverse SV can follow its linear development for a longer time, so that even for  $A_{SV}^2 = 1$  a sustained corresponding phase is observable. At least part of the answer can be read from Fig. 6.17 where the time development of  $v_\perp$  up to  $t = \tau/2$  is shown for the parallel ( $\alpha = 0^\circ$ ) and the transverse SV ( $\alpha = 90^\circ$ ). One sees the parallel SV developing considerably stronger gradients (note that

Figure 6.18: As Fig. 6.17, but for  $\tau = 30\text{min}$ .

$\lambda_{\parallel}$  for the parallel SV is also shorter than for the transverse SV), which can lead both to faster viscous damping and to stronger instabilities. Indeed corresponding calculations have shown that the parallel SV in its early stage allows stronger tangent linear instabilities than the other structure, so that it cannot go unimpeded through its full linear growth phase, while the opposite is true for the transverse SV (not shown).

#### 6.4.2 Long optimization time $\tau = 30\text{min}$

As much in contrast to the linear theory as the stronger growth of the transverse SV vs. the parallel SV for small  $\tau$  is the second result that overall the SVs for longer  $\tau$  cannot grow considerably in eddy energy. Indeed, due to its larger initial energy the leading parallel SV for  $\tau = 30\text{min}$  has some impact on the IGW, which is however weaker than that of the leading transverse SV for  $\tau = 5\text{min}$ . The early development of  $v_{\perp}$  for the two SVs analyzed here is shown in Fig. 6.18. In comparison to Fig. 6.17 one sees at the same  $t/\tau$  a stronger impact from the nonlinear advection, which already explains the reduced

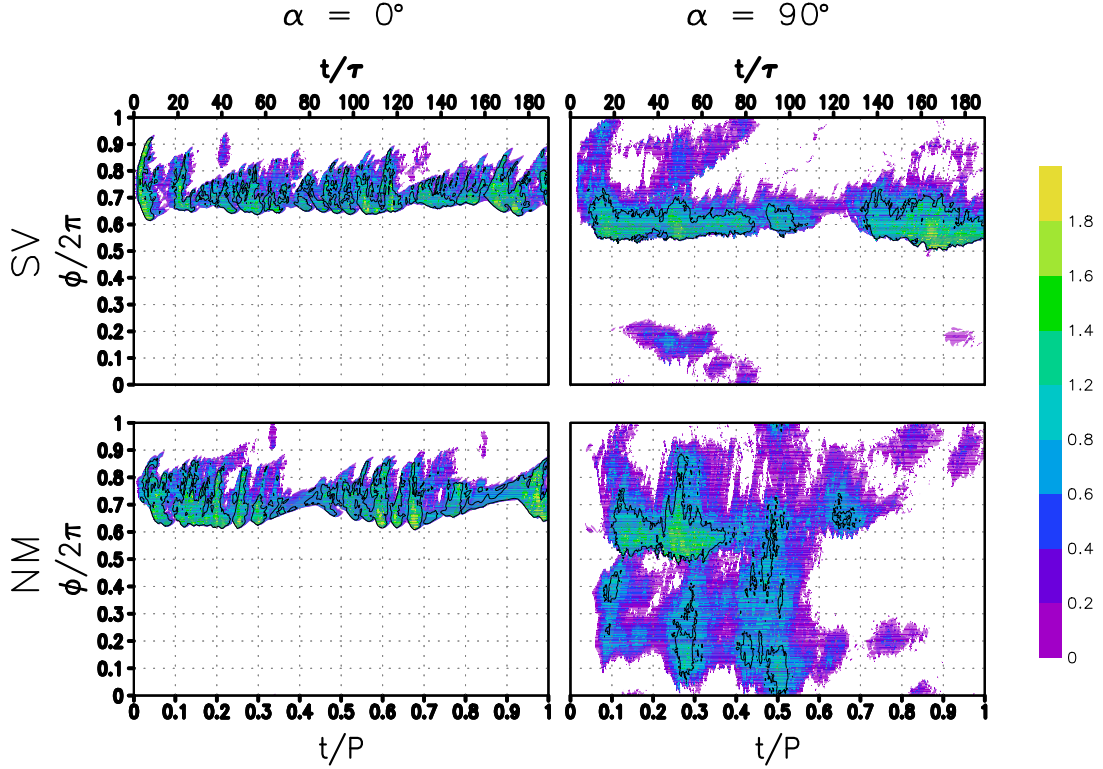


Figure 6.19: From the integrations of the statically unstable IGW ( $a = 1.2$ ) perturbed by its leading SVs or NMs at  $\alpha = 0^\circ, 90^\circ$ , the time dependence of the eddy dissipation rate  $\epsilon'$ . Shown is  $\log_{10}[\epsilon' / (\text{mW/kg})]$ . The color scale is the same in all four panels. Only values larger than 1 mW/kg are shown. The contour encloses regions with  $\epsilon' > 10 \text{ mW/kg}$ .

ability of the SVs to go unimpeded through their whole linear growth. It is just the fact that  $\tau$  is larger but the nonlinear interactions are not correspondingly smaller and thus act faster over the normalized time  $t/\tau$  which keeps these SVs from attaining the full energy they would acquire according to the linear theory.

## 6.5 Comparison to observations

A detailed comparison of the breaking of a monochromatic IGW in a background without vertical shear, as discussed here, with observations where these conditions are never met in purity, will probably never be possible. Nonetheless an attempt shall be made to point out a few observational facts indicating at least some consistency between the theory and the real world. Some of these refer to observations of so-called ripples in the



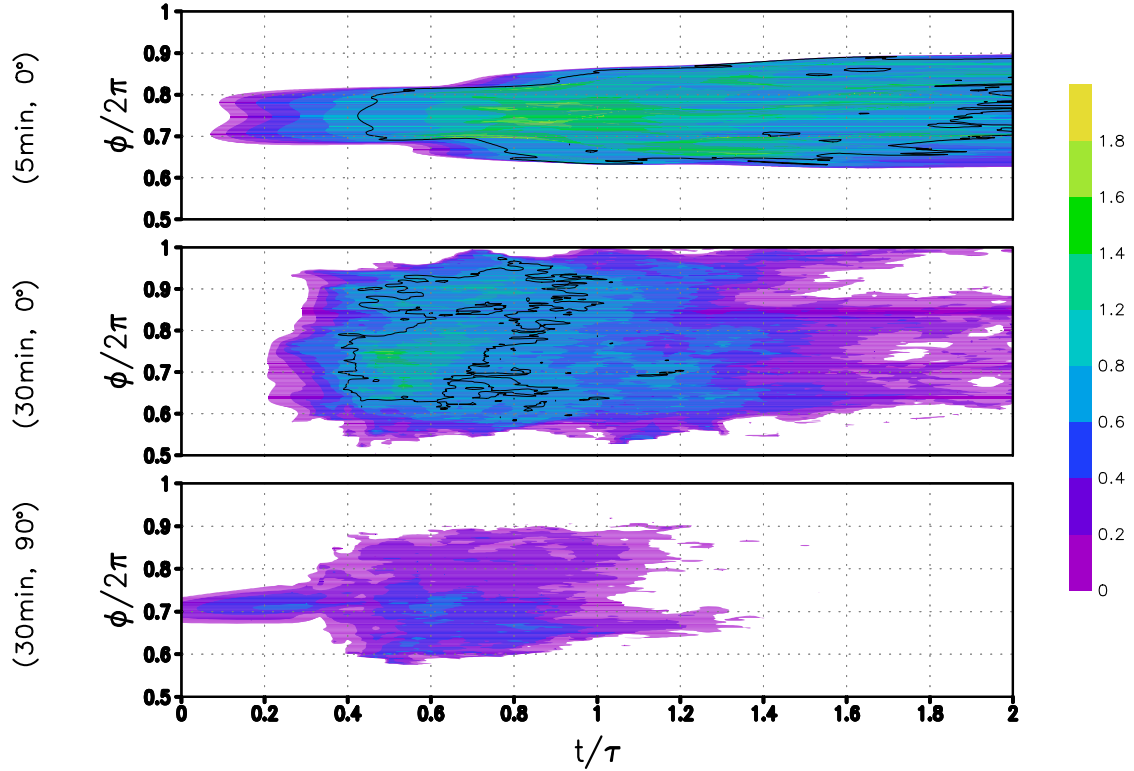


Figure 6.20: From the integrations of the statically and dynamically stable IGW ( $a = 0.87$ ) perturbed by its leading parallel SVs for  $\tau = 5\text{min}$  (top panel) or 30min (middle) or the leading transverse SV for  $\tau = 30\text{min}$  (bottom, initial amplitude in all cases  $A_{\text{SV}}^2 = 10^{-1}$ ), the time-dependent eddy dissipation rate  $\epsilon'$  in the phase range  $\pi \leq \phi \leq 2\pi$ . Shown is  $\log_{10} [\epsilon' / (\text{mW/kg})]$ . The contour interval is 1, with the lowest contour also at 1.

airglow layer, which are commonly interpreted as instability structures from GW breaking (Hecht, 2004). The literature seems to indicate that in cases where ripples are observed simultaneously with a statically unstable IGW (Hecht et al., 1997, 2000) they have a tendency to propagate in a more or less transverse horizontal direction with respect to the IGW. The wavelength of these structures is below 10km. A simulation of ripples from a statically unstable IGW has been done by Fritts et al. (1997), where the IGW (plus an additional HGW) has been perturbed by random noise. The results here, where the leading transverse NM appears as the most effective perturbation of an IGW with  $a > 1$ , might give an explanation for why the occurring ripples have the observed direction of propagation. Additional support for this hypothesis might come from the wavelength of

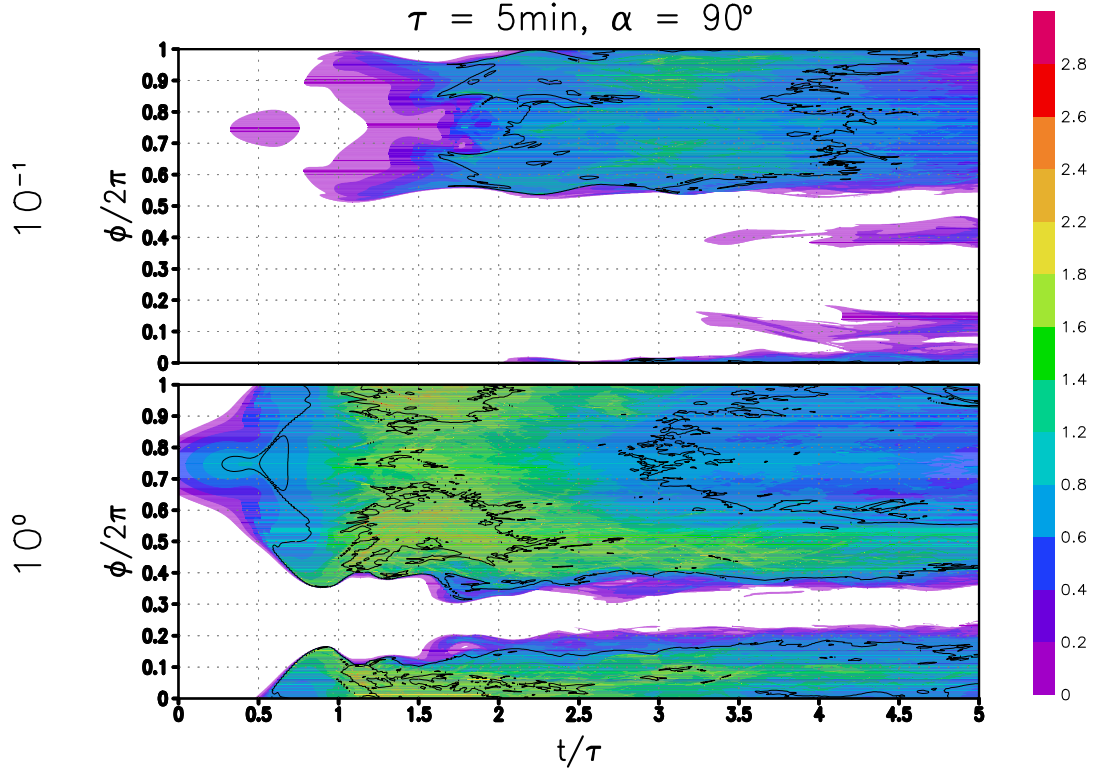


Figure 6.21: As Fig. 6.20, but now from integrations after a perturbation of the IGW by its leading transverse SV for  $\tau = 5\text{min}$ , with initial amplitude  $A_{\text{SV}}^2 = 10^{-1}$  (top panel) or  $10^0$  (bottom) between  $0 \leq t \leq 5\tau$ .

the NM (about 8km) which is consistent with the empirical results.

Another point of interest are estimates of turbulent dissipation rates where spectra of vertical profiles of relative density fluctuations from in-situ rocket measurements are fitted to models of the spectrum of a passive tracer advected in homogeneous isotropic turbulence. Essentially the location of the transition from the inertial to the viscous subrange of the spectrum is then used to determine the dissipation rate. These analyses (Lübken, 1997; Müllemann et al., 2003) lead to values of  $\epsilon$  in the middle atmosphere between 1 and 1000mW/kg. Interesting is also that not in all cases turbulence can be clearly attributed to either static or dynamic instability. The long-term development of the eddy dissipation rates  $\epsilon'$  resulting from the above-discussed integrations for the statically unstable IGW is shown in Fig. 6.19. The dissipation  $\bar{\epsilon}$  of the horizontal mean is found to be much weaker (not shown). One sees that the former are in all four cases in the range

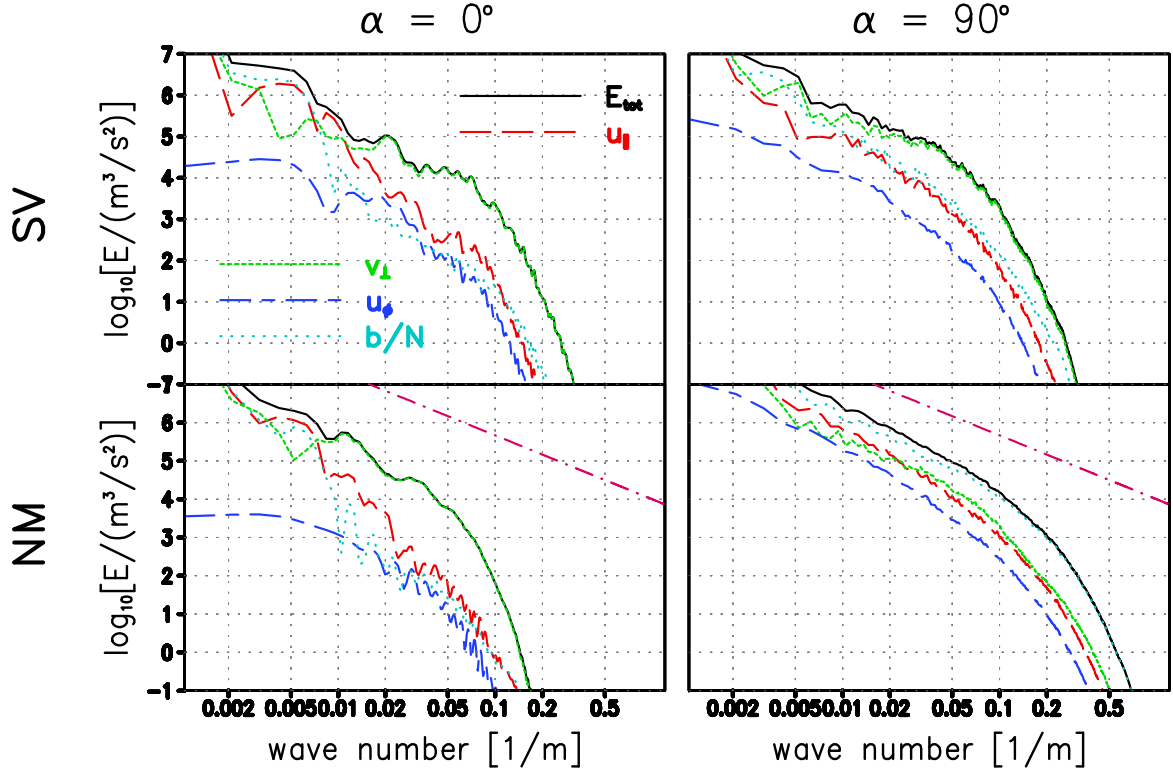


Figure 6.22: For  $t = 40\tau$  in the integrations shown in Fig. 6.19, half the horizontally averaged spectra of the profiles of  $u_{\parallel}$ ,  $v_{\perp}$ ,  $u_{\phi}$ , and  $b/N$  in  $\phi$ -direction, and the sum, i.e. the spectrum of total energy. For better orientation the two lower panels also show a spectral slope  $\propto m^{-5/3}$ , where  $m$  is the wavenumber in  $\phi$ -direction.

of observed values. The eddy dissipation rates from the SV runs for the IGW with  $a < 1$  are shown in Figs. 6.20 and 6.21. While most SVs produce values of a few 10mW/kg, the leading transverse SV for the short optimization time can lead to dissipation rates of a few 100mW/kg, provided its initial amplitude is large enough. SVs thus seem to offer a possibility to explain the occurrence of turbulence in cases where neither static nor dynamic instability predict corresponding NM growth<sup>1</sup>. Also here, however, a caveat applies. Fig. 6.22 shows the horizontally averaged spectra of the vertical profiles (i.e.

<sup>1</sup>In passing it shall also be noted that the spatial distribution of  $\epsilon'$  for the short-time transverse SV results from the action of the roll mechanism at the flanks of the maximum of  $v_{\perp}$ , an effect not to be expected in turbulence generated by a Kelvin-Helmholtz layer. It is also interesting that it stays clearly away from the phase region  $\phi = \pi/2$  which can be explained via the critical-layer effect predicted by the linear theory

in  $\phi$ -direction) of all four model variables at  $t = 40\tau$  from the integrations of the IGW with  $a = 1.2$  perturbed by its leading parallel or transverse SV or NM. The dominance of  $K'_\perp$ , noted before in all integrations up to the one after perturbing the IGW by its leading transverse NM, obviously extends down into the viscous subrange, and also at all scales  $u_\parallel$  carries more energy than  $u_\phi$ . Similar results are found for the cases with  $a < 1$  (not shown). This anisotropy might point to either (1) a limitation of the 2.5D approach taken here or (2) a fundamental property of turbulence from IGW breaking. A corresponding analysis is beyond the scope of this study but at the present stage one should at least keep this apparent inconsistency with the basic assumptions behind the retrieval of turbulent dissipation rates from the spectra of density fluctuations in mind. Nonetheless, the author sees the agreement in the orders of magnitude between empirical and theoretical dissipation rates still as an indication of consistency between theory and measurements.

## 6.6 Summary

As part of an effort to construct a picture of the nonlinear interaction between IGWs and their leading NMs and SVs this chapter reports corresponding direct numerical simulations for IGWs which are either statically unstable (amplitude  $a$  with respect to the overturning threshold larger than 1) or dynamically and statically stable ( $a < 1$ ,  $\text{Ri} > 1/4$ , no NM instabilities). The two spatial dimensions of the problem are given by the direction along the IGW wave vector and the horizontal wave vector of the perturbation, while the velocity field, simulated together with the buoyancy field within the framework of the nonlinear Boussinesq equations, is fully 3D. This type of 2.5D approach is also able to handle azimuth angles  $\alpha \neq 0$ . The model parameters are typical for the upper mesosphere.

An interesting aspect of the results is how much of the observed dynamics can be understood based on the corresponding linear theory in chapters 4 and 5. An especially prominent role in the turbulence onset can be attributed to the statically enhanced roll mechanism, where the counter-gradient flux of the eddy horizontal velocity component  $v'_\perp$ , in the direction perpendicular to the horizontal direction of propagation of the per-

turbation, leads to a corresponding gain in the eddy kinetic energy, thus producing a considerable anisotropy in the turbulent velocity field. This must be seen in connection with the role of the elliptic polarization of the IGW horizontal velocity field. It provides the key for understanding the spatial distribution of the eddy energy and turbulent dissipation with respect to the wave phase. This refers on the one hand to its role in determining where the roll mechanism can work. On the other hand it also leads, as in the linear theory, to critical layers for the transverse perturbations ( $\alpha = 90^\circ$ ), half a wavelength away from the statically least stable location, which the flux of turbulent energy typically does not cross. The present study thus adds interesting facets to the results from other studies on turbulence onset via Kelvin-Helmholtz instabilities (with a one-dimensional shear) where these phenomena are not visible.

In contrast to expectations from the linear theory, however, for  $a < 1$  the leading SVs for longer optimization times ( $\tau = 30\text{min}$ ) are not able to grow to the largest observed eddy energies. At initial SV amplitudes large enough for triggering nonlinear behavior, nonlinear advection acts too fast for allowing these perturbations to go through their full linear growth phase. In a comparison between the impact of the remaining leading parallel ( $\alpha = 0^\circ$ ) or transverse short-time SVs (for  $\tau = 5\text{min}$ ) or NMs (for  $a > 1$ ) on the IGW the overall finding is that, at equal local peak energy density, the more vigorous effect comes from the spatially broadest structure (in IGW-phase direction), which is the leading transverse NM for  $a > 1$  and the leading transverse SV for  $a < 1$ . These structures, with horizontal wavelengths roughly of the order of the total wavelength of the IGW, are the most energetic and thus have the largest eddy fluxes with a corresponding effect on the horizontal mean. They might help explaining the wavelengths and preferentially more or less transverse orientation of airglow ripples typically observed in conjunction with a statically unstable IGW (Hecht et al., 1997, 2000).

One should also note that the reduction of the IGW amplitude is stronger than to be expected from standard static or dynamic stability considerations. Both for the case of the IGW initially statically unstable and statically and dynamically stable the amplitude is reduced to near 0.7, although a removal of dynamically unstable regions with  $\text{Ri} < 1/4$  would only necessitate a reduction to near 0.9 (see Fig. 2.2). For SVs this depends

on the initial strength of the perturbation which is not taken into account in present parameterization schemes for the impact of gravity waves on the large-scale circulation.

Finally, the resulting turbulent dissipation rates are in all cases examined within the range of values determined from the spectra of vertical density fluctuation profiles (Lübken, 1997; Müllemann et al., 2003), even for the case  $a = 0.87$ . Optimal perturbations thus indeed seem to be a candidate for the explanation of turbulence onset in IGWs where the wave amplitude precludes NM instabilities. A major difference between statically unstable and stable IGWs is that the turbulence in the latter occurs in rather short bursts over a time span of a few Brunt-Vaisala periods  $N/2\pi$ , while in the former the turbulent layer is much more persistent.

## Chapter 7

# Monochromatic high-frequency gravity waves

The final aspect investigated in this study is the nonlinear dynamics occurring after the perturbation of a HGW by its most important NMs or SVs. With regard to the impact of NM perturbations much has already been covered by Fritts et al. (2003, 2006) who report the results from comprehensive 3D simulations of a statically stable or unstable HGW perturbed by low-level random noise. As was to be expected from the linear theory, they find that the wave amplitude is reduced way below the static instability threshold. For a statically unstable HGW the final amplitude is near  $a = 0.3$ . A statically stable HGW is removed nearly completely while another GW with more vertical phase propagation is generated. The question here therefore cannot be what happens to the HGW but how it happens. It is of interest whether a distinct perturbation of the HGW by one of its NMs can produce the same behavior, and then also which NM this is. Beyond that one can ask about details of the wave breaking process as to where and how the turbulent energy is generated, and also what this means for the final turbulent dissipation rates, once again for the comparison to the observations. Finally, also the dynamics occurring after the perturbation of the HGW by its leading SVs shall be examined.

The model within which this is done is completely identical to the one used for the calculations in chapter 6, including the special reference system chosen which also enables the examination of the impact of non-parallel perturbations on the HGW within a 2.5D

$\Theta/^\circ$	$a$	$\Lambda/\text{km}$	perturbation type	$\tau/\text{min}$	$\alpha/^\circ$	$\lambda_{\parallel}/\text{km}$	$n_{\parallel}$	$n_{\phi}$
70	1.40	6	NM (1)	-	0	1.995	576	2304
70	1.40	6	NM (1)	-	90	6.310	2304	2304
70	1.40	6	SV	5	0	0.631	288	2304
70	1.40	6	SV	5	90	0.501	144	2304
70	1.20	6	NM (1)	-	0	1.995	576	2304
70	1.20	6	NM (1)	-	90	6.310	2304	2304
70	1.00	6	NM (1)	-	0	3.162	1152	2304
70	1.00	6	NM (1)	-	90	5.012	2304	2304
70	0.85	6	NM (1)	-	0	3.162	1152	2304
70	0.85	6	NM (1)	-	90	5.012	2304	2304
70	0.70	6	NM (1)	-	0	3.981	1152	2304
70	0.70	6	NM (2)	-	0	12.589	4608	2304
70	0.70	6	NM (1)	-	90	12.589	4608	2304
70	0.70	6	NM (2)	-	90	5.012	2304	2304
70	0.70	6	SV	5	0	1.259	576	2304
70	0.70	6	SV	5	90	0.794	288	2304

Table 7.1: Model extent  $\lambda_{\parallel}$  in the horizontal and  $\Lambda$  in HGW-phase direction, as well as the corresponding numbers of grid points  $n_{\parallel}$  and  $n_{\phi}$ , for all discussed integrations, of an HGW with an amplitude  $a$  with respect to the overturning limit, perturbed by either its leading SV (optimization time  $\tau$ ) or its leading (1) or a secondary (2) NM, at azimuth angle  $\alpha$ .  $\Lambda$  is also the HGW wavelength, while  $\lambda_{\parallel}$  agrees with the horizontal wavelength of the respective perturbations.  $\Theta$  is the inclination angle between the HGW wave vector and the horizontal.

simulation. Again the  $f$ -plane is located at  $70^\circ\text{N}$ , the Brunt-Vaisala frequency is  $N = 2 \cdot 10^{-2}\text{s}^{-1}$ , and viscosity and diffusivity are  $\nu = \mu = 1\text{m}^2/\text{s}$ . The HGW parameters together with those from the NMs and SVs, and the model resolution used in the different simulations are summarized in table 7.1



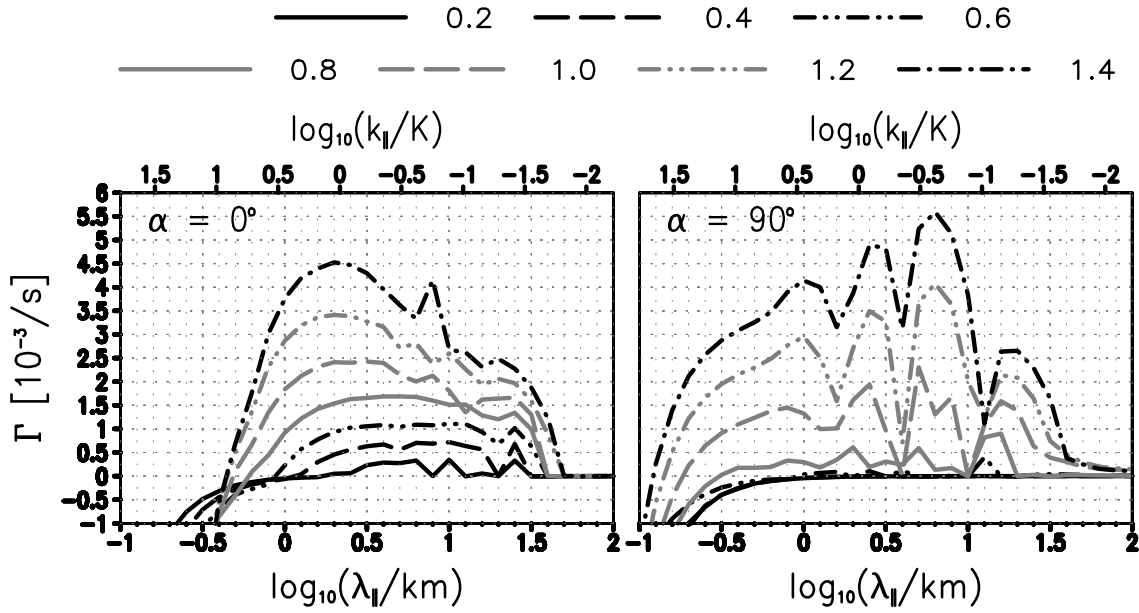


Figure 7.1: For HGWs with amplitude  $a$  between 0.2 and 1.4, the growth rate of the leading parallel ( $\alpha = 0^\circ$ ) or transverse ( $90^\circ$ ) NM with horizontal wavelength  $\lambda_{\parallel}$  and corresponding wavenumber  $k_{\parallel} = 2\pi/\lambda_{\parallel}$ . Wavelength and inclination angle for all HGWs are  $(\Lambda, \Theta) = (6\text{km}, 70^\circ)$ .  $K = 2\pi/\Lambda$  is the wavenumber of the HGW.

## 7.1 Perturbation of the wave by normal modes

All simulations, of the HGW either perturbed by a NM or a SV, have been done with an HGW at  $\Theta = 70^\circ$ . This is the most upwardly directed HGW analyzed in chapter 5 and it also comes close to the wave studied by Fritts et al. (2003, 2006) which has  $\Theta = 72^\circ$ . The linear analysis shows that the leading NMs are at either  $\alpha = 0^\circ$  (parallel NMs) or  $\alpha = 90^\circ$  (transverse NMs). The corresponding growth rates are shown in Fig. 7.1 for various  $a$  between 0.2 and 1.4. One sees that for  $a > 1$  the most quickly growing NM of all is transverse. As shown below (Figs. 7.4 and 7.9) this results from a positive contribution of both shear production and convective production to the growth of the transverse NM. In contrast to this the parallel NM is fuelled by convective production but there is a damping contribution from shear production. For  $a < 1$  the parallel NMs take the lead since for these the especially positive impact of the convective production is stronger than for the transverse NMs, while in both modes the shear production does not act as a damping term. At  $a \leq 0.6$  transverse NM growth is negligible, so that

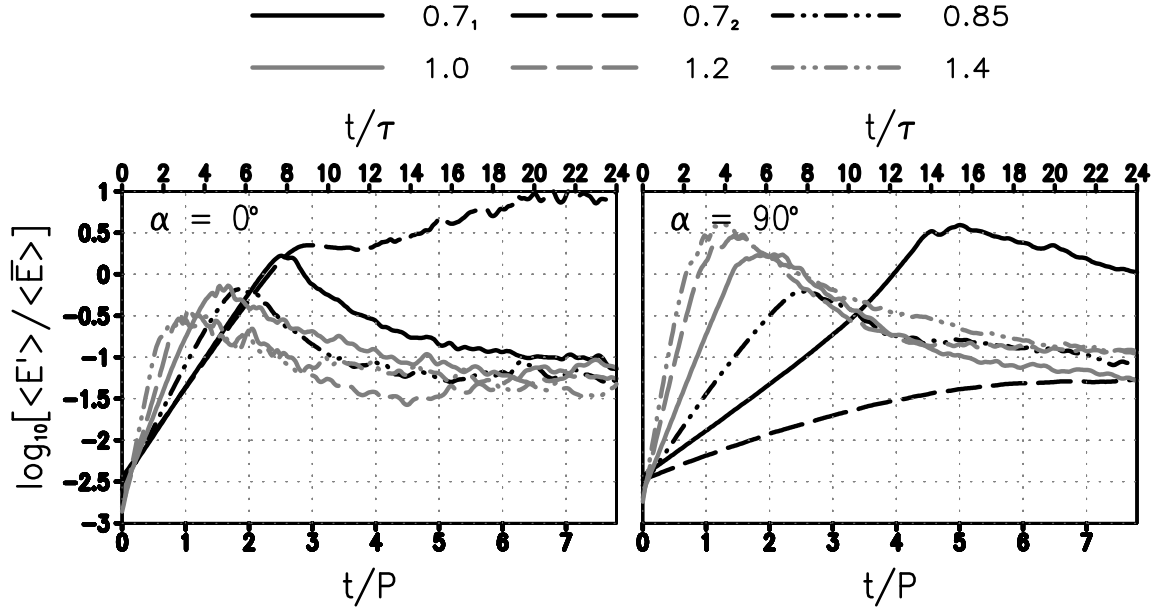


Figure 7.2: From simulations of the nonlinear development of HGWs with amplitude  $a$  between 0.7 and 1.4 after a perturbation by the leading (or leading secondary, for  $a = 0.7$ ) parallel (left panel) or transverse NM (right), the time development of the total energy of the eddies, i.e. the deviations from the horizontal mean, normalized by the horizontal-mean energy. The wave period  $P$  is 920s. For easier comparison time has also been normalized by the SV optimization time  $\tau = 5\text{min}$  used below.

for these HGWs the instability seems to be predominantly determined by 2D wave-wave interactions (McComas and Bretherton, 1977; Klostermeyer, 1991; Lombard and Riley, 1996). The reader should also note the secondary growth-rate peak for parallel NMs at large wavelengths. As will be seen below the corresponding NMs can be quite relevant for low-amplitude HGWs.

As in chapter 6 the resulting fields are split up into the mean over  $x_{\parallel}$  (the "horizontal" mean, which initially is identical to the basic HGW) and the residual between the total and the horizontal mean (the "eddies", initially identical to the perturbation). The eddy energy from model integrations of the HGW (with  $a$  between 0.7 and 1.4) after a perturbation by one of the NMs is shown in Fig. 7.2. In all cases the initial amplitude of the NM was chosen so that the peak ratio between its local energy density

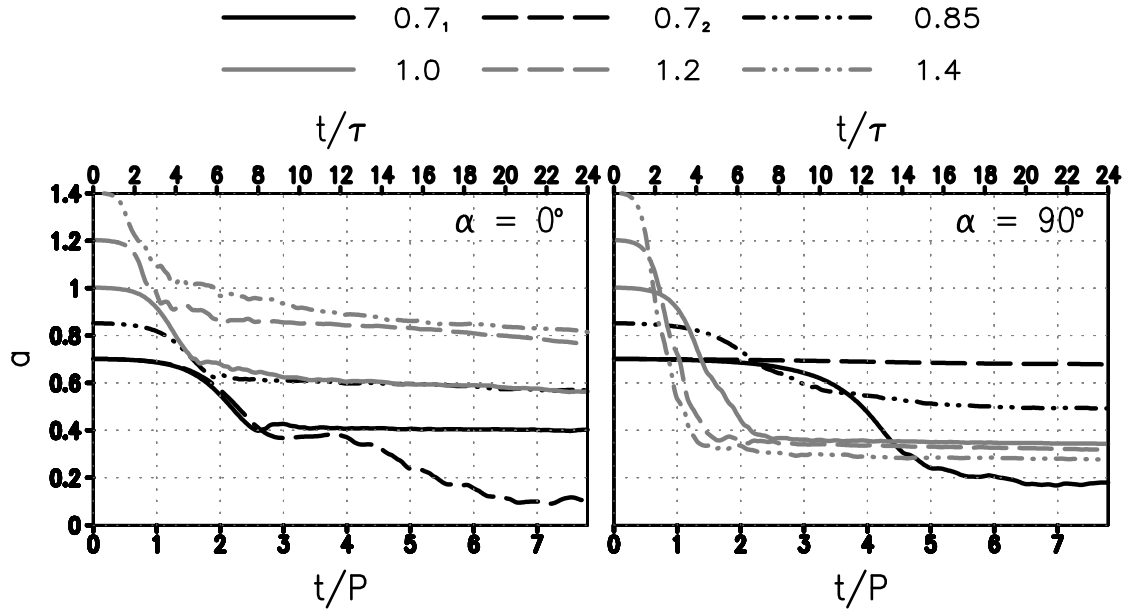


Figure 7.3: From the same integrations as shown in Fig. 7.2, the amplitude of the basic HGW with respect to its overturning threshold.

$e'(x_{\parallel}, \phi) = (u_{\parallel}^2 + v_{\perp}^2 + u_{\phi}^2 + b^2/N^2)/2$  and the corresponding field  $\bar{e}$  from the HGW<sup>1</sup> is  $A_{\text{NM}}^2 = \max_{x_{\parallel}, \phi} (e') / \bar{e} = 10^{-2}$ . As initial perturbation of the HGW either the leading NM was taken or (for  $a = 0.7$ ) the leading large-scale NM (see also table 7.1). In agreement with the linear theory the initial growth is at  $a > 1$  strongest for  $\alpha = 90^\circ$ , leading to a transient phase with more eddy energy than energy in the horizontal mean, followed by eddy-energy decay, so that the final state is again dominated by its horizontal-mean contribution. At  $a < 1$  strongest growth is observed for the parallel NMs. Only for  $a = 0.7$  the eddy energy rises over that of the horizontal mean, which is a temporary effect for the transverse leading NM, but permanent for the large-scale parallel NM.

Following the procedure outlined in the appendix D the horizontal mean has been decomposed into its contributions from GWs with upward and downward moving phase (among the latter the basic GW) and vortical modes. The time dependent amplitude of the basic GW with respect to its overturning threshold is shown in Fig. 7.3. Not surprisingly, strong wave damping is found in the simulation of the HGWs at  $a \geq 1$

<sup>1</sup>Also here one has that  $\bar{e}$  is at  $t = 0$  uniform and identical to  $\bar{E} = \bar{K} + \bar{A}$ , which is  $\bar{E}(t = 0) = (a^2/2) c^2 / (\sin \Theta \cos \Theta)^2$  (see chapter 6).

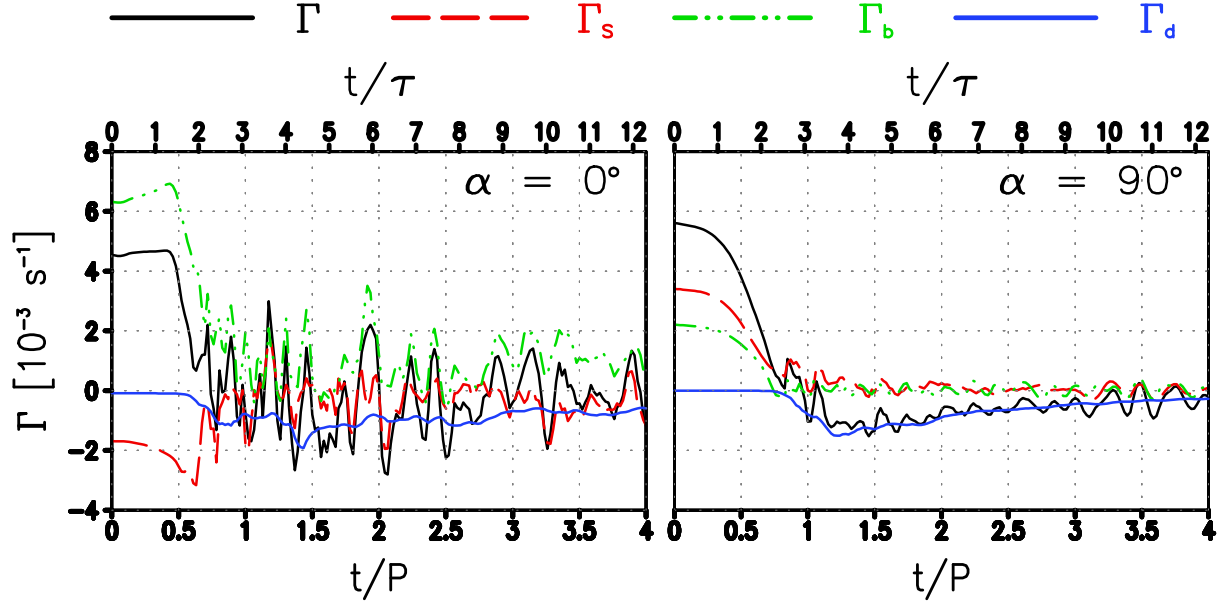


Figure 7.4: From the integrations from Figs. 7.2 and 7.3 with initial  $a = 1.4$ , the decomposition of the total amplification rate  $\Gamma$  into its contributions from convective production  $\Gamma_b$ , shear production  $\Gamma_s$ , and viscous-diffusive damping  $\Gamma_d$ .

perturbed by their respective leading transverse NM. For all these cases a final wave amplitude  $a_\infty \approx 0.3$  is reached. This is in good agreement with the results of Fritts et al. (2003, 2006) who have done fully 3D simulations of a randomly perturbed HGW. Apparently essential aspects of the breaking process are also captured in a 2.5D DNS as here. One should also note that the final HGW amplitude cannot be derived from the linear stability analysis, since the wave instability to transverse perturbations is already virtually halted near  $a = 0.5$ . As visible in Fig. 7.1, below this amplitude the HGW has no unstable NMs anymore. Seemingly there is an overshooting beyond this linear threshold which is completely due to nonlinear dynamics. Another interesting aspect is that wave decay is quite ubiquitous, even for initial  $a < 1$ . These cases are characterized by a predominant impact from the parallel NMs. The respective 2D behavior leads for initial  $a = 0.7$  to a rather strong damping down to  $a_\infty \approx 0$ , if the initial perturbation is chosen to be the leading large-scale NM. Also this is in interesting agreement to the results from Fritts et al. (2003, 2006). Notably, however, the leading transverse NM also has a strong effect on the HGW, by leading to a wave decay down to  $a_\infty \approx 0.2$ .

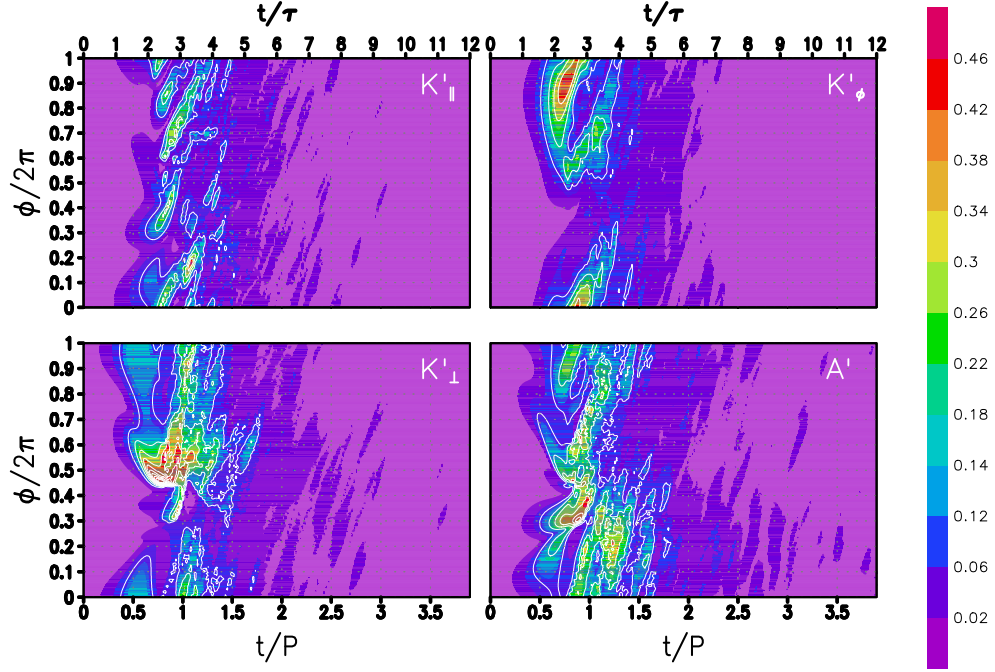


Figure 7.5: From the simulation of the HGW with  $a = 1.4$  perturbed by its leading transverse NM, the dependence of the four energy densities on time and HGW phase. Shown is the ratio between the respective energy density and the initial total energy density of the HGW. Contours are in steps of 0.1, with the lowest contour at 0.1

### 7.1.1 Statically unstable HGWs

Some information on the energetics of the 2.5D breaking process for initial  $a \geq 1$  can be drawn from Fig. 7.4 where the amplification-rate decomposition according to (6.11), with a shear-production contribution  $\Gamma_S = \Gamma_{||} + \Gamma_{\perp} \approx \Gamma_{\xi}$ , is shown for  $a = 1.4$ . One sees how the leading transverse NM is preferentially excited by to the positive impact of both shear production and convective production, the former being larger than the latter, whereas the leading parallel NM is hampered in its growth by a damping contribution from shear production. After about one HGW period  $P$  the linear growth phase ends, followed by comparatively strong viscous-diffusive damping of the eddies. While then a new state of equilibration has been reached for  $\alpha = 90^\circ$ , the other case shows even by  $t = 4P$  a rather strong variability in the total growth rate. One recognizes an especially positive

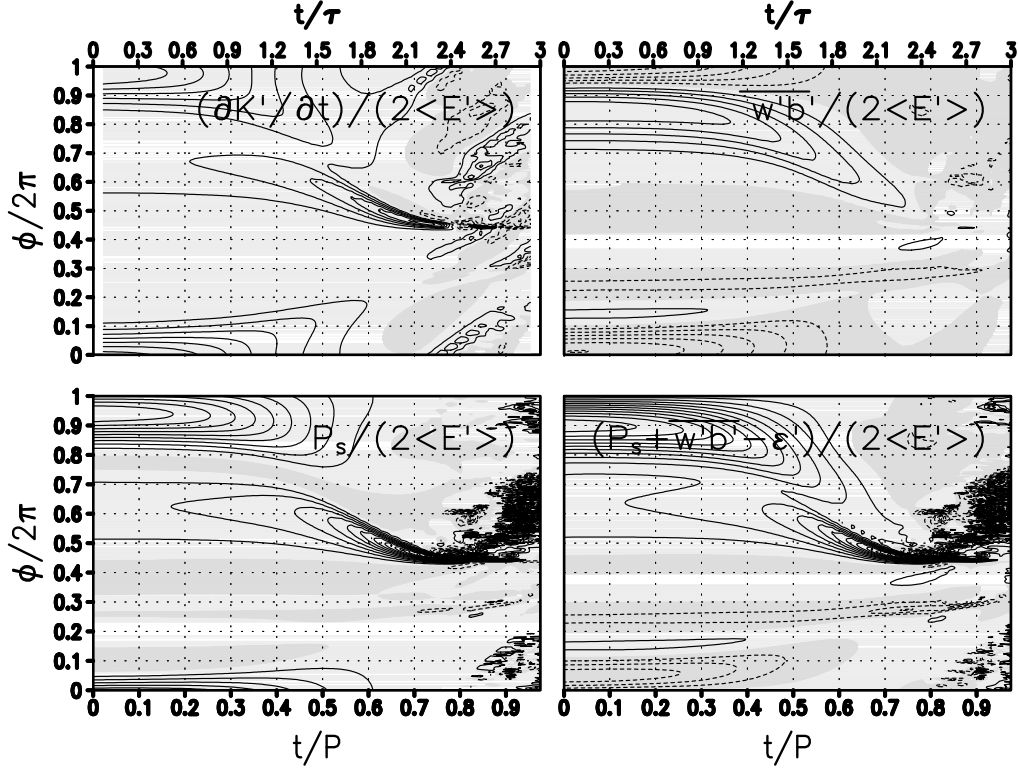


Figure 7.6: From the same integration as shown in Fig. 7.5, the dependence on time and HGW phase of the tendency of the total eddy kinetic energy density (upper left panel), total shear production (lower left), the truly vertical buoyancy flux (upper right), and the sum of all contributions to  $\partial K'/\partial t$  up to the energy flux divergence (lower right). All fields have been divided by  $\langle 2E' \rangle$ . The contour interval is  $2 \cdot 10^{-3} \text{s}^{-1}$ . The zero contour is not drawn. Negative values are indicated by dashed contours and shading.

impact from the convective production, as in the initial NM. Indeed, given the transient HGW amplitude in Fig. 7.3 and the corresponding positive growth rates in Fig. 7.1 for parallel NMs at  $\lambda_{\parallel} \geq 1 \text{km}$ , one expects continuing eddy growth at larger scales. At the same time the increased viscous-diffusive damping indicates that some eddy energy has cascaded down to smaller scales where it can be dissipated. Thus the late amplification-rate composition for  $\alpha = 0^\circ$  indicates a continuing competition between linear growth at large eddy scales and nonlinear energy transfer to smaller scales where viscosity and diffusion remove the eddy energy, hence the transient equilibration at  $a > 0$  although NM instabilities there still exist.

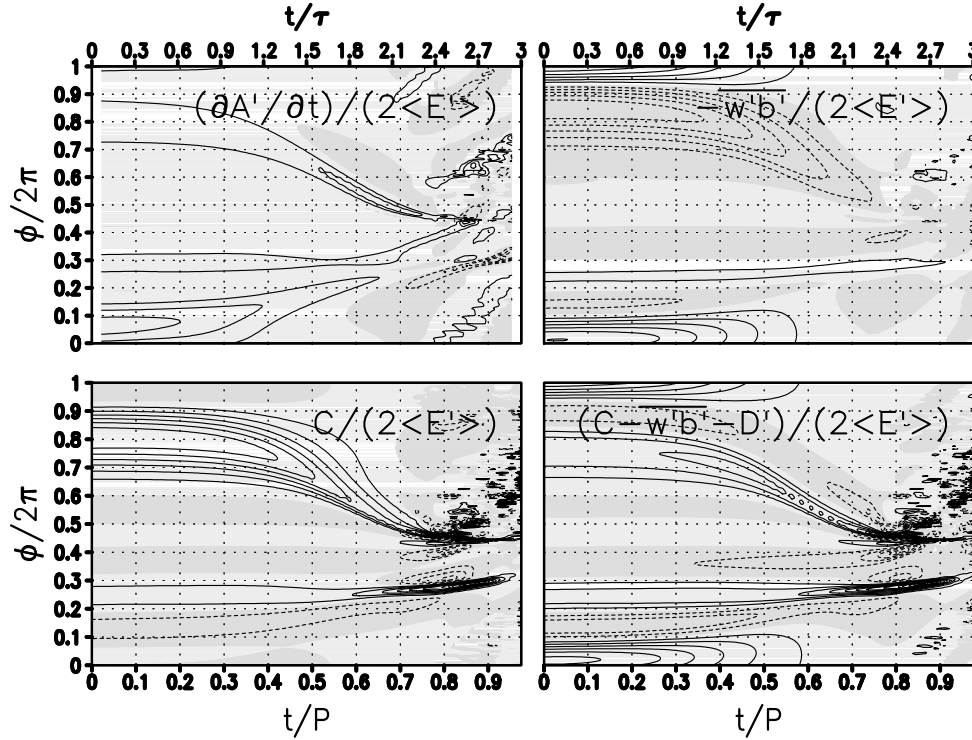


Figure 7.7: From the same integration as shown in Fig. 7.5, the dependence on time and HGW phase of the tendency of the total eddy available potential energy density (upper left panel), total convective production (lower left), the negative truly vertical buoyancy flux (upper right), and the sum of all contributions to  $\partial A'/\partial t$  up to the energy flux divergence (lower right). All fields have been divided by  $\langle 2E' \rangle$ . The contour interval is  $2 \cdot 10^{-3} \text{s}^{-1}$ . The zero contour is not drawn. Negative values are indicated by dashed contours and shading.

The spatial distribution of the eddy energy in the simulation of the HGW with  $a = 1.4$  perturbed by its leading transverse NM is shown in Fig. 7.5. The corresponding spatially dependent exchange terms are given in Figs. 7.6 and 7.7. Most prominent in the kinetic energy is the temporary accumulation of  $K'_\perp$  near  $\phi = \pi$ , resulting from a corresponding shear production. The latter is due to a transient sharp edge in  $\bar{v}_\perp = \bar{u}_\xi$  near this location (not shown). One also sees that the energy flux divergence, i.e. the residual between  $\partial K'/\partial t$  and the right-hand side of (6.8), and the buoyant exchange term tend to smoothen the final distribution. Similarly the main growth of  $A'$  is between  $\phi = 0.6\pi$  and  $0.8\pi$ , due to a temporary deformation of the buoyancy field in the horizontal mean, with shifts of the

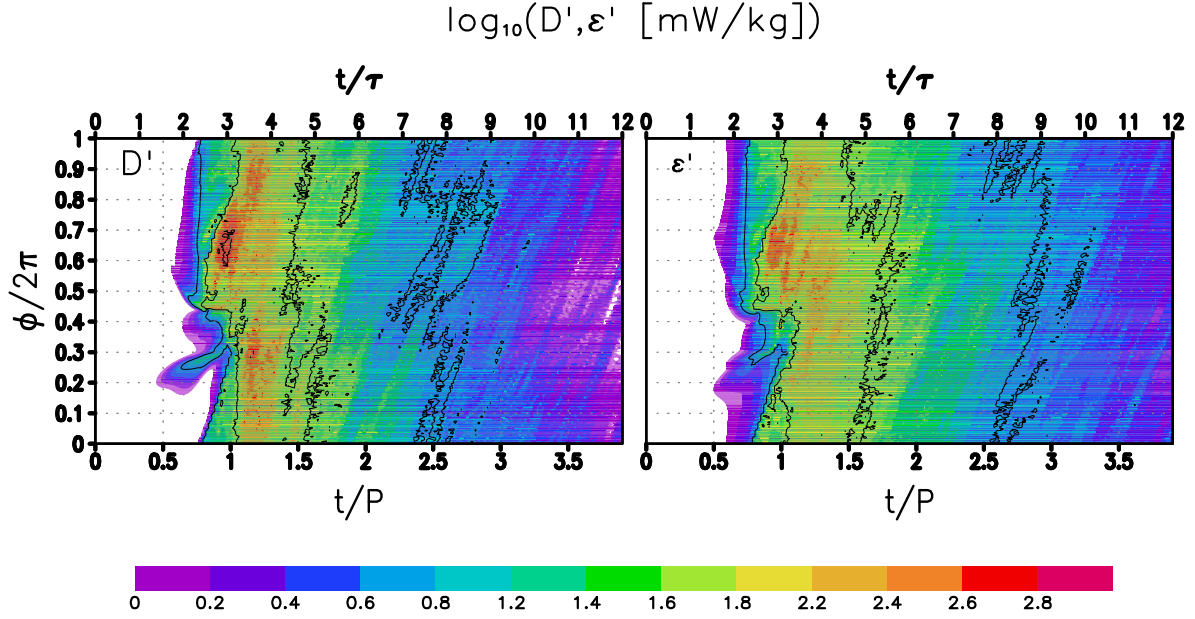


Figure 7.8: From the same integration as shown in Fig. 7.5, the dependence on time and HGW phase of  $\log_{10}(D' \text{ [mW/kg]})$  (left panel) and  $\log_{10}(\epsilon' \text{ [mW/kg]})$  (right). Contours are in steps of 1, beginning at 1.

leading gradients into this region (also not shown), so that the convective production also mainly acts there. The corresponding turbulent diffusion rate  $D'$  and dissipation rate  $\epsilon'$ , especially the latter of interest for comparisons to the available observations, are shown in Fig. 7.8. Downstream of the regions of largest turbulent energy these also maximize, with values of several  $10^2 \text{ mW/kg}$ . Both terms contribute nearly equally to the total energy sink for the turbulence, however with an especially strong transient peak in  $D'$ . A feature reminiscent of the behavior of SVs (see below) is that in the turbulent phase the main structures move upwards at a velocity very close to minus the phase velocity of the HGW, i.e. by  $2\pi$  in one HGW period  $P$ . Remembering that the coordinate system is moving downwards at exactly this velocity one can conclude that the turbulent structures seem to be frozen in the flow while the HGW moves over them.

### 7.1.2 Statically stable HGWs

The amplification-rate decomposition of the integrations of the perturbed HGW with  $a = 0.7$  resulting in the strongest decay of that wave, i.e. after a perturbation by the



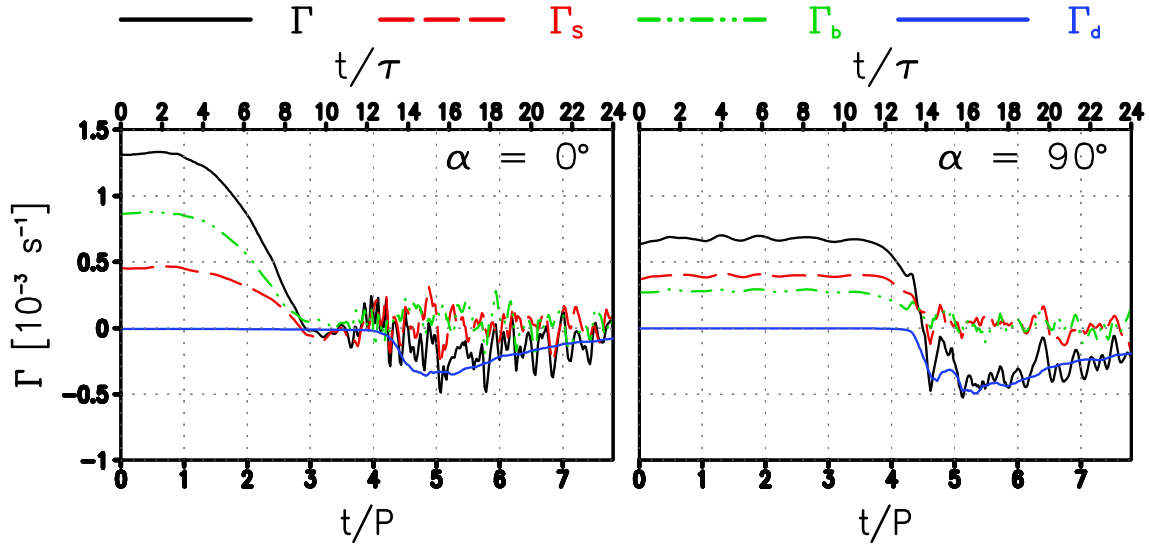


Figure 7.9: As Fig 7.4, but showing the amplification-rate decomposition from a simulation in which an HGW with  $a = 0.7$  was perturbed by its leading parallel large-scale NM (left panel), or its leading transverse NM (right panel).

leading large-scale parallel NM or the leading transverse NM, are shown in Fig. 7.9. Initially both shear production and convective production act as instability sources. For the case of the parallel NM the latter acts especially strongly, so that the resulting growth rate is larger. The transition to the turbulent phase with strong viscous-diffusive losses is later, near  $t = 3P$ , than for initial  $a > 1$ . The local analysis analogous to Figs. 7.5 – 7.7 gives similar results as there, however with a stronger impact from the energy flux divergence (not shown) so that the dynamics of the corresponding NMs is of a more global kind.

Perhaps a better understanding can be derived by getting back, similar to Fritts et al. (2006), to the findings from the classic linear analyses (Klostermeyer, 1991, e.g.) that at low HGW amplitude the dynamics of its NMs can be interpreted via resonant wave-wave interactions. For this the data have been decomposed into the free NMs of the Boussinesq equations, with two GWs (with positive or negative intrinsic frequency) and a vortical mode for each combination of horizontal wavenumber  $\kappa_{\parallel}$  and vertical wavenumber  $\mu$ . Details are given in the appendix D. The decomposition of the the parallel NM ( $\kappa_{\parallel} = k_{\parallel}$ ) is shown in the left panel of Fig. 7.10. One sees contributions from both GW types at

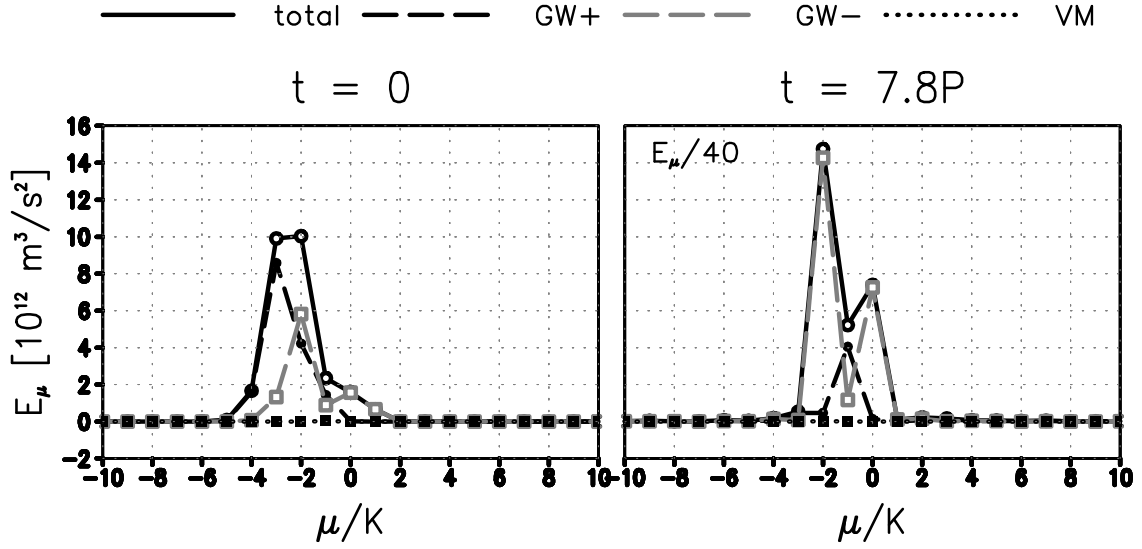


Figure 7.10: From the integration of the HGW with initial  $a = 0.7$  perturbed by its leading large-scale parallel NM, the decomposition of the energy density of the eddy component at the horizontal wavenumber  $\kappa_{\parallel} = k_{\parallel}$  into its contributions from the corresponding free NMs at the wavenumbers  $\mu$  in HGW-phase direction. The contributing free NMs are GWs with positive and negative intrinsic frequency, and the vortical mode. The left panel shows the decomposition of the parallel NM (i.e. at time  $t = 0$ ), while the right panel shows a late state at  $t = 7.8P$ . There all energies have been divided by a factor 40.

wavenumbers between  $\mu = -4K$  and  $\mu = K$ . A resonant first-order wave-wave interaction between any two of these modes (labelled by the indices 1 and 2) and the basic HGW is possible if they have wavenumbers  $\mathbf{k}_{1,2}$  and frequencies  $\tilde{\omega}_{1,2}$  so that

$$\mathbf{k}_1 \pm \mathbf{k}_2 = (0, 0, K) \quad (7.1)$$

$$\tilde{\omega}_1 \pm \tilde{\omega}_2 = 0 \quad , \quad (7.2)$$

remembering that in the reference system chosen the basic HGW has zero frequency. The respective modal frequencies are shown in Fig. 7.11. One sees two possible pairs of modes allowing a resonant difference interaction. These are the GW with positive intrinsic frequency (GW+) at  $\mu = -3K$  and the GW with negative intrinsic frequency (GW-) at  $\mu = -2K$ , and the GW+ at  $\mu = -2K$  and the GW- at  $\mu = -K$ . Their eigenfrequencies are also sufficiently close to that of the unstable parallel NM ( $0.016 \text{ s}^{-1}$ ) to allow an interpretation of the dynamics of the NM via resonant wave-wave interactions. Similar

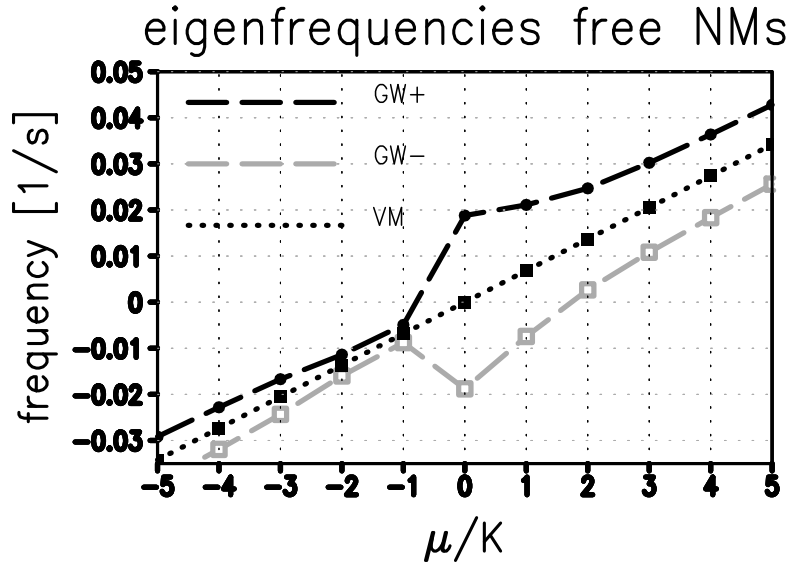


Figure 7.11: Within the coordinate system chosen here for the representation of the dynamics of the basic HGW so that it is stationary, the eigenfrequencies of the free NMs (GWs with positive and negative intrinsic frequency, and the vortical mode) at horizontal wavenumber  $\kappa_{\parallel} = k_{\parallel}$  and vertical wavenumber  $\mu$ .

findings also apply to the leading transverse NM, there however with the dominant effect coming from resonant interactions between a free GW, a vortical mode, and the basic HGW (not shown).

The structural development of the buoyancy fields in the two integrations is shown in Fig. 7.12. In the case of the HGW perturbed by the large-scale parallel NM one sees a transition from the highly turbulent phase into a late state which is characterized by a dominance of the horizontal and vertical wavenumbers  $\kappa_{\parallel} = \pm k_{\parallel} = \pm 2\pi/\lambda_{\parallel}$  and  $\mu = \pm 2K$ , respectively. The decomposition of the horizontal-wavenumber part at  $\kappa_{\parallel} = k_{\parallel}$  into the various free NMs at the respective vertical wavenumbers (right panel of Fig. 7.10) identifies as dominant structure the GW- at  $\mu = -2K$ , which seemingly survives as the dominant component from the various contributors in the resonant triads in the initial NM, followed by a contribution from the GW- at  $\mu = 0$ , and one from the GW+ at  $\mu = -K$ , while the initially especially prominent GW- at  $\mu = -3K$  has virtually disappeared. Transforming the results back into the geostationary reference frame one can find that the resulting wave (GW- at  $\mu = -2K$ ) has an inclination angle  $\Theta \approx 83^\circ$ , and

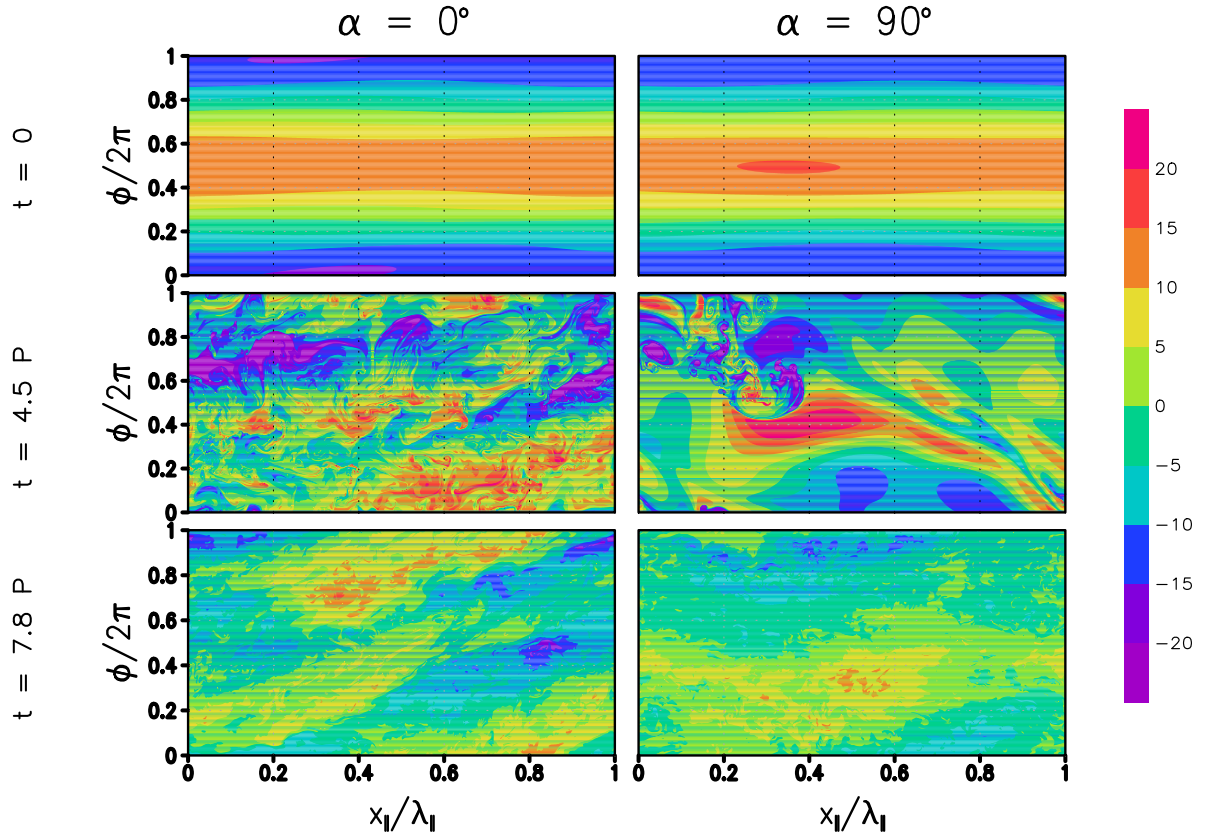


Figure 7.12: From the two integrations shown in Fig. 7.9, the normalized buoyancy field  $b/N$  at the three time instances  $t = 0$  (top row),  $t = 4.5P$  (middle), and  $t = 7.8P$  (bottom). Units are m/s.

thus has a steeper phase propagation than the original HGW. Seemingly the initial NM structure can only give limited clues on the final outcome of the wave-wave interactions here. Lastly also the turbulent-diffusive losses shall be documented, which is done in Fig. 7.13. One sees that also here both the eddy dissipation and the eddy diffusion reach values of several 10mW/kg, which is for the turbulent dissipation rates quite typical for turbulence measured in the middle atmosphere (Lübken, 1997; Müllemann et al., 2003).

## 7.2 Singular vectors

For an overview of the possible impact of SVs on HGWs the latter have, at initial  $a = 0.7, 1.4$  been perturbed by their leading parallel and transverse SVs for an optimization time  $\tau = 5\text{min}$ , i.e. about one Brunt-Vaisala period  $2\pi/N$ . As shown in chapter 5 the

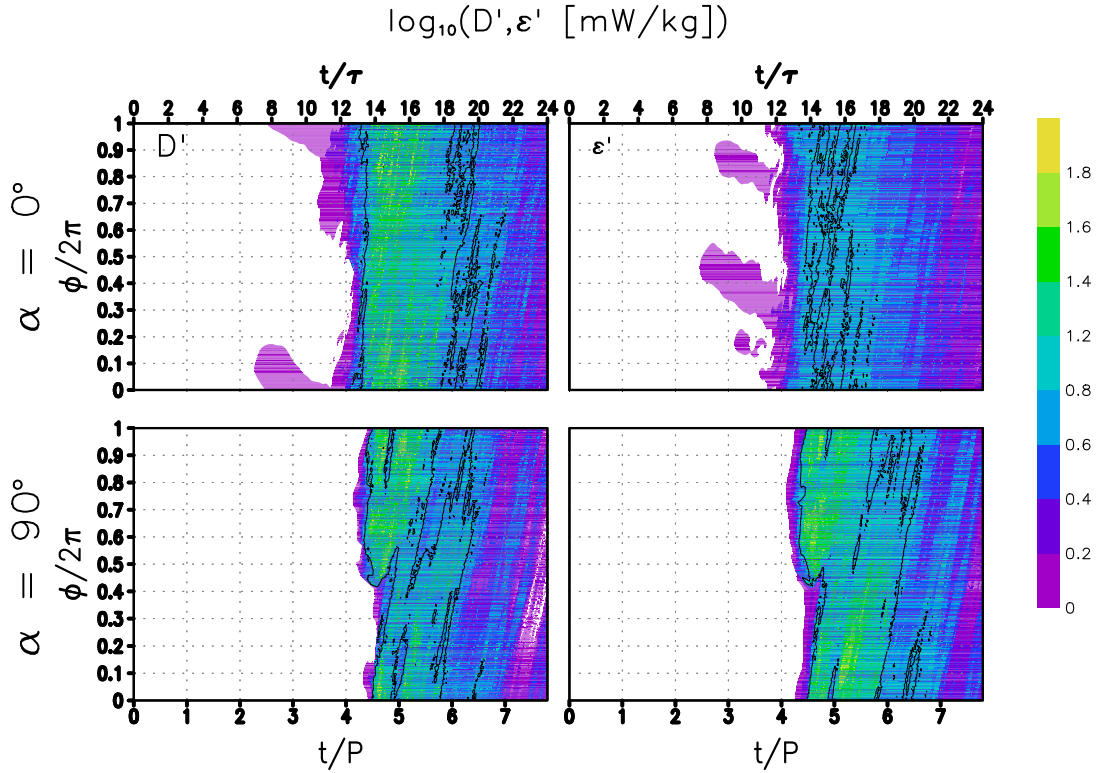


Figure 7.13: From the integrations shown in Fig. 7.9 after a perturbation of the HGW with  $a = 0.7$  by the leading large-scale parallel NM (upper row) or the leading transverse NM (lower row), the dependence of the turbulent eddy diffusion rate  $D'$  (left column) and the turbulent dissipation rate  $\epsilon'$  (right) on time and HGW phase. Shown is  $\log_{10}$  of these quantities in units of mW/kg. The contours are in steps of 1, beginning at 1.

strongest optimal growth for this  $\tau$  is found for  $\alpha = 90^\circ$ . The horizontal wavelengths of all SVs, identical to the respective horizontal domain extension in the simulation, are given in table 7.1. For larger  $\tau$  the leading SV converges more and more towards the leading NM. In the present cases the SVs have much shorter horizontal scales than the leading NMs so that also the NM behavior they might finally converge to cannot be as vigorous as shown above. For an oversight the initial strength of the SVs has been chosen so that its peak relative energy density  $A_{SV}^2$ , defined in analogy to  $A_{NM}^2$  above, was either  $10^{-2}$ ,  $10^{-1}$ , or 1.

The time dependent HGW amplitude obtained in the simulations is shown in Fig. 7.14. Clearly the SV impact on the HGW is weaker than that from the leading NMs.

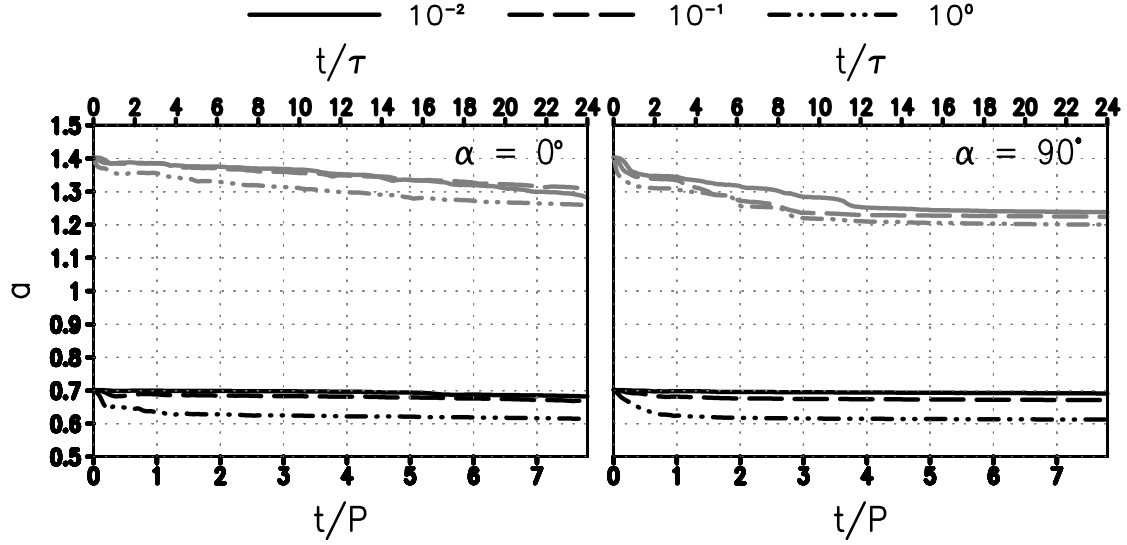


Figure 7.14: From the simulations of an HGW with an initial amplitude with respect to the overturning threshold  $a = 0.7$  (black lines) or  $1.4$  (grey) perturbed by its leading parallel (left panel) or transverse (right) SV (for optimization time  $\tau = 5\text{min}$ ) with relative peak energy density  $A_{SV}^2$  either  $10^{-2}$ ,  $10^{-1}$ , or  $10^0$ , the time dependence of the HGW amplitude developing after the perturbation. The wave period is  $P = 920\text{s}$ .

This has several reasons. One is that the SV itself has not only smaller horizontal, but also smaller vertical scales. As also shown in chapter 5, all SVs have more or less the form of sharply peaked pulses with a very narrow extent in HGW phase. Therefore their impact on the HGW can only be very local, the more so as the convergence of the SV towards the leading NM (at the horizontal wavelength of the SV) is typically very slow (see chapter 5). Therefore the SV impact is typically hampered by nonlinear processes before it can show a major effect. An example is shown in Fig. 7.15 where one can see the time development of the amplification rate decomposition from the simulation of the HGW with  $a = 1.4$  perturbed by its leading parallel or transverse SV. The feature of interest here is the rather early departure from the regular behavior characterizing the linear growth phase documented in chapter 5, especially the early impact from the viscous-diffusive damping.

The latter has, however, a measurable effect. As an example, Fig. 7.16 shows the dependence of  $\epsilon'$  and  $D'$  on time and HGW phase, from the integration of the HGW

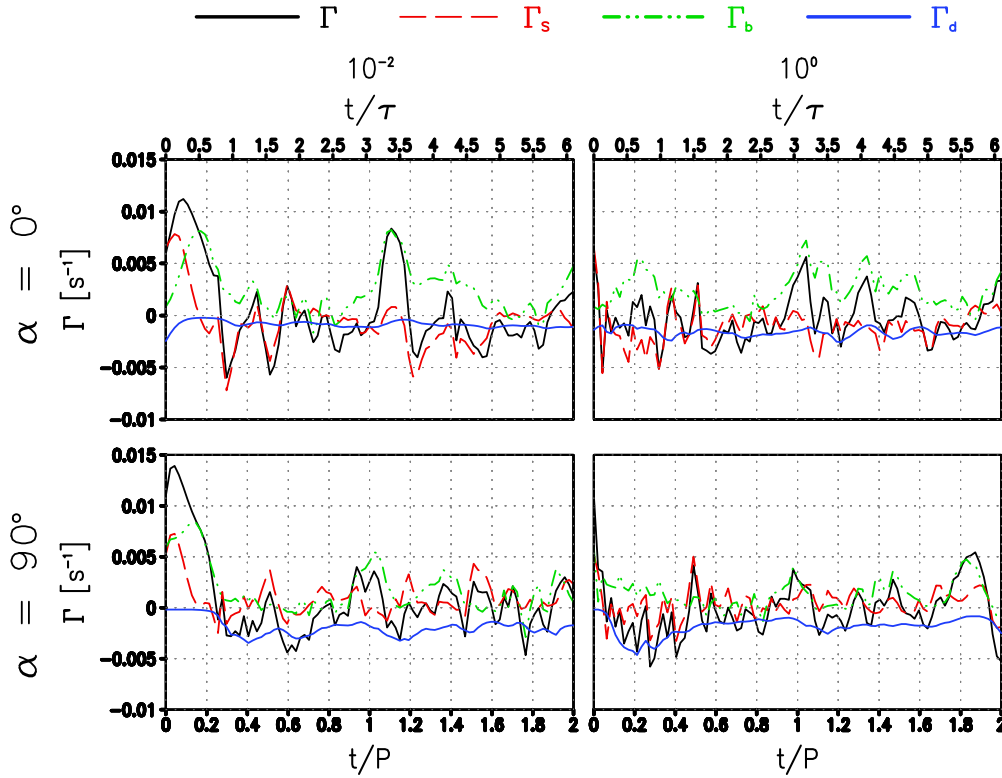


Figure 7.15: From the integrations in Fig. 7.14, of the HGW with  $a = 1.4$  perturbed by its leading parallel (top row) or transverse (bottom) SV with initial relative peak energy density  $A_{SV}^2$  either  $10^{-2}$  (left column) or  $10^0$  (right), the decomposition of the instantaneous amplification rate  $\Gamma$  into its contributions from convective production  $\Gamma_b$ , shear production  $\Gamma_s$ , and viscous-diffusive losses  $\Gamma_d$ .

perturbed by its leading transverse SV with  $A_{SV}^2 = 10^0$ . One sees that values of several 100mW/kg are reached, and that this happens earlier than in the NM cases. As was to be expected from the linear dynamics, both  $\epsilon'$  and  $D'$  are confined to sharply peaked pulses. These are apparently moving through the model domain at the negative phase speed of the HGW, i.e. in reality they seem to be frozen in the flow while the HGW moves over them. Perhaps interesting to see is that repeatedly periods of little viscous-diffusive damping, when the SV is near  $\phi = \pi$ , alternate with periods of stronger damping, when the SV is near  $\phi = 0, 2\pi$ . Returning to Fig. 7.15 one sees that the stronger active phases are preceded by a positive energy input from mainly convective production, when the SV 'passes'  $\phi = 3\pi/2$ , but also shear production near  $\phi = 2\pi$ . Similar results are obtained

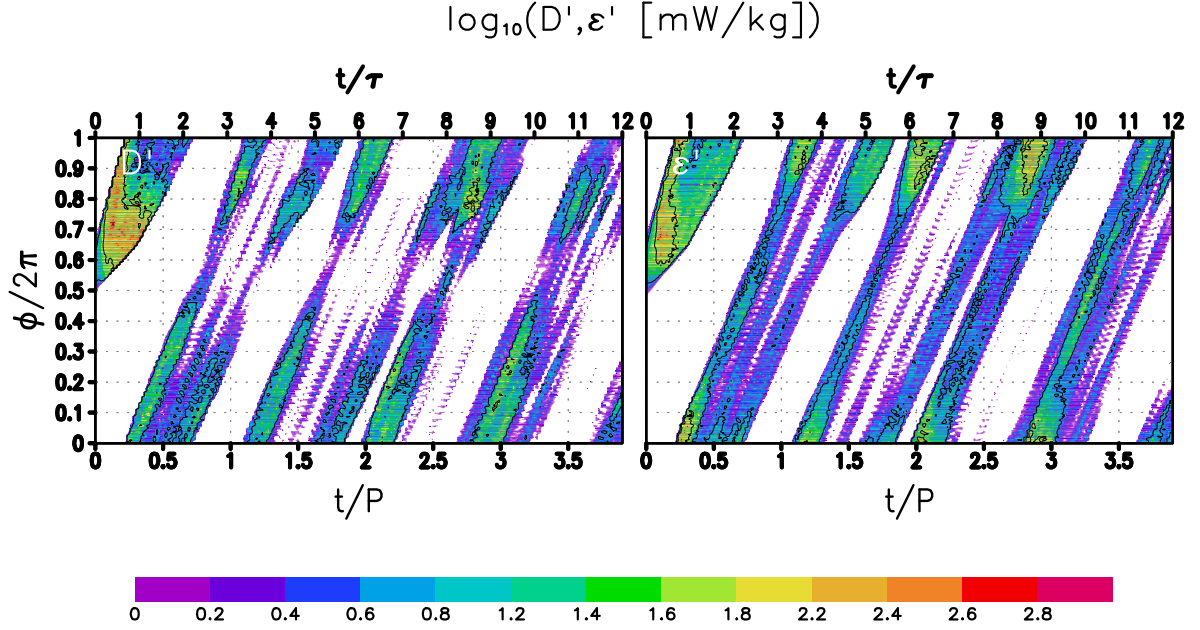


Figure 7.16: From the integration of an HGW with  $a = 1.4$ , perturbed by its leading transverse SV for  $\tau = 5\text{min}$  (initial relative peak energy density  $A_{SV}^2 = 10^0$ ), as also in Figs. 7.14 and 7.15, the dependence of the turbulent eddy diffusion rate  $D'$  (left panel) and the turbulent dissipation rate  $\epsilon'$  (right) on time and HGW phase. Shown is  $\log_{10}$  of these quantities in units of mW/kg. The contours are in steps of 1, beginning at 1.

for the HGW with initially  $a = 0.7$ , then however with values for  $\epsilon'$  and  $D'$  of the order of several 10mW/kg (not shown). SVs thus seem to be of minor importance for the problem of HGW damping, but they can still lead to considerable turbulent dissipation rates within the range of observed values. Especially the fact that in the mesosphere turbulence is often observed in rather thin layers (Müllemann et al., 2003; Strelnikov et al., 2003) indicates that SVs might there still be of relevance for the problem of turbulence onset. One should also remember that the range of dissipation rates measured there is between 1 and  $10^3\text{mW/kg}$ , which the simulations again seem to be consistent with.

### 7.3 Summary

The primary nonlinear dynamics resulting from a perturbation of an HGW ( $\Theta = 70^\circ$ ) by its most important NMs or SVs has been studied in this chapter by direct numerical



simulations (DNS). Since the effect of possible secondary instabilities has been neglected, the DNS could use the same 2.5D approach as in the previous chapter. Viscosity and diffusivity, as well as the HGW wavelength were again given values typical for the upper mesosphere.

Similar to the results from Fritts et al. (2003, 2006) it is found that both statically unstable and statically stable HGWs can decay considerably after a perturbation by NMs. For statically unstable HGWs the NM of greatest impact is the leading transverse NM which is driven both by shear and convective production, but more by the former. Interestingly the same final HGW amplitude  $a_\infty \approx 0.3$  is reproduced in the present 2.5D approach as identified by the authors above in their 3D simulations. One might thus hope that 2.5D simulations can be a helpful tool in studies of GW breaking which might supplement the most comprehensive analyses using 3D DNS.

Also in agreement with the authors above the instability of a statically stable HGW ends in the transfer of energy from that wave into another parallel wave ( $\alpha = 0^\circ$ ) which has (in the present case) about half the wavelength in the direction of HGW phase propagation, and twice the wavelength in the direction orthogonal to that, yielding an inclination angle near  $\Theta \approx 83^\circ$ . The turbulent, seemingly resonant, wave-wave interaction thus results in energy transfer from the HGW into another one with steeper phase propagation. The present study teaches us that this process is due not to the impact of the leading parallel NM but of a larger-scale parallel NM. A comparison between the impact of the two patterns indicates that the former is, due to its smaller scales, impeded earlier in its growth by nonlinear secondary instabilities, resulting in rapid energy transfer to even smaller scales and viscous-diffusive losses (not shown).

As for the impact of the most prominent short-term SVs, it is found that these are considerably less effective in initiating HGW decay. The main reason for this is the smaller scale of SVs in comparison to NMs, so that their effect on the HGW is only local and thus slower (as the HGW propagates over the SV). This is rather soon blocked by a nonlinear decay of the SV, resulting in turbulent dissipation and diffusion of magnitudes which are, as well as those obtained from the NM integrations, often in the range of values (between 1 and  $10^3 \text{ mW/kg}$ ) observed in the mesosphere (Lübken, 1997; Müllemann et al.,

2003). Also here, however, a similar caveat as in chapter 6 applies in that also the spectra obtained from the simulations in this chapter exhibit a considerable anisotropy between the horizontal and vertical flow-field components (not shown) which is inconsistent with the basic assumptions behind the retrieval of the turbulent dissipation rates from relative density fluctuations measured by in-situ rocket soundings. Beyond that, perhaps an interesting aspect is that the turbulence from SV decay is typically, as the SV itself, more locally confined. SVs might thus be helpful in explaining the layering often observed in mesospheric turbulence.

# Chapter 8

## Summary and conclusions

With the intent to improve our present understanding of GW breaking in the atmosphere and ocean the work summarized in this thesis has first delved into the corresponding linear theory, and then moved on to extend its results to the nonlinear domain. Perhaps a case to be made on that basis is how helpful it can be to take this kind of systematic approach. It turned out to be decisive for finally being able to also interpret many features of the complex nonlinear simulations. The outcome is a clearer and more complete oversight of the characteristics of GW breaking than we had before.

An important extension of the linear theory has been achieved by the application of generalized stability theory (Farrell and Ioannou, 1996a,b) to GWs. The thesis gives an oversight of the possible optimal perturbations (or SVs), investigates their dynamics, and compares them, where applicable, to the corresponding NMs. It is found that quite strongly growing SVs exist even in cases where, as for statically and dynamically stable IGWs, no NM instabilities are found. With regard to the interpretation of turbulence measurements in cases without a clear respective instability (Müllemann et al., 2003, e.g.) this enlarges the range of possibilities we have. So far the only way to understand such measurements on the basis of GW breaking was to assume the existence of an unstable HGW. Indeed, the DNS show that the breaking of statically and dynamically stable IGWs initialized by SV perturbations can lead to turbulent dissipation rates consistent with available observations. It also leads to an IGW decay far below presently employed instability thresholds which present parameterization schemes do not yet have on the list.

Certainly this is conditioned on the GW being exposed to perturbations of sufficient initial strength, but a scenario where this could be the case is that of the GW moving into a region with fossil turbulence from a previous breaking event.

Conceptually the linear theory turns out to be quite enlightening. Especially attractive is the possibility to understand important aspects of the core dynamics of SVs for IGWs on the basis of an analytic theory for a stratified shear layer with reduced static stability. Based on related work by Farrell and Ioannou (1993a,b) and Bakas et al. (2001) for shear layers without reduced static stability the fundamental processes at work are found to be the statically enhanced Orr and roll mechanism, each of them interacting in a specific way with the shear in the wave, but substantially aided in doing so by a vertical convective transport due to the reduced static stability. Based on the analytic theory important aspects of the non-simplified optimal-growth process can be understood, be it with regard to the dependence on the optimization time, the detailed mechanisms, or the NM interference at the heart of the whole.

Going beyond the shear-layer approximation, other phenomena are identified in the linear theory for SVs of IGWs which help in interpreting the nonlinear DNS. Among these is a merging of the Orr and roll mechanisms in the dynamics of the transverse short-term SV which turns out to be the most effective perturbation in the nonlinear simulations of statically and dynamically stable IGWs. This perturbation also exhibits an interesting critical-layer behavior, impeding a substantial radiation of the SV from the IGW, but also explaining the transport barrier for the turbulent energy found in corresponding DNS.

As another linear mechanism, ducting generally prevents the other short-term SVs from radiating, but for SVs for longer optimization times it is shown and explained how all but the transverse SVs take a time development leading to the radiation of secondary GWs by a basic IGW packet, although the latter does not exhibit any NM instability. This offers an alternative mechanism for a mesospheric GW source to the excitation of gravity waves by ageostrophic body forcing resulting from GW breakdown (Vadas and Fritts, 2001; Zhou et al., 2002) or by normal-mode instabilities of statically unstable IGWs (Kwasniok and Schmitz, 2003). Predictions are made about the scale dependence of this radiation on its azimuth angle which might be checked in empirical tests.

Special emphasis should be given to the importance of the roll mechanism. It turns out that the spatial distribution of the turbulence in a decaying IGW is to a large part controlled by the action of this mechanism in the elliptically polarized flow field of the IGW. A specific feature resulting from this is that a perturbation preferentially grows in turbulent energy in the horizontal flow component transverse to its direction of propagation, but parallel to the sheared wind, once again offering the possibility of an experimental test. It thus even leads to a conspicuous anisotropy in the turbulent spectra which might, however, disappear once the impact of secondary 3D instabilities is taken into account.

Similarly, the decay of HGWs can also be understood better on the basis of the linear theory. In agreement with corresponding predictions transverse NMs turn out to be most important for the breaking of a statically unstable HGW, and parallel NMs take this role for statically stable HGWs. Due to its strong local confinement the SV feedback on the HGW is rather weak. As also visible in the linear theory, however, the SVs take the character of thin turbulent layers frozen in the flow, with dissipation rates which can, depending on the initial perturbation level, be sufficiently strong so that SVs might contribute to the explanation of the conspicuous layering of turbulence often seen in the middle atmosphere (Müllemann et al., 2003; Strelnikov et al., 2003, e.g.).

A special case shall also be made for the type of DNS done here. Based on the linear results it is 2.5D, i.e. the GW is perturbed specifically by either a NM or a SV, so that the spatial dependence is restricted to the direction of phase propagation of the GW and the horizontal direction of propagation of the perturbation. The simulated velocity field, however, is fully 3D, and one is not limited to the simulation of the impact of perturbations propagating in the same plane as the GW. True, one might expect that 3D secondary instabilities will eventually modify the results from these DNS, but the latter provide a reference frame within which fully 3D simulations can be discussed more easily. As an example, several findings from the 3D DNS of breaking HGWs by Fritts et al. (2003, 2006) are reproduced, with the difference that we can now say which perturbation they can be attributed to. This is not to say that 3D simulations are not necessary, on the contrary they are indispensable for providing a complete picture, but 2.5D DNS seem to be an additional helpful tool.

In order to round up the reference to empirical findings, the dominance of the transverse perturbations of IGWs, especially of the NMs for  $a > 1$ , might help explaining the wavelengths and preferentially more or less transverse orientation of airglow ripples typically observed in conjunction with a statically unstable IGW (Hecht et al., 1997, 2000). Another observational fact of interest are the turbulent dissipation rates obtained from in-situ density measurements in the middle atmosphere (Lübken, 1997; Müllemann et al., 2003). These are typically between 1 and  $10^3 \text{ mW/kg}$ , which is also the range of values obtained in the simulations. This comparison, however, has to be seen with a bit of caution, since the turbulent spectra obtained here also exhibit a considerable anisotropy between the horizontal and the vertical flow, which is inconsistent with the basic assumptions behind the retrieval process of the turbulent dissipation rates from the density fluctuation spectra. This is one problem which should be addressed in the future.

So what have we learned so far which might be relevant for parameterizations? Perhaps the most important message is that wave breaking sets in earlier, and that the GW deposits much more of its momentum than typically assumed nowadays. Partly this was already clear from the previous linear NM theory of HGW instability (Mied, 1976; Klostermeyer, 1982, 1983, 1991; Lombard and Riley, 1996; Sonmor and Klaassen, 1997) and corresponding 3D DNS by Fritts et al. (2003, 2006), but it is supplemented by the additional option of IGW decay due to the impact of nonmodal perturbations, and as a whole none of these findings has yet found its way into a parameterization scheme. Unfortunately, a major problem remaining is the question as to whether it is possible to understand and predict the final amplitude of the GW, and whether and which other GWs it produces in the course of the process. Next to the GW properties, this also seems to be sensitively dependent on the specific initial perturbations and their strength. Much work remains to be done here.

Nonetheless, it is the author's belief that the systematic approach taken here, from the linear theory to the 2.5D DNS, was already able to shed more light on the GW stability problem. It seems worthwhile to continue following this path. An important aspect to be studied systematically are secondary instabilities indeed, to all expectations leading to a full three-dimensionalization of the turbulent fields (Klaassen and Peltier, 1985; Winters

and D’Asaro, 1994; Andreassen et al., 1994; Fritts et al., 1994). As an example, it will be interesting how much of the spectral anisotropy found here will also be obtained under such conditions. Another task that deserves attention in the future is the certainly difficult one of the parameterization of turbulence in breaking GWs. The available DNS data might be used for testing and improving corresponding sub-grid-scales scheme so that eventually LES models (Germano et al., 1991; Lilly, 1992; Ferziger, 1996; Meneveau et al., 1996, e.g.) might be available which could be applied with confidence to the problem. This might then open the option of studies of whole spectra of GWs developing both in space and time, a scenario which is presumably of great relevance. Once this is possible, but probably only then, we might gather new hope for more trustworthy GW parameterization schemes than the ones we have at present.

**Acknowledgements:** I most gratefully acknowledge the continuous support by Prof. Gerhard Schmitz who not only stimulated and accompanied this thesis but also was a mentor of great importance for my scientific and professional development.

Among the many colleagues at IAP who influenced this work in some way or other I foremost want to mention with appreciation Dr. Erich Becker, my officemate for now more than 13 years, Dr. Markus Rapp, Prof. Franz-Josef Lübken, and Dr. Frank Kwasniok. Beyond that, the friendly environment provided first of all by the colleagues from the theory section, but also by the institute as a whole, was a background helping in getting over all the minor or major troubles which quite inevitably go along with scientific research, at least to my experience. Specifically this also includes the administration and the technical staff who are extraordinarily successful in keeping the day-to-day technicalities away from the scientists at IAP.

I also want to mention the colleagues from my previous incarnation in geophysical fluid dynamics, most importantly Grant Branstator and Theo Opsteegh, whose company was of help not only in acquiring techniques which continue to be useful in my present work, but also in shaping me in my approach to the mysteries of nature as a whole.

Last but absolutely not least I thank my wife Sabine and our two children Benedikt and Frederike. They showed a lot of tolerance with a family member often absent either physically or in thoughts, and their warming company is an essential of my happy life.

# Appendix A

## Technical aspects of the algorithms for normal modes and singular vectors

For not too high-dimensional problems one can calculate NMs or optimal perturbations directly via an eigenvalue analysis of  $\mathcal{A}$  or a singular value analysis of  $\mathcal{L}$ , respectively. For the latter one needs the propagator matrix which can either be determined by initializing the tangent linear model with all possible unit vectors or (in the case of a time-independent background) by first doing an eigenvalue analysis of  $\mathcal{A}$ , transforming the initial perturbation to the eigenvector basis via

$$\mathbf{x}(0) = \sum_{\nu=1}^N a_{\nu}(0) \mathbf{n}_{\nu} \quad , \quad (\text{A.1})$$

integrating the tangent linear model analytically using

$$a_{\nu}(t) = a_{\nu}(0) e^{-i\omega_{\nu}t + \gamma_{\nu}t} \quad , \quad (\text{A.2})$$

and transforming back to the original grid-point representation. In the case of large problems where storage of  $\mathcal{A}$  and  $\Phi$  is too demanding for the available computer memory iterative techniques are required. Since high-dimensionality is a problem e.g. in the SV calculations for the full two-dimensional IGW packet reported in chapter 4 such techniques have been used in the present analysis. Provided only a few leading patterns are desired this can also speed up the calculations.



For the calculation of the leading NMs of a time-independent background the fact is used that these are also eigenvectors of  $\Phi(\tau)$  with eigenvalue  $\exp(-i\omega_\nu\tau + \gamma_\nu\tau)$ . With the help of the software package ARPACK (Lehoucq et al., 1998) a desired number of leading eigenvectors (with largest eigenvalue modulus  $\exp(\gamma_\nu\tau)$ ) have been determined via an implicitly restarted Arnoldi Method. In this approach  $\Phi(\tau)\mathbf{q}$  is required for initial states  $\mathbf{q}$  determined in the algorithm at each iteration. Integrating from  $t = 0$  to  $t = \tau$  this mapping is obtained from the linear model. The iterations stop when the required NMs, eigenfrequencies, and growth rates have been calculated at a chosen accuracy.

The same software package is also employed in the determination of a required number of leading optimal perturbations. For this one solves the eigenvalue problem (3.5). As in the NM analysis, ARPACK requires the user at each iteration to provide  $\bar{\mathcal{L}}^t \mathcal{L}\mathbf{q}$  for initial states  $\mathbf{q}$  determined by the algorithm. After having obtained  $\mathbf{r} = \bar{\mathcal{N}}^t \mathcal{N}\Phi(\tau)\mathcal{N}^{-1}\mathbf{q}$  with the help of the linear model this necessitates also taking the product  $\bar{\Phi}^t(\tau)\mathbf{r}$ . For this the adjoint Boussinesq model is used which has been extracted from the linear model code with the help of the adjoint model compiler TAMC (Giering and Kaminski, 1998). Also in this analysis the iterations stop when a required accuracy for the desired number of leading optimal perturbations is reached.

There is one additional aspect to the problem here which needs special treatment. The Boussinesq equations require the flow field to be non-divergent, i.e. purely rotational. The pressure is determined so that the divergence of a flow field is conserved. In the search of the optimal rotational perturbation one must therefore modify the propagator matrix by first decomposing the initial flow field  $\mathbf{v}$  into its rotational and its divergent part. For this a velocity potential  $\chi$  has been determined such that  $\nabla^2\chi = \nabla \cdot \mathbf{v}$ . The projection is done by mapping  $\mathbf{v} \mapsto \mathbf{v} - \nabla\chi$ . Since the kinetic energy of the flow field can be split up into its contributions from the rotational part and the divergent part, this leads to a reduction of the kinetic energy. By maximizing the energy growth in the course of the integration the SV algorithm then automatically identifies among all initial flow fields with the same rotational part their least energetic, i.e. purely rotational, member.

## Appendix B

# Optimal growth in the stratified-shear-layer approximation

Using  $E_{klm}$  as norm one finds from application of (4.22) and (4.26)–(4.28) that

$$E_{klm} = \bar{\mathbf{a}}^t \bar{\Phi}^t \mathcal{M} \Phi \mathbf{a} \quad , \quad (\text{B.1})$$

where

$$\mathbf{a} = (a_+, a_-, a_v)^t \quad (\text{B.2})$$

$$\bar{\Phi}^t \mathcal{M} \Phi = \frac{e^{-2D}}{2} \begin{pmatrix} g^{1/2} e^{-i(\phi - \bar{\phi})} & g^{1/2} e^{i(\bar{\phi} + \phi) \frac{\epsilon_-}{\epsilon_+}} & g^{1/4} e^{i\bar{\phi} \frac{\beta_c}{\sqrt{\epsilon_+ N_{tot}}}} \\ g^{1/2} e^{-i(\phi + \bar{\phi}) \frac{\epsilon_-}{\epsilon_+}} & g^{1/2} e^{i(\phi - \bar{\phi})} & -g^{1/4} e^{-i\bar{\phi} \frac{\beta_c}{\sqrt{\epsilon_+ N_{tot}}}} \\ g^{1/4} e^{-i\phi \frac{\beta_c}{\sqrt{\epsilon_+ N_{tot}}}} & -g^{1/4} e^{i\phi \frac{\beta_c}{\sqrt{\epsilon_+ N_{tot}}}} & 1 \end{pmatrix} \quad (\text{B.3})$$

with  $\epsilon_- = 1 - \beta_c^2 / |N_{tot}|^2 - |N_{tot}|^2 / N^2$ .  $\mathcal{M}(t=0)$  results from (B.3) by setting  $g = 1$ ,  $D = 0$ , and  $\phi = 0$ . The optimal perturbations are given by the three eigenvectors  $\mathbf{a}_\nu$  satisfying

$$\left( \bar{\Phi}^t \mathcal{M} \Phi \right) (\tau) \mathbf{a}_\nu = \sigma_\nu^2 \mathcal{M}(0) \mathbf{a}_\nu \quad (\text{B.4})$$

with a corresponding eigenvalue equation  $\det \left[ \left( \bar{\Phi}^t \mathcal{M} \Phi \right) (\tau) - \sigma_\nu^2 \mathcal{M}(0) \right] = 0$ . This yields a third-order polynomial for  $\sigma_\nu^2$  which can be solved analytically, albeit by rather complicated expressions for the eigenvalues. More interesting, however, is that in the two cases  $\beta_s = 0$  (parallel perturbation with  $g = 1$  and  $\phi = N_{tot} k \tau / \sqrt{k^2 + m^2}$ ) and  $\beta_c = 0$  (transverse perturbation) there is the exact solution  $\sigma_2^2 = \exp(-2D)$ . With this knowledge the

characteristic polynomial can be reduced to second order with the comparatively simple solutions

$$\sigma_{1,3}^2 = g^{1/2} e^{-2D} \left( \frac{\delta}{2} \pm \sqrt{\frac{\delta^2}{4} - 1} \right) \quad , \quad (\text{B.5})$$

where for  $\beta_s = 0$

$$\begin{aligned} \delta = & 2 - \frac{N^2}{4N_{tot}^2} \left( 1 - \frac{N_{tot}^2}{N^2} \right)^2 (e^{i\phi} - e^{-i\phi})^2 \\ & + \frac{\beta_c^2 N^2}{4N_{tot}^4} \left[ (e^{i\phi/2} - e^{-i\phi/2})^4 - \frac{N_{tot}^2}{N^2} (e^{i\phi} - e^{-i\phi})^2 \right] \quad , \end{aligned} \quad (\text{B.6})$$

and for  $\beta_c = 0$

$$\begin{aligned} \delta = & \frac{N^2}{4|N_{tot}|^2} \left( 1 + \frac{|N_{tot}|^2}{N^2} \right)^2 \\ & \times \left[ e^{-i(\phi-\bar{\phi})} + e^{i(\phi-\bar{\phi})} - \left( \frac{1 - |N_{tot}|^2/N^2}{1 + |N_{tot}|^2/N^2} \right)^2 (e^{-i(\phi+\bar{\phi})} + e^{i(\phi+\bar{\phi})}) \right] \quad . \end{aligned} \quad (\text{B.7})$$

In the limit  $\beta_c^2/|N_{tot}|^2 = 1/|\text{Ri}| \gg 1 \gg |N_{tot}|^2/N^2$  one obtains from (B.6)

$$\delta \approx \beta_c^2 N^2 / (4N_{tot}^4) (e^{i\phi/2} - e^{-i\phi/2})^4 \gg 1 \quad , \quad (\text{B.8})$$

whence results (4.29). Similarly one obtains (4.37) from (B.7) in the limit  $|N_{tot}|^2/N^2 \ll 1$ .

The structure of the optimal perturbations is derived by reinserting the growth factor into (B.4). One finds at  $\beta_s = 0$  for the  $i$ -th perturbation

$$\begin{aligned} \frac{a_{\pm}}{a_v} = & \frac{\beta_c}{\sqrt{\epsilon_+ N_{tot}}} \frac{1}{\left[ e^{-i(\phi-\bar{\phi})} - s_i^2 \right] \left[ e^{i(\phi-\bar{\phi})} - s_i^2 \right] - \frac{\epsilon_-^2}{\epsilon_+^2} \left| e^{-i(\phi+\bar{\phi})} - s_i^2 \right|^2} \\ & \times \left\{ \begin{aligned} & - (e^{i\bar{\phi}} - s_i^2) \left[ e^{i(\phi-\bar{\phi})} - s_i^2 \right] - \frac{\epsilon_-}{\epsilon_+} (e^{-i\bar{\phi}} - s_i^2) \left[ e^{i(\phi+\bar{\phi})} - s_i^2 \right] \\ & (e^{-i\bar{\phi}} - s_i^2) \left[ e^{-i(\phi-\bar{\phi})} - s_i^2 \right] + \frac{\epsilon_-}{\epsilon_+} (e^{i\bar{\phi}} - s_i^2) \left[ e^{-i(\phi+\bar{\phi})} - s_i^2 \right] \end{aligned} \right\} \quad , \end{aligned} \quad (\text{B.9})$$

where  $s_i^2 = e^{2D} \sigma_i^2$ . In the limit of  $\beta_c^2/|N_{tot}|^2 = 1/|\text{Ri}| \gg 1 \gg |N_{tot}|^2/N^2$ , and hence large  $s_1^2$ , this reduces for  $i = 1$  to (4.33). At  $\beta_c = 0$  the second optimal perturbation is just  $(a_+, a_-, a_v) = (0, 0, 1)$  while for  $i = 1, 3$  one obtains  $a_v = 0$  and

$$\frac{a_+}{a_-} = \frac{\epsilon_-}{\epsilon_+} \frac{s_i^2 - e^{i(\bar{\phi}+\phi)}}{e^{-i(\phi-\bar{\phi})} - s_i^2} \quad , \quad (\text{B.10})$$

where  $s_i^2 = e^{2D} g^{-1/2} \sigma_i^2$ . For  $i = 1$  this yields in the limit  $|N_{tot}|^2/N^2 \ll 1$  the approximate relation  $a_+ \approx -a_-$ , as long as  $s_1^2$  is large.

# Appendix C

## WKB theory for the explanation of the time dependence of the SV scales for monochromatic gravity waves

To a large degree, the time dependence of the scales in the various SVs discussed in chapter 5 can be understood on the basis of a standard WKB theory (Bretherton, 1966, 1971). This appendix first describes the theory in general, and then gives the applications.

### C.1 General theory

The WKB theory assumes that the spatial scale over which the wavelength of the SV varies is comparatively long. The same holds for the time scale describing variations of the period of the oscillations within the SV. One thus uses the ansatz

$$\begin{pmatrix} \mathbf{v} \\ b \end{pmatrix}(\phi, t) = \begin{pmatrix} \tilde{\mathbf{v}} \\ \tilde{b} \end{pmatrix}(\epsilon\phi, \epsilon t) e^{i\chi(\epsilon\phi, \epsilon t)/\epsilon} \quad , \quad (\text{C.1})$$

where  $\epsilon \ll 1$  is a slowness parameter and  $\chi$  the local phase of the wave packet<sup>1</sup>. One then introduces the slow spatial and time coordinates  $\Phi = \epsilon\phi$  and  $T = \epsilon t$ , defines the local frequency  $\omega = -\partial\chi/\partial T$  and the local wavenumber  $\mu = K\partial\chi/\partial\Phi$ , and inserts (C.1) into

---

<sup>1</sup>In chapter 4 it is additionally assumed that also  $\tilde{v}_\perp$  scales with  $\epsilon$ , which would certainly be more correct. For the discussion here, however, this does not make a difference.

(5.1)–(5.5). Assuming also the GW fields to only depend on  $\Phi$ , i.e. to be slowly dependent on the phase, and neglecting rotation, viscosity, and diffusion one finds to lowest order in  $\epsilon$  the WKB dispersion relation

$$\begin{aligned}\omega(\Phi, T) &= \tilde{\omega}[\mu(\Phi, T), \Phi] \\ &= U_\xi \kappa + V\lambda - \frac{\Omega}{K}\mu \pm N_{tot} \sqrt{\frac{\lambda^2 + (\kappa \sin \Theta + \mu \cos \Theta)^2}{\kappa^2 + \lambda^2 + \mu^2}},\end{aligned}\quad (\text{C.2})$$

which simply is the dispersion relation for GWs in a constant background flow without rotation, but with modified static stability  $N_{tot}^2 = N^2 + \partial B / \partial z$ , in the special rotated and translated reference system used in chapter 5. Since  $\partial \mu / \partial T = -K \partial \omega / \partial \Phi$  (C.2) also gives rise to the eikonal equations

$$\left( \frac{\partial}{\partial T} + c_g K \frac{\partial}{\partial \Phi} \right) \omega = 0 \quad (\text{C.3})$$

$$\left( \frac{\partial}{\partial T} + c_g K \frac{\partial}{\partial \Phi} \right) \mu = -K \frac{\partial \tilde{\omega}}{\partial \Phi}, \quad (\text{C.4})$$

where  $c_g = \partial \tilde{\omega} / \partial \mu$  is the group velocity of the perturbation. Along rays defined by this group velocity the frequency is therefore a conserved quantity, so that for any frequency the wavenumber  $\mu$  can be calculated from (C.2) as a function of  $\phi$ .

## C.2 Optimal perturbations of inertia-gravity waves

In the case of the SVs of IGWs one can use that, as shown in chapter 4, the frequency of the developing optimal perturbations is determined to a good approximation by the advection of the perturbation in its direction of propagation by the corresponding horizontal flow-field component at the statically least stable location  $\phi = 3\pi/2$ , i.e.  $\omega = U_\xi(\phi = 3\pi/2)\kappa$  (since  $V$  vanishes at this location). In addition, the phase velocity of the IGW  $\Omega/K$  is very small, so that it can be neglected in (C.2).

Assuming also  $\cos \Theta = 0$ , and  $\sin \Theta = 1$ , one finds for *parallel* SVs, where  $\lambda = 0$ , and assuming  $\kappa > 0$ ,

$$\frac{U_\xi(3\pi/2) - U_\xi}{N_{tot}/\kappa} = \pm \frac{1}{\sqrt{1 + \mu^2/\kappa^2}}. \quad (\text{C.5})$$

Obviously, since the left-hand side is always negative (for  $a < 1$ ), only the branch with the minus sign in front of the square root (the branch with upwards pointing group velocity

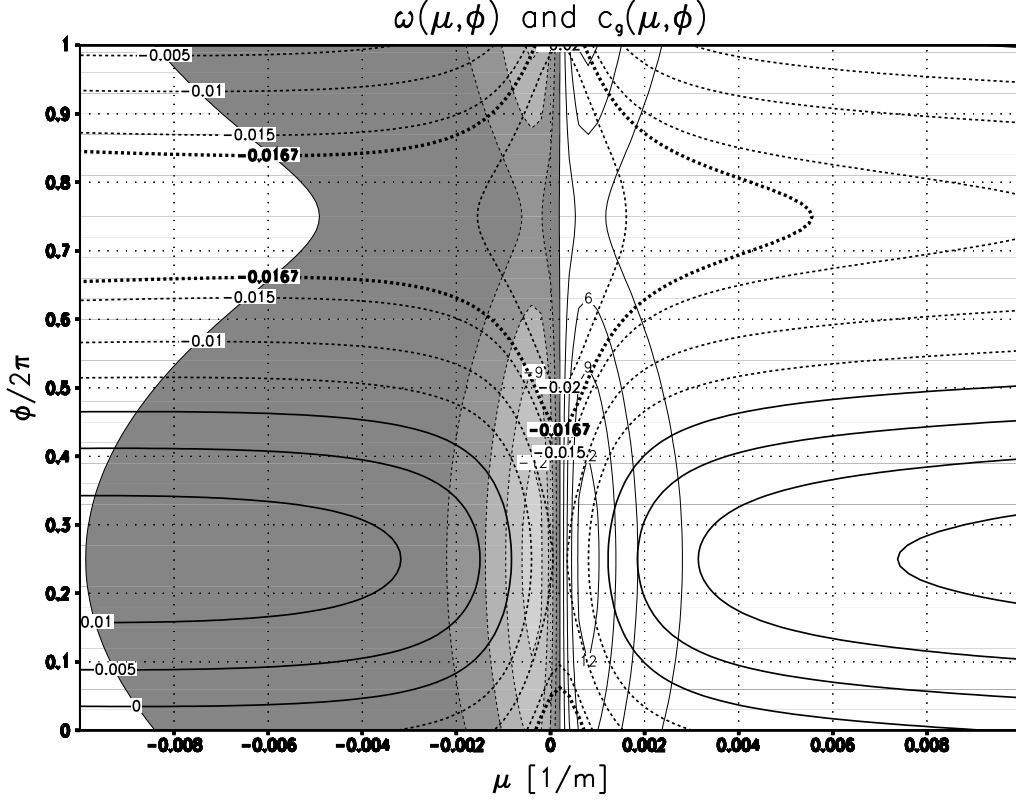


Figure C.1: For the parallel SV of the subcritical IGW ( $\Theta = 89.5^\circ$ ) with  $A = 0.55$  and  $a = 0.87$ , the dependence of frequency (in units of  $s^{-1}$ , thick contours) and group velocity (in units of  $m/s$ , thin contours, negative values indicated by shading), according to a WKB theory, on the IGW-phase  $\phi$  and the wavenumber  $\mu$  in phase direction. The isoline corresponding to the parallel SV for  $\tau = 30\text{min}$ , where  $\omega \approx -0.0167s^{-1}$ , is drawn extra fat. The movement of a ray is along isolines of constant frequency, while the velocity in  $\phi$ -direction is given by the group velocity.

at  $\mu > 0$ ) can satisfy this equation. Note that, the nearer one is to the maximum of  $U_\xi$  at  $\phi = \pi/2$ , the smaller  $\mu$  must be, so that near this location the vertical wavelength in the SV gets largest. Moreover, propagation through  $\phi = \pi/2$  is only possible if there

$$1 > \frac{U_\xi - U_\xi(3\pi/2)}{N_{tot}/\kappa} = \frac{4A}{\sqrt{1+a}} \frac{\kappa}{K} \quad . \quad (C.6)$$

Radiation is thus only possible for  $\kappa$  small enough. At  $A = 0.55$ , and thus  $a = 0.87$ , this is neither the case for the parallel SV for  $\tau = 5\text{min}$ , where  $\kappa/K = 9.5$ , nor for the parallel SV for  $\tau = 30\text{min}$ , where  $\kappa/K = 0.76$ . In the latter case, however, one is nearer to the radiation condition, so that energy can move close to  $\phi = \pi/2$ , explaining the near-vertical

structures at  $\phi = \pi/2$  in Fig. 5.15. For this case Fig. C.1 also shows the distribution of frequency and group velocity according to (C.2) in the  $(\mu, \phi)$ -plane. One also sees there that rays with  $\omega = U_\xi(\phi = 3\pi/2)\kappa \approx -0.167\text{s}^{-1}$  cannot propagate through  $\phi = \pi/2$ , but get progressively larger in scale (i.e. smaller in  $\mu$ ) as they approach this location.

Similarly one derives for *transverse* SVs, where  $\kappa = 0$ , and assuming  $\lambda > 0$ ,

$$-\frac{V\lambda}{N_{tot}} = \pm \frac{1}{\sqrt{1 + \mu^2/\lambda^2}} \quad . \quad (\text{C.7})$$

One sees directly that near the zero-lines of  $V$ , i.e. at  $\phi = \pi/2, 3\pi/2$ , the vertical scale of the SV collapses (i.e.  $\mu \rightarrow \infty$ ), leading to the critical-layer behavior visible for all transverse SVs of the IGW. Without neglect of the IGW phase velocity the divergence of  $\mu$  is modified to a development towards finite large wavenumbers (Broutman and Young, 1986), but the basic effect remains as described.

### C.3 The scale oscillation of parallel singular vectors in high-frequency gravity waves

The oscillation between weak and strong viscous and diffusive damping for the leading parallel SV for HGWs, e.g. visible for  $(\Theta, a) = (70^\circ, 1)$  in Figs. 5.17 and 5.21, is due to an oscillation of the scale of this perturbation in  $\phi$ -direction which can be seen in Fig. 5.20. It has the shape of a nearly monochromatic wave packet with a wavelength which, consistent with the observed time dependence of the viscous and diffusive losses, is especially small when it passes  $\phi = \pi/2$ , and which maximizes as the SV is near  $\phi = 3\pi/2$ . Also this behavior can be explained using the WKB theory.

Since the SV moves approximately with the negative phase velocity of the GW, i.e.  $c_g \approx -\Omega/K$ , the square root in (C.2), i.e. the intrinsic-frequency contribution, can be neglected, yielding

$$\mu = K (U_\xi \kappa - \omega) / \Omega \quad , \quad (\text{C.8})$$

since for parallel perturbations  $\lambda = 0$ . The spatial dependence of  $\mu$  thus results from that of  $U_\xi$ .

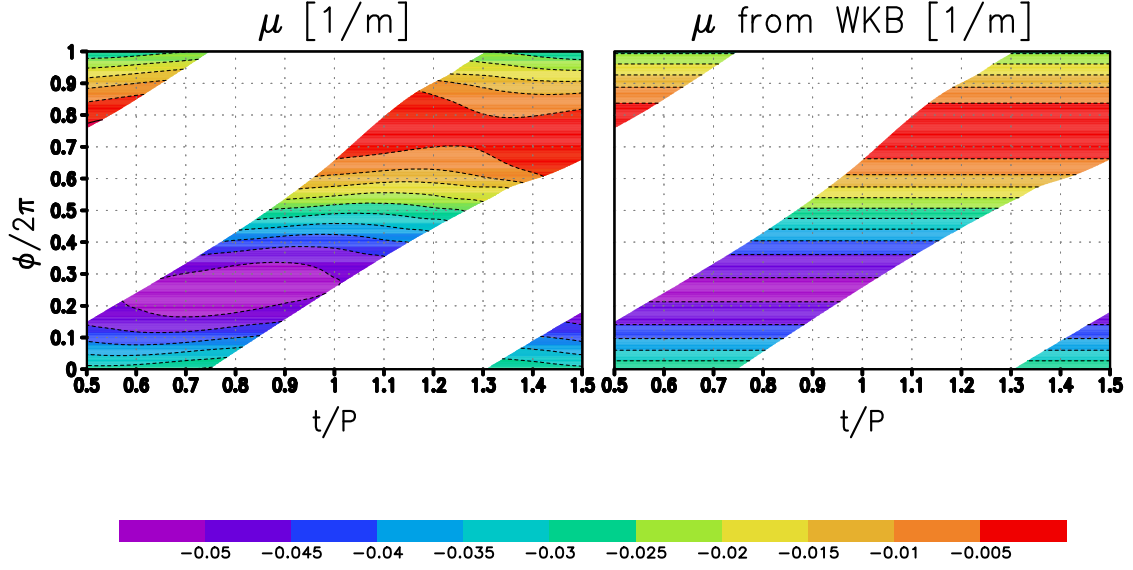


Figure C.2: Time dependence in the wavenumber  $\mu$  in  $\phi$ -direction in the sub-cycle of the short-term parallel SV for the GW with  $(\Theta, a) = (70^\circ, 1)$  also shown in Fig. 5.21, as diagnosed from the data of the linear model (left) or predicted from the WKB theory (right). The shading scale is defined in the shading bar.

For a test whether (C.8) actually describes the scale behavior of the parallel SV shown in figure C.2  $\mu(\phi, t)$  has been determined diagnostically by minimizing

$$C(\mu) = \left| K \frac{\partial}{\partial \phi} \begin{pmatrix} \mathbf{v} \\ b \end{pmatrix} - i\mu \begin{pmatrix} \mathbf{v} \\ b \end{pmatrix} \right|^2. \quad (\text{C.9})$$

Figure C.2 shows the result, agreeing quite well with the qualitative expectation of small  $\mu$  near  $\phi = 3\pi/2$  and large  $\mu$  near  $\phi = \pi/2$ . In the same manner one also could have determined the frequency  $\omega$  from time derivatives. It turns out, however, that the time oscillation in all fields is so regular that one can just count peaks, which gave a single period of about 35s. This has been inserted into (C.8), yielding the predicted wavenumber also shown in figure C.2.



# Appendix D

## Projection onto free normal modes

For a meaningful analysis of the horizontal mean and the eddies in the nonlinear simulations one can use an orthogonality property of the respective free normal modes of the inviscid-nondiffusive Boussinesq equations. Linearizing the latter about a fluid at rest with zero buoyancy and taking for the perturbation fields the ansatz  $(\mathbf{v}', b')(x_{\parallel}, \phi, t) = (\mathbf{v}, b) \exp \left[ i \left( \kappa_{\parallel} x_{\parallel} + \mu \phi / K - \tilde{\omega} t \right) \right]$ , i.e. with wavenumbers  $\kappa_{\parallel}$  and  $\mu$  parallel to the horizontal direction of propagation of the perturbation pattern and in GW-phase direction, respectively, and frequency  $\tilde{\omega}$ , one obtains, in a manner similar to chapter 5,

$$-i\hat{\omega}u_{\parallel} - f(\sin \Theta v_{\perp} - \sin \alpha \cos \Theta u_{\phi}) + i\kappa_{\parallel}p + b \cos \alpha \cos \Theta = 0 \quad (\text{D.1})$$

$$-i\hat{\omega}v_{\perp} + f(\sin \Theta u_{\parallel} + \cos \alpha \cos \Theta u_{\phi}) - b \sin \alpha \cos \Theta = 0 \quad (\text{D.2})$$

$$-i\hat{\omega}u_{\phi} - f(\sin \alpha \cos \Theta u_{\parallel} + \cos \alpha \cos \Theta v_{\perp}) + i\mu p - b \sin \Theta = 0 \quad (\text{D.3})$$

$$-i\hat{\omega}b + N^2(-\cos \alpha \cos \Theta u_{\parallel} + \sin \alpha \cos \Theta v_{\perp} + \sin \Theta u_{\phi}) = 0 \quad (\text{D.4})$$

$$i\kappa_{\parallel}u_{\parallel} + i\mu u_{\phi} = 0 \quad , \quad (\text{D.5})$$

where  $\hat{\omega} = \tilde{\omega} + \Omega\mu/K$  is the intrinsic frequency. The resulting eigenmodes are best obtained by first transforming the equations back into the geostationary  $(x, y, z)$  coordinate system. One obtains three solutions for each combination of  $\kappa_{\parallel}$  and  $\mu$ . One of these is the vortical mode with  $\hat{\omega} = 0$  and structure

$$(u, v, w, b) = \frac{\sqrt{2}Nf}{\sqrt{f^2m^2 + N^2(k^2 + l^2)}} \left( -i\frac{l}{f}, i\frac{k}{f}, 0, im \right) \quad , \quad (\text{D.6})$$

where  $(u, v, w)$  and  $(k, l, m)$  are, respectively, the velocity and wavenumber vector in the geostationary reference frame. The latter can be obtained from  $\kappa_{\parallel}$  and  $\mu$  via

$$k = \kappa \sin \Theta + \mu \cos \Theta \quad (\text{D.7})$$

$$l = \kappa_{\parallel} \sin \alpha \quad (\text{D.8})$$

$$m = -\kappa \cos \Theta + \mu \sin \Theta \quad (\text{D.9})$$

$$\kappa = \kappa_{\parallel} \cos \alpha \quad . \quad (\text{D.10})$$

The other solutions are free GWs with intrinsic frequency  $\hat{\omega} = \hat{\omega}_{\pm} = \pm \sqrt{[f^2 m^2 + N^2 (k^2 + l^2)] / (k^2 + l^2 + m^2)}$  and structure

$$(u, v, w, b) = \frac{m}{\sqrt{k^2 + l^2 + m^2}} \left( \frac{k + ilf/\hat{\omega}}{\sqrt{k^2 + l^2}}, \frac{l - ikf/\hat{\omega}}{\sqrt{k^2 + l^2}}, -\frac{\sqrt{k^2 + l^2}}{m}, iN \frac{N}{\hat{\omega}} \frac{\sqrt{k^2 + l^2}}{m} \right) \quad (\text{D.11})$$

The representation of the modes in the coordinate system used here can be obtained via the rotations

$$u_{\parallel} = u_{\xi} \cos \alpha + v \sin \alpha \quad (\text{D.12})$$

$$v_{\perp} = -u_{\xi} \sin \alpha + v \cos \alpha \quad (\text{D.13})$$

$$u_{\phi} = u \cos \Theta + w \sin \Theta \quad (\text{D.14})$$

$$u_{\xi} = u \sin \Theta - w \cos \Theta \quad . \quad (\text{D.15})$$

Having defined an energy-metric scalar product

$$\left\langle \begin{pmatrix} \mathbf{v} \\ b \end{pmatrix}_1, \begin{pmatrix} \mathbf{v} \\ b \end{pmatrix}_2 \right\rangle = \frac{\bar{\mathbf{v}}_1 \cdot \mathbf{v}_2}{2} + \frac{\bar{b}_1 b_2}{2N^2} \quad (\text{D.16})$$

for any two modes  $(\mathbf{v}, b)_{1,2}$  (the overbar denotes complex conjugation) one can easily check that the normal modes are orthonormal (most easily in the geostationary coordinate system). Among these the GW with  $(\kappa_{\parallel}, \mu) = (0, K)$  and downwards directed phase velocity is the basic GW of the problem. A decomposition into the contribution from the various free modes, and thus also extraction of that of the basic GW, can so be done by Fourier decomposition (into the contributions from the different  $\kappa_{\parallel}$  and  $\mu$ ) and straightforward projection.

# Bibliography

- Achatz, U., 2005: On the role of optimal perturbations in the instability of monochromatic gravity waves. *Phys. Fluids*, **17**, 094107 1–27.
- Achatz, U. and G. Schmitz, 2006a: Shear and static instability of inertia-gravity wave packets: Short-term modal and nonmodal growth. *J. Atmos. Sci.*, **63**, 397–413.
- 2006b: Optimal growth in inertia-gravity wave packets: Energetics, long-term development, and three-dimensional structure. *J. Atmos. Sci.*, **63**, 414–434.
- Alexander, M. J. and T. J. Dunkerton, 1999: A spectral parameterization of mean-flow forcing due to breaking gravity waves. *J. Atmos. Sci.*, **56**, 4167–4182.
- Andreassen, Ø., C. E. Wasberg, D. C. Fritts, and J. R. Isler, 1994: Gravity wave breaking in two and three dimensions. 1. Model description and comparison of two-dimensional evolutions. *J. Geophys. Res.*, **99**, 8095–8108.
- Bakas, N. A., P. J. Ioannou, and G. E. Kefaliakos, 2001: The emergence of coherent structures in stratified shear flow. *J. Atmos. Sci.*, **58**, 2790–2806.
- Becker, E. and G. Schmitz, 2002: Energy deposition and turbulent dissipation owing to gravity waves in the mesosphere. *J. Atmos. Sci.*, **59**, 54–68.
- 2003: Climatological effects of orography and land-sea heating contrasts on the gravity wave-driven circulation of the mesosphere. *J. Atmos. Sci.*, **60**, 103–118.
- Bender, C. M. and S. A. Orszag, 1978: *Advanced mathematical methods for scientists and engineers*. McGraw-Hill, New York.

- Boberg, L. and U. Brosa, 1988: Onset of turbulence in a pipe. *Z. Naturforschung*, **43A**, 697–726.
- Booker, J. R. and F. P. Bretherton, 1967: The critical layer for internal gravity waves in a shear flow. *J. Fluid Mech.*, **27**, 513–539.
- Bretherton, F. P., 1966: The propagation of groups of internal gravity waves in a shear flow. *Quart. J. Roy. Met. Soc.*, **92**, 466–480.
- 1971: The general linearized theory of wave propagation. *Lectures in Applied Mathematics*, **13**, 61–102.
- Broutman, D. and W. R. Young, 1986: On the interaction of small-scale oceanic internal waves with near-inertial waves. *J. Fluid Mech.*, **166**, 341–358.
- Bühler, O. and M. E. McIntyre, 1999: On shear-generated gravity waves that reach the mesosphere. Part II: Wave propagation. *J. Atmos. Sci.*, **56**, 3764–3773.
- Butler, K. M. and B. F. Farrell, 1992: Three dimensional optimal perturbations in viscous shear flow. *Phys. Fluids A*, **4**, 1637–1650.
- Cahn, A., 1945: An investigation of the free oscillations of a simple current system. *J. Meteor.*, **2**, 113–119.
- Chimonas, G. and C. O. Hines, 1986: Doppler ducting of atmospheric gravity waves. *J. Geophys. Res.*, **91**, 1219–1230.
- Drazin, P. G., 1977: On the instability of an internal gravity wave. *Proc. R. Soc. London A*, **356**, 411–432.
- Dunkerton, T. J., 1997: Shear instability of internal inertia-gravity waves. *J. Atmos. Sci.*, **54**, 1628–1641.
- Durrán, D. R., 1999: *Numerical methods for wave equations in geophysical fluid dynamics*. Springer, New York.
- Ellingsen, T. and E. Palm, 1975: Stability of linear flow. *Phys. Fluids*, **18**, 487–488.

- Farrell, B. F., 1988a: Optimal excitation of neutral rossby waves. *J. Atmos. Sci.*, **45**, 163–172.
- 1988b: Optimal excitation of perturbations in viscous shear flow. *Phys. Fluids*, **31**, 2093–2102.
- Farrell, B. F. and P. J. Ioannou, 1993a: Optimal excitation of three-dimensional perturbations in viscous constant shear flow. *Phys. Fluids A*, **5**, 1390–1400.
- 1993b: Transient development of perturbations in stratified shear flow. *J. Atmos. Sci.*, **50**, 2201–2214.
- 1996a: Generalized stability theory. Part I: Autonomous operators. *J. Atmos. Sci.*, **53**, 2025–2040.
- 1996b: Generalized stability theory. Part II: Nonautonomous operators. *J. Atmos. Sci.*, **53**, 2041–2053.
- Ferziger, J. H., 1996: Large eddy simulation. *Simulation and modeling of turbulent flows*, T. B. Gatski, M. Y. Hussaini, and J. L. Lumley, eds., Oxford University Press, 109–154.
- Fritts, D. C. and M. J. Alexander, 2003: Gravity wave dynamics and effects in the middle atmosphere. *Rev. Geophys.*, **41**, 1003, doi:10.1029/2001RG000106.
- Fritts, D. C., C. Bizon, J. A. Werne, and C. K. Meyer, 2003: Layering accompanying turbulence generation due to shear instability and gravity-wave breaking. *J. Geophys. Res.*, **108**, 8452, doi:10.1029/2002JD002406.
- Fritts, D. C., J. R. Isler, and Ø. Andreassen, 1994: Gravity wave breaking in two and three dimensions. 2. Three-dimensional evolution and instability structure. *J. Geophys. Res.*, **99**, 8109–8124.
- Fritts, D. C., J. R. Isler, J. H. Hecht, R. L. Walterscheid, and Ø. Andreassen, 1997: Wave breaking signatures in sodium densities and OH nightglow. 2. Simulation of wave and instability structures. *J. Geophys. Res.*, **102**, 6669–6684.

- Fritts, D. C. and P. K. Rastogi, 1985: Convective and dynamical instabilities due to gravity wave motions in the lower and middle atmosphere: Theory and observations. *Radio Sci.*, **20**, 1247–1277.
- Fritts, D. C., S. L. Vadas, K. Wan, and J. A. Werne, 2006: Mean and variable forcing of the middle atmosphere by gravity waves. *J. Atmos. Sol.-Terr. Phys.*, **68**, 247–265.
- Fritts, D. C. and L. Yuan, 1989a: An analysis of gravity wave ducting in the atmosphere: Eckart’s resonances in thermal and doppler ducts. *J. Geophys. Res.*, **94**, 18455–18466.
- 1989b: Stability analysis of inertio-gravity wave structure in the middle atmosphere. *J. Atmos. Sci.*, **46**, 1738–1745.
- Garcia, R. R. and S. Solomon, 1985: The effect of breaking gravity waves on the dynamics and chemical composition of the mesosphere and lower thermosphere. *J. Geophys. Res.*, **90**, 3850–3868.
- Germano, M., U. Piomelli, P. Moin, and W. H. Cabot, 1991: A dynamic subgrid-scale eddy viscosity model. *Phys. Fluids A*, **3**, 1760–1765.
- Giering, R. and T. Kaminski, 1998: Recipes for adjoint code construction. *ACM Trans. Math. Software*, **24**, 437–474.
- Hecht, J. H., 2004: Instability layers and airglow imaging. *Rev. Geophys.*, **42**, RG1001, doi:10.1029/2003RG000131.
- Hecht, J. H., C. Fricke-Begemann, R. L. Walterscheid, and J. Höffner, 2000: Observations of the breakdown of an atmospheric gravity wave near the cold summer mesopause at 54N. *Geophys. Res. Lett.*, **27**, 879–882.
- Hecht, J. H., R. L. Walterscheid, D. C. Fritts, J. R. Isler, D. C. Senft, C. S. Gardner, and J. S. Franke, 1997: Wave breaking signatures in OH airglow and sodium densities and temperatures. 1. Airglow imaging, Na lidar, and MF radar observations. *J. Geophys. Res.*, **102**, 6655–6668.

- Hines, C. O., 1960: Internal atmospheric gravity waves at ionospheric heights. *Can. J. Phys.*, **38**, 1441–1481.
- 1997a: Doppler spread parameterization of gravity-wave momentum deposition in the middle atmosphere. Part 1. Basic formulation. *J. Atmos. Sol. Terr. Phys.*, **59**, 371–386.
- 1997b: Doppler spread parameterization of gravity-wave momentum deposition in the middle atmosphere. Part 2. Broad spectra and quasi monochromatic spectra, and implementation. *J. Atmos. Sol. Terr. Phys.*, **59**, 387–400.
- Holton, J. R., 1982: The role of gravity wave induced drag and diffusion in the momentum budget of the mesosphere. *J. Atmos. Sci.*, **39**, 791–799.
- 1983: The influence of gravity wave breaking on the general circulation of the middle atmosphere. *J. Atmos. Sci.*, **40**, 2497–2507.
- Houghton, J. T., 1978: The stratosphere and mesosphere. *Q. J. R. Meteorol. Soc.*, **104**, 1–29.
- Howard, L., 1961: Note on a paper of John W. Miles. *J. Fluid Mech.*, **10**, 509–512.
- Isler, J. R., D. C. Fritts, Ø. Andreassen, and C. E. Wasberg, 1994: Gravity wave breaking in two and three dimensions. 3. Vortex breakdown and transition to isotropy. *J. Geophys. Res.*, **99**, 8125–8138.
- Klaassen, G. P. and W. R. Peltier, 1985: The onset of turbulence in finite-amplitude Kelvin-Helmholtz billows. *J. Fluid Mech.*, **155**, 1–35.
- Klostermeyer, J., 1982: On parametric instabilities of finite-amplitude internal gravity waves. *J. Fluid Mech.*, **119**, 367–377.
- 1983: Parametric instabilities of internal gravity waves in Boussinesq fluids with large Reynolds numbers. *Geophys. Astrophys. Fluid Dyn.*, **26**, 85–105.
- 1991: Two- and three-dimensional parametric instabilities in finite amplitude internal gravity waves. *Geophys. Astrophys. Fluid Dyn.*, **61**, 1–25.

- Koch, S. E., B. D. Jamison, C. Lu, T. L. Smith, E. I. Tollerud, C. Girz, N. Wang, T. P. Lane, M. A. Shapiro, D. D. Parrish, and O. R. Cooper., 2005: Turbulence and gravity waves within an upper-level front. *J. Atmos. Sci.*, **62**, 3885–3908.
- Kwasniok, F. and G. Schmitz, 2003: Radiating instabilities of internal inertio-gravity waves. *J. Atmos. Sci.*, **60**, 1257–1269.
- Landahl, M. T., 1980: A note on an algebraic instability of inviscid parallel shear flows. *J. Fluid Mech.*, **98**, 243–251.
- Lane, T. P., J. D. Doyle, R. Plougonven, M. A. Shapiro, and R. D. Sharman, 2004: Observations and numerical simulations of inertia-gravity waves and shearing instabilities in the vicinity of a jet stream. *J. Atmos. Sci.*, **61**, 2692–2706.
- Lehoucq, R. B., D. C. Sorensen, and C. Yang, 1998: *ARPACK users' guide: Solution of large-scale eigenvalue problems with implicitly restarted Arnoldi methods*. SIAM.
- Lelong, M. P. and T. J. Dunkerton, 1998a: Inertia-gravity wave breaking in three dimensions. Part I: Convectively stable waves. *J. Atmos. Sci.*, **55**, 2473–2488.
- 1998b: Inertia-gravity wave breaking in three dimensions. Part II: Convectively unstable waves. *J. Atmos. Sci.*, **55**, 2489–2501.
- Lilly, D. K., 1992: A proposed modification of the germano subgrid-scale closure method. *Phys. Fluids A*, **4**, 633–635.
- Lindzen, R. S., 1981: Turbulence and stress owing to gravity wave and tidal breakdown. *J. Geophys. Res.*, **86**, 9707–9714.
- Lombard, P. N. and J. R. Riley, 1996: Instability and breakdown of internal gravity waves. I. Linear stability analysis. *Phys. Fluids*, **8**, 3271–3287.
- Lott, F., 1997: The transient emission of propagating gravity waves by a stably stratified shear layer. *Q. J. R. Meteorol. Soc.*, **123**, 1603–1619.



- Lübken, F.-J., 1997: Seasonal variation of turbulent energy dissipation rates at high latitudes as determined by in situ measurements of neutral density fluctuations. *J. Geophys. Res.*, **102**, 13441–13456.
- 1999: Thermal structure of the arctic summer mesosphere. *J. Geophys. Res.*, **104**, 9135–9149.
- Lübken, F.-J. and U. von Zahn, 1991: Thermal structure of the mesopause region at polar latitudes. *J. Geophys. Res.*, **96**, 20841–20857.
- Machenhauer, B., 1977: On the dynamics of gravity oscillations in a shallow water model, with application to normal mode initialization. *Contrib. Atmos. Phys.*, **50**, 253–271.
- Mathews, J. and R. Walker, 1970: *Mathematical methods of physics*. Addison-Wesley, New York.
- McComas, C. H. and F. P. Bretherton, 1977: Resonant interaction of oceanic internal waves. *J. Geophys. Res.*, **82**, 1397–1412.
- McFarlane, N. A., 1987: The effect of orographically excited gravity wave drag on the circulation of the lower stratosphere and troposphere. *J. Atmos. Sci.*, **44**, 1775–1800.
- Medvedev, A. S. and G. P. Klaassen, 1995: Vertical evolution of gravity wave spectra and the parameterization of associated gravity wave drag. *J. Geophys. Res.*, **100**, 25841–25854.
- Meneveau, C., T. S. Lund, and W. H. Cabot, 1996: A lagrangian dynamic subgrid-scale model of turbulence. *J. Fluid Mech.*, **319**, 353–385.
- Mied, R. P., 1976: The occurrence of parametric instabilities in finite amplitude internal gravity waves. *J. Fluid Mech.*, **78**, 763–784.
- Miles, J. W., 1961: On the stability of heterogeneous shear flows. *J. Fluid Mech.*, **10**, 496–508.

- Moffat, H. K., 1967: The interaction of turbulence with strong shear. *Atmospheric Turbulence and Radio Wave Propagation*, A. M. Yaglom and V. I. Tatarskii, eds., Nauka, 139–161.
- Müllemann, A., M. Rapp, and F.-J. Lübken, 2003: Morphology of turbulence in the polar summer mesopause region during the MIDAS/SOLSTICE campaign 2001. *Adv. Space Res.*, **31**, 2069–2074.
- Müller, P., G. Holloway, F. Henyey, and N. Pomphrey, 1986: Nonlinear interactions among internal gravity waves. *Rev. Geophys.*, **24**, 493–536.
- Orr, W. M., 1907: The stability or instability of the steady motions of a perfect liquid and of a viscous liquid. Part I: A perfect liquid. *Proc. Roy. Irish Acad.*, **27A**, 9–68.
- Palmer, T. N., G. J. Shutts, and R. Swinbank, 1986: Alleviation of a systematic westerly bias in general circulation and numerical weather-prediction models through an orographic gravity wave drag parametrization. *Q. J. R. Meteorol. Soc.*, **112**, 1001–1039.
- Pavelin, E., J. A. Whiteway, R. Busen, and J. Hacker, 2002: Airborne observations of turbulence, mixing, and gravity waves in the tropopause region. *J. Geophys. Res.*, **107**, doi:10.1029/2001JD000775.
- Rossby, C. G., 1938: On the mutual adjustment of pressure and velocity distribution in certain simple current systems, II. *J. Mar. Res.*, **1**, 239–263.
- Schmid, P. J. and D. S. Henningson, 2001: *Stability and transition in shear flows*. Springer, New York.
- Scinocca, J. F. and N. A. McFarlane, 2000: The parametrization of drag induced by stratified flow over anisotropic orography. *Q. J. R. Meteorol. Soc.*, **126**, 2353–2393.
- Shapiro, M. A., 1980: Turbulent mixing within tropopause folds as a mechanism for the exchange of chemical constituents between the stratosphere and the troposphere. *J. Atmos. Sci.*, **37**, 994–1004.

- Sonmor, L. J. and G. P. Klaassen, 1997: Toward a unified theory of gravity wave stability. *J. Atmos. Sci.*, **54**, 2655–2680.
- Strelnikov, B., M. Rapp, and F.-J. Lübken, 2003: A new technique for the analysis of neutral air density fluctuations measured in situ in the middle atmosphere. *Geophys. Res. Lett.*, **30**, 2052, doi:10.1029/2003GL018271.
- Tapp, M. C. and P. W. White, 1976: A non-hydrostatic mesoscale model. *Quart. J. Roy. Meteor. Soc.*, **102**, 277–296.
- Temperton, C., 1988: Implicit normal mode initialization. *Mon. Wea. Rev.*, **116**, 1013–1031.
- Trefethen, L. N., A. E. Trefethen, S. C. Reddy, and T. A. Driscoll, 1993: Hydrodynamic stability without eigenvalues. *Science*, **261**, 578–584.
- Tribbia, J. J., 1984: A simple scheme for higher order nonlinear normal mode initialization. *Mon. Wea. Rev.*, **112**, 278–284.
- Vadas, S. L. and D. C. Fritts, 2001: Gravity wave radiation and mean responses to local body forces in the atmosphere. *J. Atmos. Sci.*, **58**, 2249–2279.
- Warner, C. D. and M. E. McIntyre, 2001: An ultrasimple spectral parameterization for nonorographic gravity waves. *J. Atmos. Sci.*, **58**, 1837–1857.
- Werne, J. and D. C. Fritts, 1999: Stratified shear turbulence: Evolution and statistics. *Geophys. Res. Lett.*, **26**, 439–442.
- Whiteway, J. A., E. G. Pavelin, R. Busen, J. Hacker, and S. Vosper, 2003: Airborne measurements of gravity wave breaking at the tropopause. *Geophys. Res. Lett.*, **30**, 2070, doi:10.1029/2003GL018207.
- Winters, K. B. and E. A. D’Asaro, 1994: Three-dimensional wave instability near a critical level. *J. Fluid Mech.*, **272**, 255–284.
- Yau, K.-H., G. P. Klaassen, and L. J. Sonmor, 2004: Principal instabilities of large amplitude inertio-gravity waves. *Phys. Fluids*, **16**, 936–951.

- Yuan, L. and D. C. Fritts, 1989: Influence of a mean shear on the dynamical instability of an inertio-gravity wave. *J. Atmos. Sci.*, **46**, 2562–2568.
- Zhou, X.-L., J. R. Holton, and G. L. Mullendore, 2002: Forcing of secondary waves by breaking of gravity waves in the mesosphere. *J. Geophys. Res.*, **107**, doi:10.1029/2001JD001204.

# Erklärung

Ich erkläre, dass ich die eingereichte Habilitationsschrift selbständig und ohne fremde Hilfe verfasst habe, andere als die von mir angegebenen Hilfsquellen und Hilfsmittel nicht benutzt und die den benutzten Werken inhaltlich oder wörtlich entnommenen Stellen als solche kenntlich gemacht habe.

Kühlungsborn, 20. März 2006



# Tabellarischer Lebenslauf

## Persönliche Daten

Name	Achatz
Vornamen	Ulrich Christian Konrad
Geburtsdatum	31. Oktober 1963
Geburtsort	München
Familienstand	verheiratet mit Sabine Titz-Achatz, geb. Titz
Kinder	Benedikt Achatz, geb. am 25. Juli 1990 Frederike Achatz, geb. am 4. Februar 1998
Anschrift	Am Molli 9, 18225 Kühlungsborn

## Schulbesuche

1969 – 1974	Deutsche Botschaftsschule in Istanbul/Türkei
1974 – 1982	Chiemgaugymnasium in Traunstein
Juni 1982	Allgemeine Hochschulreife

## Studium

Oktober 1982 – Juli 1984	Studium der Physik an der Ruprecht-Karls-Universität Heidelberg
Juli 1984	Vordiplom in Physik
August 1984 – Juni 1985	Studium der Physik an der University of Nebraska, Lincoln, NE, USA
Oktober 1985 – März 1989	Studium der Physik an der Rheinischen Friedrich-Wilhelms-Universität Bonn

März 1988 – Februar 1989	Diplomarbeit am Max-Planck-Institut für Radioastronomie in Bonn
März 1989	Diplom in Physik

### **Promotion, Zivildienst und Berufsweg**

April 1989 – September 1989	Beginn der Doktorarbeit am Max-Planck-Institut für Radioastronomie in Bonn
Oktober 1989 – Februar 1990	Zivildienst am Kolpingwerk in Köln
März 1990 – Juli 1992	Fortsetzung der Doktorarbeit am Max-Planck-Institut für Radioastronomie in Bonn
Juli 1992	Promotion zum Dr. rer. nat. an der Rheinischen Friedrich-Wilhelms-Universität Bonn
August 1992 – Januar 1993	Wissenschaftlicher Mitarbeiter am Max-Planck-Institut für Radioastronomie in Bonn
seit Februar 1993	Wissenschaftlicher Mitarbeiter am Leibniz-Institut für Atmosphärenphysik an der Universität Rostock in Kühlungsborn
August 1998 – Juni 1999	Gastwissenschaftler am Königlich-Niederländ. Meteorologischen Institut (KNMI) in De Bilt, Niederlande